

SQUID Geomagnetic Signal Analysis and Modelling of Schumann Resonances in the Earth-Ionosphere Cavity

Christian Kwisanga

*Dissertation presented for the Degree of Doctor of Philosophy in the Faculty of Engineering
at Stellenbosch University*



Supervisor:
Prof. Coenrad J. Fourie

March 2016

Declaration

By submitting this dissertation electronically, I declare that the entirety of the work contained therein is my own original work, that I am the sole author thereof (save to the extent explicitly otherwise stated), that reproduction and publication thereof by Stellenbosch University will not infringe any third party rights and that I have not previously in its entirety or in part submitted it for obtaining any qualification.

Signature: C. Kwisanga

Date: March 2016

Acknowledgements

I wish to thank my supervisor Prof. Coenrad Fourie for his guidance, and all the people close or afar who made this project possible.

I would like to thank my colleagues in the postgrad office E211A in the E&E building for the support they gave me during these years: Thanks Maguu for your wisdom and for your encouragements, thanks Bakolo for your kindness and for introducing me to *Lyx*. Thanks Lucas for being very helpful and for translating my abstract to Afrikaans. Thanks Emile, Thabang, Joey, Kyle and Ruben for your support and for your kindness.

I would not forget friends I made in the department; thanks Mutonx for all the discussions and help that I could get from you, You really made me take a giant's leap with my work. As far as I remember, I cannot even count the number of *Windhoek* glasses that we had together. Thanks for being a fantastic person. Thanks Joely for being very smart, our discussions were always enriching and insightful. I gained a lot from you. Thanks Isingizwe for being such a supportive and very helpful brother. You are someone I could really count on anytime. Thanks Temwani for being a good friend, I gained a lot from you, I also would like to express my gratitude towards the Rwandan community in Stellenbosch and friends who made this journey happier; Kalenga, you have been a real friend all along, thank you for the bundle of joy and happiness that you are. Thank you *Canticum Novum*, you guys made my time in Stellies filled with so many good memories!

Last and not least goes to my family; thanks Mzee for taking me to school early, I hope I could make you proud where you are. Thanks Mama for being there for me, for your prayers and for being such a caring parent, I wouldn't be where I am if it weren't for you. Thanks, Kwizera and Kwitonda, you guys make me proud and every time I felt like giving up, you were my sources of strength to persevere.

Thank you all, dear friends from nearby or afar, who made this journey more enjoyable. I really can't thank you enough!

May everlasting blessings be with all of you!

Abstract

Due to its extreme sensitivity to magnetic flux, vast dynamic range and wide bandwidth, the Superconductive Quantum Interference Device (SQUID) is at the frontier of all existing magnetic field sensors. The direct current SQUID principle is based on quantised flux induced current tunnelling across weak link barriers embedded in a superconductive ring. The SQUID can sense a field of the order of 10^{-15} T, in the same range as the neuron-cell magnetic activity and operates from quasi-dc to the GHz range. The extreme versatility of the SQUID technology makes it an instrument of choice in state-of-the-art applications including monitoring the Earth's magnetic field.

The geomagnetic field is by far one of the most complex systems, as it encompasses field generation phenomena inside the Earth, and the extension of the field into the near-Earth environment, where interaction of ions from the Sun, solar magnetic field and Earth's magnetic field create a highly dynamic plasma system controlled by the magnetic field. The currents generated in the geomagnetic system induce a magnetic field to the Earth, which are measured in the Ultra Low Frequency (ULF [$3 \times 10^{-3} - 3$] Hz) domain. Between the solid Earth and the layer of ionised gases in the atmosphere, a natural potential difference builds up. Breakdown occurs in forms of short-lived intense channels of current between the Earth and the cloud and beyond: Lightning. There is approximately fifty lightning flashes from approximately a thousand active thunderstorms worldwide every second. From this random generation process emanates electromagnetic radiation that propagates around the Earth, and interferes to form a permanent background noise in the Extremely Low Frequency (ELF [$3 - 3000$] Hz), where it forms spectra of highly damped resonances observable in the frequency range $0 - 100$ Hz, the Schumann resonances.

In quiet magnetospheric conditions, Schumann resonances behave as transverse magnetic components, where the electric field is radial and magnetic field is tangential to the Earth's surface. The Schumann resonances' intensity is associated with the thunderstorm sources. The interdependence between tropical temperature and thunderstorm generation processes has led to an investigation of the link between global warming and the intensity of the first Schumann resonance. A connection between Schumann resonance disturbances and anomalies in the ionosphere and prior to strong earthquakes has also been observed.

Therefore, monitoring the Earth's magnetic field for natural disaster mitigation has been one of the main priorities of the SQUID network established in partnership between France and South Africa. This project correlates the SQUID response of two SQUIDs installed at *Laboratoire Souterrain à Bas bruit* in Rustrel, France and at the Space Science directorate of the South African National Space Agency (SANSA) located in Hermanus, South Africa. In this project, along with data spectral analysis, a Finite-Difference Time-Domain (FDTD) based simulation of the entire Earth-Ionosphere system is done using commercially available software: CST Microwave Studio.

Opsomming

Die Supergeleidende Kwantum Interferensietoestel (SQUID) is op die voorfront van alle bestaande magneetveldsensors, omdat dit uiters sensitief is vir magnetiese vloed en 'n breetmeetbare het. Die gelykstrom SQUID is gebaseer op die beginsel dat kwantifiseerde vloed stroom indusseer wat tonnel deur swak-kontak versperrings binne 'n supergeleidende ring. Die SQUID kan veld tot die orde van $10^{-15}T$ waarneem, wat in dieselfde orde is as neuronaktiwiteit en funksioneer vanaf kwasi-gelykstrom tot THz frekwensies. Die uiterste veelsydigheid van die meettegniek maak die SQUID 'n instrument van keuse in die voorste toepassings, insluitend die monitering van die Aarde se magneetveld.

Die Aarde se magneetveld is 'n baie komplekse stelsel, omdat dit veld-opwekkingsverskynsels binne die Aarde, asook die pad van die veld in die naby-aarde omgewing behels. Interaksie tussen ione van die Son, Son se magneetveld en Aarde se magneetveld skep 'n hoogs dinamiese ioniese gassisteem wat deur die magneetveld beheer word. Die strome wat in die geomagnetiese stelsel genereer word indusseer 'n magneetveld tot die Aarde, wat in die ultra-lae frekwensiegebied (ULF [$3 \times 10^{-3} - 3$] Hz) gemeet word. 'n Potensiaalverskil word opgebou tussen die soliede Aarde en die laag van ioniese gasse in die atmosfeer. Afbreking vind plaas deur middle van 'n kort, intense stroom tussen wolke en die Aarde en so meer: weerlig. Daar is na beraming vyftig weerligflitse van ongeveer 'n duisend aktiewe donderstorms per sekonde wêreldwyd. Vanuit hierdie toevals-opwekkingproses word elektromagnetiese bestraling uitgestraal wat rondom die Aarde propageer, en interferensie veroorsaak wat 'n permanente agtergrondruis in die ekstreemlaagfrekwensie band (ELF [$3 - 3000$] Hz) skep en 'n spektrum van hoogs gedempte resonansies skep wat waargeneem kan word in die $0 - 100$ Hz frekwensieband – die Schumann-resonansies.

In 'n stil magnetosfeer toestand kom die Schumann-resonansies voor soos transversale magneetveldkomponente, waar die elektriese veld radiaal is en magneetveld tangent is. Die intensiteit van Schumann-resonansies word assosieer met die bronne van die donderstorms. Die verbinding tussen tropiese temperature en opwekkingsprosesse van donderstorms het gelei tot 'n ondersoek in die afhanklikheid tussen aardverwarming en die intensiteit van die eerste Schumann-resonansie. 'n Verband met steurnisse in Schumann-resonansies is ook vasgestel. Dit is ook waargeneem dat anomaliteite in die ionosfeer Schumann-resonansies beïnvloed.

Die verligting van natuurrampe deur monitering van die Aarde se magneetveld is 'n hoofprioriteit van die SQUID-netwerk wat gevestig is in die samewerking tussen Frankryk en Suid-Afrika. Die projek korreleer die SQUID-respons van twee SQUIDs, wat installeer is by *Laboratoire Souterrain à Bas bruit* in Frankryk en by die Ruimtetwetenskap Direkoraat van die Suid-Afrikaanse Nasionale Ruimteagentskap (SANSA). Spektrale analise van data is gedoen asook Eindige-Verskil Tydgebied (FDTD) gebaseerde simulاسie van die Aarde-ionosfeerstelsel as geheel, met behulp van 'n kommersieël-beskikbare sagtewarepakket: CST Microwave Studio.

Contents

1	Introduction	1
1.1	Background	1
1.2	Motivation	3
1.3	Objectives	4
1.4	Contributions	4
1.5	Research Output	5
1.6	Outline of the Thesis	5
2	Overview of SQUID Magnetometers	7
2.1	Introduction	7
2.2	General Theory of Superconductivity	7
2.2.1	Solving Maxwell's equations	8
2.2.2	Diamagnetism and Meissner Effect	9
2.2.3	Flux Quantisation	10
2.2.4	Flux Vortices in Type II Superconductors	11
2.3	Josephson Junction	12
2.3.1	Intensity Driven Junction	13
2.3.2	Voltage Driven Junction	14
2.4	The <i>dc</i> SQUID	14
2.5	RCSJ Approximation	16
2.6	<i>dc</i> SQUID as a Magnetometer	18
2.6.1	Flux-locked Loop (FLL)	18
2.6.2	<i>dc</i> SQUID Magnetometer Design	20
2.7	Conclusion	20

3	Background of Analytical and Numerical Electromagnetic Propagation Models	22
3.1	Introduction	22
3.2	Solving Maxwell's Equations in Spherical Coordinates	23
3.3	Waveguide Analytical Approach	23
3.3.1	Spherical Cavity Model	23
3.3.2	Schumann's Formulation [1]	25
3.3.3	Stratified Ionosphere Model [2]	26
3.4	Finite-Difference Time-Domain (FDTD) Method	29
3.4.1	Maxwell's Equations and Yee Algorithm	30
3.4.2	Finite Differences	31
3.4.3	Yee's FDTD algorithm	32
3.4.4	Dispersion and Stability Conditions	32
3.4.5	Absorbing Boundary Conditions (ABCs)	33
3.5	Conclusion	35
4	Modelling of the Uniform Earth-Ionosphere Cavity Using CST Microwave Studio®	36
4.1	Introduction	36
4.2	CST Microwave Studio	36
4.2.1	Simulation Parameters	38
4.3	Simulation Results	40
4.3.1	Propagation Model Validation	40
4.3.2	Electric and Magnetic Wave Propagation	41
4.3.3	Electric and Magnetic field spectra: Schumann Resonances	44
4.4	Conclusion	48
5	Geomagnetic Field Measurement in the ELF range	49
5.1	Introduction	49
5.2	The Quasistatic Geomagnetic Field	49
5.3	Origins of the Geomagnetic Field in the ELF Range	52
5.3.1	Solar Activity	52
5.3.2	Near-Earth Environment	53
5.3.3	The Ionosphere and Solid Earth Waveguide	55

5.3.4	Sources of Excitation	55
5.4	Experimental Characteristics of SR	55
5.4.1	Resonance Frequency	56
5.4.2	Quality Factor	57
5.4.3	Intensity	57
5.5	Magnetometers in the ELF Range	58
5.5.1	Induction Coil Magnetometer	59
5.5.2	Fluxgate Magnetometers (FGM)	61
5.6	SQUID Geomagnetometers	63
5.7	The <i>Laboratoire Souterrain à Bas Bruit, Rustrel</i> (LSBB)	63
5.7.1	Site Description	63
5.7.2	Track Record of the [SQUID] ² System	64
5.8	SANSA Hermanus	65
5.8.1	Site Description	65
5.8.2	Facilities Description	66
5.8.3	HSQH System Description	66
5.9	Conclusion	66
6	Spectral Analysis of SQUID Geomagnetic Components	70
6.1	Introduction	70
6.2	Continuous Fourier Transform	70
6.2.1	Periodic signals	71
6.2.2	Non-Periodic signals	74
6.3	Discrete Fourier Transform	75
6.3.1	Sampling theorem	75
6.3.2	The Fast Fourier Transform (FFT)	76
6.4	Random Signal Processing	76
6.4.1	Random variables	77
6.4.2	Energy and Power Spectral Densities	78
6.4.3	Windowing, Averaging and Overlapping Segments: The Welch's Method	79
6.5	Practical implementation of Welch's Method	81
6.5.1	Window parameters	81

6.5.2	Overlapping parameters	84
6.5.3	Computation of Spectral Parameters	87
6.5.4	Averaging of segment spectra	87
6.5.5	Spectra Representation	88
6.6	Conclusion	89
7	Polarisation Properties of SQUID Geomagnetic Horizontal Components	92
7.1	Introduction	92
7.2	Computation of Polarisation Properties	93
7.2.1	Coherence	94
7.2.2	Ellipticity	95
7.2.3	Phase Difference and Ellipticity	96
7.2.4	Inclination Angle of the polarisation Ellipse	97
7.3	Application to LSBB Datasets	97
7.3.1	Coherence Measure Spectra	97
7.3.2	Validation of the Coherence Matrix Method	99
7.4	Signal-to-noise ratio (<i>snr</i>)	104
7.5	Conclusion	105
8	Correlation of SQUID Datasets in LSBB and HERMANUS with FG and ICM Networks	111
8.1	Introduction to Dataset Correlation	111
8.2	Time Correlation SQUID-FGM Datasets	113
8.3	Schumann Resonances	113
8.3.1	Quiet Day Spectra at LSBB	113
8.3.2	ELF SQUID-ICM Correlation	117
8.3.3	SQUID Dataset Correlation in LSBB and Hermanus	121
8.3.4	Few Characteristics of HSQH spectra in 2013	123
8.4	Conclusion	123
9	General Discussion	126
9.1	Introduction	126
9.2	The Numerical Model	126
9.3	Polarisation Analysis	127
9.4	SQUID signal correlation	128
9.5	Conclusion	128

10 General Conclusion and Recommendations

129

List of Figures

2.1	Characteristic resistance-temperature curve for a Superconductor. There is a sharp transition to zero resistance at T_c	8
2.2	Meissner effect for type I superconductor. A normal metallic material (left) and a <i>type I</i> superconductor material (right)	9
2.3	Meissner effect in <i>type I</i> and <i>II</i> superconductors.	10
2.4	Current vortices in type II superconductors in the mixed state. Magnetic flux density B , charge density n_s and vortex current density j are represented	12
2.5	Josephson junction. S represents the superconductive component and I the insulator.	12
2.6	Voltage variation as a function of the phase of the <i>dc</i> JJ. Note that $V_{J0} = \Phi_0 I / (\pi I_B)$ is the peak amplitude across the JJ.	13
2.7	SQUID layout and characteristic current - voltage curve for an overdamped JJ. $J_{1,2}$ are Josephson junctions 1 and 2. S represents the superconductive component and I is the insulator.	15
2.8	The <i>dc</i> SQUID (a) the diagram representation with R, C the JJ resistance and capacitance respectively, (b) I-V characteristic at integer and half integer values of applied flux set by the bias current I_B , and (c) voltage versus flux ratio Φ/Φ_0	16
2.9	Flux-locked loop for a <i>dc</i> SQUID. I_B is the bias current applied to the SQUID and V_0 the output voltage of the system	17
2.10	Representation of magnetic flux modulation for a SQUID magnetometer in a lock-in amplifier. The output voltage V_L is a linear response to the flux applied to the SQUID.	18
2.11	Typical design of a Low- T_c <i>dc</i> SQUID (a) the pick-up coil in the middle of the area lies over the superconductor layer and the JJs at the left (b) Zoomed-in view of the JJs and resistance shunts [3].	19
3.1	Spherical coordinate (R, θ, ϕ) representation. The radial component is in R direction and the angular components are θ in the meridional (elevational) azimuthal direction and ϕ in the equatorial azimuthal direction.	24
3.2	Angular solution for zonal harmonic series. The source is located at the meridional pole position $\theta = 0$. The azimuthal equatorial magnetic field $B_\phi = \mu_0 H_\phi$ and the radial electric field are depicted [4].	28

3.3	Yee cell showing the alternating electric and magnetic fields in the (y,z) plane. . . .	31
4.1	Concentric shell layout drawn in CST MWS for FDTD simulation of the E-I system. The radius of the inner shell is the Earth radius $R_E = 6370$ km. Each layer represented is 10 km thick. The light-grey colored layers represent the lower σ profile, and the dark ones the higher σ profile. Both profiles are separated at the <i>knee</i> height. The triangle at the right side depicts the position of the discrete excitation port. E and H field probes are placed at 1 Mm interval from the source along the arc of the sphere in the (x, y) plane, in the light grey area.	37
4.2	Knee model as introduced by [5]. Values of $\zeta_{0,1}$ and σ are derived from [6]. The solid line represents the model and the hollow dots represent experimental data.	38
4.3	A typical ELF transient return-stroke model (a) in time and (b) in frequency domain. Its intensity is ten times higher than a typical lightning return stroke defined in [7]. .	39
4.4	Graph representing the rate of attenuation of \mathbf{E} versus frequency in the E-I cavity as simulated with 3D-FDTD (round dots). The straight line represents the experimental Ishaq-Jones' attenuation rate [8].	41
4.5	Propagation of vertical \mathbf{E} (top panel) and horizontal \mathbf{H} (bottom) waveforms originating from an ELF transient the E-I cavity. The pulses recorded at distances of 5, 10, 15 and 20 Mm are drawn in thick line.	42
4.6	Attenuation of the peak amplitude of the \mathbf{E} and \mathbf{H} waves in dB scale.	43
4.7	\mathbf{E} and \mathbf{H} pulse propagation in time measured at field detectors placed at 10Mm (thick line) and 20 Mm (thin line).	43
4.8	Amplitude spectra of \mathbf{E} and \mathbf{H} . The unit for both is arbitrary, hence $1 \text{ a.u.}_1 = 10^{-4}$ and $1 \text{ a.u.}_2 = 2 \times 10^{-7}$	45
4.9	Peak SR frequency and amplitude and Q-factor variation of the \mathbf{E} and \mathbf{H} spectra versus the source-observer distance. The source is located in Cartesian position 0 Mm. The labels for the modes are represented in 4.9b.	46
5.1	Earth's magnetic field configuration. Dipolar magnetic field of the Eath with S_m and N_m are respective North and South magnetic poles.	50
5.2	Ground geomagnetic field. In (a), the directions are $X \equiv \textit{South} - \textit{North}$, $Y \equiv \textit{West} - \textit{East}$ and $Z \equiv \textit{Zenith} - \textit{Nadir}$. The parameters represented in maps (b,c,d) were calculated for IGRF model in 1990 [9].	51
5.3	Full range of amplitude spectrum of the Earth's magnetic field showing phenomena with cycle period from 10 million years to 10^{-4} s. The range of interest here is the tiny portion of the lower ELF ranging from $[1s > T > 0.01s]$ indicated as <i>Schumann resonances</i> [10].	52
5.4	Overview of 30-day averaged sunspot number plotted for a 24-year duration from 1991 [11]. The current solar cycle (2009 – 2020) is the 24 th	53

5.5	Sketch showing the structure of the magnetosphere with its electric current system. Note that the dayside is towards the left and the nightside is towards the right of the image [12].	54
5.6	Amplitude spectrum of \mathcal{H} component showing typical (background signal) SR spectrum detected from Antarctica [4].	58
5.7	Magnetisation process of a ferroelectric material. Magnetic saturation is observed in the lower panel of (b). The upper panel of (b) shows a completely demagnetised system.	60
5.8	Depiction of an angular pattern for an inductance coil magnetometer measured for symmetric and asymmetric winding. In this case, sensitivity is maximum for waves that propagate along 90° and 270° direction and zero for 0 and 180° direction. Sensitivity also depends on the symmetry of the coil windings [13].	61
5.9	Designs of fluxgate magnetometers with different shapes of ferromagnetic cores (a) a double bar and (b) a ring core [14].	62
5.10	Fluxgate magnetometer working principle shown in two columns: At the left is the FGM working without any external field and the right, with the magnetic field applied. [15].	62
5.11	Working range and sensitivity of different ELF magnetometers. Magnetoresistive (MR sensors) represented in (b) are not described in this work. [14]	63
5.12	The <i>Grande Montagne</i> , the mountain in which the LSBB capsule system is built. The network of tunnels is shown with arrows, (A) entrance, (B) capsule (C) emergency exit and (D) top of the mountain.	64
5.13	Depiction of the SQUID system in Hermanus (a) non-magnetic hut housing the SQUID (b) A view inside the hut showing the full installation of SQUID in the Dewar flask (c) a close-up view of the Programmable Feedback Loop (PFL) controllers [16].	67
5.14	The Hermanus SQUID network system as it was designed by van Vuuren [17].	68
6.1	Representation of the basis functions $\cos(\omega_0 t)$ and $\sin(\omega_0 t)$. T_0 is the period.	71
6.2	Drawing of the overlapping of segments of the signal $y(n)$	80
6.3	Comparative performance of Hamming (solid line) and Hanning (dotted line) windows in the time domain.	82
6.4	Window function spectra for random signal processing	83
6.5	Amplitude flatness versus overlapping rate for the Hanning window. The overlap increment step is $n/10N$ for (a) and is added at each step from bottom to top. The AF is reached at 50% of the overlapping.	85
6.6	Amplitude flatness versus overlapping rate for the <i>Kaiser10</i> window. The overlap increment step is $n/10N$ for Fig. 6.6a evolving from bottom to top. The AF is reached at 66.6% of the overlapping.	86

6.7	Comparative variation of the amplitude flatness (AF) and the overlap correlation (OC) for the Hanning and the Hamming windows.	86
6.8	Perspective representation of geomagnetic \mathcal{H} spectra PSD on 2007–11–07 at 1324 UT (the daily maximum power). The total length of the dataset is $N = 4096$ and $M = 1, 4, 16, 32, 64, 128$ represents the number of segments averaged. Notice the powerful peak at 50-Hz corresponding to the power-grid induced magnetic component. The graphs are offset to create an effect of 3D depth for clarity.	88
6.9	Daily \mathbf{H} spectra represented in the 3 directional components; North-South, East-West and Vertical Z axes. In (a),(b) and (c), the power is represented in dB scale .Datasets are taken on 2007-11-07 and represented in function of Universal Time (UT).	91
7.1	Sketch of the elliptical polarisation of the horizontal \mathbf{H} , where a, b represent the semi-major and semi-minor axes of the ellipse. Axes x and y represent the WE and SN directions. θ represents the inclination angle of the major axis of the ellipse to the x axis. The direction of polarisation represented here is right handed in the direction of z	96
7.2	Spectrograms showing the variation in frequency and time of the spectra of \mathcal{H} on a quiet day 2007-09-26 (a) the coherent power spectral density (b) coherence (c) the ellipticity of the wave and (d) the polarisation ellipse inclination	99
7.3	Frequency response of the resonator used for polarised event counting. The top graph represents the gain and the bottom the phase variation at the bottom for $f_0 = 8$ Hz, $r = 99.9\%$ and a sample size $N = 4096$. (b) The spectra of the H_{EW} and H_{NS} signal from 2007 – 09 – 26 13 : 36UT at LSBB, filtered through a resonator at 8Hz and (b) phase difference between the components.	100
7.4	The spectra of \mathcal{H} measured on the 2007-09-09 and 2007-09-27 sampled. 13:36 UT along with data sampled on 2007-09-01 and 2007-09-05	102
7.5	Classification of polarised events for the two datasets 2007-09-09 and 2007-09-09-26 in the range 7.6 - 7.9 Hz.	106
7.6	Modes of polarisation taken from the maximal amplitude events in the most populous of the ellipticity categories displayed in Fig. 7.5	107
7.7	The LHP and RHP mode distribution across the first SR on the two datasets on 2007-09-09 and 2007-09-26 described in Fig. 7.5	108
7.8	Comparative representation of bandpass filtered raw magnetic signal with the averaged ellipticity of the signal on (a) day 1 and (b) day 2	108
7.9	Comparative representation of bandpass filtered raw magnetic signal with the of the variation inclination of the signal on (a) day 1 and (b) day 2 sampled at 13:36 UT for 24 min	109
7.10	Signal-to-noise ratios of geomagnetic signal in two regimes, regime 1 and 2	109
7.11	Spectra of the incoherent magnetic signals on four quiet days of September 2007	110

8.1	Geographical location of the different magnetometer sites that will be used for time correlation. The <i>Intermagnet</i> together with SQUID network are represented. The arrows indicate the position of the <i>Intermagnet</i> sites considered for the time correlation. The flashes indicate the position of the maximal Thunderstorm activity (TSA). Adapted from [18]	112
8.2	Magnetic time variation for \mathcal{H} and Z datasets on 2013-01-25 and 2013-01-26 at <i>Intermagnet</i> stations CLF, EBR, FUR, HBK, HER and SQUID stations at LSBB and HSQH. At 2013-01-25 16:30 UTC is an onset of a substorm [$Dst < 50$ nT, $Kp < 4$].	114
8.3	Spectral properties of \mathcal{H} obtained from 2007 – 11 – 07 datasets at LSBB. Each graph represents 24 min. of data. (a) polarised PSD (b) signal-to-noise power ratio (c) ellipticity and (d) the inclination of the wave polarisation ellipse. The nuances of black and grey are for visual clarity.	115
8.4	Ten day [SQUID] ² signal-to-noise power ratio from 2007 – 11 – 01 to 2007 – 11 – 10 encompassing the quietest days of the same month	117
8.5	Cumulated power densities of \mathcal{H} spectra on 2008 – 08 – 21 obtained at CARISMA stations.	118
8.6	Power density and ellipticity daily variation spectrograms of \mathcal{H} at (a) MSTK and (b) THRF, on 2008 – 08 – 21.	119
8.7	Comparative graphs between CARISMA and [SQUID] ² \mathcal{H} power and ellipticity spectra on 2008 – 08 – 21.	120
8.8	Stacked representation of diurnal variation of SR peak frequency of the \mathcal{H} component at MSTK, THRF and LSBB on 2008 – 08 – 21. df represents the difference between the peak frequency at each sampled spectrum and the minimum frequency of the first SR measured in the day	122
8.9	\mathcal{H} SQUID data taken at HER and at LSBB taken in the same instant. The durations are indicated in the graph windows in hours.	122
8.10	\mathcal{H} SQUID data taken simultaneously at Hermanus and LSBB on 2013 – 04 – 20 06 – 0800 UT. The durations are indicated in the labels.	123
8.11	Graph showing SRs observed in \mathcal{H} . component in HSQH	124
9.1	Comparison between SR long-term resonance parameters from [19] with FDTD data.	127

Nomenclature

1D	one-dimension
2D	two-dimension
3D	three-dimensions
<i>ac</i>	Alternating current
a.u.	Arbitrary unit
<i>B</i>	Magnetic density intensity
B	Magnetic flux density vector
BCS	Bardeen Cooper and Schriffer theorem
BPF	band pass filter
BW	Bandwidth
CARISMA	Canadian Array for Realtime Investigations of Magnetic Activity
CLF	Chambon-la-Forêt (France)
CM	Coherence Matrix
CST-MWS [®]	Computer Simulation Technology - MicroWave Studio
<i>dc</i>	Direct current
DFT	Direct Fourier Transform
<i>Dst</i>	<i>Daily Storm Time</i> index
E or \vec{E}	Electric field
<i>E</i>	Electric field intensity
EBR	Ebro (Spain)
EE - SU	Electrical and Electronics Engineering, Stellenbosch University
E-I	Earth-Ionosphere

ELF	Extremely Low Frequency [3 – 3000] Hz
EM	Electromagnetic
\mathcal{F}	Geomagnetic total intensity
FDTD	Finite Difference Time Domain
<i>High</i> – T_c	High critical temperature
<i>Low</i> – T_c	Low critical temperature
FFT	Fast Fourier Transform
FGM	Fluxgate Magnetometer
Fig.	Figure
FLL	Flux locked loop
FLL	Flux locked loop
FUR	Furstenfeldenbruck (Germany)
GFZ	GeoForschungsZentrum [German Research Centre for Geosciences]
G-L	Ginsburg-Landau
GMF	Geomagnetic field
GOES	Geostationary Operational Environmental Satellite
\mathbf{H} or \vec{H}	Magnetic field
\mathcal{H}	Geomagnetic horizontal intensity
H	Magnetic field intensity
HBK	Hartebeetshoek (South Africa)
HER	Hermanus (South Africa)
HSQH	<i>high</i> – T_c SQUID at Hermanus
$I - V$	Current-Voltage
IAR	Ionospheric Alfvén resonance
ICM	Induction coil magnetometer
IDFT	Inverse Direct Fourier Transform
i.e.	<i>id est</i> , That is ...
IGRF	International Geomagnetic Reference Field
JJ	Josephson Junction

K_p	Index of disturbance of the geomagnetic field
LHP	Left hand polarization
LSBB	Laboratoire souterrain à bas-bruit
MSTK	Ministik Lake
NENBW	Normalised Equivalent Noise Bandwidth
NMR	Nuclear magnetic resonance
PBA	Perfect Boundary Approximation [®]
PDE	Partial differential equation
PEC	Perfect Electrical Conductor
PFL	Programmable feedback loop
PML	Perfectly Matched Layer
P-wave	Primary seismic wave
PSD	Power Spectral Density
Q	Quality factor
RAM	Random Access Memory
RCSJ	Resistively and Capacitively Shunted Junction
R_E	Earth's radius
RGB	Red-Green-Blue
RHP	right hand polarization
r_{ov}	recommended overlap
SAA	Southern Atlantic Anomaly
SANSA	South African National Space Agency
snr	Signal-to-noise ratio
SOD	Source-Observer distance
SOHO	Solar and Heliospheric Observatory
[SQUID] ²	SQUID with Shielding Qualified for Ionosphere Detection
SQUID	Superconductive Quantum Interference Device
SR	Schumann resonance
SW	Solar wind

T_c	Critical temperature
TEM	Transverse Electromagnetic
THRF	Thief River Falls (USA)
TLE	Transient Luminous Events
TM	Transverse magnetic
TSA	Thunderstorm activity
TST	Thin Sheet Technology [®]
ULF	Ultra-low frequencies [3 mHz-3 Hz]
UPML	Uniaxial Perfectly Matched Layer
USGS	US Geological Survey
UT	Universal time
UV	Ultra-violet
VLF	Very Low Frequency [3 – 30]kHz
YBCO	Yttrium-barium-copper oxide
ZHS	Zonal Harmonic Series

Chapter 1

Introduction

1.1 Background

The Earth is shrouded in the magnetic field generated by dynamo effect in its molten iron outer core. The geomagnetic field (GMF) is usually approximated to that of a dipole [20], diverging from the north magnetic pole and converging towards the south pole, while extending into space and reaching far¹ beyond Earth's surface. Around the Earth, the geomagnetic field forms up with ionised gases a complex and highly dynamic system called the geomagnetic cavity. The Earth's magnetic system plays an essential role in maintaining optimal conditions for life on Earth, by absorbing ionising radiations and highly energetic particles from the Sun that continuously gush towards our planet. On the ground, the effect of Earth's magnetic field force is easily observed with a mere compass. It always points the magnet northwards. This property has been used for centuries for navigation. Nowadays, the geomagnetic field is still used for navigation purposes, but also, there is a growing interest in exploring the unsolved riddles of the dynamics of Earth's interior and its geomagnetic cavity [21].

Electromagnetic wave propagation in the medium bounded by the Earth and ionosphere has been studied since the beginning of the twentieth century, after the discovery of the ionised layer of gas known today as the ionosphere [22]. The discovery meant that the cavity behaved as a natural electromagnetic (EM) waveguide, with typical eigenmodes that depend on the size of the planet. A basic formalism of the propagation and resonance properties by perfectly bounded cavity ionosphere was first introduced by Schumann [1] who postulated that natural harmonic resonance is set to develop between the conductive Earth and upper layers in the ionosphere, predominant in the Extremely Low Frequency (ELF [3 – 3000 Hz]) range. Balser and Wagner [23, 24] were the first to measure and characterise the global resonances and their diurnal variations. Ever since, the interest in the Schumann resonances (SR) has grown, firstly in an attempt to develop techniques of ELF communications system in the early 60's [25, 26]. Throughout the 80's, the interest on SR faded and was rekindled in the 90's when Williams [27] demonstrated the longterm correlation between Earth's global temperature change and the average amplitude variation of the first SR.

¹the effects of the geomagnetic field extend as far as tens of Earth's radii

SRs are ELF electromagnetic standing waves in the Earth-Ionosphere (E-I) cavity that are triggered by thunderstorms occurring continuously around the globe at a rate of nearly fifty flashes every second [28]. The EM waves generated undergo multiple reflections between the Earth and the lower conductive layer (D-layer) of the ionosphere in the radial direction while they interfere in the azimuthal direction around the globe [29]. For ELF waves, Earth's surface and the top layers of the ionosphere at an altitude beyond 60 km from the ground can be considered as good conductors. These layers are made of ionised gases whose conductive properties are high enough to reflect the waves back to the ground. At lower altitudes, the properties of the layers show very little electric conductivity causing a lossless propagation of electromagnetic waves. In an ideal model, the medium between the two conductive boundaries is assumed to be a perfect dielectric bounded by perfectly electrical conducting (PEC) boundaries. The electric field (\mathbf{E}) component tangential to the PEC boundary vanishes, forcing \mathbf{E} to be radial and magnetic field (\mathbf{H}) to be oriented in the tangential direction to the spherical surface. This mode of propagation is called transverse magnetic (TM) or quasi-transversal electromagnetic (quasi-TEM) mode and its resonance properties are determined by the geometry of the cavity [1]. In realistic conditions, however, waves are dissipated depending on their frequency due to multiple reflections and refractions at boundaries, and phase distortions that occur due to anisotropy and inhomogeneities in properties of the ionosphere [19].

1.2 Motivation

The variation of the geomagnetic field is monitored by a network of fluxgate magnetometers which form the International Real-time Magnetic Observatory Network Organization (*Intermagnet*). It is completed with satellites in the geospatial cavity and beyond (e.g. GOES, SOHO, etc). Most of the ground-based observatories use fluxgate magnetometers. They sample at a rate of 1 sample/second for the most advanced detectors [21], which limits their range below 0.5 Hz. In the ELF domain, however, the horizontal \mathbf{H} components are measured using Induction Coils Magnetometer (ICM) few metres long lying at the measuring site. The magnetometers consist of a coil with a very large number of turns of wire wrapped around a high permeability core. They present advantages of being simple to design and operate, having a wide dynamic range and a wide bandpass ranging from *dc* to few kHz [30]. A network of high latitude ICM of particular importance is the Canadian Array for Realtime Investigations of Magnetic Activity (CARISMA).

Despite the fact that the induction method does not measure the static field, the method has been successfully used for magnetic field measurements for the last 50 years in the ELF range. It presents some disadvantages however: The core's permeability depends on the magnetic field intensity and temperature. But a careful design of the core significantly reduces the discrepancies. Therefore, in order to monitor more accurately the geomagnetic field variation in the ELF range, a more sophisticated field measuring technique based on the Superconducting Quantum Interference Device (SQUID) is proposed. The SQUID magnetometer is capable of measuring extremely weak intensity of magnetic induction \mathbf{B} , in the order of 10^{-15} T, that to say 11 orders of magnitude lower than the ambient Earth's magnetic field intensity. This high sensitivity feature outdistances common geophysical magnetometers such as ICM (10^{-12} T) and fluxgates (10^{-9} T). Moreover, the SQUID is a wideband detector with a bandwidth ranging from quasi - *dc* to the GHz range without attenuation [3].

The first use of SQUID magnetometer for geophysical continuous monitoring was the *Laboratoire Souterrain à Bas Bruit* (LSBB) or low-noise underground laboratory (in English) located in Rustrel, France. The LSBB offers a combination of shielding against acoustic, seismic and electromagnetic noise. The SQUID at LSBB operates at 4.2 K inside an underground Faraday cage where the geomagnetic field intensity is reduced to a sixth of the nominal value outside [31]. Magnetic dataset fluctuations have been successfully correlated with seismic events and electromagnetic discharges in the atmosphere have been identified in magnetograms at the LSBB. Electromagnetic pulsations in the mHz range associated with interactions in the geomagnetic cavity have been recorded, magnetic pulsations associated with seismic shock wave arrival in the ionosphere have also been detected, as well as pulses associated with thunderstorm activity [31]. In this regard, these high performance and extremely sensitive instruments are of interest in geophysical science today, in the scope to develop abilities to detect anomalous signals associated with earthquakes and for early warning system implementation. For a project dubbed *Monitoring Space and Earth Hazards with Advanced Magnetometers* (MARMOTS), a network of *dc* SQUID magnetometers has been established between South Africa and France [17]: Two SQUID systems are operational for now, the SQUID Qualified for Ionospheric Detection ([SQUID]²) at LSBB and the High-temperature SQUID in Hermanus (HSQH), located at the South African National Space Agency (SANSA) Space Science directorate ², South

²Hermanus is also a station of the *Intermagnet* network.

Africa. HSQH operates at 77 K in a liquid nitrogen dewar flask in an open unshielded environment and thus measures the Earth's field unattenuated. Previous research showed a good correlation between fluxgate in Hermanus and SQUID magnetic signals for geomagnetic cavity pulsations in the ultra low frequency (ULF [3mHz-3Hz]) range [16, 32].

1.3 Objectives

In this work, signals of interest are global SR in the E-I cavity. We first study the structure and models of the Earth-ionosphere resonator, then measure SR properties with ground SQUID magnetometers at LSBB and Hermanus. The main objectives of this work can be outlined as follows:

1. Developing a numerical model to validate the resonant properties of the natural EM waveguide:
 - (a) Uniform model: Evaluation of SR peak frequencies, the spectral power and the quality factor variation in the waveguide.
2. Developing a spectral analysis technique adapted to random signals in the lower ELF lower range [0 – 30 Hz] based on a method of averaging and accumulating spectral densities in the Fourier domain to analyse SQUID horizontal \mathbf{H} data. .
3. Developing a method of analysis for SQUID dataset horizontal \mathbf{H} polarisation properties using a matrix of the cross-correlation and autocorrelation of the field intensity:
 - (a) Application of the coherence matrix to SQUID horizontal \mathbf{H} spectra in Objective 2.
 - (b) Application to uniform model spectra in Objective 1.
4. Establish a correlation between spectra obtained from SQUID magnetograms at LSBB and SANSA- Hermanus:
 - (a) A comparative study of the daily variation of the first Schumann resonance.
 - (b) A comparative study of the Q-factor.

1.4 Contributions

The contributions of this thesis are listed as follows:

1. A model of ELF radiowave propagation in the E-I cavity is developed using a computational electromagnetics commercial software used in time domain simulation based on Finite Difference Time Domain (FDTD). This method presents the ionosphere as an azimuthally uniform stratified medium.
2. polarisation properties of horizontal \mathbf{H} variations monitored continuously in terms of frequency and time. This allows obtaining spectra of signal-to-noise ratio and establishing clearly the SR peak patterns in the spectra. The study of polarisation may allow the detection of the first SR mode splitting.

3. The correlation of SQUID magnetic variations from two stations separated by $\sim 10,000$ km in latitude and with ICM datasets ~ 7000 km apart.

1.5 Research Output

In terms of research, the output of this thesis can be summarised as follows:

1. A Conference presentation was made on the Correlation between SQUID Measurements at Hermanus and LSBB Datasets for Space Weather Effects. The workshop was held in Chambéry, France from 01 – 03 July 2013, and involved all the stakeholders of the MARMOTS project from France and South Africa.
2. A research article has been submitted to the international peer-reviewed journal *IEEE Antennas and Propagation Society*. This article is titled “Three-Dimensional Modelling of Electromagnetic Wave Propagation in the Uniform Earth-Ionosphere Cavity Using CST Microwave Studio”.

1.6 Outline of the Thesis

Overall, this thesis is made of two parts: The modelling of ELF wave propagation in the E-I cavity and experimental measurement of the SRs with two SQUID magnetometers located in France and South Africa. The content of the thesis is organised as follows:

Chapter 1: *Introduction*

This chapter is dedicated to the generalities of the Earth and ionospheric system and SRs. It expresses the motivations and objectives and draws an outline for this work.

Chapter 2: *Overview of SQUID*

This part reviews the theory of superconductivity in general but focuses on the application of a *dc* SQUID as a magnetometer.

Part I

Chapter 3: *Background of Analytical and Numerical Electromagnetic Propagation Models*

Theoretical models in the spherical E-I cavity are reviewed. They comprise a perfectly conducting boundary model, a stratified ionospheric model and an impedance matrix based method. A numerical method based on FDTD is also presented.

Chapter 4: *Modelling the cavity with CST Microwave Studio*

A model based on FDTD simulates the full-wave propagation in the E-I cavity of ELF radiowaves. The simulation software is Computer Simulation Technology-Microwave Studio® (CST-MWS) that is commonly used in the domain of computational electromagnetics. An impulsive excitation is triggered and the response is simulated in the layout. Time propagation constants are deduced and in the spectra, peak frequency and waveguide Q-factor variation are determined.

Part II

Chapter 5: *Geomagnetic Field measurement in ELF range*

This chapter covers basics on the geomagnetic field properties and then deals with methods used to measure ambient field in the Earth's cavity at ELF range. Special attention is dedicated to novel SQUID magnetometer technique and its systems installed at the LSBB and SANSA Hermanus.

Chapter 6: *Spectral Analysis of Geomagnetic Field Components*

In this chapter, Spectral analysis of time SQUID datasets is undertaken using the Fourier transform. Because of the random component in the horizontal \mathbf{H} , a special method based on the windowing, averaging and overlapping of spectra is applied to the spectra in order to minimise the random component in the spectra.

Chapter 7: *Polarisation Properties of Geomagnetic Field Components*

SQUID geomagnetic horizontal components are analysed to separate the polarised signal from the noisy signal. polarisation properties such as the phase difference between the horizontal geomagnetic components and the arrival angles of the wave are computed. polarisation parameters are studied and compared to previous research.

Chapter 8: *Correlation of SQUID Magnetic Datasets*

SQUID time datasets at LSBB and Hermanus are compared. In the frequency domain, Schumann resonance spectra and quality factor are presented. The data are compared to the ICM data from the CARISMA network that are available online.

Chapter 9: *General Discussion*

The outcomes from previous chapters are combined and discussed in order to put them into perspective vis-à-vis previous research. The achievements and shortcomings of this method are addressed.

Chapter 10: *General Conclusion and Recommendations*

General conclusions from the work are presented and recommendations for future work are proposed.

Chapter 2

Overview of SQUID Magnetometers

2.1 Introduction

Due to its extreme sensitivity to the magnetic field, the SQUID makes an ideal tool to operate as a magnetometer. The operation of a SQUID relies on the underlying quantum interference of superconductive currents across its components and on the control circuitry that optimises its output and makes its use relevant. This chapter overviews the basics of superconductivity and highlights basic properties of components that make up the SQUID. Particular attention is paid to the design that makes the SQUID the most sensitive magnetometer to this day.

2.2 General Theory of Superconductivity

Superconductivity is a macroscopic quantum phenomenon by which the electrical resistance of a material abruptly drops to zero when a certain critical temperature T_c of the superconductive state of the material is attained [33]. The effect was discovered by Kamerlingh Onnes in 1911 while studying the electrical conductivity of mercury in the vicinity of the boiling temperature of helium (4.2 K). This effect is depicted in Fig. 2.1. Superconductivity is the manifestation of infinite conductivity and can be defined as the transition from a normal conductive to a superconductive state in the same material. Two types of superconductors arise: *Low* - T_c superconductors are generally pure elements, examples are mercury (*Hg*), aluminium (*Al*) and lead (*Pb*) and have very low critical temperatures from 0.001 to 9.3 K [33]. *High* - T_c superconductors are generally complex alloys and display T_c from 25 up to 125 K [33]. An example of this type is the $YBa_2Cu_3O_{7-x}$ known as the Yttrium-Barium-Copper oxide (YBCO).

The phenomenon of superconductivity is not limited to zero resistance below T_c . A couple of other interesting phenomena are also associated with superconductivity. Moreover, these materials display the absence of thermoelectric effects: there is neither Joule effect nor conduction due to differences in temperature. In addition to that, the superconductive material develops a total or partial rejection of weak magnetic field from its core, known as the *Meissner effect*. In particular, *type I* superconductors are perfect diamagnetic materials. Furthermore, when an external magnetic

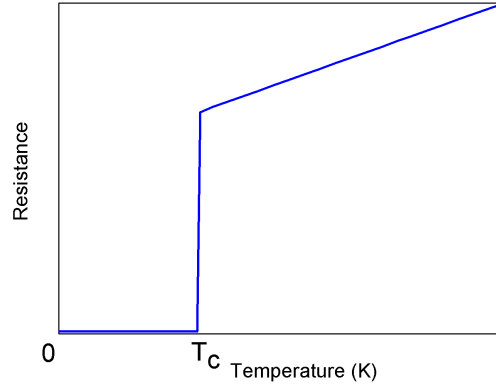


Figure 2.1: Characteristic resistance-temperature curve for a Superconductor. There is a sharp transition to zero resistance at T_c .

field is applied through a superconductive ring, the magnetic flux across the ring is constant and increases in discrete quantities of magnetic flux as the applied field increases. This quantum “leaping” effect is determined by the states of energy available.

Therefore, three main characteristic parameters of superconductivity are defined:

- The critical temperature T_c which is the transition temperature below which the superconductive state is maintained,
- the critical current I_c which is the maximum current that can be carried by a superconductor material and
- the critical magnetic field intensity H_c which is the maximal intensity of the field below which the superconductivity is maintained.

2.2.1 Solving Maxwell’s equations

Considering an EM wave propagating in a linear medium, Maxwell’s equations in their differential formulation are written as follows

$$\nabla \times \vec{E} = -\mu \frac{\partial \vec{H}}{\partial t} \quad (\text{Faraday's law}) \quad (2.1)$$

$$\nabla \times \vec{H} = \epsilon \frac{\partial \vec{E}}{\partial t} + \vec{J} \quad (\text{Ampère's law}) \quad (2.2)$$

$$\nabla \cdot \vec{E} = 0 \quad (\text{Gauss's law for the electric field}) \quad (2.3)$$

$$\nabla \cdot \mu \vec{H} = 0 \quad (\text{Gauss's law for the magnetic field}) \quad (2.4)$$

where \vec{E} and \vec{H} represent the electric and magnetic field respectively and ϵ, μ are the electric and magnetic permittivity of the medium.

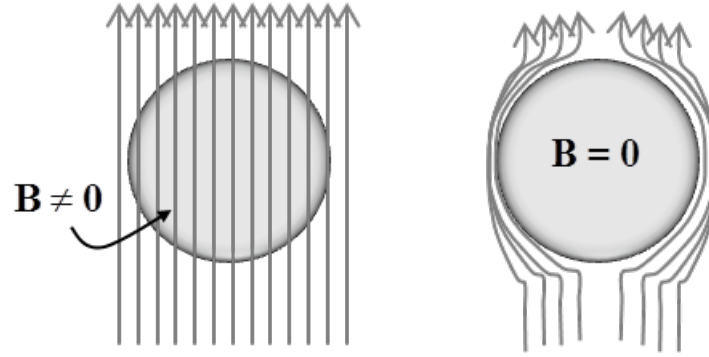


Figure 2.2: Meissner effect for type I superconductor. A normal metallic material (left) and a *type I* superconductor material (right)

2.2.2 Diamagnetism and Meissner Effect

The Meissner effect is the expulsion of field lines from superconductors due to screening currents which flow in such a way to create a field in opposite directions to the applied field which result in the cancellation of the applied field in the core of the superconductor as shown in Fig. 2.2. In type I superconductors, the Meissner effect is total, i.e. the magnetic field is totally expelled from the superconductor material and shows a pure diamagnetic effect. In the material, the total magnetic flux density vector \mathbf{B} can be described as a sum of the applied field and the demagnetization field in the superconductor that cancel each other as follows,

$$\vec{B} = \mu (\vec{H} + \vec{M}) = 0. \quad (2.5)$$

Here, $M = \chi H$ represents the internal magnetisation and χ the magnetic susceptibility. Here $\chi = -1$ significant for pure diamagnetic materials.

In *type II* superconductors, however, two critical values for the magnetic field appear, the lower and higher critical field H_{c10} and H_{c20} respectively. As shown in Fig. 2.3, by considering a constant temperature lower than T_c and increasing the magnetic field intensity gradually from 0 to a field slightly greater than H_{c20} , this sequence of phenomena happens:

$H < H_{c10}$, Meissner effect is maintained and the total magnetic flux is expelled. $B=0$

$H_{c10} < H < H_{c20}$, Partial flux penetration called the vortex state ($B \neq 0$)

$H > H_{c20}$, Normal metallic state ($B \neq 0$)

The fact that the field is maintained far beyond H_{c10} of the pure superconductor has been demonstrated [34]: The boundaries in type II alloys tend to increase electron collision rate in the structure. This leads to a shallower penetration of the field into the structure. The effect is described by the London formulation [35]. The screening current density J_s in the superconductor can be expressed

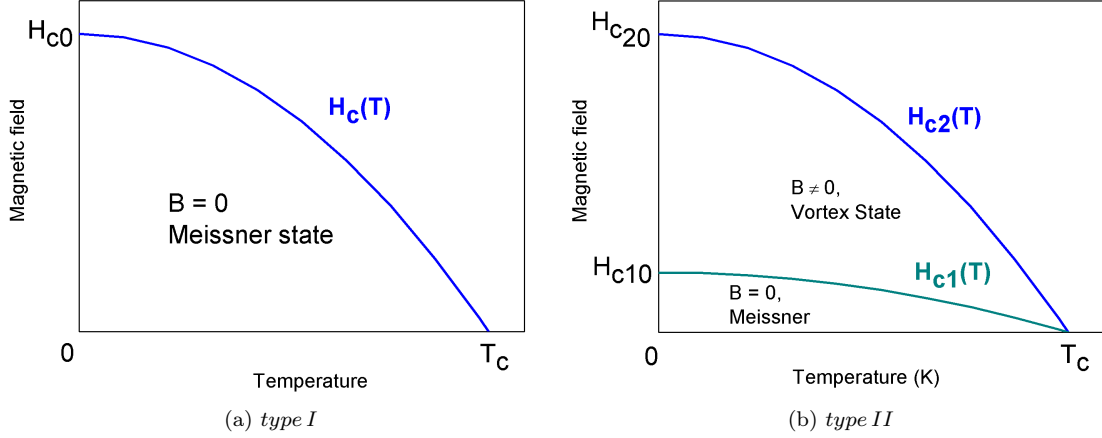


Figure 2.3: Meissner effect in *type I* and *II* superconductors.

as follows:

$$\vec{E} = \frac{n_s e^2}{m} \frac{\partial \vec{J}_s}{\partial t}, \quad (2.6)$$

$$\vec{\nabla} \times \vec{J}_s = -\frac{n_s e^2}{m} \mu_0 \vec{H}, \quad (2.7)$$

where e , n_s and m are superconductive electron charge, density of charge and mass respectively. The expressions (2.6) and (2.7) are known as London equations [35]. In the superconductor state, it can be assumed that the only contribution to the current is J_s . Ampère's law (2.2) becomes therefore

$$\nabla \times \vec{H} = \vec{J}_s. \quad (2.8)$$

By plugging (2.7) and (2.7) into the Ampère's law for superconductors (2.8), a quadratic equation is obtained. From the resultant equation, the following expression of the penetration depth is obtained:

$$\lambda = \sqrt{\frac{m}{n_s e^2 \mu_0}}. \quad (2.9)$$

The field penetration depth is an intrinsic property of all superconductors [33]. It represents the depth at which the field is reduced to a value of $1/e$ of its amplitude in the superconductive material. For pure Nb at $T = 0$ K, it is estimated to 170 \AA [3].

2.2.3 Flux Quantisation

Flux quantisation was independently observed by Deaver and Fairbanks using a superconductive filament subjected to a harmonic external magnetic field [36], and by Doll and Näbauer using a superconducting ring exposed to a static magnetic field [37]. Both groups proved experimentally that magnetic flux trapped in a superconductive material is a natural multiple of the magnetic flux quantum and that it increased in cascades with the increase in H applied, adding on one quantum of flux at a time at each step. The magnetic flux quantum value is $\Phi_0 = \frac{h}{2e} = 2.068 \times 10^{-15} \text{ T/m}^2$,

where h is Planck's constant. In superconductive electronics, it is possible to work with a single quantum flux of magnetic field. [3].

In order to explain quantum effects of superconductivity, a microscopic theory of superconductivity was developed by *Bardeen, Cooper* and *Shriffer*, and is referred to as *BCS* theory of superconductivity [38–40]. This theory describes mathematically the microscopic origins of the energy gap in superconducting state and electron pairing into Cooper pairs which are responsible for the infinite conductivity in superconductors. However, it does not explain the behaviour at macroscopic level, for instance, the presence of a *vortex state* in *type II* superconductors. In this case, thermodynamic and electromagnetic effects have been combined into the macroscopic quantum model (MQM) that was developed concurrently by *Ginzburg* and *Landau* [41].

2.2.4 Flux Vortices in Type II Superconductors

Flux quantisation can be explained by the macroscopic wave function

$$\Psi(\vec{r}, t) = |\Psi(\vec{r}, t)| \exp [i\phi(\vec{r}, t)] \quad (2.10)$$

that shows a periodic boundary condition around the superconducting loop. In this case the magnetic flux H_m created inside the material originates from a potential A so that $\frac{\partial}{\partial r} \times \vec{A} = \mu (\vec{H} + \vec{H}_m)$. By minimising the wavefunction (2.10) and by applying the periodic boundary condition around the loop, the following expression is obtained [41]:

$$\frac{\partial}{\partial r^2} H_{tot} = \frac{H_{tot}}{\lambda_1^2}, \quad \lambda_1 = \frac{m}{2\mu_0 e^2 |\Psi|^2} = \frac{m\beta}{2\mu_0 e^2 \alpha T} \quad (2.11)$$

where λ_1 is the *Ginsburg-Landau penetration depth*, α, β are thermodynamic coefficients and T is the absolute temperature. In the material $\lambda_1 \sim \frac{1}{T}$, meaning that the field penetrates further in the superconductive material as the temperature increases until T_c is reached. In the absence of external field $\vec{A} = 0$ and small fluctuation of the wavefunction $|\Psi|^2 \ll \frac{\alpha}{\beta} T$, the relation (2.10) yields the difference equation $(\partial^2 \Psi / \partial r^2) = 1/\xi^2$, where $\xi = \hbar^2 / 4(m\alpha T)$ is the *Ginsburg-Landau coherence length* of the fluctuations. The *Ginsburg-Landau parameter* is defined as the ratio

$$\kappa = \frac{\lambda_1}{\xi} = \sqrt{\frac{2m^2\beta}{\hbar^2\mu_0\epsilon^2}}, \quad (2.12)$$

where $\hbar = \frac{h}{2\pi}$ is the reduced Planck's constant. The generalised *G-L parameter* describes every type of superconductor depending on the value taken into consideration. This condition theoretically predicts the presence of two types of superconductors, describing *type II* superconductors as a phase transition between a Meissner state and a normal conducting state [42]. Abrikosov [42] describes the partial diamagnetism into *type II* superconductors as a partial passage of magnetic flux through the superconducting core thus creating cylindrical swirls of supercurrents surrounding a cylindrical normal conductor domain through which a certain amount of magnetic flux passes. 2.4a. In the vortex, \mathbf{B} is maximal at the center and reduces exponentially from the center of the vortex towards the superconductive matrix as shown in Fig. 2.4b. The swirling current and the density of charge variation around the vortex can be seen in Fig. 2.4b as well.

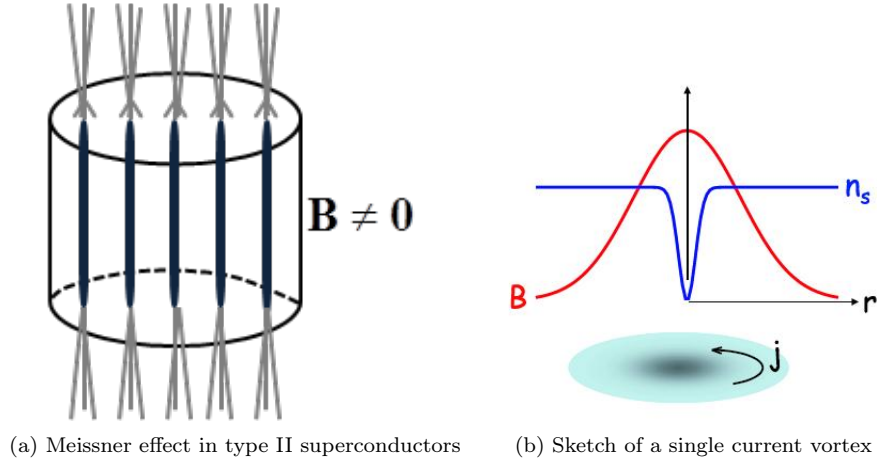


Figure 2.4: Current vortices in type II superconductors in the mixed state. Magnetic flux density B , charge density n_s and vortex current density j are represented

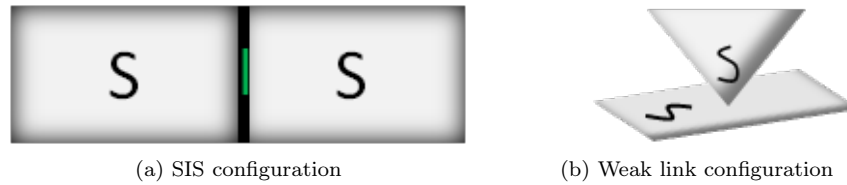


Figure 2.5: Josephson junction. S represents the superconductive component and I the insulator.

2.3 Josephson Junction

A Josephson junction (JJ) is a superconductive device made of two weakly joined superconductors or more generally a relatively thin layer of a dielectric sandwiched between two superconductive materials. The main effect responsible for transport of charge through the potential barrier is the tunnelling effect. Tunnelling is a phenomenon that is owed to the wave-particle nature of electrons, that can cross thin barriers of potential in the same way as a coherent wave diffracts around edges. This effect is known as Josephson tunnelling [43]. The most common representation is a Superconductor-Insulator-Superconductor (SIS) junction as shown in Fig. 2.5a. The BCS theory predicts a gap of energy and that electrons must have an energy greater than the gap to tunnel. However, in the superconductive state there are no electrons, rather Cooper pairs. Hence, a threshold voltage $V = \frac{\Delta}{e} = \frac{E_g}{2e}$ must be reached to break the pairs. Here Δ is half of the energy gap E_g [3].

The Josephson tunnelling current is given by the relation [34]

$$I = I_c \sin(\varphi_1 - \varphi_2) = I_c \sin \delta, \quad (2.13)$$

where δ is the phase difference between the two superconductor wavefunctions, I is the current through the junction and I_c is the critical current of the junction. The phase variation in time can

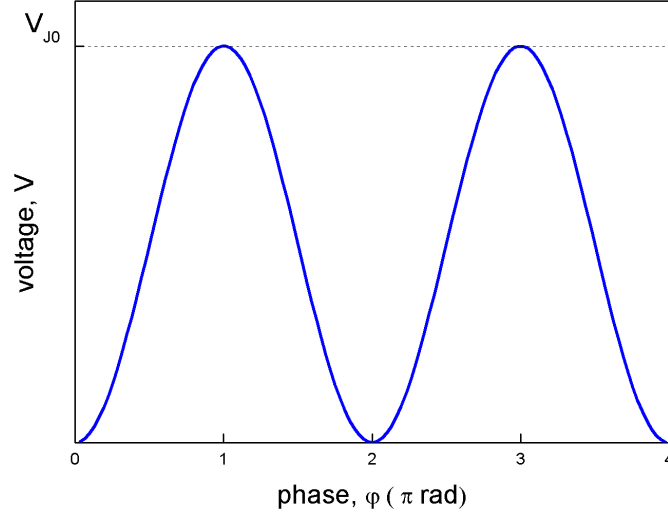


Figure 2.6: Voltage variation as a function of the phase of the *dc* JJ. Note that $V_{J0} = \Phi_0 I / (\pi I_B)$ is the peak amplitude across the JJ.

be derived as a function of the voltage across the JJ as follows [34]

$$\frac{\partial \varphi}{\partial t} = \frac{2e}{\hbar} V = \frac{2\pi V}{\Phi_0}, \quad V = \frac{\Phi_0}{2\pi} \frac{\partial \varphi}{\partial t}. \quad (2.14)$$

Using (2.13) and (2.14) we can obtain the $I - V$ characteristics of the junction. By applying an intensity or a voltage across the junction, two main operation modes of the JJ are described: the static (*dc*) and the dynamic (*ac*) mode.

2.3.1 Intensity Driven Junction

The JJ is connected with a bias *dc* current slightly exceeding the critical current $I_B > I_c$, a *dc* voltage develops across the junction. The voltage across the junction is given by [34],

$$V = \frac{\Phi_0 I_c}{2\pi I_B} (1 - \cos \varphi) = V_{J0} \sin^2 \left(\frac{\varphi}{2} \right). \quad (2.15)$$

Here $V_{J0} = \frac{\Phi_0 I_c}{\pi I_B}$ is the peak *dc* voltage as a function of the phase. As shown in Fig. 2.6, $V(\varphi) =$

$$\begin{cases} 0 & \varphi = 2n\pi \\ V_{J0} & \varphi = (2n+1)\pi \end{cases} \text{ for } n = 0, 1, 2, 3, \dots$$

The voltage V across the JJ is independent of time but rather varies with the phase associated with I_c . Hence, a *dc* voltage develops across the intensity driven JJ. This property is used in the superconductive digital electronic applications, specifically in the development of *dc* SQUID and Rapid Single Flux Quantum (RSFQ) circuits [44].

2.3.2 Voltage Driven Junction

On the other hand, a voltage V_0 across the junction generates an alternating current (*ac*) due to the phase variation in time. The differential equation in (2.14) yields

$$\varphi = \frac{2\pi V_0}{\Phi_0} t + \varphi_0, \quad (2.16)$$

where φ_0 is the value of the constant determined at initial conditions. The current intensity of the JJ is obtained by substituting (2.16) into (2.13) to yield

$$I(t) = I_c \sin\left(2\pi \frac{V_0}{\Phi_0} t + \varphi_0\right) = I_c \sin(2\pi f_J t + \varphi_0). \quad (2.17)$$

The expression (2.17) represents a harmonic mode of the JJ. Here f_J is the characteristic frequency of the junction

$$f_J = \frac{V_0}{\Phi_0} \cong 483 V_0 \text{ GHz/mV}. \quad (2.18)$$

From (2.18), the frequency response in *ac* mode depends on the voltage (in mV = 10^{-3} V). With few mV, it is possible to excite frequencies to the order of the THz (10^{12} Hz). With the *ac* mode, another type of SQUID can be designed from a single JJ locked in a superconducting ring: the radio-frequency, the *rf* SQUID [3].

In order to model more precisely JJ characteristics, it is adequate to incorporate the conduction and the displacement currents across the thin insulating layer. These are represented respectively by an ohmic resistor (R) and a capacitor (C) connected in parallel to the JJ, to make the Resistively and Capacitively Shunted Junction model (RCSJ) described in [3,34].

2.4 The *dc* SQUID

The *dc* SQUID is a combination of two JJ connected in parallel, that are mounted in a superconducting ring of area A and $n\Phi_0$.

When a *dc* current I is applied to the ring, the current is split into the two branches of the circuit as follows

$$I = i_1 + i_2 = I_c (\sin \varphi_1 + \sin \varphi_2) \quad (2.19)$$

The phase difference across the junctions must fulfil the quantization condition of the JJ as follows

$$\varphi_1 - \varphi_2 = \frac{e}{\hbar} \Phi = 2\pi \frac{\Phi}{\Phi_0}. \quad (2.20)$$

The phases at each JJ can be deduced from (2.20) and expressed in function of an arbitrary phase difference δ_0 across the SQUID as follows

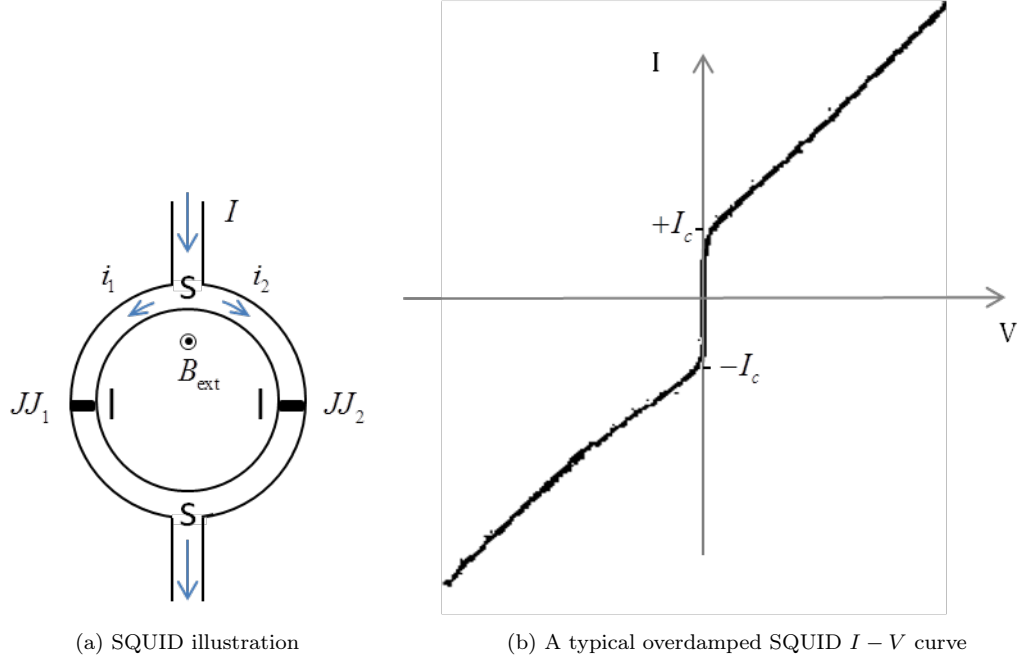


Figure 2.7: SQUID layout and characteristic current - voltage curve for an overdamped JJ. $JJ_{1,2}$ are Josephson junctions 1 and 2. **S** represents the superconductive component and **I** is the insulator.

$$\varphi_1 = \pi \frac{\Phi}{\Phi_0} + \delta_0 \quad \text{and} \quad \varphi_2 = -\pi \frac{\Phi}{\Phi_0} + \delta_0 \quad (2.21)$$

Therefore, from the combination of (2.19) and (2.21) the current across the SQUID is obtained

$$I = 2I_c \cos\left(\pi \frac{\Phi}{\Phi_0}\right) \sin \delta_0. \quad (2.22)$$

And the maximal amplitude is therefore

$$I_{\max} = 2I_c \cos\left(\frac{\Phi}{\Phi_0}\right). \quad (2.23)$$

Considering in this case, an external magnetic field that is applied normal to the SQUID with a field \mathbf{B}_{ext} pointing out of the paper in shown Fig. 2.7a. The total flux becomes $\Phi = \Phi_{\text{ext}} + \Phi_{\text{loop}}$ and the loop's internal flux is associated with its inductance. In most practical cases, the external flux is much greater than the inner flux, $\Phi_{\text{ext}} \gg \Phi_{\text{loop}}$, therefore the peak current of (2.23) becomes

$$I_{\max} = 2I_c \cos\left(\frac{\Phi_{\text{ext}}}{\Phi_0}\right). \quad (2.24)$$

The previous formulation assumes that the JJs used are structurally identical.

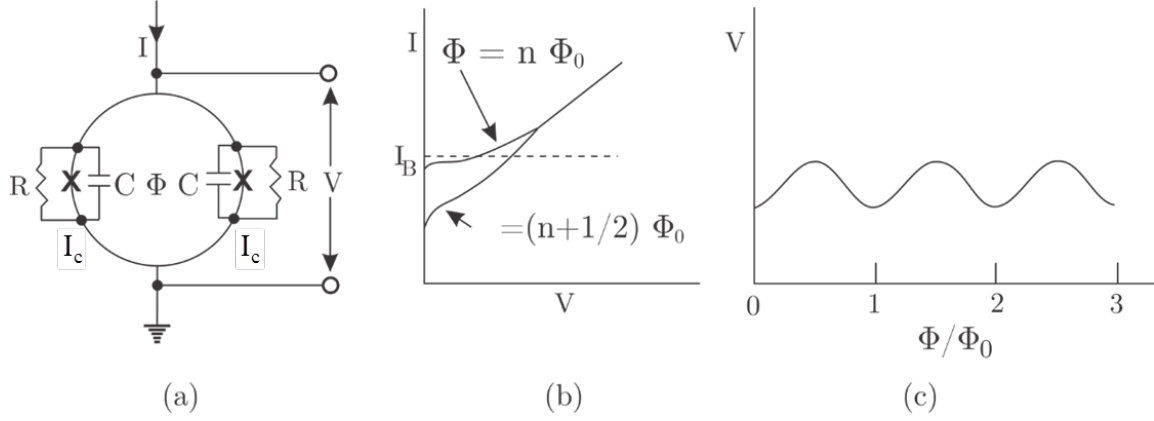


Figure 2.8: The *dc* SQUID (a) the diagram representation with R, C the JJ resistance and capacitance respectively, (b) I-V characteristic at integer and half integer values of applied flux set by the bias current I_B , and (c) voltage versus flux ratio Φ/Φ_0 .

2.5 RCSJ Approximation

An RCSJ circuit depicting the *dc* SQUID is represented in Fig. 2.8a. When there is no shunt resistance to the *dc* SQUID, the I-V characteristic is a hysteresis as shown in Fig. 2.8b. The incorporation of the shunt resistance removes the hysteresis if the following condition is fulfilled [46]

$$\beta_c = 2\pi f_J RC \leq 1. \quad (2.25)$$

Equation (2.25) represents the optimisation of RC circuits inside each JJ. As a reminder, $V_0 = I_c R$ and the $I - V$ characteristic becomes

$$V = R\sqrt{I^2 - I_c^2}. \quad (2.26)$$

The voltage approaches IR for very large values of I as shown in Fig. 2.7. When a *dc* SQUID is biased at a current I_B , the voltage varies sinusoidally in function of the magnetic flux as shown in Fig. 2.8c. The peak amplitude of the voltage is obtained at $\partial\{V(\Phi_{\text{ext}})\}/\partial\Phi_{\text{ext}} = 0$ for values of $\Phi_{\text{ext}} = (2n + 1)\Phi_0/4$. By introducing this condition into (2.25), one obtains the maximum voltage across the device

$$V_{pp} = V(\Phi_0) - V_0 = IR \left[\frac{1}{2} - \sqrt{\frac{1}{4} - \frac{I_c^2}{I^2}} \right] \quad (2.27)$$

Here, V_{pp} is the peak-to-peak voltage across the SQUID in terms of phase. In this regime, the variation of voltage $\delta V = V_\phi \delta \Phi_0$ is almost linear. Empirical model shows that there is a screening condition for the inductance to be optimised [46]. Hence, the SQUID inductance parameter becomes

$$\beta_L = \frac{2LI_0}{\Phi_0} = 1. \quad (2.28)$$

The slope of the variation of the voltage in terms of Φ is therefore

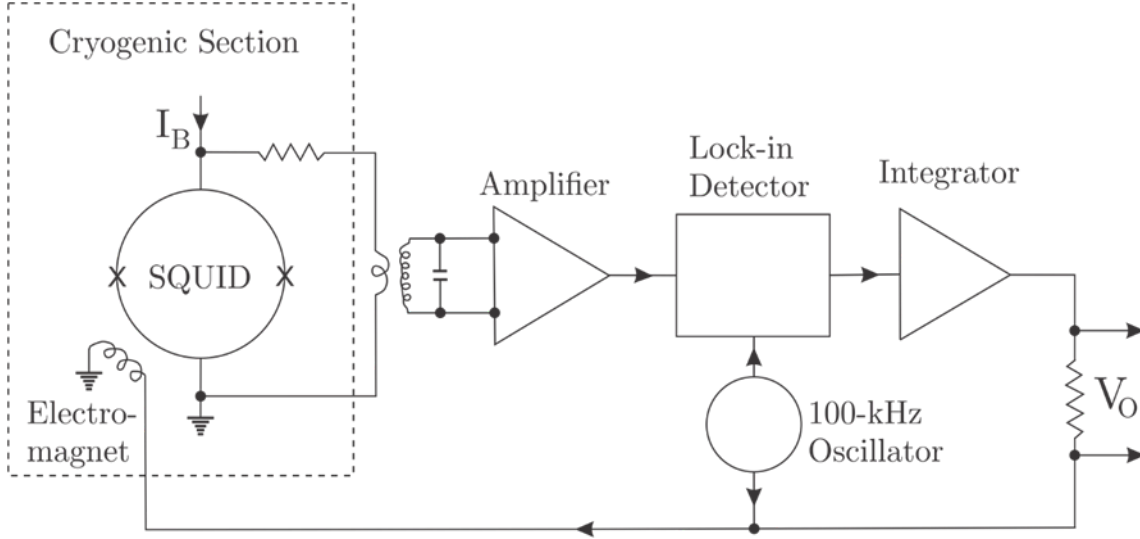


Figure 2.9: Flux-locked loop for a *dc* SQUID. I_B is the bias current applied to the SQUID and V_O the output voltage of the system

$$V_\Phi \approx \frac{R}{L} \approx \sqrt{\pi LC} \quad \text{for } \beta_L = \beta_C = 1, \quad (2.29)$$

and the width in terms of flux for which the SQUID response is linear is obtained from the ratio

$$W = \frac{V_{pp}}{V_\Phi} \approx \frac{IR^2}{L} \left[\frac{1}{2} - \sqrt{\frac{1}{4} - \frac{I_c^2}{I^2}} \right] \approx \pi L^2 C \left[\frac{1}{2} - \sqrt{\frac{1}{4} - \frac{I_c^2}{I^2}} \right]. \quad (2.30)$$

Thermal noise imposes an upper limit on SQUID inductance, so that $\Phi_0^2/2L \gg 2\pi k_B T$. Unless this condition is satisfied, quantum interference will be buried in white noise. The maximum inductance is $L = 6 \text{ nH}$ at 4.2 K and 0.32 nH at 77 K. The flux noise density of the SQUID is by definition [46]

$$S_\Phi(f) = \frac{S_V(f)}{V_\Phi^2} = 16k_B T \frac{L^2}{R}. \quad (2.31)$$

From the expression of the density of noise (2.31), it is easy to deduce the noise energy of the *dc* SQUID, $\varepsilon(f) = S_\Phi(f)/2L$. For *Low*- T_c SQUIDs, the level of the noise is in relative agreement with theory [3]. Thermal noise is generally represented as a ratio of the thermal energy to the coupling energy of the JJs:

$$\Gamma \equiv \frac{\text{thermal noise}}{\text{coupling energy}} = \frac{2\pi k_B T}{I_c \Phi_0} \quad (2.32)$$

$\Gamma \ll 1$ determines the condition for a low noise SQUID. On the other hand, $\Gamma = 1$ determines the minimal critical current for the SQUID signal to appear beyond noise: $I = 0.17 \mu\text{A}$ at 4.2 K and $3.2 \mu\text{A}$ at 77 K [47].

Flicker noise also known as $1/f$ noise also affects SQUIDs. It is generated by defects in the material that trap and release superconductive charge carriers in a random way. It may also originate from flux hopping from vortices in high- T_c superconductors. The random fluctuation of generation and

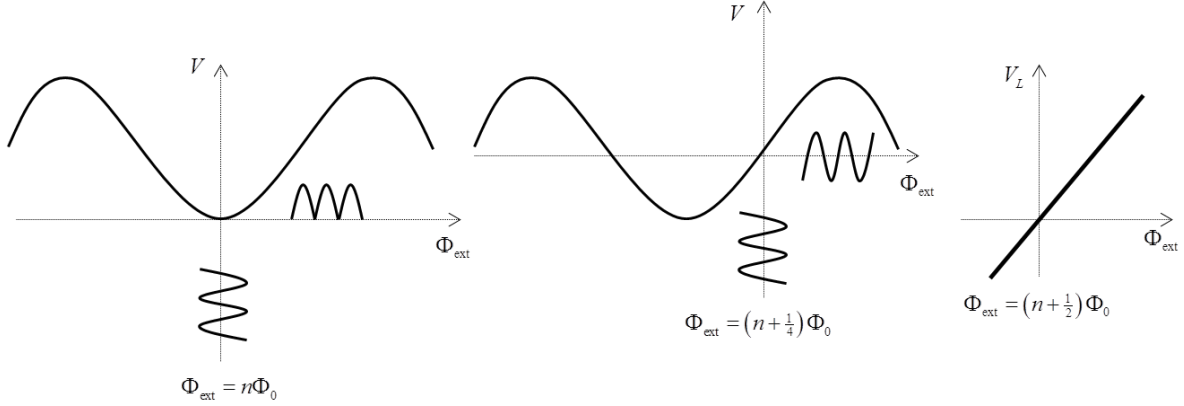


Figure 2.10: Representation of magnetic flux modulation for a SQUID magnetometer in a lock-in amplifier. The output voltage V_L is a linear response to the flux applied to the SQUID.

trapping of charges generates fluctuations in I_c . When operating a *dc* SQUID for magnetic field detection, some techniques are used to increase the signal-to-noise ratio. They are described in the following section.

2.6 *dc* SQUID as a Magnetometer

A SQUID magnetometer is a *dc* SQUID that is customised for the detection of the ambient magnetic field. The device is operated in flux-locked loop (FLL) for three main reasons:

- to linearise and amplify the SQUID response,
- to track external magnetic flux change in function of superconductor loop flux,
- to detect flux less than Φ_0 .

2.6.1 Flux-locked Loop (FLL)

Linearisation of the response is achieved by amplifying V_{pp} by applying a negative feedback that locks Φ_{loop} to zero. This is achieved by placing the SQUID in a feedback locked loop, where an electromagnet generates an equal flux but in opposite direction to Φ_{loop} . The output signal from the SQUID is amplified. The amplifier, however, generates levels of noise ten times more than SQUID's (which is approximately $10^{-6}\Phi_0 \text{ Hz}^{-\frac{1}{2}}$) [3]. To reduce the noise, a step-up transformer is mounted in the circuit after the SQUID. The feedback flux locked loop is operated in reversal bias mode in order to mitigate the low-frequency $1/f$ noise owed to I_c fluctuations across the JJs [47]. A circuit diagram of the FLL circuit is represented in Fig. 2.9.

Flux modulation is achieved by an oscillator that generates the *ac* bias of amplitude $\sim \Phi_0/2$ in a range from 100 kHz to few MHz. This signal is fed into the lock-in detector. The output voltage from the lock-in amplifier is labelled V_L in Fig. 2.10. Flux modulation matches the amplifier output with a signal generated in the oscillator, depending on the flux generated in by the SQUID:

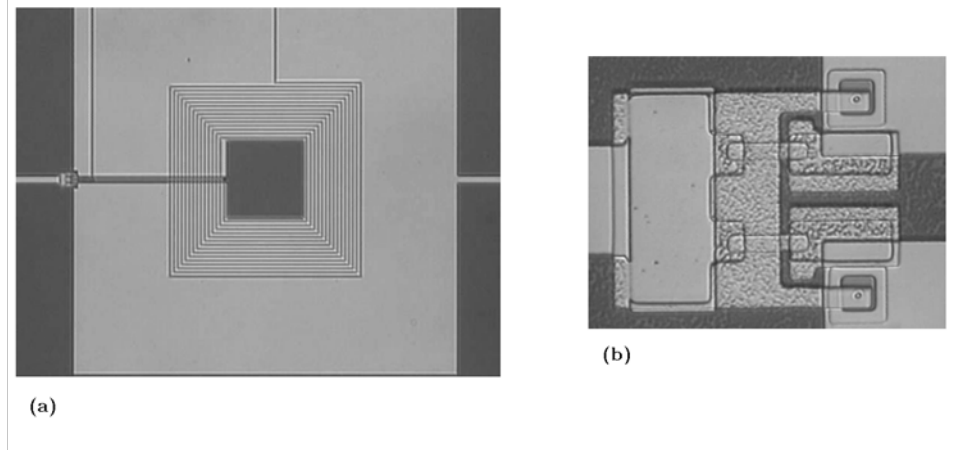


Figure 2.11: Typical design of a Low- T_c dc SQUID (a) the pick-up coil in the middle of the area lies over the superconductor layer and the JJs at the left (b) Zoomed-in view of the JJs and resistance shunts [3].

- If the flux input is $n\Phi_0$, the output voltage becomes a full-wave rectified sinusoidal function as depicted in Fig. 2.10(left graph). The lock-in detector which resonates at the oscillator resonance assigns the output voltage to zero.
- When the flux applied becomes $(n + \frac{1}{4})\Phi_0$, the output is maximum. The output voltage linearly increases from $n\Phi_0$ to $(n + \frac{1}{4})\Phi_0$, as in Fig. 2.10(middle graph) The output from the lock-in detector increases.
- In the case where Φ_{ext} reduces; if for instance it goes from $n\Phi_0$ to $(n - \frac{1}{4})\Phi_0$, then the output from the lock-in detector becomes negative as shown in Fig. 2.10(right graph).

Therefore, the output from the lock-in detector is fed into an integrator, which is connected resistively to the electromagnet coil exciting the dc SQUID. This programmable feedback loop (PFL) maintains a constant flux across the SQUID: for any external flux variation $\delta\Phi_{\text{ext}}$ applied to the SQUID, the FLL generates a flux of amplitude $-\delta\Phi_{\text{ext}}$ that is fed back into the SQUID [3]. The output of the FLL- dc SQUID system is a voltage V_L that is directly proportional to the external flux variation detected, as shown in Fig. 2.10.

The periodicity of $V(\Phi_0)$ offers the possibility to operate over a large number of periods. This offers a very wide bandwidth to the device, ranging from quasi-static up to few GHz. In theory, the dynamic range of the FLL-SQUID is of the order of 120 dB and the maximum rate of flux that the FLL can track is $10^6 - 10^7 \Phi_0/s$ [3]. However, extremely fast changes in external flux may cause the FLL response to lag behind the SQUID. This is, for instance, typical of extremely fast changes during thunderstorms; Signals of intensity 10^{-5} T within 10 ms in an area of a mm^2 corresponding to approximately $10^4\Phi_0$, yielding a staggering $10^6\Phi_0$ per second [47]. This generally results in a flux jumps in continuous time magnetic signals [48]. Henceforth, very large flux changes in the external magnetic field cannot be measured.

2.6.2 *dc* SQUID Magnetometer Design

The main function of a SQUID magnetometer is to measure the variation of external magnetic flux precisely and fast with a minimal level of noise. Ideally, the larger the area the better. $\Delta\Phi_{\text{ext}} = \Delta B_{\text{ext}} \cdot A$, where A is the inner area of the SQUID junction. But two problems arise; A bigger ring increases significantly the inductance L yet it is limited by (2.28).

The design of the *dc* SQUID minimises the area of the loop while maximising the superconductor's area. This reduces the inductance but also focuses the applied external field lines into the inner area A . The defining parameter is the effective area $A_{\text{eff}} = Dd$, where D and d are the outer and the inner dimensions respectively. Moreover, a flux transformer coil may be used to increase A_{eff} . A typical design can be seen in Fig. 2.11, where A is in dark grey and the surrounding superconductor in light grey. A superconducting flux transformer can be seen on top of the SQUID from which it is electrically insulated [3]. The design also includes the electromagnet's loop with the same configuration as the transformer. As shown in Section 2.6.1, the total flux applied to the SQUID being at all times zero, the transformer current density is $J_t = -NS B_{\text{ext}}/L$, where N is the number of coil turns and L the inductance of the coil. The coupling between the transformer and the SQUID can be defined by the mutual inductance $M = \alpha\sqrt{LL_S}$ with α a coupling constant and L_S the superconductor's inductance. The field coupled into the SQUID is therefore

$$B_S = -B_{\text{ext}}N \frac{A}{A_{\text{eff}}} \alpha \sqrt{\frac{L_S}{4L}} \quad (2.33)$$

This relation takes into consideration the feedback loop identical to the transformer. This device can provide a high magnetic field sensitivity of the order of $1 \text{ nT}/\Phi_0$ is with $A \sim 50\text{mm}^2$ loop with $L = 200 \text{ pH}$ [3].

Low – T_c SQUIDs are generally made from thin films of polycrystalline aluminium oxide sandwiched between niobium superconductor layers (Nb-AlO_x-Nb). Because of operating at very low temperature, an external shunt resistance is required. *High* – T_c SQUIDs, however, are mainly made of bi-crystalline YBCO layers, with the junction at the grain boundary. The advantage of this design is that because of defects in the YBCO structure, the shunt resistance effect is incorporated in the structure [3].

However, noise is predominant in *high* – T_c SQUIDs. Eventually, thermal noise is more important at 77 K than at 4 K. Moreover, $1/f$ noise also happens due to the vortices of flux in the volume of the layer as shown in Fig. 2.4. The consequence of this is the trapping of flux in the core of the superconductors during the cooling process. Therefore, it is important to cool the SQUID in a magnetically shielded environment. And more specifically for *high* – T_c magnetometers that operate in the ambient field, the superconductive layer should be fabricated with ground plane holes, so that the field lines are pushed through the holes instead of the superconductive layer.

2.7 Conclusion

The high performance of a *dc* SQUID has been described. Its usage as a magnetometer presents unprecedented advantages in terms of sensitivity and dynamic range. *Low* – T_c SQUID present

a very interesting profile in terms of low noise. Thanks to innovative designs [47], the high- T_c performances are also improving. The main advantage of the *high* - T_c over the *low* - T_c rely on cryogenics: helium is expensive¹ to manufacture and requires a sophisticated system to maintain it below its boiling temperature. On the other hand, nitrogen comes at a much lower cost and is much easier to handle.

¹He costs as much as 40 US Dollars per litre in some US labs [49].

Chapter 3

Background of Analytical and Numerical Electromagnetic Propagation Models

3.1 Introduction

A wide variety of magnetic phenomena that occur inside the Earth or in the near vicinity or as far as the Sun influence directly or indirectly the behaviour of the magnetic field on the ground. These effects appear in widely different ranges of frequencies, mostly as background noise in magnetic data-sets. In the ULF range, for instance, the noise that dominates is essentially due to the solar wind (SW) interaction with the magnetic field in the cavity [50], and in the ELF, the main background noise originates from incessant thunderstorm activity in the Earth's atmosphere. The main feature of these signals is that they manifest themselves as a form of resonances of the geomagnetic system; the sources may be wideband and occur randomly but the geomagnetic system configuration interacts with particular eigenmodes and eigenfrequencies that are subsequently amplified. This phenomenon is called resonance. In the ULF range, for instance, the main resonances are magnetic field line resonances and cavity volume resonances [51]. In the ELF range, however, it is assumed that thunderstorm activity generates electromagnetic signals that interfere and resonate between conductive layers of the ionosphere and the Earth surface, known as Schumann resonances (SR).

In this chapter, methods of modelling the ELF wave propagation in the E-I cavity are described. Two main aspects arise; analytical and numerical models. Analytical methods solve Maxwell's equations by assuming a series of simplifications of the physical properties of the medium. Most of the analytical models have been thoroughly described in many works on ELF wave propagation and SR in E-I cavity [2, 19, 52]. Here, a brief overview will be presented. Time propagation of ELF waves will also be studied using a numerical method known as the Finite Difference Time Domain (FDTD). Numerical methods in general and the FDTD, in particular, present an advantage of being versatile: the capability of depicting a discretised description of the physical effects of the medium of propagation in time and in space provide a deeper analysis of ELF propagation problems.

3.2 Solving Maxwell's Equations in Spherical Coordinates

In spherical coordinates, Maxwell's equations (2.1)-(2.1) yield a set of three coupled partial differential equations (PDE) that have intertwined variables. Because in the spherical coordinates (r, θ, ϕ) the derivatives dr , $d\theta$ and $d\phi$ are not linearly independent of each other, in order to uncouple the PDE, it is required to reduce the solution into a product of variable independent terms $\psi(r, \theta, \phi) = f(r)g(\theta)h(\phi)$ that fulfils linear wave propagation condition [53], known as a Helmholtz equation

$$\nabla^2 \psi(r, \theta, \phi) = -\beta^2 \psi(r, \theta, \phi), \quad (3.1)$$

where $\beta = (\omega/c)$ is the wavenumber of the propagation.

3.3 Waveguide Analytical Approach

After this brief description of the properties of the Earth and its ionospheric medium, a review of the analytical methods used to model and predict the properties of EM propagation in the E-I cavity is given. The study starts from very simplified models of the cavity which are gradually enhanced to approach the physical model. The most basic formulation is the spherical waveguide theory was introduced by Schumann [1]. It considers the system as a concentric spherical structure made of two PEC shells and solves the Maxwell's equations for resonant waveguide modes between the shells. Wait's formulation is designed to find a solution of EM fields by considering them as sums of travelling wave modes, called Zonal Harmonic Series (ZHS). The solution is derived from a PEC Earth boundary and a stratified ionospheric medium where σ , ϵ and μ are defined. Galejs [54] method includes EM boundary conditions by adopting a model based on ionospheric surface impedances. This approach becomes very handy when analysing EM propagation in nonlinear media.

3.3.1 Spherical Cavity Model

EM resonance properties inside a spherical PEC shell are studied by applying the Laplacian to the decoupled auxiliary function in (3.1) to yield single variable equations. For instance in the radial component the Laplacian of $f(r)$ is deduced. By assuming $f(r) = \frac{1}{\sqrt{r}}u_n(r)$, where $u_n(r)$ is the radially dependent amplitude, the following expression is obtained [55]:

$$\left[\frac{d^2}{dr^2} + \frac{1}{r} \frac{d}{dr} + \beta^2 - \frac{(n + \frac{1}{2})^2}{r^2} \right] u_n(r) = 0 \quad n = 0, 1, 2, \dots, \quad (3.2)$$

whose solutions are radial Bessel's equations of index $\nu = n + \frac{1}{2}$. The solution writes

$$f_{nm}(r) = \frac{A_{nm}}{\sqrt{r}} J_{n+\frac{1}{2}}(\beta r) + \frac{B_{nm}}{\sqrt{r}} N_{n+\frac{1}{2}}(\beta r). \quad (3.3)$$

The expression (3.3) is the sum of Bessel spherical functions of first and second kind. Regular Bessel functions are given by,

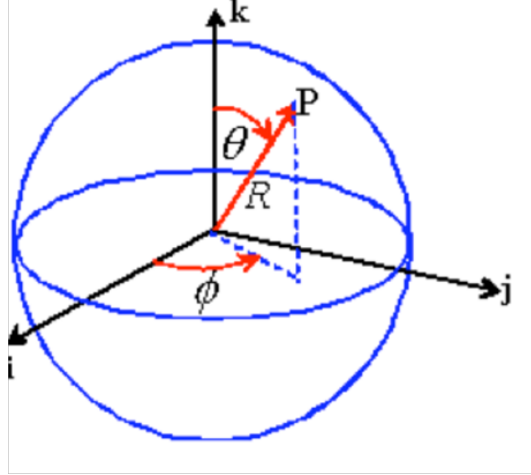


Figure 3.1: Spherical coordinate (R, θ, ϕ) representation. The radial component is in R direction and the angular components are θ in the meridional (elevational) azimuthal direction and ϕ in the equatorial azimuthal direction.

$$\begin{aligned} j_n(\beta r) &= \sqrt{\frac{\pi}{2\beta r}} J_{n+\frac{1}{2}}(\beta r) \\ n_n(\beta r) &= \sqrt{\frac{\pi}{2\beta r}} N_{n+\frac{1}{2}}(\beta r) \end{aligned} \quad (3.4)$$

The wave solutions in the radial direction can be summarized in a formulation involving travelling in the radial outwards or inwards direction. Hankel functions of the first kind $h_n^{(1,2)}$ and second kind $h_n^{(2)}$ are represented

$$h_n^{(1,2)}(\beta r) = [j_n(\beta r) \pm n_n(\beta r)]. \quad (3.5)$$

The Helmholtz equations (3.1) of the angular parts can be presented as follows [53]

$$\left\{ \frac{1}{\sin \theta} \frac{d}{d\theta} \left(\sin \theta \frac{d}{d\theta} \right) + \left[n(n+1) - \left(\frac{m}{\sin \theta} \right)^2 \right] \right\} g = 0 \quad (3.6)$$

$$\frac{d^2 h}{d\phi^2} = -m^2 h$$

The general solution to the Helmholtz equation is given by the combination of the radial solution and the azimuthal solutions. It is written as

$$\psi(r, \theta, \phi) = \sum_{n,m} \left[A_{nm}^{(1)} h_n^{(1)}(\beta r) + A_{nm}^{(2)} h_n^{(2)}(\beta r) \right] Y_{nm}(\theta, \phi), \quad (3.7)$$

where $A_{nm}^{(1,2)}$ are coefficients that are determined by boundary conditions and $Y_{nm}(\theta, \phi)$ are spherical harmonics solutions to the azimuthal PDEs in (3.1).

The continuity of transverse components of H at the PEC interface of the waveguide leads us to consider the presence of radial TM modes, so that the radial component $H_r = 0$. For simplicity, the fields E and H have no dependence in ϕ . Hence, the spherical harmonic function in (3.7) will be reduced to [55]

$$Y_{nm}(\theta, \phi) = \sqrt{\frac{(2n+1)(n-m)!}{4\pi(n+m)!}} P_n^m(\cos \theta) e^{im\phi}, \quad (3.8)$$

where $P_n^m(\cos \theta)$ are Legendre's associated polynomials of order m . In light of (2.4), if $H_r = 0$ and H_ϕ does not depend on ϕ , then $\vec{\nabla}_\phi \vec{H}_\phi = 0$. Hence $H_\phi \neq 0$. By applying (2.4) to the ϕ - component of the magnetic field, the expression $\vec{\nabla}_\phi \times \vec{E}_\phi = -\mu \frac{\partial \vec{H}}{\partial t}$ vanishes because H_ϕ is a constant, leading to $E_\phi = 0$. Therefore, radial TM modes present only three non-zero components

$$E_r, E_\theta \text{ and } H_\phi. \quad (3.9)$$

where, (r, θ, ϕ) are the three spherical components displayed in Fig. 3.1.

The solution to the quadratic equation obtained by combining (2.1) and (2.2) in spherical coordinate can be solved by incorporating only non-zero components cited in (3.9). The ϕ component of the equation yields solutions of the form [55],

$$H_\phi(r, \theta) = \frac{u_n(r)}{r} P_n^1(\cos \theta), \quad (3.10)$$

where $P_n^1(\cos \theta)$ is associated Legendre polynomial of the first kind. In the radial direction however, Helmholtz equation (3.1) forms a Bessel type PDE of the form

$$\left[\frac{d^2}{dr^2} + \beta^2 - \frac{n(n+1)}{r^2} \right] u_n(r) = 0. \quad n = 0, 1, 2, \dots \quad (3.11)$$

Equation 3.11 is the radial component definition of TM modes in the spherical cavity.

By using Ampere's law (2.2) and (3.10), properties of the components of the fields in the cavity are derived. The radial and angular (θ) component of \mathbf{E} becomes

$$E_r(r, \theta) = \frac{ic^2}{\omega r \sin \theta} \frac{\partial}{\partial \theta} (\sin \theta H_\phi) = -\frac{ic^2}{\omega r} n(n+1) \frac{u_n(r)}{r} P_n(\cos \theta), \quad (3.12)$$

$$E_\theta(r, \theta) = \frac{ic^2}{\omega r} \frac{\partial}{\partial r} (r H_\phi) = -\frac{ic^2}{\omega r} \frac{\partial u_n(r)}{\partial r} P_n^1(\cos \theta). \quad (3.13)$$

3.3.2 Schumann's Formulation [1]

The spherical waveguide is transformed into a resonant cavity made of two concentric perfectly conductive shells, with inner radius is R_E and the outer radius is $R_E + h$. The boundary conditions for tangential components of \mathbf{E} at the upper and lower boundaries becomes

$$E_\theta = 0 \text{ at } r = \begin{cases} R_E \\ R_E + h \end{cases} \iff \frac{\partial u_n(r)}{\partial r} \Big|_{r=R_E} = \frac{\partial u_n(r)}{\partial r} \Big|_{r=R_E+h} = 0. \quad (3.14)$$

From Bessel's PDE (3.11) and the boundary condition for tangential E component (3.14), the eigenfrequencies ω_n can be obtained. The propagation equation for radial component is deduced from (3.11) and written in a form of a propagating wave Helmholtz equation as

$$\frac{d^2 u_n(r)}{dr^2} + k^2 u_n(r) = 0, \quad (3.15)$$

where the constant k is the mode wavenumber. The dispersion relation of the wave propagation is

$$k^2 = \beta^2 - \frac{n(n+1)}{R_E^2}. \quad (3.16)$$

Here, it becomes necessary to make some approximation about the size of the waveguide. Its inner radius is $R_E = 6370$ km while the PEC shell outwards is located at a relative height $h = 100$ km. The assumption that $h \ll R_E$ is valid. The boundary conditions (3.14) applied to the harmonic solutions of (3.15) yield

$$u_n(r) = A \cos[k(r - R_E)], \quad (3.17)$$

where A is the amplitude of the function u_n . For $h \ll R_E$, the condition $\frac{\partial u_n(r)}{\partial r} |_{r=R_E} = 0$ is fulfilled when $k(r - R_E) = m\pi$ with $m = 0, 1, 2, \dots$ [55]. Therefore, the dispersion relation (3.16) for $h \ll R_E$ becomes

$$\omega_{mn} = c \sqrt{\left(\frac{m\pi}{h}\right)^2 + \frac{n(n+1)}{R_E^2}}, \quad m = 0, 1, 2, \dots, n = 0, 1, 2, \dots \quad (3.18)$$

This relation is a typical dispersion relation of TM_{mn} modes propagation in a spherical waveguide. It encompasses transversal TM_{m0} and longitudinal TM_{0n} modes. The radial TM_{m0} are standing modes between the PEC walls at angular frequencies $\omega_m = c\left(\frac{m\pi}{h}\right)$ for $m \geq 1$. They only depend on the local ionospheric height and are observed in the Very Low Frequency (VLF [3–30] kHz) range at $f_m = 1.5, 3, 4.5, \dots$ kHz for $m = 1, 2, 3, \dots$. The type of resonances of interest here are longitudinal resonances TM_{0n} commonly known *Schumann resonances*. These waves circumnavigate the entire sphere confined between the PEC shells and resonate along the entire circumference of the structure with \mathbf{E} oriented in the radial direction and \mathbf{H} tangential to the surface. The dispersion relation of these resonances is expressed as

$$\omega_n = \frac{c}{R_E} \sqrt{n(n+1)} \quad (3.19)$$

where ω_n is the angular frequency of the n th resonance. The eigenfrequencies $f_n = \omega_n/2\pi$ are named after W.O. Schumann who formulated the above theoretical model for a perfectly conducting Earth-Ionosphere cavity [1]. They are predominant in the lowest part of the ELF namely in the range [1 – 100Hz]. The resonance frequencies predicted by of the Schumann model (3.19) are

$$f_n = 10.6, 18.36, 25.96, 33.52, \dots \quad n = 1, 2, 3, 4, \dots, \quad (3.20)$$

and ($m = 0$) the EM fields can be expressed as follows

$$E_r^n \sim \frac{1}{r^2} P_n(\cos \theta) \text{ and } H_\phi^n \sim \frac{1}{r} P_n^1(\cos \theta). \quad (3.21)$$

3.3.3 Stratified Ionosphere Model [2]

The layered lossy medium approach was first proposed by Wait [2] and uses spherical harmonics known as zonal harmonic series to model the fields travelling in a cavity with PEC boundary conditions on the ground and a layered continuous lossy medium in the upper ionosphere. As shown in the Schumann formulation in Section 3.3.2, only TM_{0n} waves propagate at ELF. The model also introduces a Dirac impulse-type source in the form of a radial linear current placed at the

North pole position ($\theta = 0$) of the spherical coordinate system. The source can be described as $M_C(\omega) = I(\omega) dl$, where $I(\omega)$ is the spectrum of the current and l is the length of the channel. The Schumann dispersion formula (3.19) is adopted but in a twisted way. A propagation constant $\nu(\omega)$ is introduced. It represents the dispersion relation of the wave in the stratified medium. In such media, it is also useful to describe the variation of the dispersion of the impedance of the wave $Z(\omega)$. The dispersion relation becomes therefore [2, 19].

$$\omega^2 - \frac{i\omega c}{h} Z(\omega) = \left(\frac{c}{R_E}\right)^2 \nu(\omega) [\nu(\omega) + 1]. \quad (3.22)$$

The field solutions obtained are represented as follows [2, 19, 52]

$$E_r(\omega) = i \frac{M_C(\omega)}{4hR_E^2} \frac{\nu(\nu+1)}{\omega} \frac{P_\nu[\cos(\pi-\theta)]}{\sin \pi\nu}, \quad (3.23)$$

$$H_\phi(\omega) = -\frac{M_C(\omega)}{4hR_E^2} \frac{P_\nu^1[\cos(\pi-\theta)]}{\sin \pi\nu}, \quad (3.24)$$

where $i = \sqrt{-1}$ and h the effective height that represents the position of the ionospheric conductive layer. $P_\nu[\cos(\pi-\theta)]$ is associated Legendre function of complex order ν and $P_\nu^1[\cos(\pi-\theta)] = \frac{\partial}{\partial \theta} P_\nu[\cos(\pi-\theta)]$. Here, $\nu(\omega)$ is complex, and $\nu_1(\omega)$ represents the wave propagation and $\nu_2(\omega)$ wave absorption.

By solving the equations (3.23) and (3.24), the propagation parameter $\nu(\omega)$ is obtained by boundary conditions imposed by the radial propagation component $u_\nu(\beta r)$ and the following asymptotic expansions for the Legendre functions are obtained [19]

$$\frac{P_\nu[\cos(\pi-\theta)]}{\sin \pi\nu} = i \sqrt{\frac{2}{\pi(\nu + \frac{1}{2}) \sin \theta}} \exp\{-i[(\nu_1 + \frac{1}{2})\theta - \frac{\pi}{4}] - \nu_2\theta\} \quad (3.25)$$

$$\frac{P_\nu^1[\cos(\pi-\theta)]}{\sin \pi\nu} = i \sqrt{\frac{2(\nu + \frac{1}{2})}{\pi \sin \theta}} \exp\{-i[(\nu_1 + \frac{1}{2})\theta - \frac{\pi}{4}] - \nu_2\theta\} \quad (3.26)$$

In Fig. 3.2, the solutions of the zonal harmonics in (3.23) and (3.24) are depicted, for an excitation located at position $\theta = 0$. Equations (3.25) and (3.26) represent direct and antipodal wave propagation where $\nu(\omega)$ is the propagation constant of the wave of frequency ω travelling in the cavity along the azimuthal direction. $\nu(\omega) = \nu_1(\omega) - \nu_2(\omega)$ and at higher frequencies $\nu \sim kR_E \gg 1$ [19]. The dispersion relation is obtained from (3.22) given that the impedance of the lower ionosphere is known. The propagation parameter can be expressed as a function of the complex sine function S_ν as follows [2]

$$S_\nu(\omega) = (\beta R_E)^{-1} \sqrt{\nu(\nu+1)} = \sqrt{1 + \frac{Z(\omega)}{kh}} \quad (3.27)$$

where $\beta = \omega/c$ is the wavenumber. From this energy parameter, the quality factor of the resonant E-I cavity can be defined as the rate of the stored energy to the loss per period [2]. It can be derived from S_ν as follows

$$Q = \frac{\Re(S_\nu)}{2\Im(S_\nu)}. \quad (3.28)$$

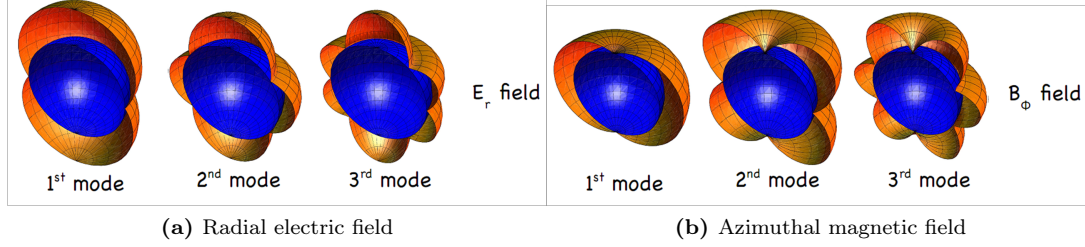


Figure 3.2: Angular solution for zonal harmonic series. The source is located at the meridional pole position $\theta = 0$. The azimuthal equatorial magnetic field $B_\phi = \mu_0 H_\phi$ and the radial electric field are depicted [4].

Propagation Parameter $\nu(f)$

For experimental SR studies, the propagation constant $\nu(\omega)$ can be determined empirically [19, 52]. It is basically determined from narrow frequency spectra in order to obtain a linear dependent function $\nu(f)$. The heuristic linear propagation parameter is expressed as follows [19]

$$\nu(f) = \frac{f - 2}{6} - \frac{if}{100} \quad (3.29)$$

The linear formulation of the propagation parameter (3.29) is called *Ishaq-Jones'* propagation model. Is allegedly one of the most accurate methods [19]. It is based on the measurement of the SR and the extrapolation of the $\nu(f)$ to the desired frequency range. It is expressed as a function of S_v as follows [8],

$$S_v = \frac{c}{V_p} - j(5.49) \frac{\alpha}{f} \quad (3.30)$$

The ratio of the speed of light c to the phase velocity of phase V_p can be determined as $\frac{c}{V_p} = 1.64 - 0.1759 \ln(f) + 0.0179 [\ln(f)]^2$ and the rate of attenuation of the wave in the cavity is written [8]

$$\alpha = 0.063 f^{0.64} \quad (3.31)$$

The Conductivity Height Profile

The conductivity profile is an approach to compute the electrical properties of the layer in order to get a precise estimate of the propagation factor in the medium. Greifinger and Greifinger [5] devised a method to approximate propagation parameters of the E-I cavity by using the exponential conductive profile of the ionosphere. The air conductivity profile is given by the exponential relation

$$\sigma(z) = \sigma_0 \exp\left(\frac{z}{\zeta_0}\right), \quad (3.32)$$

where z is the height and ζ_0 is the height scale of the conductivity profile. The model proposes a two height profile for the reflection of resonant EM fields: h_0 for the reflection of E - field and the height of diffusion of H into the ionospheric plasma h_1 [5]. The height profiles $h_{0,1}$ can be determined for

every frequency f given the condition that $\sigma(z)_{z=h_0} = \omega\epsilon_0$. Therefore,

$$h_0(\omega) = \zeta_0 \ln\left(\frac{\omega\epsilon_0}{\sigma_0}\right) \quad \text{and} \quad h_1(\omega) = h_0(\omega) - 2\zeta_0 \ln\left(\frac{\omega\zeta_0}{c}\right) \quad (3.33)$$

This double height profile explains the EM propagation dependence to the frequency. The model [5] has been widely used in ELF propagation models. It was used for instance by Nickolaenko and Hayakawa [56, 57] in the modal propagation solutions (3.23) and (3.24) to derive the properties of electromagnetic impulse in the spherical earth-ionospheric cavity both in the time and frequency domain, which proved to yield accurate results. It was also validated by a rigorous analytical study of dissipation in the ionosphere [58]. The selection of h_0 is not obvious; It becomes therefore necessary to define a *reference* height G , where the displacement and conduction currents are equal at a specific frequency (usually 10 Hz is considered for the study of the first SR). Hence, the conductivity profile becomes

$$\sigma(z) = \omega\epsilon_0 \left(\frac{z - G_h}{\zeta_0}\right), \quad (3.34)$$

and the initial height is given by $h_0 = G_h + \zeta_0 \ln(f)$.

The effective conductive layer is determined thanks to Ohm's law in its harmonic form, $\vec{J} = (\sigma + j\omega\epsilon)\vec{E}$. The real component is the conductive current and the complex part the displacement current. Hence, \vec{J} is real when the conduction current amplitude dominates the displacement current. Therefore, in the ELF range, the solid earth can be considered as PEC because the conductive current exceeds the displacement current (σ ranges from 10^{-3} to $5\Omega^{-1}m^{-1}$) resulting in the wave reflection over the surface because $\sigma \gg 2\pi f\epsilon_0$. In the lower ionosphere however, the conductivities range from $10^{-14} - 10^{-3}\Omega^{-1}m^{-1}$ from 0 to 100 km of altitude. At $f = 10$ Hz for instance, the EM reflection condition ($\sigma = 20\pi\epsilon_0\Omega^{-1}m^{-1}$) is observed at heights between 50 – 60 km above the ground, called the *effective* height. With this method, it is therefore essential to map the variation of electrical properties in the ionosphere. The electrical properties of the medium are σ, ϵ and μ , and only linear phenomena are taken into consideration.

3.4 Finite-Difference Time-Domain (FDTD) Method

The FDTD is a numerical method that approximates time-dependent Maxwell's equations by an approach based on Taylor series. The FDTD algorithm for a 3D cell was first introduced by Yee [59] who proposed to solve Maxwell's equations using finite difference operators on cubical lattices regularly arranged in space and time. In 1980, Taflove [60] applied Yee's algorithm to simulate the penetration depth of EM waves in metals and dielectrics and obtained very accurate results. More recently, Taflove and Hagness [61] extensively covered the subject of the FDTD from Yee's algorithm in 1D, 2D, 3D and described non-orthogonal lattices. The FDTD techniques are nowadays widely used in Science and Engineering to model EM wave propagation in various kinds of media. The number of scientific publications on FDTD has increased significantly in the last thirty years to reach approximately 2000 papers in 2006 [62].

For the E-I cavity propagation in particular, Thevenot and Bérenger [63] were the first to apply Yee's algorithm to the propagation of ELF waves in the E-I waveguide and found a good agreement

between the FDTD and the waveguide model. Cummer [64] developed a 2D lattice model to operate below 30 kHz in the cavity. He reported extremely good agreement between the FDTD and analytical model. Simpson and Taflove [65] developed a 3D model of the entire E-I waveguide, by using a non-orthogonal grid which fits relatively well the spheroidal shape of the Earth surface. They proposed a 3D latitude-longitude meshing which is square in the equatorial region ($40 \times 40 \text{ km}$), gradually trapezoidal in high latitudes and pentagonal for the poles, while in the radial direction the mesh (5 km) follows a spherical symmetry as proposed by Holland [66]. The applications of this model are quite vast, it has been applied to the study of lithospheric radiations associated with earthquakes [67], to the development of techniques for underground mineral deposit detection [68, 69] and localised ionospheric anomalies [70]. Other researchers [71, 72] have used the spherical body symmetry FDTD algorithm [66] to examine the propagation of ELF waves and resonances of ELF in the cavity. The most notable attribute of studies cited above is the high degree of correlation between FDTD and analytical solutions (experimental data) despite the simplicity of the method.

3.4.1 Maxwell's Equations and Yee Algorithm

By developing the curl equations (2.1) and (2.2) and rewriting their left-hand side components in the Cartesian frame, where \vec{J} is the electric current density. $\vec{J} = \sigma \vec{E} + \vec{J}_0$ with σ the electrical conductivity of the medium and \vec{J}_0 the source current density. We obtain the following equations,

$$\frac{\partial E_x}{\partial t} = \frac{1}{\epsilon} \left[\frac{\partial H_z}{\partial y} - \frac{\partial H_y}{\partial z} - \sigma E_x - J_{0x} \right] \quad (3.35)$$

$$\frac{\partial E_y}{\partial t} = \frac{1}{\epsilon} \left[\frac{\partial H_x}{\partial z} - \frac{\partial H_z}{\partial x} - \sigma E_y - J_{0y} \right] \quad (3.36)$$

$$\frac{\partial E_z}{\partial t} = \frac{1}{\epsilon} \left[\frac{\partial H_y}{\partial x} - \frac{\partial H_x}{\partial y} - \sigma E_z - J_{0z} \right] \quad (3.37)$$

$$\frac{\partial H_x}{\partial t} = \frac{1}{\mu} \left[\frac{\partial E_y}{\partial z} - \frac{\partial E_z}{\partial y} \right] \quad (3.38)$$

$$\frac{\partial H_y}{\partial t} = \frac{1}{\mu} \left[\frac{\partial E_z}{\partial x} - \frac{\partial E_x}{\partial z} \right] \quad (3.39)$$

$$\frac{\partial H_z}{\partial t} = \frac{1}{\mu} \left[\frac{\partial E_x}{\partial y} - \frac{\partial E_y}{\partial x} \right] \quad (3.40)$$

Equations (3.35) - (3.40) are coupled partial differential equations in 3D Cartesian frame. Using discretised material properties specified for each lattice point, \mathbf{E} and \mathbf{H} components can be calculated.

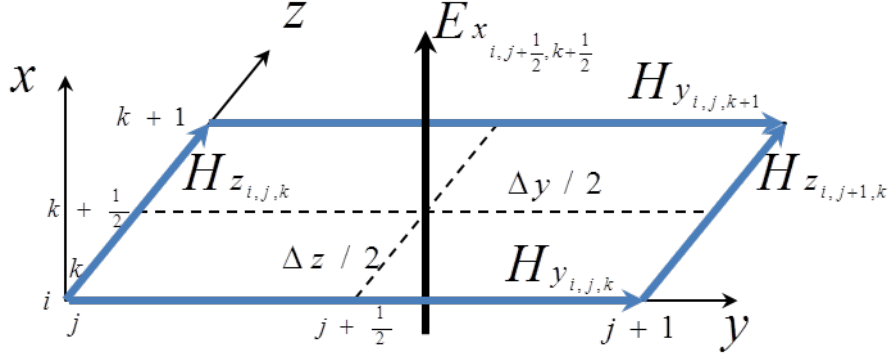


Figure 3.3: Yee cell showing the alternating electric and magnetic fields in the (y, z) plane.

3.4.2 Finite Differences

A function of space and time $u(x, t)$ at a time $t = t_n$ is defined. If the function is continuous in space, it can be described in the vicinity of the point $x = x_i$ at the first order of derivation as follows

$$u(x_i + \Delta x)|_{t=t_n} = u(x = x_i)|_{t=t_n} + \frac{\Delta x}{1!} \frac{\partial u(x = x_i)|_{t=t_n}}{\partial x} + \mathcal{O}[(\Delta x)^2], \quad (3.41)$$

where the function $\mathcal{O}[(\Delta x)^2]$ is the remainder function of the Taylor series at the second order of derivation. By defining a regular 1D lattice, where the step is $\Delta x = x/i$, the function u is obtained at every node of the lattice. The notation $u(x_i + \Delta x)|_{t=t_n}$ is the forward term of u , written as u_{i+1}^n . The partial derivative $\frac{du}{dx}$ can be approximated using a forward, backward or central differences. This depends on the direction taken to iterate the function and the sequence of nodes of the lattice taken into account.

The forward difference is defined as

$$\frac{du}{dx} = \frac{u_{i+1}^n - u_i^n}{\Delta x} + \mathcal{O}[(\Delta x)^2], \quad (3.42)$$

and the backward difference is given by

$$\frac{du}{dx} = \frac{u_i^n - u_{i-1}^n}{\Delta x} + \mathcal{O}[(\Delta x)^2]. \quad (3.43)$$

The central difference for the first derivative is evaluated between the forward and backward node values as follows

$$\frac{du}{dx} = \frac{u_{i+1}^n - u_{i-1}^n}{2\Delta x} + \frac{(\Delta x)^2}{6} \frac{d^3 u}{dx^3} + \mathcal{O}[(\Delta x)^4]. \quad (3.44)$$

In a similar fashion, $\frac{du}{dt}$ can be evaluated at a fixed lattice point by iterating the function in time. A central difference for instance yields

$$\frac{du}{dt} = \frac{u_i^{n+1} - u_i^{n-1}}{2\Delta t} + \mathcal{O}[(\Delta t)^3], \quad (3.45)$$

where Δt is the step in time, or *leapfrog*.

3.4.3 Yee's FDTD algorithm

The function $u(x, t)$ can be adapted to the temporal 3D Cartesian lattice $u(x, y, z, t) = u(i\Delta x, j\Delta y, k\Delta z, n\Delta t)$ and be written $u_{i,j,k}^n$. Yee used a second order central difference method in time and in space with an increment of $1/2$ to alternate \mathbf{E} and \mathbf{H} by half of the lattice length. Fig. 3.3 shows a unit lattice of such a mesh as defined by Yee in [59]. By evaluating Faraday's law on the lattice (y, z) -plane as represented in (3.35) and then applying an average of consecutive terms in time; a temporal algorithm for E_x normal to the plane at $(i, j + 1/2, k + 1/2)$ in the lattice can be computed [61]

$$E_x|_{i,j+1/2,k+1/2}^{n+1/2} = \left(\frac{1 - \frac{\sigma_{i,j+1/2,k+1/2}}{2\epsilon_{i,j+1/2,k+1/2}}}{1 + \frac{\sigma_{i,j+1/2,k+1/2}}{2\epsilon_{i,j+1/2,k+1/2}}} \right) E_x|_{i,j+1/2,k+1/2}^{n-1/2} + \left(\frac{\frac{\Delta t}{\epsilon_{i,j+1/2,k+1/2}}}{1 + \frac{\sigma_{i,j+1/2,k+1/2}}{2\epsilon_{i,j+1/2,k+1/2}}} \right) \left[\begin{array}{c} \frac{H_z|_{i,j+1,k+1/2}^n - H_z|_{i,j,k+1/2}^n}{\Delta y} \\ - \frac{H_y|_{i,j+1/2,k+1}^n - H_y|_{i,j+1/2,k}^n}{\Delta z} \\ - J_{0x}|_{i,j+1/2,k+1/2}^n \end{array} \right] \quad (3.46)$$

In the same way, Maxwell's equations (3.36)-(3.40) can be computed. The subject is extensively covered in the book by Taflove and Hagness [61].

3.4.4 Dispersion and Stability Conditions

Due to the interaction between the numerical wave and the grid structure, the FDTD wave propagation is distorted by the accumulation of delay and phase errors. Large structures impose a certain limit to the accuracy of the FDTD simulation. Taking into consideration a wave that travels in a 3D-Yee grid, the dispersion is given by the relation [61]

$$\left[\frac{1}{c\Delta t} \sin\left(\frac{\tilde{\omega}\Delta t}{2}\right) \right]^2 = \left[\frac{1}{\Delta x} \sin\left(\frac{\tilde{k}_x\Delta x}{2}\right) \right]^2 + \left[\frac{1}{\Delta y} \sin\left(\frac{\tilde{k}_y\Delta y}{2}\right) \right]^2 + \left[\frac{1}{\Delta z} \sin\left(\frac{\tilde{k}_z\Delta z}{2}\right) \right]^2 \quad (3.47)$$

where c is the phase velocity of the wave (speed of light), $\tilde{\omega}$ is the numerical wave pulsation, and \tilde{k}_x , \tilde{k}_y and \tilde{k}_z are numerical wavevector components in respective directions of space. The solution of the numerical propagation in a Yee grid (3.47) converges to the linear, isotropic and non-dispersive medium solution $(\omega/c)^2 = k_x^2 + k_y^2 + k_z^2$, if these following conditions are met

1. Space and time must be finely sampled $\Delta x, \Delta y, \Delta z, \Delta t \rightarrow 0$.
2. The time-dependent function is bounded to the domain where its solution is stable. Hence, the maximal iteration timestep limit becomes [61]

$$\Delta t \leq \frac{1}{c\sqrt{\frac{1}{\Delta x^2} + \frac{1}{\Delta y^2} + \frac{1}{\Delta z^2}}} \quad (3.48)$$

The latter is known as the Courant stability condition. It is a crucial factor that ensures the stability of Yee's algorithm. In practice however, there are other criteria that should be taken into account, such as the type of mesh, of material used and the boundary conditions imposed to each mesh entity.

An example of this is when the mesh is non-uniform; the Courant condition (3.48) reduces

$$\Delta t \leq \left(c \sqrt{\frac{1}{\Delta x_{\min}^2} + \frac{1}{\Delta y_{\min}^2} + \frac{1}{\Delta z_{\min}^2}} \right)^{-1}, \quad (3.49)$$

where Δx_{\min} , Δy_{\min} and Δz_{\min} represent the minimum space increment in the respective 3D. Here, the material is considered uniform. In the case of lossy materials (dispersive or nonlinear such as plasma), the space increment must be well refined to accurately model local fields [61].

3.4.5 Absorbing Boundary Conditions (ABCs)

Modelling simple propagation problem would require a huge computer memory if one does not consider a limit to the domain of computation. A finite boundary which simulates the wave propagation to infinity is appropriate for the simulation to avoid a lack of memory. Such a boundary is called an Absorbing Boundary Condition (ABC) and it is integrated into the code that we were using in this work. ABCs can be applied to a wide range of materials and has been extensively adapted to different types of meshes. ABCs can be subdivided into two distinct groups. The oldest design is based on annihilating reflection at boundaries by the use of PDEs and finite differences [73, 74] and a more advanced method based on the simulation of properties of an absorbing material at the boundary of the simulation domain called the Perfect Matched Layer (PML) [75].

Differential ABC

The differential ABC was developed by Engquist and Majda [73] and is based on a backwards difference technique. A linear partial differential equation is defined on the bounded system which expresses the wave absorption in one direction.

By assuming an EM wave that propagates across a rectangular bounded area in the $(x, y) -$ plane. The wave equation is given by

$$\frac{\partial^2 u(x, y, t)}{\partial x^2} + \frac{\partial^2 u(x, y, t)}{\partial y^2} - \frac{1}{c^2} \frac{\partial^2 u(x, y, t)}{\partial t^2} = 0 \quad (3.50)$$

where $u(x, t)$ is the electromagnetic perturbation on the area. x is bounded by $[0, h]$ and y by $[0, h_1]$.

This equation can be expressed in the form of $GU = 0$ where G represents the differential operator and U the electromagnetic perturbation. G represents accounts for a propagating (G^+) and an exponentially decaying wave (G^-). G equals to $G = G^+G^-$ and the root G^- is then used as the ABC. The ABC principle is applied to U for the cancellation the boundary reflections. An extensive coverage of the implementation of this type of ABC can be found in [61].

The Perfect Matched Layer (PML)

The PML is an ABC method that exploits the absorbing properties of a lossy artificial material at the boundary of the simulated structure. The technique was invented by Bérenger [75] for a 2D structure. It was since adapted to 3D FDTD problems and is nowadays very popular in the

domain of Computational Electromagnetics [76]. Prior to the PML, several attempts were made to develop a boundary that could absorb EM waves emanating from the computational domain. The reason behind this was because the differential ABCs could not provide a -50dB absorption, yet -70dB of noise cancellation could be achieved in anechoic chambers in the 1980s [76]. In those days, the absorbing medium that was used was only effective for normal incidence [77]. Bérenger [75] revolutionised the wave matching technique by splitting the normal field into two components in a 2D setup. The PML method provided unprecedented effectiveness in absorbing incident waves for any polarisation, frequency and angles of incidence.

Gedney and Taflove formulation [77] Consider an incident TE_z wave with a magnetic component $\vec{H} = H_0 \exp(-j(\beta_{1x}x + \beta_{1y}y))z$ propagating in a lossless medium 1 that impinges at an angle θ on a (x, y) plane infinitesimally thin boundary plane disrupting the medium at $(x = 0)$. the transmitted wave is defined as

$$\begin{aligned}\vec{H} &= H_0 e^{-\sigma\eta_1 x} e^{-jk_1 x} \hat{z} \\ \vec{E} &= H_0 \eta_1 e^{-\sigma\eta_1 x} e^{-jk_1 x} \hat{y}\end{aligned}\quad (3.51)$$

where $\eta_1 = \sqrt{\mu_1/\epsilon_1}$ is the impedance of the medium and $\beta_{1x} = k_1 \cos \theta$, $\beta_{1y} = k_1 \sin \theta$ are propagation constants in x and y direction respectively and $k_1 = \omega\sqrt{\epsilon_1\mu_1}$ is the wavenumber. Therefore, only for normal incidence the wave is transmitted with no reflection and decays exponentially by a factor $-\sigma\eta_1$ in the layer. An interesting aspect of this formulation is that the frequency dependence of the incident wave is not altered and the phase remains constant.

Bérenger's PML [75] In order to attain total absorption of the incident wave into the layer, the normal field in the medium is split in orthogonal components, $H_z = H_{zx} + H_{zy}$. Each components depends on a magnetic (σ_x^*, σ_y^*) and electric conductivity (σ_x, σ_y) in x and y directions respectively. By considering the current densities as $J = \sigma E$ and $M = \sigma^* H$, the application of Faraday's laws (3.35) and (3.36) to components E_x and E_y and Ampere's law (3.40) to the field H_z leads to the following transmitted wave expressions

$$\begin{aligned}\vec{H} &= H_0 e^{-\sigma\eta_1 x \cos \theta} e^{-j\beta_{1x}x - j\beta_{1y}y} \hat{z} \\ \vec{E} &= H_0 \eta_1 (-\sin \theta \hat{x} + \cos \theta \hat{y}) e^{-\sigma\eta_1 x \cos \theta} e^{-j\beta_{1x}x - j\beta_{1y}y}\end{aligned}\quad (3.52)$$

This is a very important feature of the Bérenger's formulation for the PML. The exponential attenuation factor $-\sigma\eta_1 \cos \theta$ is independent of the signal frequency so that the phase velocity remains constant. The incident electromagnetic waves are attenuated without dispersion at all polarisations, all frequencies and at all angles of incidence; In 2D, the application of the PML on a 10 layer mesh provides an absorption down to -85dB [76].

The PML concept was extended to 3D-FDTD simulation model by Katz *et al* [78]. The most used formulation is known as uniaxial PML (UPML) and it is based on an anisotropic and lossy medium formulation. The UPML yields similar performance as the PML in a more elegant manner [79]. However, the UPML involves the calculation of electric and magnetic flux vectors \mathbf{D} and \mathbf{B} which yet increases the computational burden. The *stretched coordinate* formulation introduced by Chew and Weedon [80] maps Maxwell's equations of the of the UPML into a complex coordinate notation.

This representation not only simplifies the PML computations but also allows the utilisation of the PML in non-orthogonal coordinate systems.

3.5 Conclusion

In this chapter, basic analytical formulations for the resolution of a spherical waveguide problem are presented along with their numerical implementation using the FDTD method. All along, our attention was focused on the use of the FDTD method to solve Maxwell's equations in a spherical cavity, using the medium's electromagnetic parameters σ , μ and ϵ , whose value distributions in the cavity are predicted by analytical models and their adjustments after analysis of experimental data. In this work, the FDTD provides the means to compute the field faster and more efficiently, but its results are always subject to scrutinised examination in comparison to the model predictions and experimental well-established data found in the literature.

Chapter 4

Modelling of the Uniform Earth-Ionosphere Cavity Using CST Microwave Studio[®]

4.1 Introduction

In this chapter, EM wave propagation in the cavity composed of solid Earth and ionospheric layers is investigated. The Earth and the ionosphere are modelled as concentric spherical structures. The Earth's crust of the model is described as a PEC layer and the ionosphere treated as a conductive layered medium described analytically by Wait [2], with the conductivity of the layers following a double exponential radial profile proposed by Greifinger [5]. A numerical method based on finite-difference time domain (FDTD) technique is used to solve Maxwell's equations in three dimensions using a commercial software package; CST Microwave Studio[®] (CST-MWS). The ionospheric layers are considered as uniform isotropic lossy dielectrics in the azimuthal direction. The design of the simulation layout consists of concentric shells 10-km thick each that are carefully designed to represent the stratified model (Fig. 4.1). Conductivity values for each layer are sampled from the Greifinger and Greifinger's *knee* model [5] depicted in Fig. 4.2.

4.2 CST Microwave Studio

CST Microwave Studio[®] is a commercial software based on the Finite Integration Technique (FIT) that was developed by Weiland [81]. The Time-Domain Solver[®] feature computes the wideband behaviour of electromagnetic waves in the 3D structure and can be tuned to fit chosen mesh dimensions. The spatial discretisation of boundaries is based on Perfect Boundary Approximation[®] (PBA) that minimises numerical errors conveyed by the stair-stepped approximation of a curved boundary [82]. The PBA performs not by conforming the meshing lattice to the surface of the simulated area, but by manipulating sub-cellular information using an algorithm with second order accuracy.

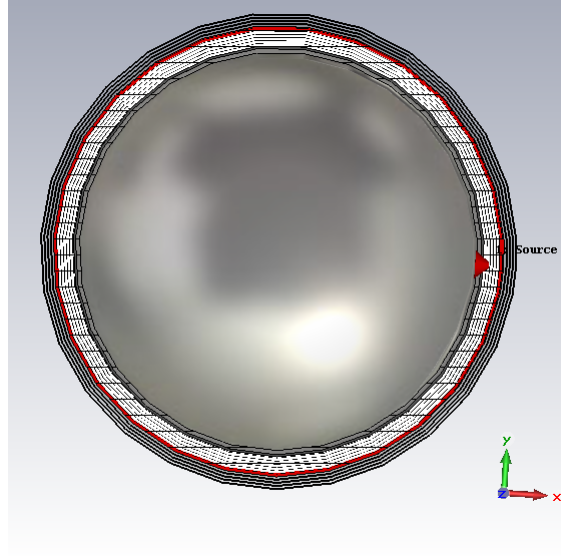


Figure 4.1: Concentric shell layout drawn in CST MWS for FDTD simulation of the E-I system. The radius of the inner shell is the Earth radius $R_E = 6370$ km. Each layer represented is 10 km thick. The light-grey colored layers represent the lower σ profile, and the dark ones the higher σ profile. Both profiles are separated at the *knee* height. The triangle at the right side depicts the position of the discrete excitation port. E and H field probes are placed at 1 Mm interval from the source along the arc of the sphere in the (x, y) plane, in the light grey area.

Also, the software embeds a Thin Sheet Technology[®] (TST) feature which resolves a PEC and a non-PEC regions contained within a single cell [82]. The time-domain simulation utilises a rectangular hexahedral mesh type. The automatic mesh generator detects important points inside the structure (fixpoints) and places node points there. Fixpoints can also be placed manually on the structure according to the desired resolution. Specific mesh resolution in function of the maximum wavelength can also be chosen by the user.

CST MWS is also equipped with the Convolutional PML [83] which is based on the Chew and Weedon formulation [80] and the convolution in the time domain that increases the absorption of evanescent waves. This provides a very good performance in complete independence of simulated medium properties, ideal for lossy, inhomogeneous, and anisotropic media. It also allows optimal memory usage. Fig. 4.1 shows the layout of the spherical Earth-Ionosphere system. The Earth solid layer is the grey inner shell and the atmospheric and ionospheric layers extend outwards. The numerical model covers temporal propagation of waves in the Earth-Ionosphere cavity and the simulation results to spectra in Fourier domain. The excitation source is a discrete port and the exciting signal is an EM model of a vertical current channel found in the literature [7, 84].

Therefore, the FDTD code computes the wave propagation in the E-I cavity using Yee hexahedral lattices [59] depicted in Fig. 3.3. The layout of the simulation is shown in Fig. 4.1. CST MWS provides considerable advantages; its user-friendly interface allows handling complex structures with ease and has proven to be one of the best computational software in terms of speed and accuracy for time-domain analysis [76]. However, the main drawback of our method is that the mesh used does not accurately reproduce the roundness of the spherical structures. A trade-off has to be found between the simulation time, the result accuracy and our computer memory which was limited to

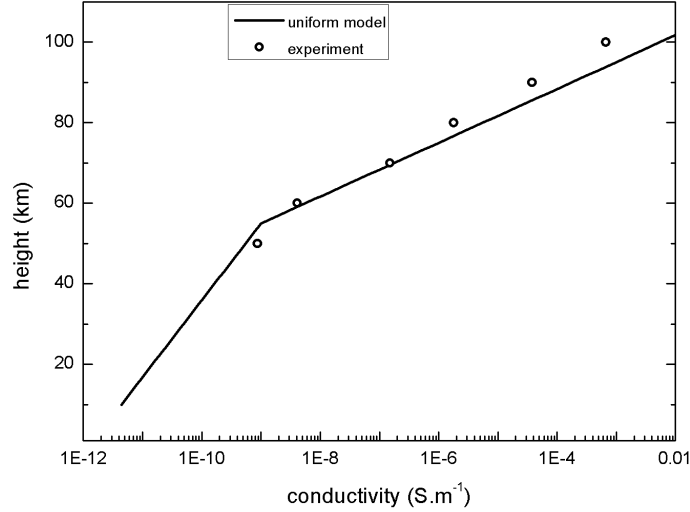


Figure 4.2: Knee model as introduced by [5]. Values of $\zeta_{0,1}$ and σ are derived from [6]. The solid line represents the model and the hollow dots represent experimental data.

16 GB of RAM.

4.2.1 Simulation Parameters

Height Conductivity Profile of the Ionosphere

Models of ionospheric conductivity have been derived analytically from measurements of ion content using artificial satellites in low orbit. Madden and Thompson [26] identified two main layers in the ionosphere: The lower layer that influences the vertical electric field while the upper region controls the horizontal magnetic field. Later on, Greifinger [5] proposed an analytical model based on Maxwell's equations to study the propagation parameters in a uniform and isotropic cavity. His approach uses a double exponential to describes the two ionospheric layers mentioned earlier. Mushtak and Williams [6] derived the *knee* model that defines the conductivity profile in the two characteristic layers. They showed that the knee is related to the inflexion between two conductivity regimes at the *reference* height (3.34) located at the lower-layer height h_{knee} as shown in Fig. 4.2. The conductivity profile is described as follows,

$$\begin{aligned} \sigma(z) &= \sigma_0 \exp[(z - h_{\text{knee}})/\zeta_0] & \text{for } z < h_{\text{knee}} \\ \sigma(z) &= \sigma_0 \exp[(z - h_{\text{knee}})/\zeta_1] & \text{for } z \geq h_{\text{knee}} \end{aligned} \quad (4.1)$$

where σ_0 is the conductivity at the *knee* altitude h_{knee} and $\zeta_{0,1}$ are the scale heights that approximate the exponential conductivity below and above h_{knee} . Fig. 4.2 shows a conductivity profile of the E-I cavity with the *knee* at a height between 50 and 60 km. From Section 3.3.3 and experimental measurements, the value of $\sigma_0 = 5.56 \times 10^{-10} \Omega^{-1}m^{-1}$ and the scale heights $\zeta_{0,1}$ can be determined respectively. For the uniform cavity model, $\zeta_0 = 8.3$ km and $\zeta_1 = 2.9$ km [6]. The conductivity values obtained from (4.1) and displayed in Fig. 4.2 are sampled for each 10-km thick ionospheric layer of the FDTD simulation as shown in Fig. 4.1. The Earth is considered as a sphere of radius

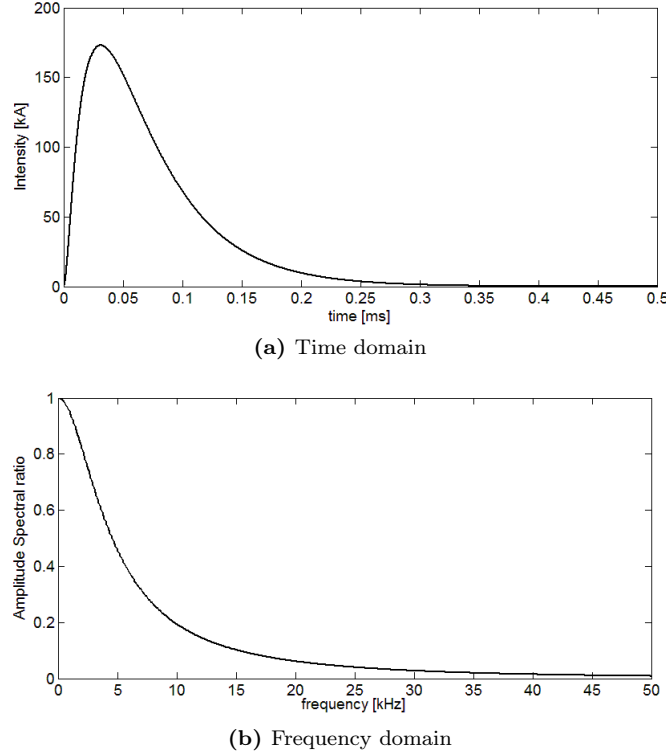


Figure 4.3: A typical ELF transient return-stroke model (a) in time and (b) in frequency domain. Its intensity is ten times higher than a typical lightning return stroke defined in [7].

$R_E = 6.37$ Mm with a 10 km thick PEC crust. The ionospheric layers extend outwards to a height of 100 km.

Excitation Signal

The return stroke current channel has been modelled as a double exponential current pulse by Bruce and Golde [7, 84]. The total intensity at the ground is given by

$$I_{\text{ground}}(t) = I_0 (\exp(-\alpha t) - \exp(-\beta t)) \quad (4.2)$$

where for a typical lightning stroke, $I_0 = 20$ kA, $\alpha = 2 \times 10^4$ s^{-1} and $\beta = 2 \times 10^5$ s^{-1} . Here, the current travels along the vertical channel of the stroke at the speed V , decreasing exponentially as $V(t) = V_0 \exp(-\gamma t)$ where $\gamma = 3 \times 10^4$ s^{-1} and $V_0 = 8 \times 10^7$ m/s. The total length of the channel is given by the integral $L = \int_0^\infty V(t) dt = V_0 \Delta t$, where Δt is the duration of the pulse. The basic length of the pulse proposed by Jones is 4 km [85]. Hence, by introducing Δt into (4.2), the total current of the stroke is

$$I(t) = I_0 \frac{V_0}{\gamma} (\exp(-\alpha t) - \exp(-\beta t)) (1 - \exp(-\gamma t)) \quad (4.3)$$

Fig. 4.3 shows a typical excitation signal used in our FDTD simulations. It has been shown that in most active thunderstorm areas, particularly powerful lightning strokes occur once in a

few minutes [86]. They are called ELF transients (or Q-bursts). They are usually 3 – 10 times more intense than the background noise in magnetic recordings and their impulse response can be recorded all over the World [87–89]. In order to study the impulse response of the entire E-I cavity, the amplitude of the exciting signal represented in Fig. 4.3 is chosen to be ten times that of the typical return stroke current signal described in (4.3). A 5-km long vertical discrete port is used to trigger the current pulse and is by default located at the equatorial Cartesian position $(R_E, 0, 0)$ to simulate a positive cloud-to-ground lightning return stroke. The polarity of the port is positive upwards, meaning that the top (cloud) is negatively charged [90]. Positive polarity strokes represents more than 85% of all the strokes that occur in the cavity [29, 88]. A set of field detectors separated by 1 Mm of distance are placed along the meridian of the solid Earth (Fig. 4.1). The spectrum of the pulse shows that its power is concentrated at lower frequencies (below 5 kHz) as shown in Fig. 4.3b.

4.3 Simulation Results

From the simulation setup in Fig. 4.1, the solid Earth PEC medium is excluded to reduce the computational burden. The electric impulse in Fig. 4.3a is set into a time window of 0.5 s and the field responses are downsampled to fit the frequency range from 1 – 100 Hz. Space resolution factor $\Delta/\lambda_0 = 80$ is chosen in all directions, so that the maximal space mesh step becomes $\Delta = 0.0125\lambda_0 = 37.5$ km, where λ_0 is the smallest wavelength in the frequency window of the simulation ($f_0 = 100$ Hz). The software adjusts the time step automatically according to the Courant condition defined in (3.49), [$\Delta t \leq 8 \times 10^{-5}$ s in this case]. An automatic timestep of $\Delta t = 8.5 \times 10^{-6}$ s requires a 10 GB RAM on average and a simulation time of 29 hours. The first step of our investigation consists of correlating the FDTD propagation model with previous research. Similarities between the simulated waveforms and the propagation distance will be evaluated in time and frequency domains. Spectral properties of the cavity will also be studied.

4.3.1 Propagation Model Validation

The electric and magnetic fields in the cavity are measured with probes placed at 1 Mm (1000 km) interval from the pulse origin (source) to 20 Mm (antipode) as shown in Fig. 4.1. To measure the cavity attenuation parameter, the electric field wave is sampled at 5 Mm and 10 Mm distances from the source respectively. The attenuation can be obtained using the ratio of the forward field spectra $R = E_{10\text{Mm}}^+/E_{5\text{Mm}}^+$. In both cases, \mathbf{E} wave is truncated to eliminate the portion reflected in the cavity and the resultant spectra yield the attenuation rate of the wave as a function of frequency [91]. In Fig. 4.4, the attenuation of the \mathbf{E} wave is plotted in logarithmic scale against the frequency in the spectral window from 1 to 250 Hz. It is shown that the rate of attenuation is 7.4×10^{-3} dB Mm $^{-1}$ Hz $^{-1}$. The slope is in accordance with previous research [65, 91]. As shown in Fig. 4.4, our FDTD simulation data and the *Ishaq-Jones*' attenuation rate in the uniform E-I cavity as defined in (3.31) display discrepancy of only 9% above 50 Hz. The simulation presents however a static offset attenuation of 0.25 dB Mm $^{-1}$ higher than *Ishaq-Jones*' rate.

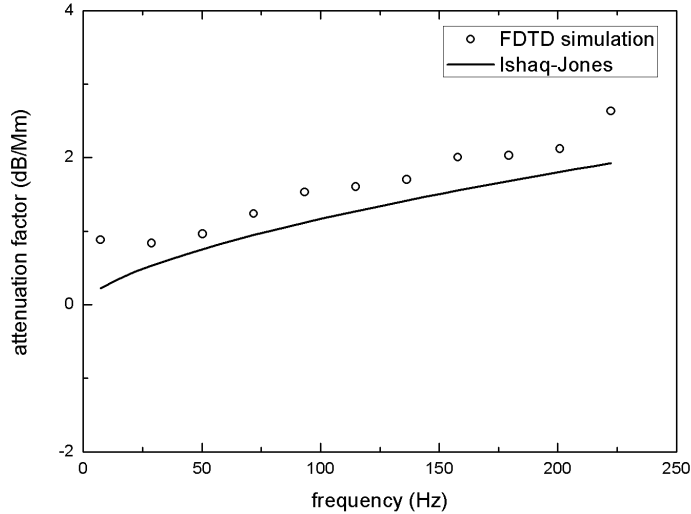


Figure 4.4: Graph representing the rate of attenuation of \mathbf{E} versus frequency in the E-I cavity as simulated with 3D-FDTD (round dots). The straight line represents the experimental Ishaq-Jones' attenuation rate [8].

4.3.2 Electric and Magnetic Wave Propagation

Fig. 4.5 shows a typical propagation of the electric field pulse (top graph) and the magnetic pulse response (bottom graph) in the spherical cavity as obtained with our 3D FDTD model. The vertical electric field component response is negative by virtue of $\mathbf{E} = -\vec{\nabla}V$ where V is the potential. V is positive because it creates an upwards positive return stroke as shown in Section 4.2.1. \mathbf{E} shows an exponential attenuation of the amplitude and a sharp amplification when the wave is close to the antipode. A progressive widening of the peak width is also observed. The wave amplitude reaches a minimal -48 dB at 18 Mm distance. The amplitude of the wave sharply increases afterwards by 10 dB due to the constructive superposition of the pulse ring towards the antipode (Fig. 4.6a). The slight amplification of the wave between 12 and 16 Mm could not be explained; it might, however, be attributed to the use of a slowly decaying excitation signal. The superposition of the tail of the excitation signal and the antipodal wave cannot be excluded.

The spherical geometry plays a crucial role in the resonance of the electric wave in the cavity; this is the main reason for the amplification of the wave in the antipode region. At the antipode, the wavefront merges into a single point and propagates back towards the source. The antipode behaves in this case as a secondary source. A detector located at 10Mm sees the primary and secondary pulses in one propagation cycle. A very powerful source can produce a signal that can bounce back and forth for enough periods to produce a detectable resonance signal. Fig. 4.7a shows clearly this effect: The \mathbf{E} pulse is shown travelling and bouncing back, at least, three times in a window of 0.5 second (20 Mm detector plot). An alternating dip (downward peak) of the field at 10 Mm and 20 Mm can be observed. For instance in the first round-the-globe *trip* of the \mathbf{E} wave, the wavefront crosses the 10 Mm milestone and reaches 20 Mm (the antipode) at 42 and 84 ms respectively. The sourcewards (antipodal) wave seen at 10 Mm at 126 ms has the same polarity as the source wave. We found the velocity of the \mathbf{E} wave equal to 238.1 Mm/s which is 0.8 times the speed of light ($0.8c$). This finding is in agreement with the results in [88–90] where a velocity of 256, 265 and 250 Mm/s are

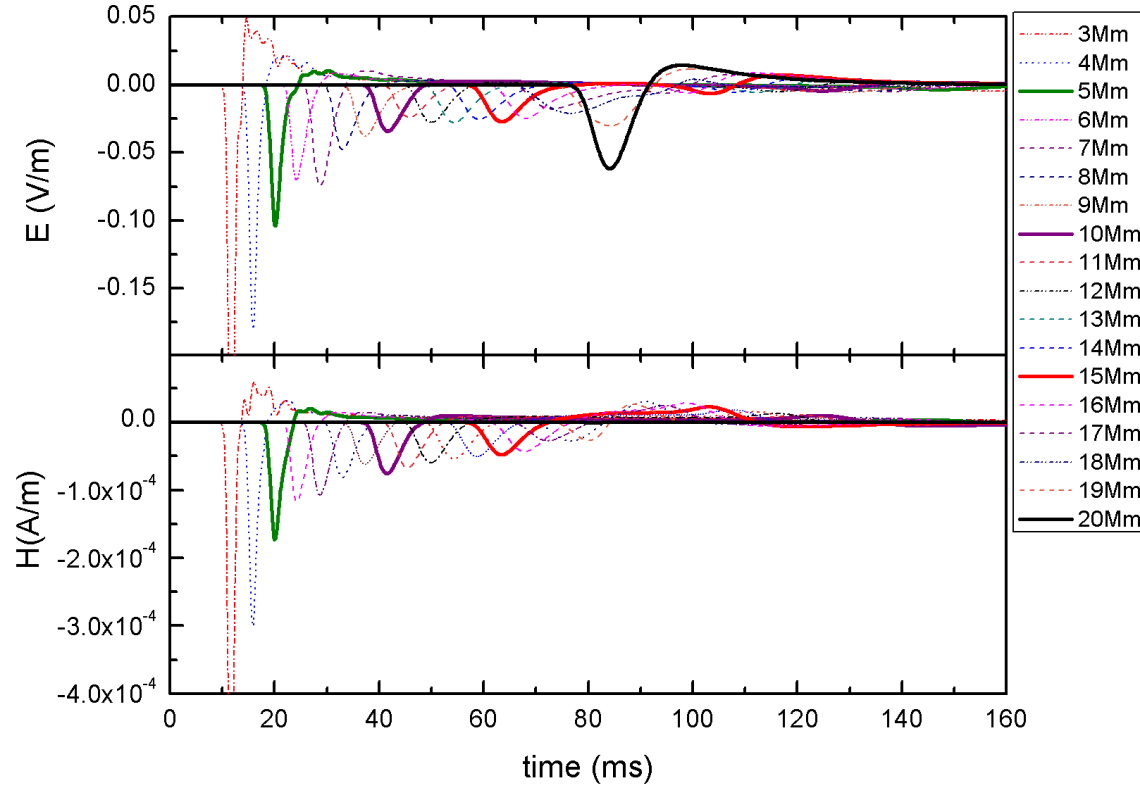


Figure 4.5: Propagation of vertical \mathbf{E} (top panel) and horizontal \mathbf{H} (bottom) waveforms originating from an ELF transient the E-I cavity. The pulses recorded at distances of 5, 10, 15 and 20 Mm are drawn in thick line.

presented. A comparison with the signal for 10 Mm shows that the wave is slightly amplified every time it reaches an antipode (a point of reflection). In the first half-round (0 – 84 ms), the linear amplification factor is roughly 2 times between the two measuring ports. A severe flattening and widening of the peaks are also observed, owed to the attenuation of high-frequency components of the field as it has been shown previously in Figs. 4.4 and 4.6a.

The bottom graph of Figs.4.5, 4.6b and 4.7b show the behaviour of the \mathbf{H} wave as it travels in the cavity. The magnetic field peak amplitude experiences a gradual exponential decay and vanishes at the antipode. In our simulation, the amplitude of the magnetic field dwindles to -80 dB of the amplitude at the origin as can be seen in Fig. 4.6b. By comparing Figs. 4.7a and 4.7b, one notices that the source and the antipodal \mathbf{E} pulse maintain the same polarity. However, the \mathbf{H} wave changes polarity every time it reaches the point of reflection as shown by the alternating positive and negative rectangular impulses observed in Fig. 4.7b (10Mm detector). Henceforth, a detector at 20 Mm sees the superposition of positive and negative pulses of the same amplitude, so that the analytical solution vanishes to zero [19]. This is confirmed by our FDTD simulation as clearly shown in Figs. 4.6b and 4.7b (20Mm detector).

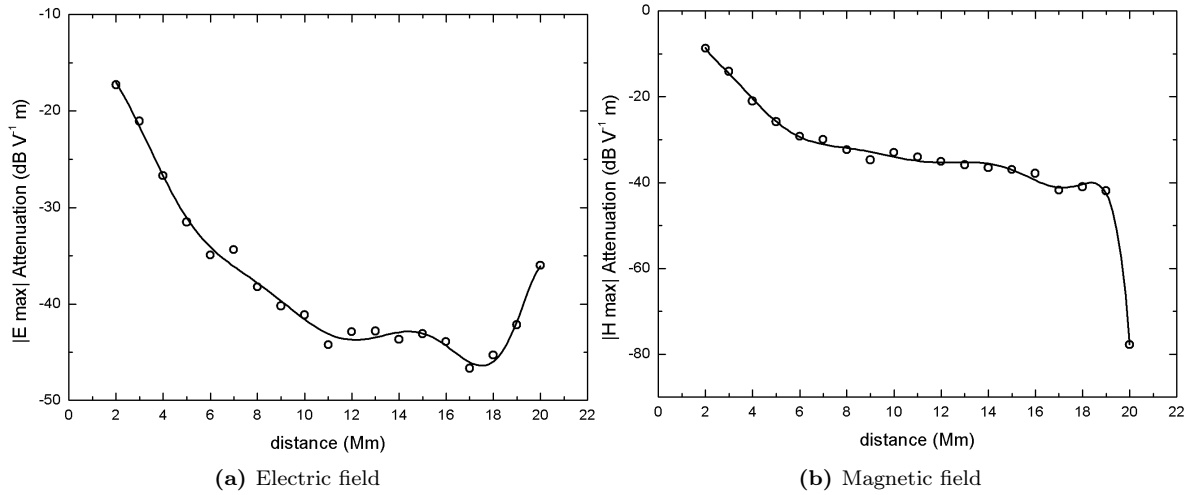


Figure 4.6: Attenuation of the peak amplitude of the \mathbf{E} and \mathbf{H} waves in dB scale.

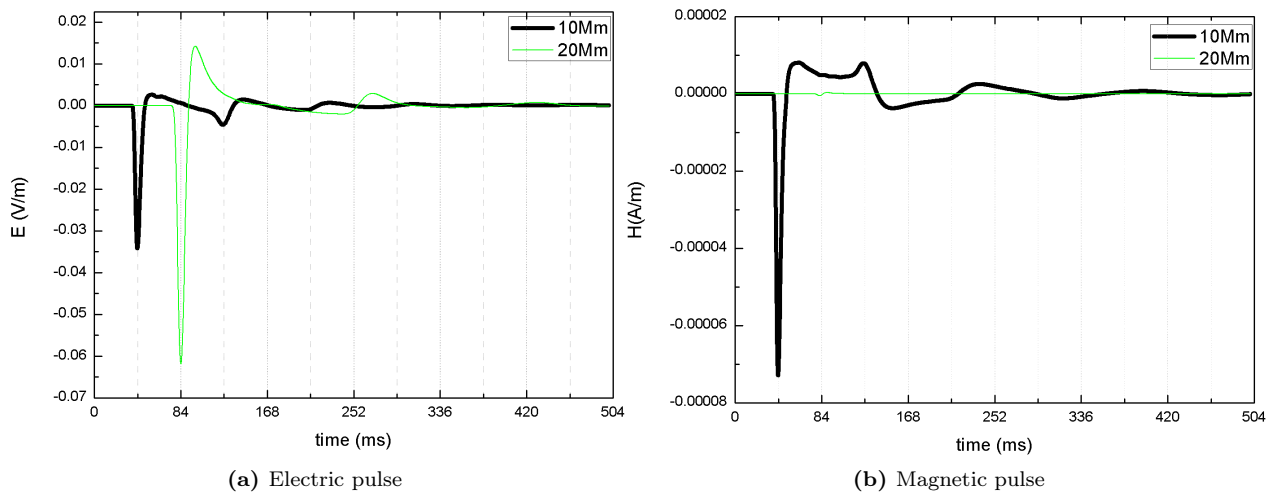


Figure 4.7: \mathbf{E} and \mathbf{H} pulse propagation in time measured at field detectors placed at 10Mm (thick line) and 20 Mm (thin line).

4.3.3 Electric and Magnetic field spectra: Schumann Resonances

Fig. 4.8 shows spectra of the electric and magnetic field propagating in the E-I cavity as simulated with 3D-FDTD. The field spectra show series of wide bandwidth resonances called Schumann resonances. The sphericity is responsible for the value of the eigenfrequencies and the modulations imposed by wave absorption along the path shift the frequency to lower values [92]. The basic formalism [1] of the spherical PEC bounded earth-ionospheric cavity predicts the characteristic resonance frequency described in (3.19) and (3.20). By taking into consideration the absorbing effect of a finite conducting ionosphere, SR peak values are reduced to the values presented in the lowest row of Table 4.1 [92].

Fig. 4.8 shows a correlation between the peak frequency, the amplitude of \mathbf{E} and \mathbf{H} spectra with the distance at which they are observed. Firstly, at shorter distances, \mathbf{E} and \mathbf{H} show fairly horizontal spectra above 20Hz. Secondly, the slope becomes increasingly tilted downwards as the source-observer distance (SOD) becomes large. This observation confirms the attenuation of high frequencies as the wave propagates in the cavity, However the effect is not really pronounced at low ELF range (the range represented in Fig. 4.8), it is more dramatic in the VLF range [19], as can be shown by the extrapolation of the slope of the attenuation in Fig. 4.4. In the time domain propagation, \mathbf{E} pulse shows maximum amplitude towards the source and antipode, whereas in \mathbf{H} the peak amplitude shows small amplitudes towards the source grows reaches a maximum in middle distance range to vanish at the antipode.

The solutions of the zonal harmonics in (3.23) and (3.24) are presented in Fig. 3.2 for an EM excitation positioned at the North pole position $\theta = 0$. Here, θ is the elevation angle. In the case of our FDTD simulation, the detectors would be placed along a meridian line at steps of $\pi/20$ from the North pole to the South pole (antipode) located at $\theta = \pi$. By comparing resonance parameters of the harmonic model with the FDTD model, it is easy to observe fundamental characteristics properties of EM resonance in the lossy spherical cavity. Firstly, as a stationary wave problem, the harmonic solutions shows zones of minimal amplitude called nodes. They are depicted in Fig. 3.2 by locations where the dark and light grey shapes touch, and zones of maximal amplitude where the shapes are the farthest apart. By taking in consideration the general standing wave theory, the angular representation of a wavelength in the meridional direction is

$$\theta_n = \frac{\lambda_n}{R_E} = \frac{2\pi}{n} \quad (4.4)$$

Table 4.1: Average SR peak frequency and Q-factor observed with 3D FDTD in CST MWS simulation. The relative error between the simulation values and experimental values is expressed in percentage.

SR order n	1	2	3	4	
\mathbf{E}	f_n (Hz)	6.97	13.07	18.81	25.09
	Δf_n (%)	10.7	6.6	5.9	3.5
	Q	1 – 2	1 – 6	1 – 5	2 – 6
\mathbf{H}	f_n (Hz)	7.02	12.88	18.15	24.07
	Δf_n (%)	9.9	8.0	9.2	7.4
	Q	2 – 3	2 – 5	2 – 6	3 – 5
\mathbf{H} [92]	f_n (Hz)	7.8	14	20	26

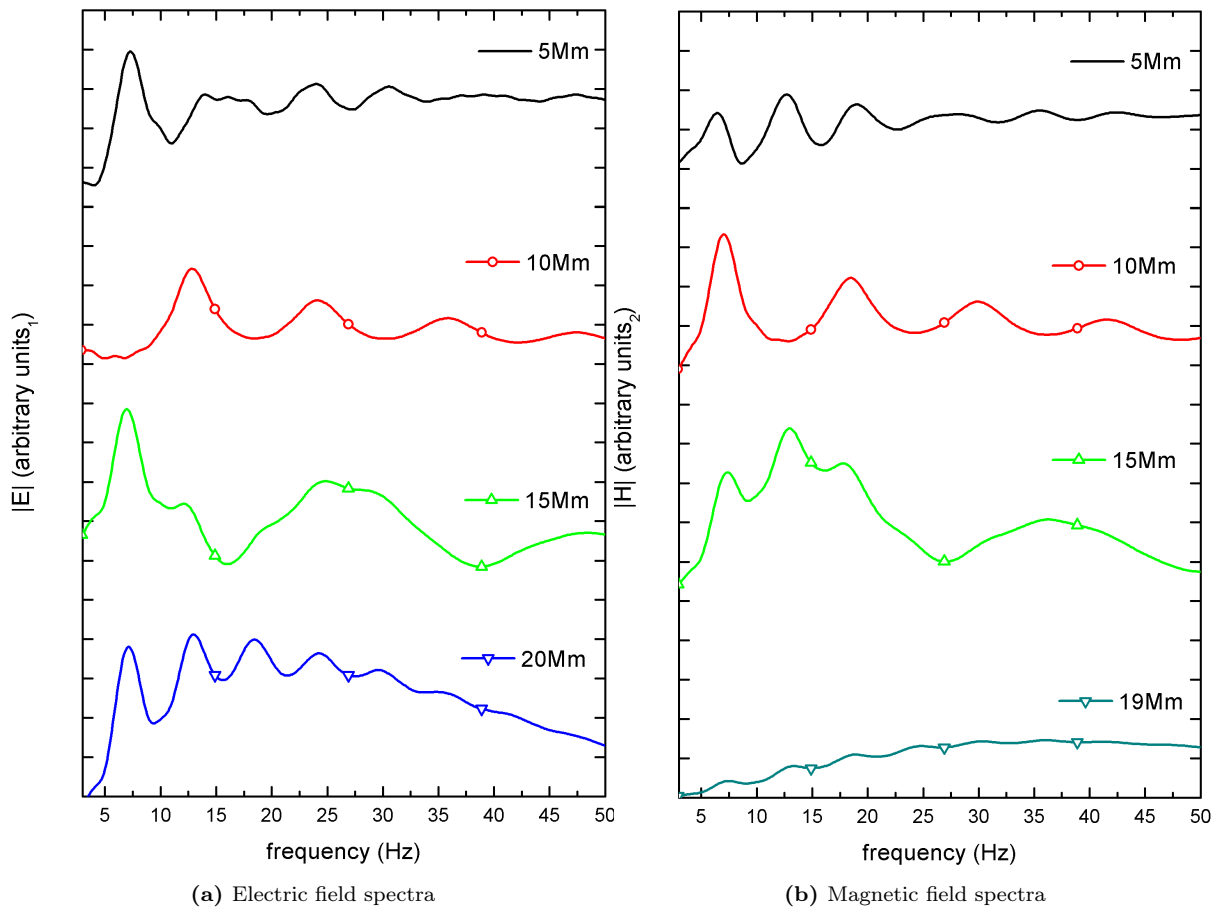


Figure 4.8: Amplitude spectra of \mathbf{E} and \mathbf{H} . The unit for both is arbitrary, hence $1 \text{ a.u.}_1 = 10^{-4}$ and $1 \text{ a.u.}_2 = 2 \times 10^{-7}$.

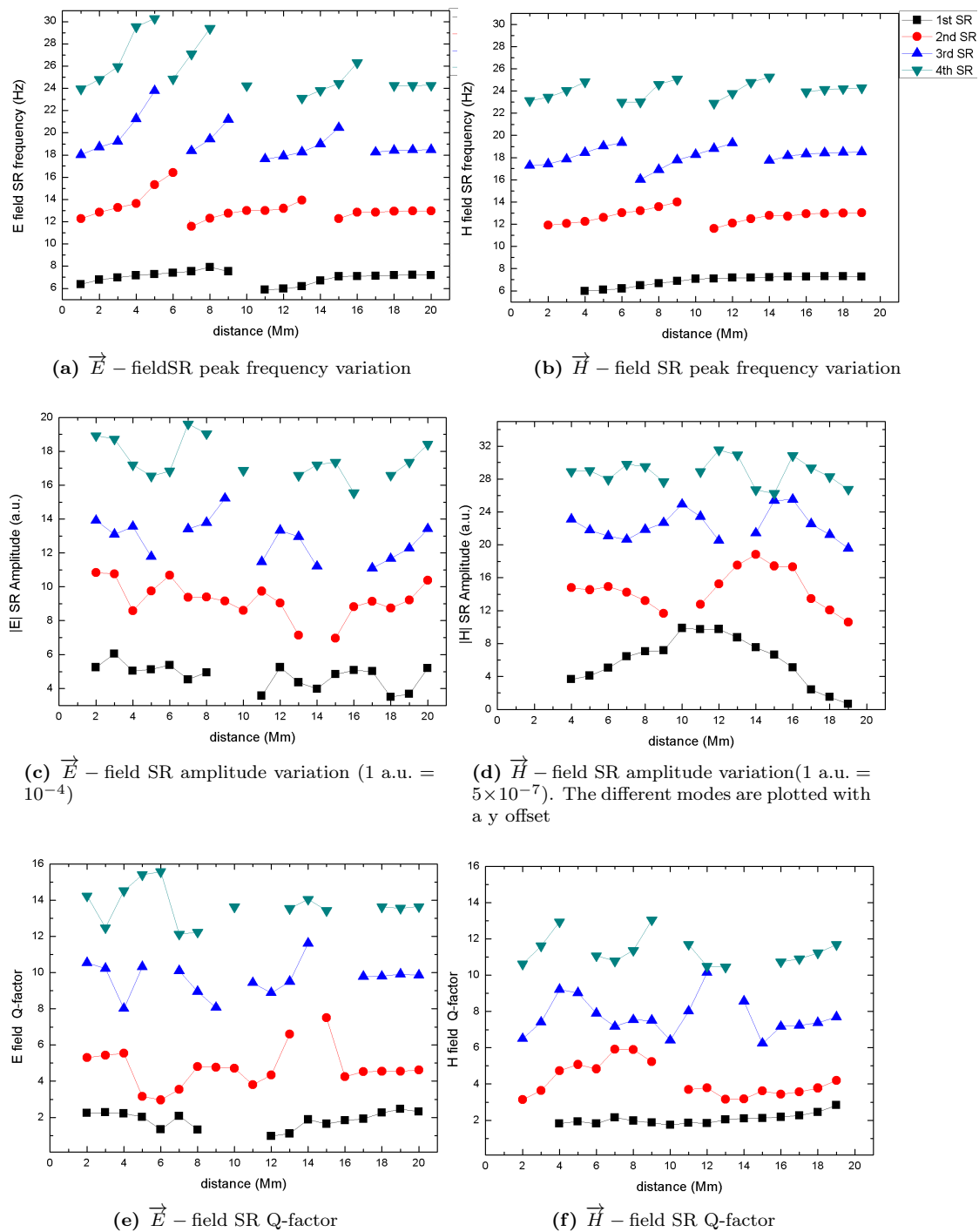


Figure 4.9: Peak SR frequency and amplitude and Q-factor variation of the \mathbf{E} and \mathbf{H} spectra versus the source-observer distance. The source is located in Cartesian position 0 Mm. The labels for the modes are represented in 4.9b.

where λ_n the wavelength of the n^{th} mode, $\lambda_n = c'/f_n$ with c' the phase velocity of the wave and f_n the resonance frequency defined in (3.19). At $\theta = 0$, two possibilities arise: a fixed boundary (node) where the amplitude is nil and an open boundary (antinode) where the amplitude is maximal at the boundary. As shown in Fig. 3.2a, **E** is antinodal at $\theta = 0$, whereas in Fig. 3.2b, **H** is nodal at $\theta = 0$.

In case of a fixed boundary condition, the nodal angular position (4.4) is given by

$$k \frac{\theta_n}{2}, \quad k = 0, 1, 2, \dots \quad (4.5)$$

And for an open boundary condition, the angular position of nodes is

$$(2k + 1) \frac{\theta_n}{4}, \quad k = 0, 1, 2, \dots \quad (4.6)$$

From (4.5) and (4.6), it is possible to demonstrate that the 10 Mm position ($\theta = \pi/2$) from the source shows only even resonance modes f_{2n} for **E** spectra and odd resonances f_{2n+1} in **H**: $\theta = \pi/2$ corresponds to node positions for f_{2n+1} **E** modes and for f_{2n} \vec{H} – field modes. The positions 0 Mm and 20 Mm ($\theta = \pi/2$) correspond to node points for all the values of k for **H** (4.5) and are antinodes for **E** (4.6).

Fig. 4.9a and Fig. 4.9b show the SR frequency variation for four SR modes. The SR frequency shows a dependence to the SOD with continuous and discontinuous portions that are observed both in **E** and **H**. The discontinuities represent the nodes of the EM standing wave in the E-I cavity and the continuous parts enclose the nodes. In Fig. 4.9c, the amplitude of the **E** shows open boundaries at 0 Mm and 20 Mm and minimal values corresponding to the discontinuities observed in frequency variation graphs in Fig. 4.9a.

H shows the same correlation between nodes and the minima in amplitude plots in Fig. 4.9b and 4.9d. The fixed boundary condition is partially observed with the minimal amplitude at 20 Mm. The variation patterns of the **H** is in accordance with the pattern described in the ZHS solutions for the magnetic field plotted in Fig. 3.2b.

The quality factor (Q) is the measure of the attenuation of the EM waves the E-I cavity. It is defined as follows

$$Q = f_n/\Delta f, \quad (4.7)$$

where Δf is the bandwidth of the resonance at -3 dB. This expression is equivalent to the definition represented in (3.28). In Figs. 4.9e and 4.9f, the variation of Q-factor values for $n = 1, 2, 3$ and 4 of **E**, **H** spectra is represented. The Q-factor repeats the SR mode pattern, with the maxima located at the antinodes and the minima at nodes. In Fig. 4.9e, the **E** Q-factor shows a progressive decrease in the interval [5, 20] Mm and becomes constant towards the antipode. As shown in Table 4.1, in terms of the first SR, the Q-factor varies between 1 to 2 for **E** spectra, and 2 – 3 for **H** spectra whereas experimental values of Q-factor in the magnetic field vary between 4 and 6 for the first SR [19, 52].

4.4 Conclusion

For our FDTD simulation of the E-I cavity, the choice of CST MWS was motivated by the fact that the software incorporates a robust PML technique, that it is appropriate for modelling lossy, inhomogeneous and anisotropic media and because the software is optimised in terms of memory usage. However, the simulated peak frequencies are lower than the experimental values as shown in Table 4.1. The average first SR peak frequency for H is ~ 7 Hz, 10% lower than the average experimental value. This red shift (to lower frequencies) might be due to the combination of a higher attenuation rate observed as shown in Fig. 4.4 and numerical dispersion originating from the use of rectangular meshes to simulate a curved shape. Cangellaris [93] found that when staircase stepped cells are used to mesh a smooth conducting surface, an error is induced to the results from numerical dispersion of the waves. The dispersion depends on the frequency component of the excitation and the direction of propagation. As shown in Section 3.4.4, the dispersion is greater in case of a diagonal propagation than along the mesh side. The TM mode in the planar waveguide is particularly affected: The wavefront is delayed and it increases with the distance travelled. The delay is more pronounced when the grid is coarser [93]. Therefore, in our 3D FDTD simulation, the numerical dispersion is unavoidable. It is owed to the relatively big size of the simulation; approximately 4×10^7 meshes imperfectly matching the spherical layers of the FDTD model is considerable. This may account for the high attenuation rate observed in Fig. 4.4, the SR lower peak frequency and the poor Q-factor of the resonator.

Chapter 5

Geomagnetic Field Measurement in the ELF range

5.1 Introduction

Geomagnetic field (GMF) observation is one of the major tasks in geophysics today. It aims to unveil the complex magnetic phenomena that are intrinsically associated with the inner Earth system dynamics, and its interactions with the cosmos. The applications are quite immense; they range from analysing the record of the magnetic field in ancient rock for tectonic plate movements prediction to monitoring the near-Earth space weather for the safety of our communication satellites.

As a supplement to the magnetometry network infrastructure that includes ground based and space-borne magnetometers, a wide dynamic range ultrasensitive SQUID technology is invoked. SQUID technology has been used for geophysical applications since the 1980's, first used in magnetotellurics for mineral and petroleum deposit prospecting [94] and in Nuclear Magnetic Resonance (NMR) for determining properties of different layers that make up the ground especially for hydrogeological applications [95]. In the 2000's, a *Low* – T_c SQUID magnetometer was for the first time used for monitoring continuously the geomagnetic field at the LSBB in France [96]. In 2011 at the South African National Space Agency (SANSA) in Hermanus was installed a *high* – T_c SQUID magnetometer system to complement the LSBB system. The two SQUID systems form the MARMOTS network for monitoring Earth's magnetic field.

5.2 The Quasistatic Geomagnetic Field

The quasistatic¹ component of the geomagnetic field (GMF) is generated by molten iron convection currents in Earth's interior by a *dynamo effect* [21]. The geomagnetic field could be approximated to that of a magnet [20]. The GMF is approximated to a dipolar field, with field lines exiting from

¹Realistically, static geomagnetic field does not exist because the generating process changes over (very long spans of) time.

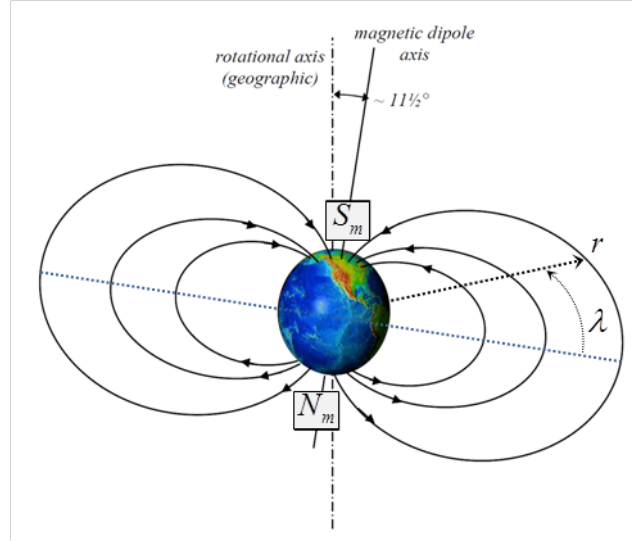


Figure 5.1: Earth's magnetic field configuration. Dipolar magnetic field of the Earth with S_m and N_m are respective North and South magnetic poles.

the North magnetic and entering the South magnetic pole. The dipole is tilted with respect to the rotation axis of the Earth by 11.2%, with the South magnetic pole located in the Canadian Arctic² ($80^\circ N$, $70^\circ W$) and the North at ($75^\circ S$, $150^\circ E$) [97] as depicted in Fig. 5.1. The magnetic dipole tilt causes an offset from the centre of the Earth by a mere 700 km. This offset introduces some irregularities in the magnetic field intensity on the ground such as the *Southern Atlantic Anomaly* (SAA). The SAA is the furthest region from the dipole and consequently, its geomagnetic field intensity is found to be lower than elsewhere [97].

The expression of the dipolar magnetic field is therefore [22]:

$$B(r, \lambda) = \frac{M}{r^3} (1 + 3 \sin^2 \lambda), \quad (5.1)$$

where $M = 8.049 \times 10^{22} \text{ Am}^2$ is Earth's dipole moment, r the distance from the centre of the Earth and λ the magnetic latitude as represented in Fig 5.1a.

On the ground, the intensity of GMF varies from 20,000 – 60,000 nT as shown in Fig. 5.2b. The magnetic field vector is defined along the three Cartesian components: northward (X), eastward (Y) and (Z) vertical intensity. The horizontal \mathcal{H} and total magnetic field intensity \mathcal{F} are also defined. The declination angle D which is the horizontal angle between true North and \mathcal{H} vector is measured positive eastwards and the inclination I angle between the horizontal plane and the total field vector, measured positive downwards. These quantities are represented as follows:

$$\mathcal{H} = \sqrt{X^2 + Y^2} \quad D = \arctan \left(\frac{Y}{X} \right), \quad (5.2)$$

$$\mathcal{F} = \sqrt{H^2 + Z^2} \quad I = \arctan \left(\frac{Z}{H} \right), \quad (5.3)$$

²These positions are the opposite of the geographic North and South poles'. The South magnetic pole attracts the North side of a compass magnet and vice versa

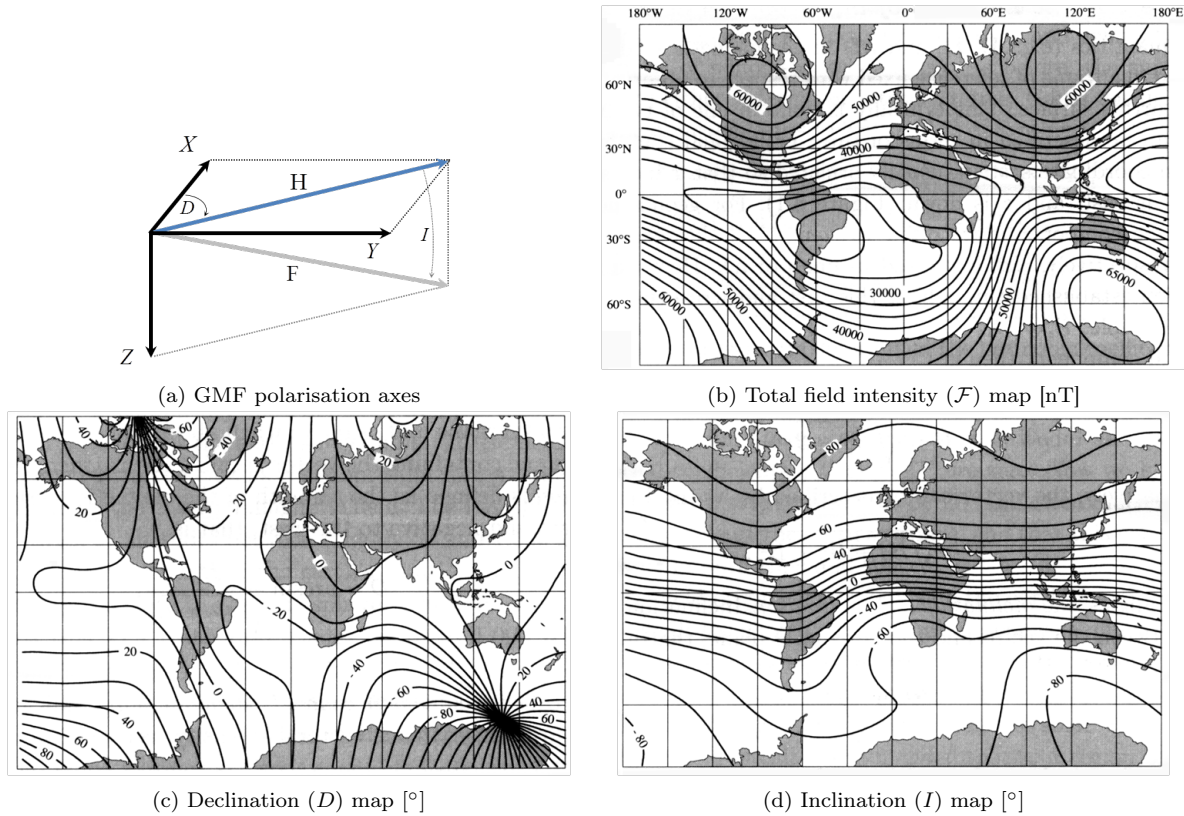


Figure 5.2: Ground geomagnetic field. In (a), the directions are $X \equiv \text{South} - \text{North}$, $Y \equiv \text{West} - \text{East}$ and $Z \equiv \text{Zenith} - \text{Nadir}$. The parameters represented in maps (b,c,d) were calculated for IGRF model in 1990 [9].

and generally intensities are expressed in nT (10^{-9} T) and angles in degrees ($^{\circ}$). Fig. 5.2a shows the different axes of polarisation of the geomagnetic field on the ground and respective characteristic angles. Based on ground and satellite data, the International Geomagnetic Reference Field (IGRF) maps the *static* geomagnetic field using spherical harmonics expansion of the scalar potential [9]. Fig. 5.2b shows a contour map of the total intensity, with an interval 2,500 nT. The map shows distinctively the minimal field intensity SAA region centred in Southern America ($\sim 25,000$ nT). Magnetic poles in Northern Canada and Eastern Antarctica can be shown with the convergence of horizontal declination isogonic lines in Fig. 5.2c and maximal inclination is observed in the proximity of magnetic poles in Fig. 5.2d. Here, isogonic lines delimitate regions where the angles of declination (or inclination) are relatively constant.

The GMF is composed of a wide range of periodical phenomena as shown in Fig. 5.3. The red side (lower frequency side) of the spectrum is occupied by long-term variations (also called secular variations) which may be associated with convection currents regime change in the Earth's core. Secular variations correspond to a time period of years and more (on a logarithmic scale). In the middle range, the GMF is dominated by relatively short periodic variations, including magnetospheric quiet daily variations that occur in calm magnetic conditions. Magnetic weather is strongly dependent on the solar wind interaction with the geomagnetic cavity. Quiet solar weather is characterised by a pronounced decrease of \mathcal{H} around midday for observatories located near the Earth's equator

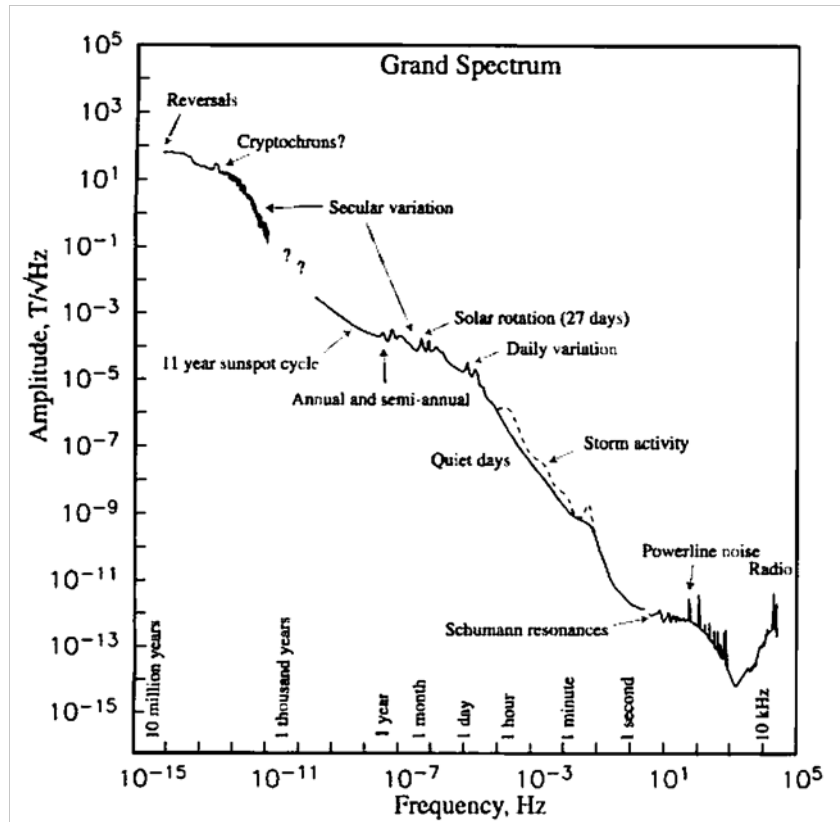


Figure 5.3: Full range of amplitude spectrum of the Earth's magnetic field showing phenomena with cycle period from 10 million years to 10^{-4} s. The range of interest here is the tiny portion of the lower ELF ranging from $[1s > T > 0.01s]$ indicated as *Schumann resonances* [10].

measured by the *Daily Storm Time* index (*Dst*) [98]. In disturbed weather, high-speed solar wind drives the near-Earth environment into a highly dynamic, time-dependent state that can last few days called magnetic storm [21]. This interaction drives harmonic electromagnetic pulsations in the upper layers of the geomagnetic cavity that are predominant in the mHz range. Their wavelengths are orders of magnitude higher than the size of the Earth, and they influence considerably the structure and the properties of the geomagnetic cavity systems in which they resonate. Towards higher frequencies in the spectrum, natural Schumann resonances of the Earth and eventually man-made noise including powerline and industrial noise are found; man-made noise is distinctive by its peaks sharpness and amplitude height beyond the background noise.

5.3 Origins of the Geomagnetic Field in the ELF Range

5.3.1 Solar Activity

Most of the energy on Earth's surface originates from our nearest star, the Sun. It is a 7×10^5 -km radius star that produces its energy from thermonuclear fusion of hydrogen nuclei into helium. The hot plasma of compressed gases that it forms is associated with a dipolar solar magnetic field that extends outwards into space. The Sun emits EM radiation, and through short-lived, intense and

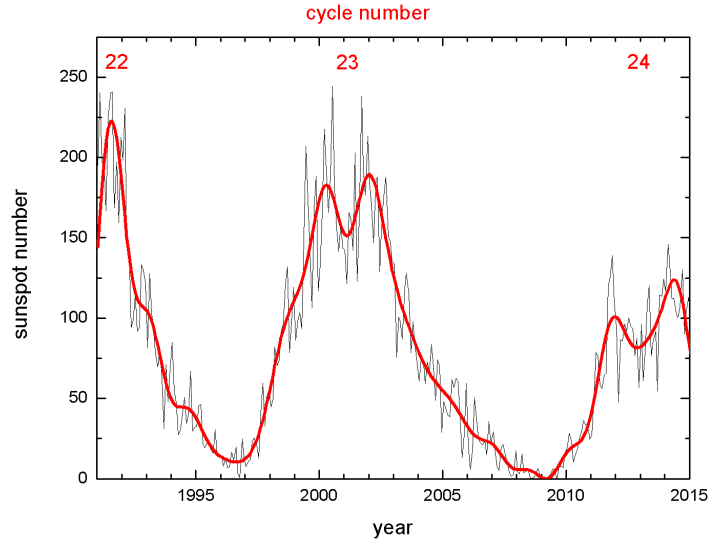


Figure 5.4: Overview of 30-day averaged sunspot number plotted for a 24-year duration from 1991 [11]. The current solar cycle (2009 – 2020) is the 24th.

localised outbursts known as solar flares, expels streams of matter known as the solar wind (SW) to space. The solar wind and its magnetic field interact constantly with the Earth and couple with the terrestrial magnetic field and ionised gases in the planet’s vicinity. [22].

Solar sunspots (dark spots on the Sun’s surface, observable in visible light) are the most active regions of the solar atmosphere, so that their number of appearance is proportional to the intensity of solar activity. Through their protruding strong magnetic flux lines, they eject solar wind (SW) and X-ray flares into space. Therefore, depending on the number of those hotspots on the surface of the Sun, two extremes of solar activity are deduced: A maximum sunspot number corresponding to an intense solar activity (more mass ejections, high-speed solar wind and more intense ionising radiation), and a minimal number of sunspots indicating very weak solar activity. Therefore, solar activity varies through peaks and troughs, and each cycle with a period of ~ 11 years. The current cycle is the 24th since the year 1775.

The activity of the Sun being the driver of the Earth geomagnetic system, there is more probability of storms/intense activity in the atmosphere in peak solar activity and vice versa. Fig. 5.4 shows the solar cycle of the past 24 years, with the latest quietest period around the year 2009 and a peak of activity in 2014.

5.3.2 Near-Earth Environment

The near-Earth environment is made of concentric regions of plasma whose dynamics are controlled by the magnetic field. It extends from a distance of about 60 km above the ground, up to $10 R_E$ in the day side of the Earth and may extend to $100 R_E$ in the night side [22]. It is usually referred to as the magnetosphere.

The magnetosphere owes its name to the fact that the magnetic field intensity is so strong there that it forms a layer of plasma whose interactions are driven by the magnetic field frozen-in to it. The

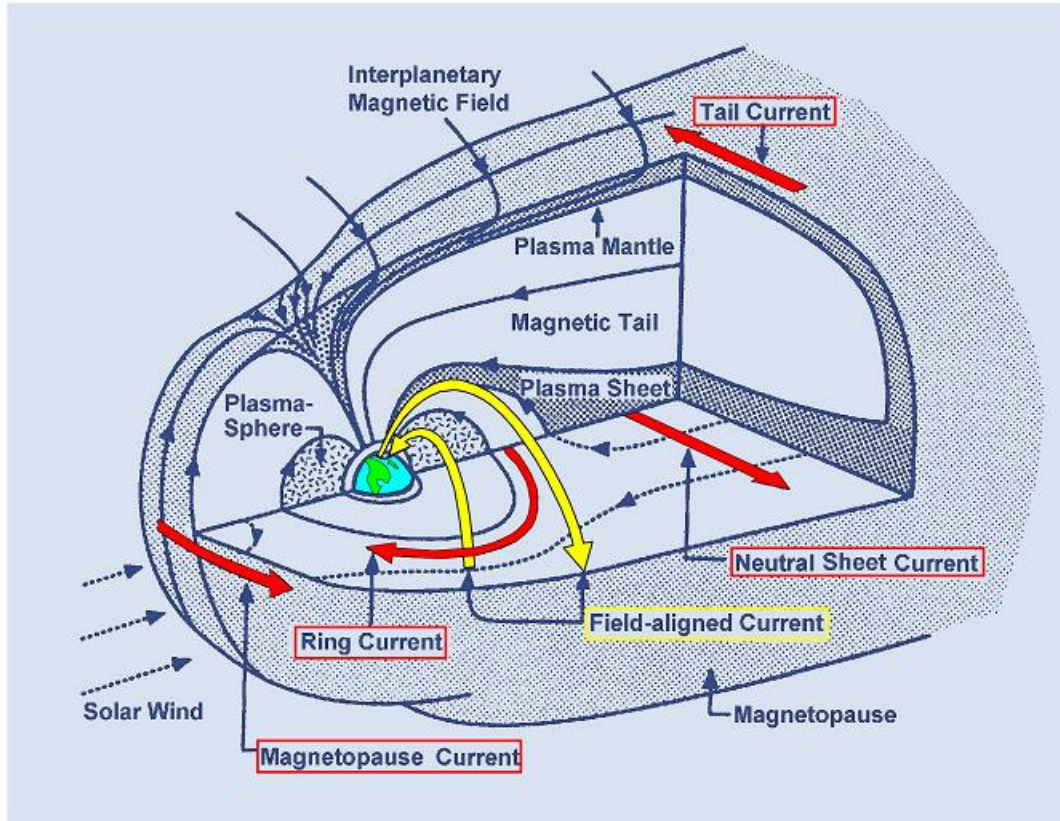


Figure 5.5: Sketch showing the structure of the magnetosphere with its electric current system. Note that the dayside is towards the left and the nightside is towards the right of the image [12].

ionised particles in the magnetosphere originate mainly from the wind of solar particles that enters in the polar regions and from ionisation by solar radiation. The motion of charged particles in the magnetosphere creates huge currents, such as the westward ring current along the dayside equatorial region and a tail current to the night side. Magnetospheric dynamos drive the wave-interaction and the particle distribution in the whole near-Earth cavity [22]. The different magnetospheric currents are depicted in Fig. 5.5.

Magnetic weather is always used to describe the steadiness of the magnetospheric system. On the ground, it is measured with two indices: The intensity of the currents in the magnetosphere (Dst) and magnetic disturbance (K_p). The Dst measures the intensity of the equatorial ring current in the magnetosphere from equatorial range *Intermagnet* observatories [98]. Dst decreases H component in the datasets. The storm intensity can be classified as follows

- intense storm, $Dst < -100$ nT,
- moderate, $DST < -50$ nT and
- minor, $Dst > -30$ nT.

The disturbance in the magnetic field is measured from 13 high latitude stations. It is estimated from the mean value of the disturbance levels in the two horizontal components and scaled logarithmically

from 0 to 9 as a function of the severity of the disturbance, where $K_p = 0$ is for very calm weather and $K_p = 9$ indicates extremely disturbed weather.

5.3.3 The Ionosphere and Solid Earth Waveguide

Below 50 km, the atmosphere aggregates 99% of the total mass of gas it contains. Above 60 km, where atoms are rarer, ultra-violet (UV) and X-ray radiation from the Sun heat and ionise the gas. Ionised particles do not recombine easily because of the low ion density. At those heights, there is a permanent density of free electrons and of ions that form a layer called the ionosphere. The ionosphere is highly conducting and can support strong electric currents. It affects radio waves, can generate EM waves and is subject to long-range interactions and instabilities characteristic of a plasma [22]. Plasma media interact strongly with the ambient geomagnetic field which affects the motion of ionised particles, modifies ionospheric electric currents and bulk movement of the plasma.

The solid Earth is a spheroidal shaped planet of average radius $R_E = 6370$ km, made of an inner molten metal core, a molten rock mantle in the outer core, all enclosed in a solid rock layer, called the lithosphere. The latter's surface is covered at 75% by oceans and continents occupy the remaining 25%. The conductivity at the Earth's surface varies from seawaters' ($5 \Omega^{-1}\text{m}^{-1}$) to granite's ($10^{-3} \Omega^{-1}\text{m}^{-1}$) [99]. In the ELF range, the solid earth can be considered as a PEC because the conductive current exceeds the displacement current resulting in the wave reflection over Earth's surface. The Earth-ionosphere (E-I) waveguide formed of conductive layers of the upper ionosphere and Earth's lithosphere form a natural ELF resonator in which EM radiation around the globe excite specific harmonic modes inside the cavity, which are characterised by eigenfrequencies due only to the spherical shape of the cavity, losses and dispersion in the ionosphere. These eigenmodes are called Schumann resonances.

5.3.4 Sources of Excitation

The main source of EM excitation in the E-I cavity is attributed to lightning activity [19, 100]. Lightning can be physically described as a transient current discharge that occurs in the atmosphere due to Coulomb potential that builds up between separated charges in thunderstorm clouds and the ground [29]. They occur randomly in time and in location but are mainly distributed on land areas. They form the background ELF noise detected on ground magnetograms [19]. Amongst these signals, single super-powerful lightning strokes occur once in a minute of time on average worldwide. These *Q-bursts* as they are called can be tens of time more intense than the average background noise. They are reflected back and forth several times in the Earth-ionosphere cavity between the source and its antipode before being attenuated to undetectable levels, creating an impulse response of the whole cavity [19]. These signals can be detected on the ground above the background signals.

5.4 Experimental Characteristics of SR

Depending on the type of excitation, ELF natural radio signals can be classified into three categories [13]: ELF background noise, Q-bursts and ELF flashes.

ELF background noise

Random generation of the thunderstorms worldwide and the modulation of wave propagation in the E-I waveguide condition the properties of the SRs to damped wave resonances. In the cavity, where they propagate, pulses interfere randomly to create a noise-like SR background signal. The EM background noise emanating from the superposition of pulses can be described mathematically as follows [101]

$$E(t) = \sum_{k=-\infty}^{\infty} A_k g_k(t - t_k), \quad (5.4)$$

$$H_x(t) = \sum_{k=-\infty}^{\infty} A_k \hat{g}_k(t - t_k) \cdot \sin(\beta_k), \quad (5.5)$$

$$H_y(t) = \sum_{k=-\infty}^{\infty} A_k \hat{g}_k(t - t_k) \cdot \cos(\beta_k), \quad (5.6)$$

where, for the k^{th} random pulse A_k is the amplitude, t_k the arrival time of the pulse $g_k(t)$, $\hat{g}_k(t)$, individual normalised electric/ magnetic pulse waveforms and β_k is the wave arrival angle of the pulse. Individual pulses occur randomly in time and independently of each other, thus, their magnetic signature superposition on a detecting instrument follows Poisson's distribution: Each event occurs in a certain interval of time and space with a known average rate and independently from one another.

Q-bursts

Q-bursts are more localised and are much more intense lightning systems that they cause an impulse response of the whole E-I cavity. They last approximately 0.3 – 1.0 s [88]. They also display slightly higher resonant properties than the ELF background counterparts.

ELF pulses

ELF pulses from nearby lightning strokes cause overload the detectors for few seconds. These may cause flux jumps in magnetograms and are not of interest in this study.

The spectral properties of SR are therefore defined by three main properties; resonance frequency, Q-factor and peak intensity.

5.4.1 Resonance Frequency

The frequency of the SRs is determined by the properties of the E-I waveguide and the origin of the thunderstorms. It is dependent on the anisotropic behaviour and time varying properties of the ionospheric lower layers. De *et al* [102] showed that a solar X-ray impulse, which ionises the ionosphere without any significant change in altitude, was followed by an abrupt increase in the frequency of the first SR; however a solar proton event which also ionises the lower ionospheric layer

Table 5.1: Experimental SR properties obtained from measurements from very distant sites [19]

n	ELF Background		Q-bursts		Fig.5.6		
	f_n	Q	f_n	Q	f_n	Q	A_n (pT Hz ^{-1/2})
1	7.9	3.9	8	3	7.95	3.63	1
2	14	4.6	14.1	5	14.06	4.01	0.6
3	20	5.1	20.2	6.7	20.41	5.38	0.4
4	26.1	5.2	26	8.6	26.66	6.06	0.27
5	31.8	5.4	32.1	9.7	33.18	5.01	0.17

was followed by a reduction in the first SR frequency. SRs show a daily variation of about ± 0.5 Hz, which is caused by the daily increase and decrease in the ionisation of the ionosphere because of variations in radiation from the sun. This has the effect of reducing the height of the ionosphere at noon local time [102]. Other researchers showed that due to inhomogeneity and anisotropy of conductivity, the frequency resonance line would split [19, 52, 86].

5.4.2 Quality Factor

The E-I as a resonating cavity is also characterised by its quality factor expressed in (3.28) and (4.7). Q represents the losses in the cavity: When Q is large, there is a lower rate of energy loss relative to the stored energy of the resonator, i.e. the waves are low-damped. For low Q-factor resonators, which is the case of the E-I system, the reverse applies.

If the E-I cavity were a perfect resonator i.e. with PEC boundaries and perfect spherical geometry, the bandwidth would be as narrow as the SR frequency value, $\Delta f = 0$ implying an infinite Q factor. However, because in the range [3 – 60] Hz the Earth can be considered as a perfect conductor, Q depends strongly on the variation the conductivity of the lower - ionospheric layers [58].

5.4.3 Intensity

The magnitude of the SR is dependent on the intensity of all thunderstorm events occurring worldwide. It also depends on the distance from the source of thunderstorm activity to the point of observation as shown in Section 4.3.3. There are three main sources worldwide; Africa, South East Asia and central America that show a maximal lightning rate over the year [56, 103]. The SR amplitude could, therefore, be a good indicator of global lightning activity. Moreover, studies in climatology showed that the rate of lightning discharge can be associated with global temperature change. Hence, the first SR amplitude can be used to measure the change of temperature on a global scale [27]. The intensity of the \mathcal{H} component varies from 0.5 to 1 pT/ \sqrt{Hz} approximately [58].

The values for the peak frequency f_n and the Q-factor are given in Table 5.1. A graph showing the extraction of the SR parameters from the spectra is shown in Fig. 5.6. In order to obtain the peak spectral amplitudes and power, the following analytical form is used [104],

$$A(f) = A_0 + \sum_n \frac{A_n}{1 + 2 \left(\frac{f-f_n}{\Delta f_n} \right)^2} = A_0 + \sum_n \frac{A_n}{1 + 2 \left(\frac{f}{\Delta f_n} - Q_n \right)^2}, \quad (5.7)$$

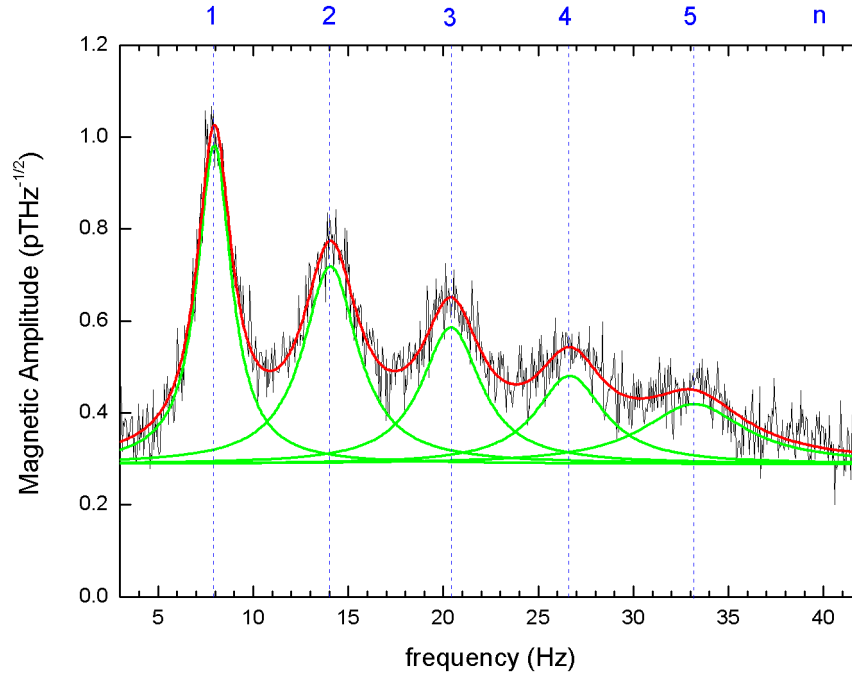


Figure 5.6: Amplitude spectrum of \mathcal{H} component showing typical (background signal) SR spectrum detected from Antarctica [4].

where A_n is the peak amplitude at the resonance, A_0 is a baseline offset and Δf the frequency bandpass at -3dB amplitude. Here the quality factor of the n^{th} mode is $Q_n = \frac{f_n}{\Delta f_n}$.

5.5 Magnetometers in the ELF Range

As demonstrated in Section 3.3.2, the SR are TM modes with a radial electric \mathbf{E}_r polarisation and an azimuthal \mathbf{H}_φ polarisation. In ELF range, only vertical \mathbf{E} and horizontal \mathbf{H} are detected due to the high conductivity of the ground [19]. \mathbf{E}_r is detected with vertical metallic ball capacitor antenna mounted on top of a few metres long vertical mast. A full description and characterisation of the antenna are available in [13, 19]. For magnetic field detection, most commonly used horizontal \mathbf{H} antennas which are search-coil and the fluxgate magnetometers. Both of these magnetometers are based on ferromagnetic³ material filled core that acts as a magnetic field concentrator, increasing the density of the magnetic field inside the coil, and therefore, increasing the sensitivity.

Introduction to Ferromagnetic Materials

Normal paramagnets are materials that are made up of tiny magnetised domains (comparable to tiny magnets) whose magnetic orientations are random in space, making the bulk appear as a non-magnetic material. However, when an external magnetic field is applied, the domains rearrange their magnetic moments in response to the applied field, and the material becomes magnetised. The rate of magnetisation is outcompeted by thermal agitation and it is very difficult to attain saturation

³Commonly amorphous permalloys with high magnetic permeability are used.

(total alignment of the moments of the tiny magnets); they require a very low temperature and a high intensity of applied magnetic field. On the other hand, ferromagnetic materials attain magnetic saturation at ambient temperatures and ambient geomagnetic field strength. In some cases, they can display spontaneous magnetisation without any external magnetic field applied. Ferromagnetic materials are characterised by a critical temperature called *Curie temperature* beyond which ferromagnetism is destroyed and they behave as paramagnets⁴. Some examples of ferromagnetic materials are iron (*Fe*), cobalt (*Co*) and nickel (*Ni*).

In the volume, the magnetic field induced \mathbf{M} depends on the strength of the applied field \mathbf{H} . By taking into account the statistical approach that describes the competition between the alignment of the tiny fields in the volume and thermal noise, the *Langevin function* [33] describes what happens when a gradually increasing field is applied to the ferromagnetic core.

$$L_f(x) = \coth(x) - \frac{1}{x} \quad x = \frac{\mu^2 H}{k_B T}, \quad (5.8)$$

where, μ , k_B and T are the permeability of the medium, Boltzmann's constant and the absolute temperature respectively. The overall magnetisation is the sum of magnetisation effect of all N_f individual ferromagnetic domains

$$M = N_f \mu L_f(x). \quad (5.9)$$

Here, two main possibilities arise

- When $x \ll 1$, $\coth(x) \ll 1/x$: $L(x) \approx \frac{x}{3}$, M is a linear function in terms of H . The effect of thermal noise is greater than the alignment of moments. Hence, the magnetisation is directly proportional to the field applied, $M = \frac{N_f \mu^3}{3 k_B T} H$. This is known as the Curie-Weiss law for ferromagnetism.
- When $x \gg 1$, $\coth(x) \rightarrow 1$: $L(x) = 1$, the effect of the magnetic field H is much greater than thermal noise. The alignment is total and the magnetisation is said to be saturated, $M_{\text{sat}} = N_f \mu$.

The evolution of L_f can be shown in Fig. 5.7. The optimal working range of the induction coil is the linear response and the fluxgate in the saturation range.

5.5.1 Induction Coil Magnetometer

ICMs are vector magnetometers made of ferromagnetic filled cores wound with induction coils. Their working principle is based on Faraday's law of induction by which the voltage induced in the core is proportional to the change in magnetic field in the coil as follows

$$V = -S_{\text{eff}} \frac{dB}{dt}, \quad (5.10)$$

⁴In this section, we only consider the case where $T > T_{\text{Curie}}$

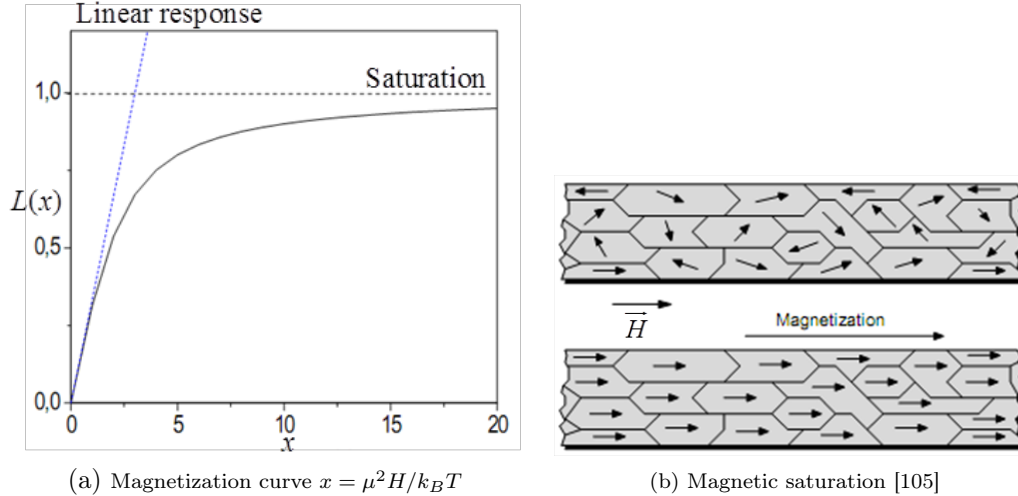


Figure 5.7: Magnetisation process of a ferroelectric material. Magnetic saturation is observed in the lower panel of (b). The upper panel of (b) shows a completely demagnetised system.

where S_{eff} is a coefficient called the effective area of the coil. A feedback winding is also wired around the core to flatten the frequency response of the magnetometer. The number of windings may vary, but they are usually more than 100,000 turns of wire. This allows an efficient voltage induction in the core of the antenna. S_{eff} is therefore [106],

$$S_{\text{eff}} = N\pi\mu_{\text{eff}}m_b^2, \quad (5.11)$$

where N is the number of windings, μ_{eff} the magnetic effective permeability dependent of the geometry, m_b the half-width (radius) of the ferromagnetic core.

Here, the ferromagnetic core geometry is approximated by an ellipsoid with major and minor half-axes m_a and m_b respectively, with the condition $m_a \gg m_b$ so that $\mu_{\text{eff}} \approx \mu$ [13,106]. For a 1 m long, 5 cm wide core, when μ is increased up to 2000 or so, the sensitivity reaches magnetic saturation, limited by the geometry [13]. Here two challenges arise, either the ICM must be tens of metres long which is not very practical or its width should be reduced, which yet increases the possibility of saturation.

On the measuring site, inductance coils are very sensitive to vibrations and to variations of temperature and, therefore, need to be buried in dry sand to operate efficiently. As depicted in Fig. 5.8, the coils detect changes in magnetic field polarised along its axis, with the sensitivity in an angular pattern in a 8 lemniscate shape. The H_ϕ field is detected using two orthogonal horizontal induction coils in respective directions *South – North* (SN) and *West – East* (WE). Due to the transverse nature of the radiowaves, WE oriented coils detects waves that are travelling along the SN direction and vice versa. Because of their angular cross-section pattern, they need to be placed carefully apart from each or in a T letter configuration from each other to avoid interference.

Induction magnetometers come in a set of various designs, The best performing design used nowadays belongs to the British Geological Survey [30] and can sample from frequencies between 0.1 and

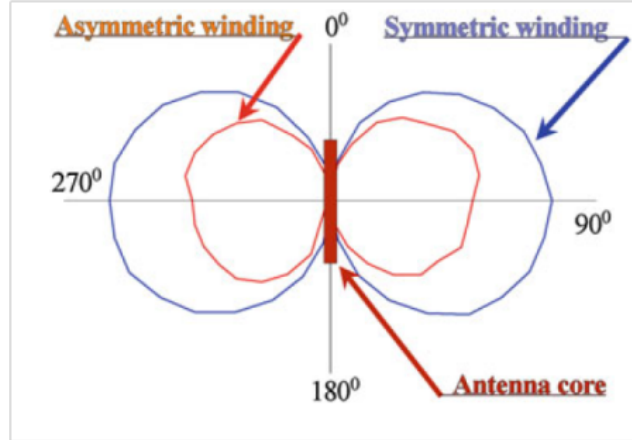


Figure 5.8: Depiction of an angular pattern for an inductance coil magnetometer measured for symmetric and asymmetric winding. In this case, sensitivity is maximum for waves that propagate along 90° and 270° direction and zero for 0 and 180° direction. Sensitivity also depends on the symmetry of the coil windings [13].

1000 Hz. The most commonly used ICM in for field detection were designed by Belyaev [107]⁵ and are used worldwide as ground magnetometers [13, 15, 19]. These types of magnetometers are used with the CARISMA network. Their bandwidth ranges from 0.001 – 30 Hz and their sensitivity is 20 mV/nT above 1 Hz, with a noise rejection ≤ 0.2 pT/ $\sqrt{\text{Hz}}$ [15].

5.5.2 Fluxgate Magnetometers (FGM)

FGMs are the most commonly used vector magnetometers for navigation applications and for Earth magnetometry⁶ [21]. Their working principle relies on the magnetic saturation of a ferromagnetic core. The different configurations of the cores are shown in Fig. 5.9. The design is made of two coils, a primary coil and the pick-up coil. The former excites the core with a strong alternating current that causes the core to reach saturation at each period and the latter is induced by a magnetic field gradient created in the material. The signals in the two coils are symmetrical as is shown in Fig 5.9b (left) and the output voltage of the fluxgate is zero as in Fig. 5.9d (left). However, when an external field is applied, the magnetic response between the two coils lose their symmetry because one coil saturates before the other (Fig. 5.9b (right)), then a harmonic voltage is developed at the terminal of the magnetometer (Fig. 5.9d (right)).

For a double core magnetometer, a high sensitivity is achieved by a long ferromagnetic core with large number of secondary coils and a high-frequency of the exciting signal. Using coils $n_1 = n_2 = 1000$, a frequency $f = 10$ kHz, on a double core 0.5 m long and an area of 2.5 mm², a sensitivity of 10 $\mu\text{V}/\text{nT}$ is achieved [108]. On the other hand, a ring core of 30 mm diameter, $n_1 = 150$, $n_2 = 1100$ shows the best performance [109].

⁵LEMI-3 magnetometers of the Lviv Centre Institute for Space Research, Ukraine <http://www.lemisensors.com>

⁶Extensively used with the *Intermagnet* network

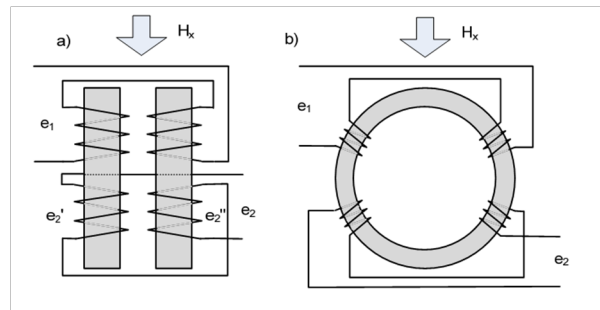


Figure 5.9: Designs of fluxgate magnetometers with different shapes of ferromagnetic cores (a) a double bar and (b) a ring core [14].

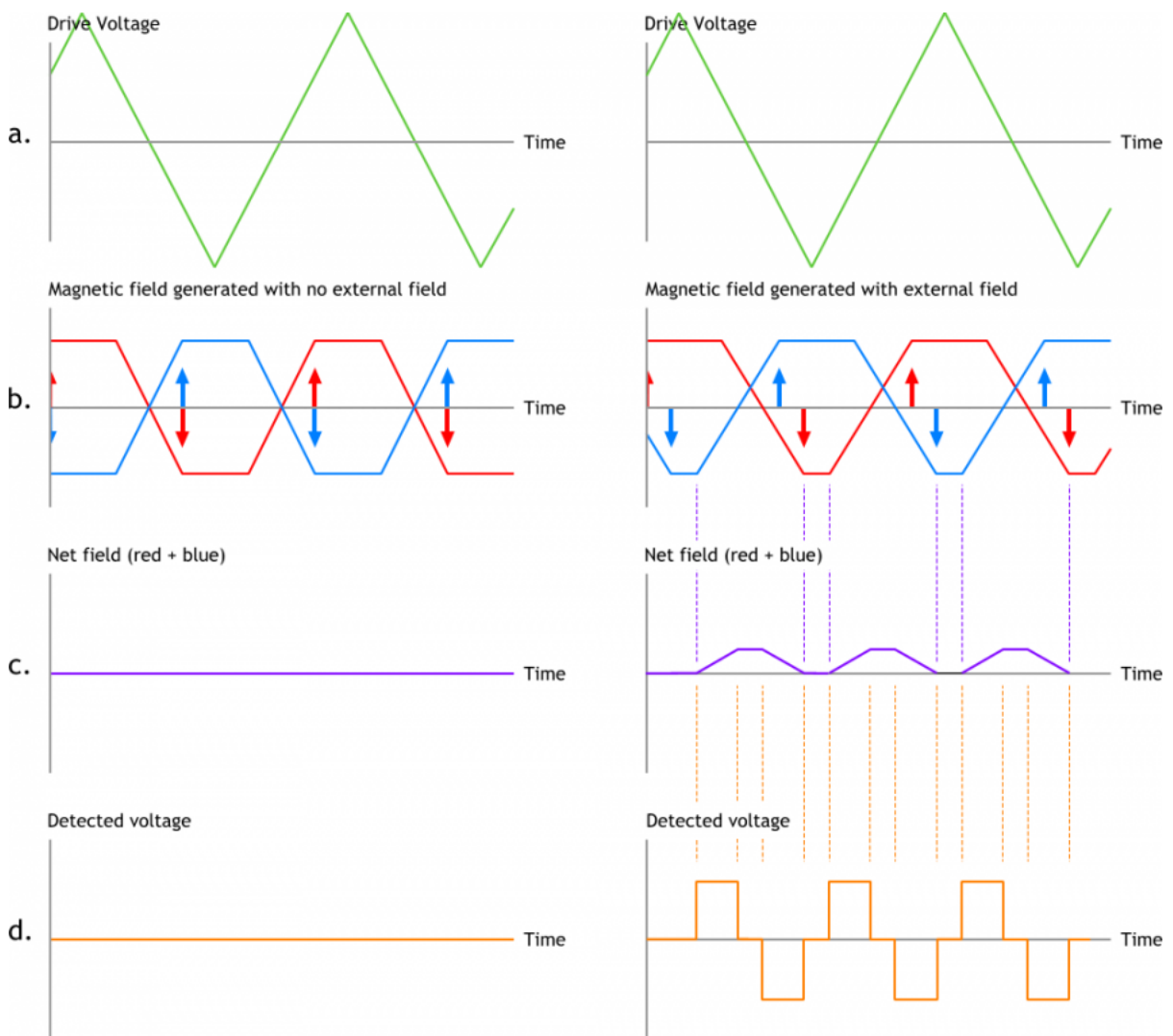


Figure 5.10: Fluxgate magnetometer working principle shown in two columns: At the left is the FGM working without any external field and the right, with the magnetic field applied. [15].

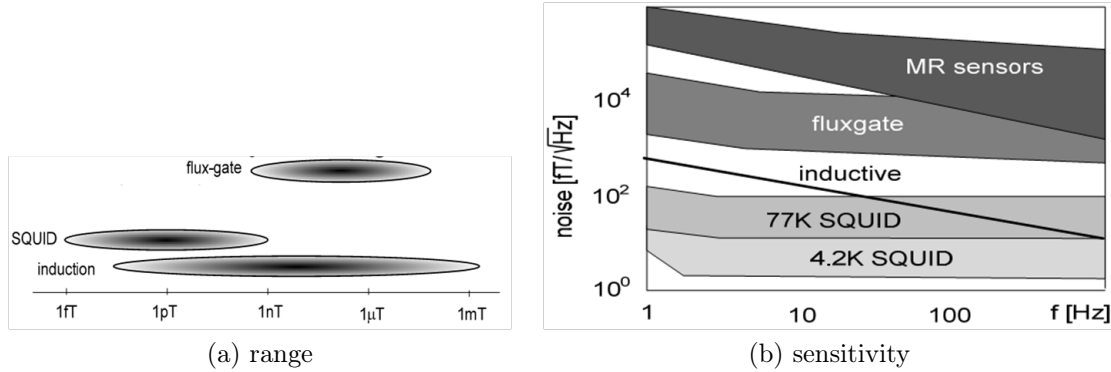


Figure 5.11: Working range and sensitivity of different ELF magnetometers. Magnetoresistive (MR sensors) represented in (b) are not described in this work. [14]

5.6 SQUID Geomagnetometers

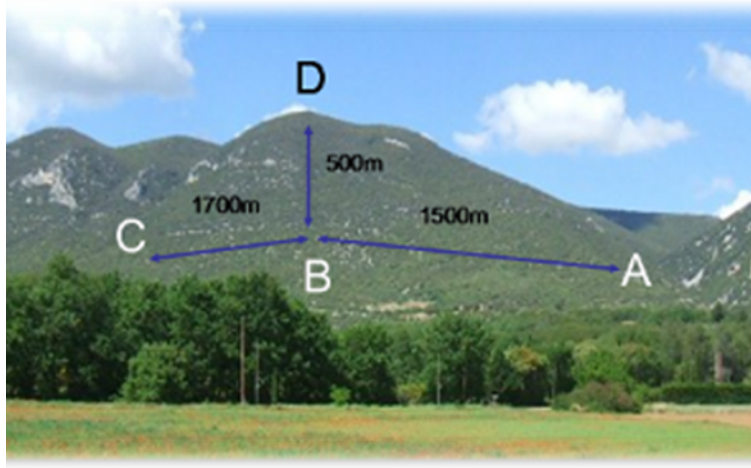
As shown in Section 2.6, the SQUID magnetometer is the most sensitive device to date, with a sensitivity to a field change ΔB of $10^{-6}\Phi_0/\text{mm}^2$ equivalent to 1 fT [3]. This makes the SQUID a magnetometer designed to monitor the faintest magnetic field variations that are below noise level of sensitivity of conventional magnetometry as shown in Fig. 5.11a.

In the ELF range, the nominal noise floor of the SQUID is very low, with the *low* - T_c SQUID leading the show at few fT/\sqrt{Hz} , the *high* - T_c at tens of fT/\sqrt{Hz} , induction coils at around a few pT/\sqrt{Hz} and fluxgates closing the gap at tens of pT/\sqrt{Hz} . The reason why the induction coil performs relatively well despite its rudimentary simplicity relies on the size of the induction core and the winding which are much higher than in common fluxgates. This makes the coils a magnetometer of choice as a passive detector of magnetic field variation in ELF range. The fluxgate, on the other hand, is a very accurate detector for a static or slowly varying magnetic field. The fluxgate is very popular in ULF detection and is rarely used for the ELF range. Also, due to the backup systems, the SQUID does not intrinsically measure the absolute value of the field, it rather measures the variation of the magnetic field in time. In applications where the absolute field magnetometer investigation is required, a fluxgate would be used as a complement.

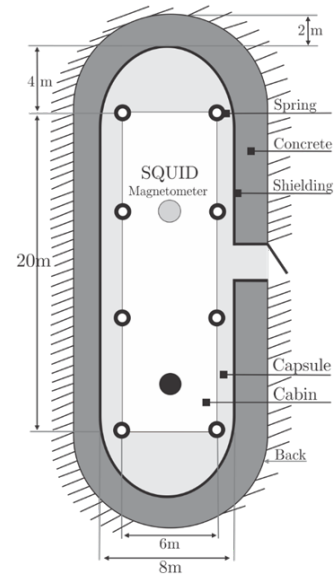
5.7 The *Laboratoire Souterrain à Bas Bruit, Rustrel* (LSBB)

5.7.1 Site Description

Located at Rustrel ($43.92^\circ N$, $5.48^\circ E$) in the mountainous area of the Provence in France (Fig. 5.12a), the LSBB was initially a land-based missile control that has been converted into a scientific laboratory [110]. The LSBB is a system built into a limestone mountain that comprises a network of tunnels, offices and a shielded capsule in which a *low* - T_c SQUID magnetometer is installed. Fig. 5.12b shows the features of the capsule. It is a 1258 m^3 box suspended from the ceiling and resting on shock absorbers, entirely enclosed in a 28 m long, 8 m diameter, 1 cm thick steel capsule and the whole contained in a 2 m-thick-wall-reinforced-concrete cylindrical structure. The capsule



(a) the site of the LSBB [113]



(b) the shielded capsule [111]

Figure 5.12: The *Grande Montagne*, the mountain in which the LSBB capsule system is built. The network of tunnels is shown with arrows, (A) entrance, (B) capsule (C) emergency exit and (D) top of the mountain.

features make it unique because it offers a combination of shielding against acoustic, seismic and electromagnetic noise. The absence of μ -metal⁷ in the shielding system makes it a low-pass filter with a cutoff at 40 Hz. As it was designed to withstand large electromagnetic pulses that might be caused by nearby nuclear explosions, it attenuates high-frequency, low-frequency and even *dc* signal. In the capsule, the ambient magnetic field is lower than 6,000 nT (whereas outside it is 46,000 nT). Long-term stability and low noise level were investigated: First, measurements using a $0.3 \times 0.3 \text{ mm}^2$ loop, a magnetic fluctuation larger than a quantum is observed in more than half a day [110] and the magnetic noise level is lower than $2\text{fT}/\sqrt{\text{Hz}}$ above 10 Hz [111]. On the other hand, the region of Vaucluse shows also a spectrum of seismic noise near the worldwide minima [112]. These LSBB special characteristics made it possible to use *low* - T_c SQUID magnetometers for geological applications and to observe E-I couplings. The system is dubbed SQUID with Shielding QUalified for Ionosphere Detection ([SQUID]²).

5.7.2 Track Record of the [SQUID]² System

Thanks to the [SQUID]² system, magnetic fluctuations associated with primary seismic waves from a magnitude $M_w = 7.6$ earthquake that occurred in Bhuj, India (2006 – 01 – 21 03 : 16 *UT*) have been observed 6250 km afar. They were associated with the vibration of the huge structure of water saturated limestone beneath the LSBB system that impinged on the magnetograms [111]. Seismo-magneto-ionospheric effects of earthquakes were observed for a couple of major tremors that occurred around the world on 2006 – 01 – 02 that could be analysed. It was found that the signals originated from primary seismic wave (P-wave) reflection from lower ionosphere above epicentres from lower

⁷ μ -metal is a nickel, iron, copper and molybdenum alloy used for magnetic shielding

ionospheric layers. It is noticed that wave packets took roughly 300 s to be detected at the LSBB after the onset of the earthquake, which was shown to be the travel times taken by the P-waves to reach the ionosphere floor [31]. Precursor effects were observed before the Sichuan-Wenchuan earthquake in China (2008 – 05 – 12 06 : 28 UT) with $M_w = 8.1$. At two times, 1 hour 30 minutes and 10 minutes before the quake, the WE component showed jumps on the SQUID measurements, comparable to a development of an intense electric field in the ground. By analysing the harmonics of the magnetic signal, the polarisation of the precursory electric field was found to be oriented in the same direction as the fault line that was created afterwards [112].

In the lower ULF range, SQUID magnetometers detect magnetic waves in the near-field regime due to the size of the wavelengths several times the circumference of the Earth. These are eigenmodes of vibration of the entire earth caused by the worldwide seismic excitation. These resonances, detected with the [SQUID]² system in the ULF range, coincide with seismic model predictions [114]. Magnetospheric ULF waves caused by particle precipitations are also observed at LSBB. These mid-latitude [SQUID]² signals exhibit frequency peaks quasi-identical to those observed at stations located at high latitudes [115]. Lightning activity and Transient Luminous Events (TLE) are also observed. Lightning is electrostatic discharges caused by unbalanced electric charge in the atmosphere and TLEs are brief electrical breakdowns in the ionosphere that are triggered by lightning strokes. They show up on the [SQUID]² magnetic signals as unipolar magnetic pulses [112].

The combination of the ultrasensitivity and a properly shielded environment provide an exceptional tool to complete the existing network of ground magnetometers. However, SQUIDs should be coupled to systems or signal processing techniques that could determine whether phenomena that are measured are local or originate from remote sources. An attempt to resolve a worldwide signal from the noise based on the wave coherence matrix is attempted in Chapter 7. On the other hand, SQUID magnetometry should be associated with a system that measures absolute magnetic field. For the moment, the SQUID magnetic measurements are paired with *intermagnet* data. But a method that could provide the same range of accuracy but capable of measuring the absolute field is needed to be paired to SQUID magnetometers.

5.8 SANSA Hermanus

5.8.1 Site Description

The Space Science Directorate of the SANSA is located in the former Hermanus (43.92°N, 5.48°E) Magnetic observatory, one of the magnetic observatories of the *Intermagnet* network, also part of the consortium of *Dst* stations because of its proximity to the magnetic equator. Located in the vicinity of the SAA area, the average magnetic field intensity is 25,000 nT. The environment is magnetically quiet with no nearby roads nor industrial activity in less than a 300-m radius. The *high-T_c* SQUID at Hermanus (HSQH) operates in an unshielded environment where it detects the ambient magnetic field undistorted and unattenuated. It presents a noise rejection of 0.15 pT/Hz at 1 Hz, in comparison to the fluxgate with 10 pT/Hz at 1 Hz [16]. The HSQH is operated as a collaboration project between the Electrical and Electronic Engineering Department of the Stellenbosch University (EE-SU) and

the SANSA Space Science, and as stated earlier in Section 5.1, it forms a global network of already two SQUID magnetometers with the [SQUID]² [16, 96].

Prior to the installation of the HSQH, a correlation study between SQUID network and *Intermagnet* fluxgate datasets was conducted at Hermanus. The first study found strong correlation between the frequency spectra of chosen fluxgate datasets close to the LSBB, the Hermanus dataset and the [SQUID]² datasets at ULF range [16]. Later on, a similar project was undertaken for the same fluxgate stations and HSQH at ULF range showed better correlations between the HSQH and HER [32].

5.8.2 Facilities Description

The HSQH is housed in a hut constructed of a non-magnetic material. A structure made of two pillars is cast in the middle of the hut, reaching down to the bedrock to stabilise the structure and minimise the vibrations. The pillars are isolated from each other by a layer of Styrofoam. In the centre of the floor, the pillar has a platform at the level of the ground, that is also covered in foam on top of which is placed a dewar flask containing the coolant N_2 . On the side, the second pillar stands at a height of ~ 1 m on top of which is mounted a jig. The jig is the structure that supports the rods holding the SQUID in the liquid nitrogen bath in the dewar. A picture of the hut and the SQUID setup is shown in Fig. 5.13.

5.8.3 HSQH System Description

HSQH is a *high* - T_c SQUID operating at 77 K. It is a 2-axis Star-Cryo electronics M2700[®] SQUID with a 2.7^2mm^2 pick-up area and noise rejection of $168\text{ fT}/\sqrt{\text{Hz}}$ [17, 95]. It is connected via FLL electronics to a control hut that comprises control electronics and data acquisition system (Fig. 5.14a). The control computer is connected via the *internet* to a server that is located in the EE Department of Stellenbosch University as detailed in Fig. 5.14b [17].

5.9 Conclusion

The versatility of the *dc* SQUID makes it a useful tool in the future of geomagnetic field monitoring networks. Its wide bandwidth allows monitoring the magnetic field associated with the geomagnetic cavity resonances in the mHz range, as well as variations higher in frequency, in the SR range without losing its sensitivity. Its high sensitivity makes it ideal for the detection of minute electromagnetic variations that might be associated with precursor signals to cataclysmic. The interest here would be to be able to detect patterns associated with earthquakes and other solar weather effects that might be embedded in the EM signals that only the SQUID could be sensitive enough to detect. Many examples of particularly interesting signals have been detected with [SQUID]², such as EM precursors to earthquakes and seismic waves from thousands of miles far away, ionospheric response to earthquakes and solar storms. One of the main requirements of such a system is an extremely quiet environment. Such a condition is fulfilled by the [SQUID]² which operates in a Faraday cage buried under 500m of a karst water-filled mountain. However, another alternative is to detect the ambient



Figure 5.13: Depiction of the SQUID system in Hermanus (a) non-magnetic hut housing the SQUID (b) A view inside the hut showing the full installation of SQUID in the Dewar flask (c) a close-up view of the Programmable Feedback Loop (PFL) controllers [16].

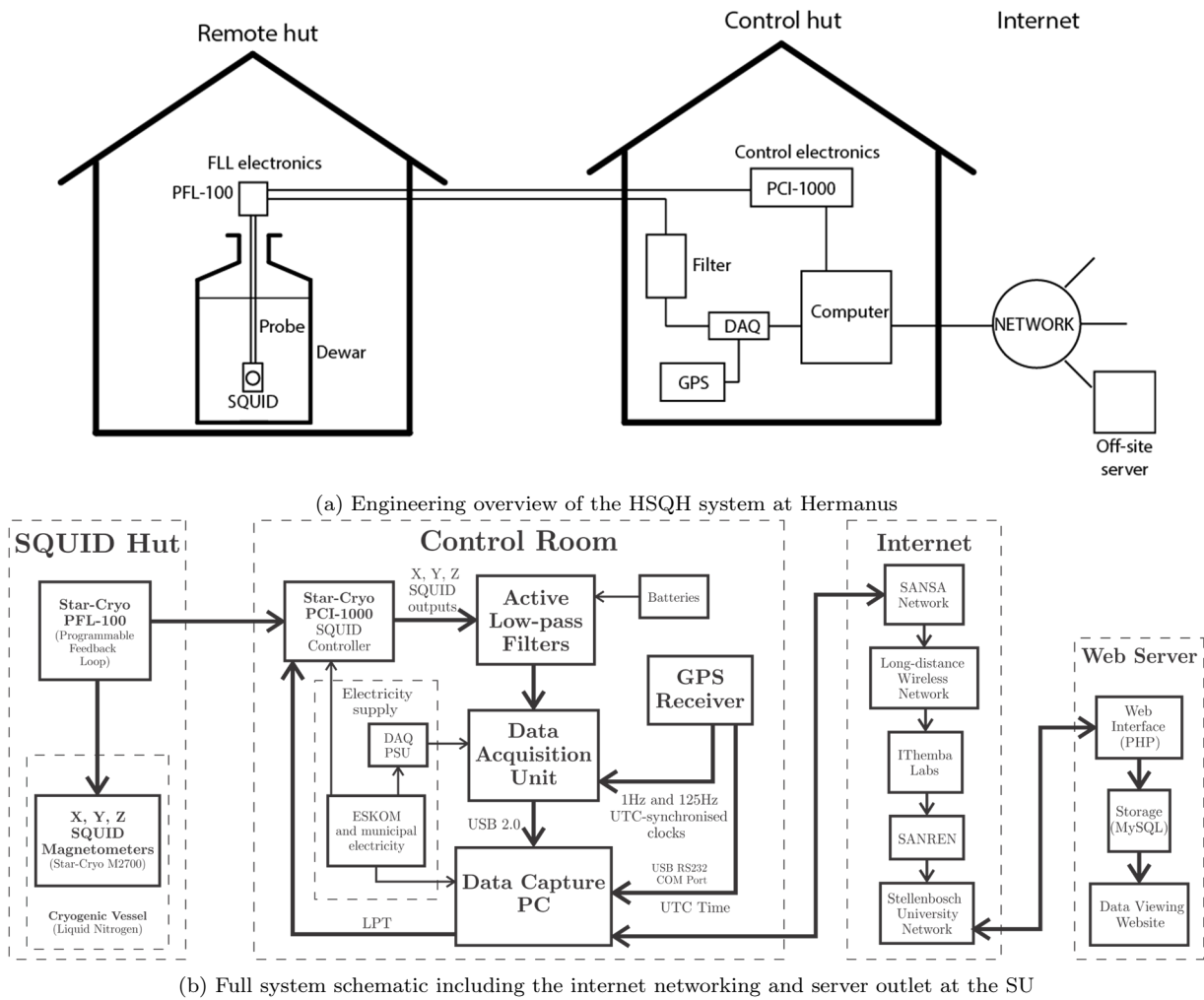


Figure 5.14: The Hermanus SQUID network system as it was designed by van Vuuren [17].

field in an unshielded environment where the field will be detected unattenuated and undistorted by shielding. The challenges of noise mitigation of such a system are many and an adequate remoteness of the measuring site is a requirement. The HSQH partially meets the magnetic quietness conditions as Hermanus is already a magnetic observatory for the *Intermagnet* network. But still, a lot needs to be done to lower the noise level at the site. SQUID geomagnetometry is a very promising in terms of performance but it is still relatively young technology compared to well-established measurements techniques that form global networks of ground and spaceborne geomagnetometer systems nowadays. SQUID data will until now be examined with reference to pre-existing methods such as fluxgates and ICMs.

Chapter 6

Spectral Analysis of SQUID Geomagnetic Components

6.1 Introduction

Spectral analysis of time signals serves to identify their spectral magnitude distribution. The Fourier transform (FT) is widely used to transform time signals to the frequency domain. Two types of signals emerge according to their variation patterns in time, namely deterministic or random. The former's evolution in time can be described by a mathematical model and hence predicted (eg: an electric dipole oscillation), and the latter are signals that vary randomly in time (eg: thunderstorm generation in the Earth's cavity) characterised by a probabilistic distribution of the events in time. For deterministic signals, the FT is sufficient to extract peak frequency and spectral magnitude properties of the signal. However for random signals, an approach based on statistical spectral density estimation should be considered to extract subtle periodicities from the signal.

The SQUID geomagnetic signal in the ELF range is such an example of a signal affected by random fluctuations, due mostly to the random nature of EM occurrence in the natural environment (atmospheric and cosmic noise) and human interferences in the signal (power grid, electrical machinery, etc) [116]. Spectral density analysis is therefore needed to efficiently extract information from the spectra.

6.2 Continuous Fourier Transform

A time signal is a temporal representation of the evolution of a given physical phenomenon. This might represent a 1D, 2D or 3D functions of space, depending on the time variables taken into account. Depending on the time dependence property of the signal, two distinct groups arise; continuous and discrete signals. Continuous signals also referred to as analog signals can be represented mathematically as continuous function of time. On the other hand, discrete signals are only represented by a series of discrete values in time. Here, a type of deterministic signal will be described.

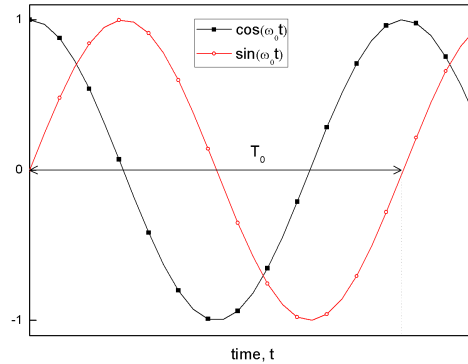


Figure 6.1: Representation of the basis functions $\cos(\omega_0 t)$ and $\sin(\omega_0 t)$. T_0 is the period.

The signal repeats its pattern in a period of time. The rate of cyclic repetitiveness of the signal is represented by its frequency, which is intrinsically related to the period duration of the signal. By applying a Fourier Transform to this type of signal, its frequency can be determined. On the other hand, an aperiodic signal is devoid of the repetitive aspect in time.

6.2.1 Periodic signals

Any periodic signal can be considered as a linear combination of elementary periodic signals called harmonics. The cumulative amplitude of the components gives an idea about the amplitude of the spectrum. This part will be concerned the determination of the properties of a continuous periodic function in time by using the properties of the Fourier series.

The Fourier basis

A periodic signal can be described as a combination of elementary trigonometric functions forming an orthonormal basis, i.e. made of unit vectors that are orthogonal and normalised. Consider a sinusoidal signal with angular frequency ω_0 defined at an instant of time t . The basis functions of the signal can be written as

$$\begin{aligned} x_1(t) &= \cos(\omega_0 t) \\ x_2(t) &= \sin(\omega_0 t) \end{aligned} \quad (6.1)$$

These two notations can be combined in the Euler formula as follows

$$x_3(t) = \cos(\omega_0 t) + i \sin(\omega_0 t) = \exp(i\omega_0 t), \quad (6.2)$$

where $i = \sqrt{-1}$ is the imaginary number. The periodicity T_0 (and frequency F_0) of the basis function is defined in terms of the angular frequency as $T_0 = 2\pi/\omega_0 = 1/F_0$. The periodicity means that $x_3(t + kT_0) = x_3(t)$ for any integer $k = \pm 1, 2, \dots, N$. The advantage of this combination is that the sine function is an odd function in time whereas the cosine is even. Odd or even functions can be represented either by the sum of sines or cosines respectively [117].

Properties of the basis

Orthogonality To prove the orthogonality of the Fourier basis, let us consider two angular frequencies ω_1 and ω_2 , with $\omega_1 \neq \omega_2$. Three cases of combination of basis functions can be defined:

Sine functions

$$\int_{-\infty}^{+\infty} \sin(\omega_1 t) \sin(\omega_2 t) dt = \frac{1}{2} \int_{-\infty}^{+\infty} \cos(\omega_1 - \omega_2)t dt - \frac{1}{2} \int_{-\infty}^{+\infty} \cos(\omega_1 + \omega_2)t dt = 0. \quad (6.3)$$

By reducing the limits of the interval to the limits of a period for each integral say, $\pm\pi/(\omega_1 - \omega_2)$ and $\pm\pi/(\omega_1 + \omega_2)$ respectively, one gets the orthogonal function (6.3) equal to zero. The same property applies to

Cosine functions

$$\int_{-\infty}^{+\infty} \cos(\omega_1 t) \cos(\omega_2 t) dt = \frac{1}{2} \int_{-\pi/(\omega_1 + \omega_2)}^{+\pi/(\omega_1 + \omega_2)} \cos(\omega_1 + \omega_2)t dt - \frac{1}{2} \int_{-\pi/(\omega_1 - \omega_2)}^{+\pi/(\omega_1 - \omega_2)} \cos(\omega_1 - \omega_2)t dt = 0, \quad (6.4)$$

Mixed sine and cosine functions

$$\int_{-\infty}^{+\infty} \sin(\omega_1 t) \cos(\omega_2 t) dt = \frac{1}{2} \int_{-\pi/(\omega_1 + \omega_2)}^{+\pi/(\omega_1 + \omega_2)} \sin(\omega_1 + \omega_2)t dt - \frac{1}{2} \int_{-\pi/(\omega_1 - \omega_2)}^{+\pi/(\omega_1 - \omega_2)} \cos(\omega_1 - \omega_2)t dt = 0. \quad (6.5)$$

Normalisation The basis has been verified to be orthogonal (6.2)-(6.5). To form an orthonormal base, the basis functions need to be normalised to 1. In the case where $\omega_1 = \omega_2$, the integrals described from (6.2)-(6.5) are not zero. The normalised expression (6.2) could be rewritten as

$$\frac{2}{T} \int_{-T/2}^{+T/2} \sin(\omega_1 t) \sin(\omega_2 t) dt = \begin{cases} 1 & \text{for } \omega_1 = \omega_2 > 0 \\ 0 & \text{for } \omega_1 \neq \omega_2 \end{cases}. \quad (6.6)$$

The same condition applies to the expression (6.6). However the mixed basis functions in (6.5) are always orthogonal. T denotes the period of the signal. This means that the sine and cosine basis functions are independent of each other; one function can be manipulated without affecting the other.

Relative phase The relative phase between the sine and cosine is $\pi/2$ and the time delay is equivalent to $T_0/4$ as shown in Fig. 6.1. The signal can be decomposed in orthogonal basis functions.

Differentiability The basis functions can be indefinitely differentiated. This property is very handy for the Fourier analysis that requires the basis signals to be differentiable.

Fourier Series

Let us consider a function $y(t)$, To define the same function in term of basis elements, it must fulfil the following conditions [118];

- $y_n(t)$ must be periodic so that it fulfils the condition $y_n(t + kT_0) = y_n(t)$ with k any integer.
- $y_n(t)$ must be continuous in the defined interval
- Its energy must be finite $\int_{-T_0/2}^{T_0/2} |y_n(t)|^2 dt < \infty$.

These conditions are called Dirichlet conditions. Any signal - that fulfils the Dirichlet conditions - can be defined as the summation of the orthonormal basis functions defined in equation (6.1);

$$y_n(t) = a_0 + \sum_{n=1}^{+\infty} (a_n \cos 2\pi n F_0 t + b_n \sin 2\pi n F_0 t). \quad (6.7)$$

This formulation is called the trigonometric Fourier's series expansion. In exponential terms, it can be expressed as

$$y_n(t) = \sum_{n=-\infty}^{+\infty} c_n \exp(2\pi n F_0 t), \quad (6.8)$$

where a_n , b_n and c_n are called Fourier coefficients. They are written as

$$a_n = \frac{2}{T_0} \int_{-T_0/2}^{T_0/2} y(t) \cos(-j2\pi n F_0 t) dt, \quad (6.9)$$

$$b_n = \frac{2}{T_0} \int_{-T_0/2}^{T_0/2} y(t) \sin(-j2\pi n F_0 t) dt, \quad (6.10)$$

and

$$c_n = a_n + j b_n = \frac{1}{T_0} \int_{-T_0/2}^{T_0/2} y(t) \exp(-j2\pi n F_0 t) dt. \quad (6.11)$$

In (6.7) the term a_0 is a special case when $n = 0$. It is henceforth expressed as

$$a_0 = \frac{2}{T_0} \int_{-T_0/2}^{T_0/2} y(t) dt \quad (6.12)$$

Parseval's Theorem

The Parseval's theorem yields an estimate of the energy in the signal by linking the Fourier coefficients (6.9)-(6.12) to the function $y(t)$. It states that the sum of the squared moduli of Fourier series

coefficients is equal to the average of the square of $|y(t)|$ over one period [119]:

$$\frac{1}{T_0} \int_{-T_0/2}^{T_0/2} |y(t)|^2 dt = \sum_{n=-\infty}^{\infty} |c_n|^2 = \frac{1}{4} a_0^2 + \frac{1}{2} \sum_{n=-\infty}^{\infty} (a_n^2 + b_n^2). \quad (6.13)$$

6.2.2 Non-Periodic signals

When the Fourier series are applied to a function devoid of periodicity, they describe its variation of the function in frequency domain. This transformation is referred to as the Fourier Transform (FT). Let us consider a function $y(t)$ continuous in time that satisfies the Dirichlet conditions [117]. The FT for the function is hence

$$Y(f) = \int_{-\infty}^{+\infty} y(t) \exp(-j2\pi ft) dt, \quad (6.14)$$

and reciprocally, the inverse Fourier transform to the time domain is given by

$$y(t) = \int_{-\infty}^{+\infty} Y(f) \exp(j2\pi ft) df, \quad (6.15)$$

where the time t is represented in seconds and the frequency f is in Hertz. In the formulations (6.14)-(6.15), the assumption is made that the period of an aperiodic signal is infinite. However, in a more elegant manner, the function (6.14) can be defined within finite boundaries as

$$\int_{-\infty}^{+\infty} y(t) dt = \lim_{T \rightarrow \infty} \frac{1}{T} \int_{-T/2}^{T/2} y(t) dt, \quad (6.16)$$

where T is a finite time interval where the function $y(t)$ is non-zero and fulfils the Dirichlet conditions. Parseval's theorem for an aperiodic signal can be stated hence as

$$\lim_{T \rightarrow \infty} \frac{1}{T} \int_{-T/2}^{T/2} |y(t)|^2 dt = \lim_{T \rightarrow \infty} \frac{1}{T} \int_{-T/2}^{T/2} |H(f)|^2 df. \quad (6.17)$$

The relation (6.17) states that the total energy of the signal is conserved both in time and frequency domain. The quantity $|H(f)|^2 df$ is the energy spectral density (ESD) in the bandwidth df . From (6.17), the power spectral density (PSD) can be defined as the ESD per unit of time in the interval T ;

$$PSD = \lim_{T \rightarrow \infty} \frac{1}{T} \int_{-T/2}^{T/2} \frac{|H(f)|^2}{T} df. \quad (6.18)$$

6.3 Discrete Fourier Transform

A physical variation in time can be represented by an analog signal which is continuous in time. In order to take a measure of the variation, one needs to define its values at discrete instants of time, called sampling. This operation is usually performed experimentally in electronics by an Analog-to-Digital converters. Consider N the total number of samples in a timespan T , the data are taken at each instant $t_n = n\Delta t$ where n is an integer and Δt the sampling time interval. The Direct Fourier transform (DFT) of a discretized time signal $y(t_n) = y_n$ is written [120];

$$Y(k) = \sum_{n=0}^{N-1} y_n \exp(-j2\pi kn/N), \quad k = 0, 1, \dots, N-1, \quad (6.19)$$

where k represents the discrete points in the frequency domain. The inverse (backwards) Fourier transform (IDFT) is given by

$$y(n) = \frac{1}{N} \sum_{k=0}^{N-1} Y_k \exp(j2\pi kn/N), \quad n = 0, 1, \dots, N-1. \quad (6.20)$$

To obtain the N values of the DFT coefficients, the computer needs to perform N^2 multiplication and $N \cdot (N-1)$ addition operations [121].

It can be shown with the forward DFT (6.19) that space and time resolution affect the resolution in the frequency domain. In the time domain, the sampling interval is $\Delta t = \frac{T}{N}$ and the sampling frequency is given by $f_s = \frac{1}{\Delta t}$. The input samples of duration Δt are sampled uniformly in the frequency domain from 0 to f_s in Hz. The input and output vectors y_n and $Y(k)$ are of the same length N [117]. Therefore,

$$\Delta f = \frac{f_s}{N} = \frac{1}{N\Delta t} = \frac{1}{T}. \quad (6.21)$$

The frequency resolution is the inverse of the timespan of the time signal.

6.3.1 Sampling theorem

Let y_n be a discrete time signal and Y_k its DFT defined in (6.19). One can chose to vary the discrete number by an integer $m > 0$, so that the total number of spectra values is $k = N + m$. Hence, (6.19) can be rewritten

$$Y_{N+m} = \sum_{n=0}^{N-1} y_n \exp[(-j2\pi n/N)(N+m)] = \sum_{n=0}^{N-1} y_n \exp[(-j2\pi n m/N)] = Y_m. \quad (6.22)$$

As shown in (6.22), increasing the spectral data points in the spectrum will repeat the high-frequency spectral components Y_m into the lower part of the spectrum Y_N , leading to a spurious effect that distorts the initial spectrum. This effect is commonly known as aliasing. To avoid this, the signal should be sampled at a higher frequency f_s at least double to the maximum frequency contained in the spectrum. This condition is known as the Shannon (Nyquist) condition for sampling [121]. It is written

$$f_{\max} \leq \frac{f_s}{2} = \frac{1}{2\Delta t}. \quad (6.23)$$

Table 6.1: Comparison between DFT and FFT number of operations.

N	DFT	FFT	$r_{\text{DFT/FFT}}$
8	64	12	5
32	1024	80	13
128	16384	448	37
1024	1048576	5120	205

The Nyquist frequency $f_s/2$ should be the highest component that can be observed with a sampling frequency of f_s . A frequency component higher than f_{\max} , say $f = f_{\max} + f_{\text{alias}}$ will appear in the spectra at the position f_{alias} .

6.3.2 The Fast Fourier Transform (FFT)

The FFT is a fast implementation of the DFT that exploits the symmetrical properties and periodicity of the DFT. The first FFT algorithm and simplest implementation were proposed by Cooley and Tukey [122]. It is based on the ‘divide-and-conquer’ principle, done in 3 distinct steps [121];

- Dividing in successive steps N in halves called decimation,
- Computing the DFT of the decimated components and
- Merging the results back together to form the full spectrum.

Hence, N needs to be a power of 2, so that $N = 2^\nu$ with ν representing the power-two dimension of the sample. Therefore, the FFT only requires $N/2^\nu = N/2 \log_2 N$ operations. This reduces considerably the number of calculations in comparison to the DFT. By only considering the number of multiplications as a measure of the computational complexity, the ratio of DFT versus FFT required amount of calculations can be computed

$$r_{\text{DFT/FFT}} = \frac{N^2}{N/2 \log_2 N}. \quad (6.24)$$

Table 6.1 shows the number of operations required for DFT and FFT and the ratio of computational time depending on the sample size N . For very large N , the number of computations (and the memory allocated) required is exponentially reduced by the FFT.

Two common ways of the decimation process are, splitting the DFT sum in odd and even indices of $y(n)$ in (6.19) called decimation-in-time, or in the frequency domain by splitting $Y(k)$ in (6.20) into summations of $N/2$ first samples and $N/2$ second samples called decimation-in-frequency. An illustrative mathematical demonstration of the decimation process can be found in [123]. A wide range of algorithms for FFT computation can be found in the digital signal processing literature [118–120].

6.4 Random Signal Processing

In the ELF range the main source of energy of EM background noise originates from worldwide lightning activity, distributed randomly in space (mainly over land areas) at a rate of ~ 50 events/second

[28]. A typical EM pulse is created, the wave expands in the Earth-ionosphere waveguide and is reflected at the opposite side of the source point in about 1/15 s. The dispersive conductivity in the ionospheric layers, the high-frequency wave components, called sferics, are strongly attenuated. In the lower end of the ELF spectrum, however, 3 – 60 Hz, EM resonances are maintained by constructive interference from round-the-globe sferics. Therefore, in SR band, the geomagnetic signal has a strong random signal component owed to the nature of the source and the medium of propagation [19]. In this case, Fourier analysis of geomagnetic signals in the SR band alone is not sufficient to extract spectral properties of the SR. As a matter of fact, the very first attempts to measure the SR - by Schumann [124] himself - failed to prove stable resonances because the random aspect of the signal was overlooked. In this section, a spectrum stabilisation method based on spectral overlapping and averaging of segmented time signals called the Welch's method [125] will be used.

6.4.1 Random variables

A random signal $y(n)$ is a physical process characterized by a random generation process $Y(n)$. Random processes can be subdivided into two sets; stationary and non-stationary signals. Stationary signals are characterised by a generation process independent of time. These, in turn, can be classified into stochastic and non-stochastic processes. A stochastic process is a type of signal that maintains the same distribution variables when the generation process is set in the same conditions [126]. A stochastic signal $y(n)$ is characterised by the same statistical density function $f_n(y)$ for all values of the signal n that generates the random variable $Y(n)$. From these basic parameters, main basic variables of the stochastic signal can be defined [126].

Mean and Variance

The mean is the expectation value of the random variable of the signal, which is given by

$$\mu(n) = \mathcal{E}[Y(n)] = \int_{-\infty}^{\infty} y f_n(y) dy, \quad (6.25)$$

and the variance is

$$\sigma^2(n) = \mathcal{E}\{[Y(n) - \mu(n)]^2\} = \int_{-\infty}^{\infty} [y(n) - \mu(n)]^2 f_n(y) dy. \quad (6.26)$$

The Covariance

Two independent stochastic processes which vary with the time index n can be correlated. The covariance is defined as the variance between these two processes X and Y

$$\begin{aligned} \text{cov}(X, Y) &= \mathcal{E}[(X(n) - \mu_X(n))(Y(n) - \mu_Y(n))] \\ &= \int_{-\infty}^{\infty} \int_{-\infty}^{\infty} (x(n) - \mu_x(n))(y(n) - \mu_y(n)) f_n(x, y) dx dy. \end{aligned} \quad (6.27)$$

The Correlation Coefficient

The correlation coefficient is the normalised covariance which is derived from (6.27) and (6.26) as

$$r_{XY} = \frac{\text{cov}(X, Y)}{\sigma_X \sigma_Y}. \quad (6.28)$$

The correlation coefficient varies from 0 to 1. $r_{XY} = 0$ denotes two uncorrelated and linearly independent signals and $r_{XY} = 1$ the signals are linearly correlated. Values in between represent two signals that are relatively correlated with a non-zero variance in the signals.

The Autocovariance and Autocorrelation Coefficient

The autocovariance is the covariance between 2 time-dependent indices n and $n + l$ of the same stochastic function y_n . It is the measure of the variance of a function at a lag l ,

$$\text{cov}(y_n, y_{n+l}) = \mathcal{E} [(y_n - \mu)(y_{n+l} - \mu)] = \int_{-\infty}^{\infty} \int_{-\infty}^{\infty} (y(n) - \mu_x(n)) (y(n+l) - \mu_y(n+l)) f_n^2(y) dy^2. \quad (6.29)$$

If the lag is $l = 0$, (6.29) becomes $\text{cov}(y_n, y_n) = \mathcal{E} [(y_n - \mu)^2] = \sigma_y^2$.

The autocorrelation function can henceforth be defined as

$$r(l) = \frac{\text{cov}(y_n, y_{n+l})}{\sigma_y^2} = \frac{\text{cov}(y_n, y_{n+l})}{\text{cov}(y_n, y_n)}. \quad (6.30)$$

The autocorrelation function at $l = 0$ is $r(0) = 1$.

6.4.2 Energy and Power Spectral Densities

The deterministic energy spectrum density can be expressed by the Parseval theorem for discrete signals (6.13). It is written

$$|Y(k)|^2 = \left| \sum_{m=-\infty}^{\infty} y(n) \exp(-j2\pi kn/N) \right|^2. \quad (6.31)$$

where $|Y(k)|^2$ is the energy spectral density. It can also be computed by Fourier transforming the autocorrelation function of the time sequence $y(n)$, called the Einstein-Wiener-Kinchin theorem [127]. It is written

$$|Y(k)|^2 = Y(k) \cdot Y^*(k) = \sum_{n=-\infty}^{\infty} r_{yy}(n) \exp(-j2\pi kn/N). \quad (6.32)$$

The autocorrelation function of the time-dependent sequence $y(n)$ is represented by $r_{yy}(n)$. Since the incrementation boundaries are infinite, the condition for obtaining a finite FT is that the energy of the signal be finite. This condition is fulfilled by ergodic stationary signals; they are random signals whose statistical characteristics (average power or covariance) are independent of time, and

their power distribution constant over different portions of the same signal [127]. For a discrete N sequence time signal, the PSD can be expressed as follows;

$$P_{YY}(k) = \frac{1}{N} \left| \sum_{n=0}^N r_{yy}(n) \exp(-j2\pi kn/N) \right| = \frac{1}{N} |Y(k)|^2 \quad (6.33)$$

The expression in (6.33) is the probability of the power of the stochastic signal in the spectrum. This distribution of the power may fluctuate randomly at different times. A procedure to stabilise the spectra is undertaken; the time signal is segmented and each segment is windowed to smoothen its spectrum. The FFT of each segment can hence be computed, and the sequence of segments is overlapped and the resulting sequence averaged to yield the overall spectrum density of the signal. This process is known as the Welch's method [125].

6.4.3 Windowing, Averaging and Overlapping Segments: The Welch's Method

Let $y(n)$ be subdivided in M blocks of length N each. The autocorrelation function of a single segment \hat{r}_{yy} can be expressed as [117]

$$\hat{r}_{yy} = \frac{1}{N - |l|} \sum_{n=0}^{N-|l|-1} y(n) y(n+l), \quad n = 0, 1, \dots, N-1, \quad (6.34)$$

where l represents the lag. Each segment must windowed prior to computing the Fourier transform. The reason for the windowing lies in the very essence of the DFT, when the frequency of the input signal is not an exact multiple of the resolution frequency or when the signal is aperiodic, distortions will be introduced in the amplitude, frequency and the shape of the spectrum. This effect is called leakage [128]. To minimise leakage, a window function is multiplied in the time domain before the FFT. The window function modulates the wave into a transient function, starting ideally at zero amplitude at the start, growing to the maximum at the middle of the sequence and decaying to zero again at the end of the sequence [117]. In order to normalize the amplitude of the correlation function to 1, a triangular window $w(n)$ can be used;

$$w(n) = \begin{cases} 1 - \frac{|l|}{N} & \text{for } |l| \leq N-1 \\ 0 & \text{elsewhere} \end{cases} \quad (6.35)$$

The power contained in the window is given by the Parseval's theorem is

$$U(n) = \frac{1}{N} \sum_{n=0}^{N-1} w^2(n). \quad (6.36)$$

The windowed signal is given by the product of the elements of \hat{r}_{yy} (6.34) and the window function $w(n)$ (6.35). Hence

$$\hat{r}_{yy} = \frac{1}{N} \sum_{n=0}^{N-|l|-1} \frac{N-|l|}{N-|l|} y(n) y(n+l) = \frac{1}{N} \sum_{n=0}^{N-|l|-1} y(n) y(n+l).. \quad (6.37)$$

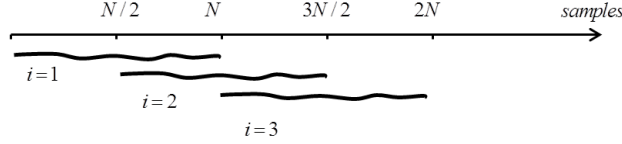


Figure 6.2: Drawing of the overlapping of segments of the signal $y(n)$.

The Welch theorem [125] stipulates that the segments be overlapped by half of their length ($N/2$). Fig. 6.2 shows a graph representing such an operation. The windowed segment PSD can then be computed for each single segment. For the i^{th} segment the expression of the PSD is

$$\hat{P}_{YY}^{(i)}(k) = \frac{1}{NU} \left| \sum_{n=0}^{N-1} w(n) y_i(n) \exp(-j2\pi kn/N) \right|^2 \quad (6.38)$$

And from (6.38), the averaged power density of the M blocks overlapped and windowed is obtained. The Welch windowed power spectrum density can be written

$$\hat{P}_{YY}^W(k) = \frac{1}{M} \sum_{i=0}^{M-1} \hat{P}_{YY}^{(i)}(k). \quad (6.39)$$

The standard deviation of the spectrum in one frequency resolution width is the estimate of the spectral density. Increasing the total number of samples N reduces the resolution frequency width without reducing the variance [129]. The variance of the overlapped segments can be obtained from the expression of the square of the standard deviation of the windowed PSD as follows [117,125]

$$\sigma^2[\hat{P}_{YY}^W(k)] = \frac{1}{M^2} \sum_{i=0}^{M-1} \sum_{j=0}^{M-1} \mathcal{E} \left[\hat{P}_{YY}^{(i)}(k) \hat{P}_{YY}^{(j)}(k) \right] - \left(\mathcal{E} \left[\hat{P}_{YY}^W(k) \right] \right)^2, \quad (6.40)$$

where $\mathcal{E}[u(k)]$ is the estimate of the function $u(k)$ described in (6.25). For half-segment overlap (Fig. 6.2), the variance is hence [125]

$$\sigma[\hat{P}_{YY}^W(k)] \approx \sqrt{\frac{11}{9M}} P_{YY}(k). \quad (6.41)$$

In the case where there is no overlap between segments, the variance (6.40) becomes [125]

$$\sigma[\hat{P}_{YY}^W(k)] = \sqrt{1/M} P_{YY}(k). \quad (6.42)$$

By comparing expressions (6.42) and (6.41), one notices a slight increase in the standard deviation by a factor $\sqrt{2/9M}$, for half-segment overlap, which is in the opposite direction of the effect desired here. However, averaging all M segments reduces the overall standard deviation by a factor $\sqrt{1/M}$ [125, 129].

6.5 Practical implementation of Welch's Method

The Welch's method [125] lays a theoretical framework for the spectral analysis of noisy signals describing adequate mathematical tools for spectral analysis. In practice, however, the choice of the window function and the overlap step is more dependent on the type of input signal and the properties of the spectral accuracy desired [129]. The role of the window function is to eliminate spectral leakage by changing the segment into a transient signal, and the recovery of the entire portion of the signal is made possible by overlapping consecutive windowed segments. The idealistic case of the overlapping is the half-segment treated by Welch and shown in Fig. 6.2. An exhaustive list of window functions can be found in [129,130], where a wide range of different window functions are catalogued according to their respective performance parameters.

6.5.1 Window parameters

Time domain parameters

The time domain function describes the shape of the window in time. Two categories are described; flat-top and sinusoidal windows. The former are characterised by a plateau in the middle range of the length of the segment, and the sinusoidal have a Gaussian (bell) shape.

Let N be the length of the discretely sampled segment described in Section 6.4.3. The window function $w(n)$ is described at $n = 0, \dots, N-1$. The most basic example of the latter is the rectangular $w(n) = 2n/N$ for $n = 0, \dots, N/2$ and $w(n) = 2(N-n)/N$ and the triangular (Bartlett) window (6.35).

Sinusoidal windows are of the shape $w(n) = \sin^\alpha \left[\frac{n}{N} \pi \right]$. The coefficient α varies from 1-4 and $\alpha = 2$ corresponds to the Hanning window [130]. A variant of the Hanning is the Hamming window characterised by the equation $w(n) = \alpha + (1 - \alpha) \cos^\alpha \left[2 \frac{n}{N} \pi \right]$, with an optimal value of $\alpha = \frac{25}{46}$ [130]. The function $w(n)$ is symmetric; hence $w_n = w_{N-n}$. A detailed description will not be done here, for each and many other functions have been extensively detailed in DSP literature [128–130].

The main attribute of a window in the time domain is to annihilate the input signal y_n at $n = 0$ and $n = N - 1$ and maintain the windowed function $\hat{y}_n = y_{N/2}$ in the middle of the range. Fig. 6.3a shows a sequence made of Hanning and Hamming windows applied to a zero-average Gaussian input signal with $N = 2048$. It can be clearly observed that the signal windowed by the Hanning performs better because it cancels the noise closer to zero. The Hamming window, on the other hand, shows a residual noise $\sim 5 - 10\%$ of the maximum amplitude at $n = 0, N - 1$. This remainder noise is the *leakage* of the window function. Mathematically, leakage cannot be zero, but the lower $w(0)$ gets the better the performance of the window function. As shown in Fig. 6.3a, the amplitude of the Hanning close to $n = 0$ is more than 3 orders of magnitude lower in amplitude.

An interesting design to minimise leakage is based on Bessel functions and is called the Kaiser function [129]. It can be defined as $w(n) = I_0(\pi\alpha\sqrt{1 - [2\frac{n}{N} - 1]^2})/I_0(\pi\alpha)$ for $n = 0, \dots, N - 1$. The function I_0 represents the Bessel function of the first kind defined as $I_0(y) = \sum_{k=0}^{\infty} \left[\frac{(y/2)^k}{k!} \right]^2$. The parameter α however represents the attenuation of the function that shapes the spectral response of the function [129].

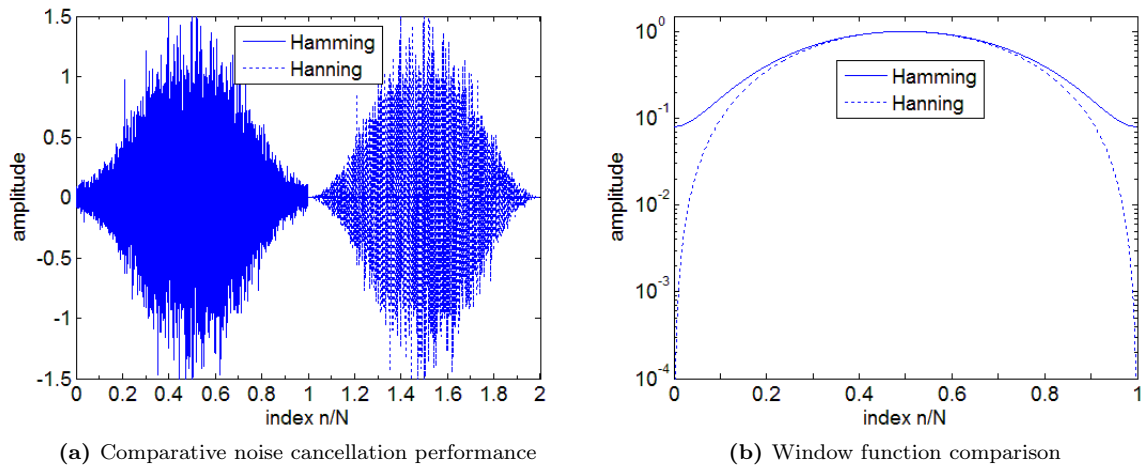


Figure 6.3: Comparative performance of Hamming (solid line) and Hanning (dotted line) windows in the time domain.

Spectral parameters

In addition to the time-domain description, the spectral response of the window provides the core attributes of the window function. Windowing in the time domain is equivalent to convolving the signal and the window spectra in the frequency domain [128]. By default, the spectral density is represented in amplitude/power and expressed in decibels (dB) as

$$\text{scale(dB)} = 20 \log\left(\frac{A(f)}{A_{\max}(f)}\right) = 10 \log\left(\frac{P(f)}{P_{\max}(f)}\right), \quad (6.43)$$

where A , A_{\max} represent the amplitude and the maximal amplitude of the spectra respectively, and P , P_{\max} for spectral power. It is convenient to express the spectra as a function of the ratio of the sampling and the resolution frequency in order to get the quantities independent from the sampling frequency. One unit of such ratio represents a width of the resolution frequency and is referred to as a frequency *bin* [128, 129].

$$\text{frequency bin} = \frac{f_s}{\Delta f} \quad (6.44)$$

The spectra of window functions are generally made of a central lobe which determines the bandwidth property of the window and side peaks at regular intervals called sidelobes.

The Bandwidth of the central lobe is the first parameter to take into consideration depending on the nature of the signal. The bandwidth is estimated at -3dB of the spectrum. Fig. 6.4 represents a comparative amplitude spectrum of the Hamming and Hanning windows. The amplitude of the window spectrum is plotted against the frequency bin number. The spectra show the same shape in the central lobe. The -3dB amplitude bandwidth (BW) is 1.44bins for the Hanning. The BW is usually expressed as normalised equivalent noise bandwidth (NENBW) that is defined using the

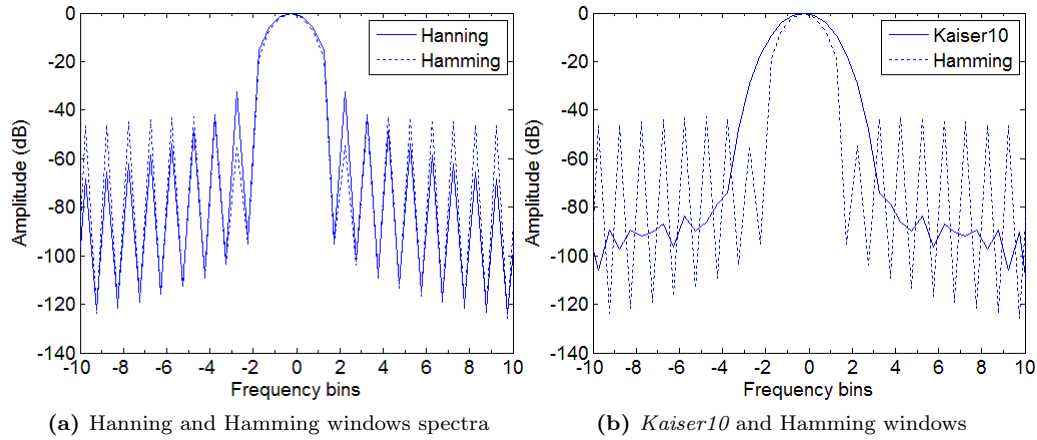


Figure 6.4: Window function spectra for random signal processing

Parseval theorem (6.13) as follows [129];

$$\text{NENBW} = N \frac{S_2}{S_1^2}, \quad (6.45)$$

where S_1 and S_2 are the normalisation sums $S_1 = \sum_0^{N-1} w(n)$ and S_2 the power content in the window defined in (6.30). The NENBW is 1.5 bins for the Hanning and 1.3 for the Hamming windows. For a signal sampled at 125 Hz for instance with $N = 2048$, the BW of the central lobe is $\text{NENBW} \times f_s/N = 0.1$ Hz.

The sidelobe height is the amplitude of the first lobe on the side of the central lobe expressed in dB. The sidelobes represent the stopband of the window and are henceforth the expression of the leakage in the spectrum i.e. the smearing out of the signal energy over a wide-band area instead of being concentrated in a the central lobe [131]. Therefore, the lower and the faster their intensity decreases in frequency, the better. The rate of decrease of the lobes is called the sidelobe *roll-off*. The Hamming and Hanning spectra are strikingly similar in the passband, however, the Hamming window provides a perfect cancellation of the first sidelobe.

The Kaiser window is designed to minimise the energy in the stopband [129]. The parameter α represents the rate of attenuation in the sidelobes called the sidelobe roll-off rate. Analytically, to design a rate of attenuation in the desired range, it is necessary to define a design parameter β , so that

$$\beta = \begin{cases} 0.11(\alpha - 8.7), & \text{for } \alpha > 50 \\ 0.584(\alpha - 21)^{0.4} + 0.0788(\alpha - 21), & \text{for } 50 > \alpha > 21 \\ 0, & \text{for } \alpha < 21 \end{cases}$$

Table 6.2 presents the properties of commonly used windows for random noise [129]. Depending on the type of signal and the properties wanted, a careful choice of the window can be made. The

Table 6.2: Parameters of window functions based on [129, 130]; the normalised equivalent noise bandwidth, the bandwidth maximum sidelobe amplitude and sidelobe amplitude *roll-off* rate are represented.

Window	NENBW (bins)	BW [$f_s = 125$ Hz, $N = 2048$] (Hz)	max. sidelobe ampl. (dB)	ampl. <i>roll-off</i> rate (dB/10bins)
Hanning	1.5	0.091	-32	-8.4
Hamming	1.30	0.080	-43	-5.1
<i>Kaiser10</i>	1.84	0.112	-83	-3.5

Kaiser filter with $\beta = 10$ (dubbed *Kaiser10* here) shows excellent cancellation noise properties in the sidelobe height despite that its central lobe bandwidth is relatively larger.

The choice of the window is motivated by the type of the input signal, and its frequency content. The window must be small enough to resolve different components of the frequency in the spectrum. Geomagnetic signals in the SR range as random stochastic signals show a frequency bandwidth of the order of ~ 1 Hz at the first SR [19]. Henceforth, all the windows listed in Table 6.2 can effectively resolve such type of signal. The main task, therefore, will consist in cancelling as much as possible the noise in the stopband. In this regard, the *Kaiser10* window perfectly fits this role. The maximum sidelobe amplitude is reduced by -40 dB in amplitude in comparison to a Hamming window and by -50 dB to a Hanning as shown in Fig. 6.3. It is worth mentioning that the Kaiser window has also been recommended for random signals in [129].

6.5.2 Overlapping parameters

Optimal conditions for overlapping depend solely on the type of window used and the statistical distribution of the random signal [129, 130]. In order to keep all the data points of the overlapped segments on relatively constant amplitude, it is important to minimise the signal at the boundaries $n = 0$ and $n = N - 1$, to avoid noise leakage in subsequent segments. In this regard, the Hamming is not a good candidate as shown in Fig. 6.3a. Moreover, a good balance should be found between the flatness of the amplitude of the overlapped segments and their overall correlation [129].

Amplitude Flatness

The total weight of the sum of two consecutive window functions of equal amplitude at the intersection point varies from the minimum (zero) to a maximum of the double amplitude for a full overlap, as the windows are overlapped at peak-to-peak distances between the peaks from n/N to 0. The process is shown in Fig. 6.5a,b for a Hanning and Fig. 6.6a,b for a *Kaiser10* window respectively. The amplitude flatness (AF) is the ratio of the minimal height at the intersection point to the maximum amplitude of the window function. Fig. 6.5b and 6.6b show the evolution of the AF as a function of overlapping ratio for a Hanning and a *Kaiser10* window. The amplitude becomes flat for the Hanning when the overlapping rate is 50%, and for the *Kaiser10* the overlap rate is 66.6%. The value of the overlapped amplitude for the Hanning is shown to be the amplitude of initial windows whereas the *Kaiser10* shows an overlapping that reaches 1.62 times the initial amplitude. Here, it is necessary to clarify that we need to achieve a flatness at the same amplitude as the initial window

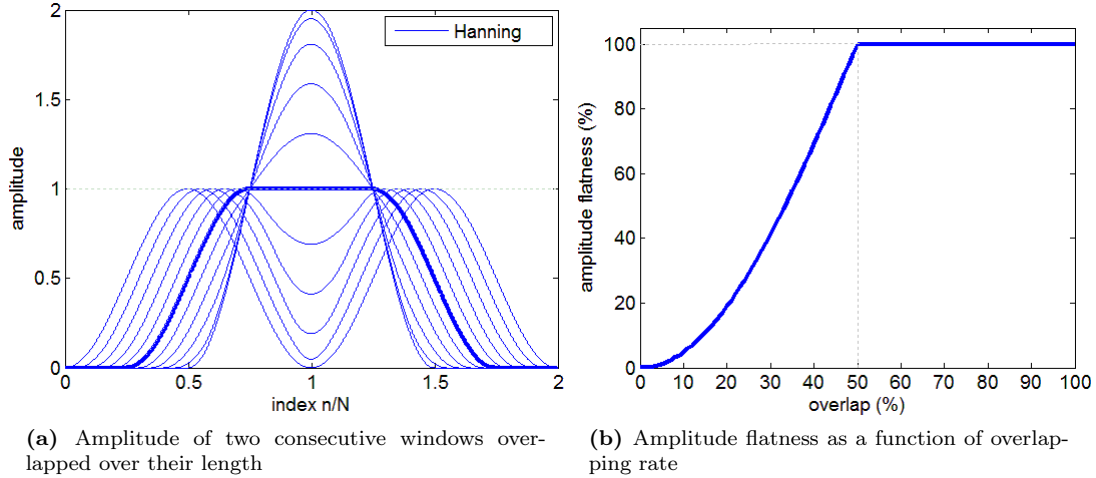


Figure 6.5: Amplitude flatness versus overlapping rate for the Hanning window. The overlap increment step is $n/10N$ for (a) and is added at each step from bottom to top. The AF is reached at 50% of the overlapping.

function which is normalised. Therefore, in the process of averaging the resultant amplitude should be divided also normalised to 1.

Overlap Correlation

When the FFT is applied to a windowed non-overlapped segment of the signal as shown in Fig. 6.3, the events that occur near the boundaries are most likely to become insignificant because of the window damping effect [130]. In order to avoid a loss of data in the spectra (especially in the detection of fast transient effects), the segments are overlapped prior to computing their Fourier transform. The degree of correlation of the random components in successive components is hence

$$OC(r) = \frac{\sum_{n=0}^{rN-1} w(n)w(n + (1-r)N)}{\sum_{n=0}^{N-1} w^2(n)} \quad (6.46)$$

where r is the overlapping rate.

The correlation of overlapped segments should be maintained at a minimum, because if the segments are highly correlated, the signal will lose its dynamic variation owed to its stochastic nature. Hence, the OC should be kept as minimal as possible. Therefore, the recommended overlap (r_{ov}) is determined by the lowest value of overlap rate r at which the AF reaches 1 because by increasing r further, the OC increases as well. Heinzel [129] proposes that the recommended overlap is where the difference between AF and OC reach a maximum. Fig. 6.7 represents the evolution of AF – OC for Hanning and *Kaiser10* windows. The match is perfect for the Hanning but has a certain overlap rate offset (3%) for the *Kaiser10*. However, the fact that the flatness is achieved in the close vicinity of the maximal range of AF – OC is more significant.

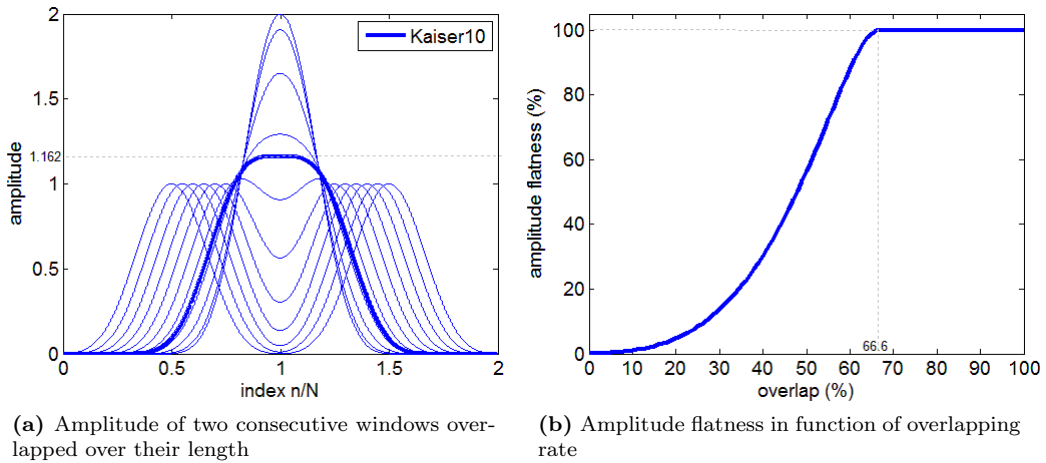


Figure 6.6: Amplitude flatness versus overlapping rate for the *Kaiser10* window. The overlap increment step is $n/10N$ for Fig. 6.6a evolving from bottom to top. The AF is reached at 66.6% of the overlapping.

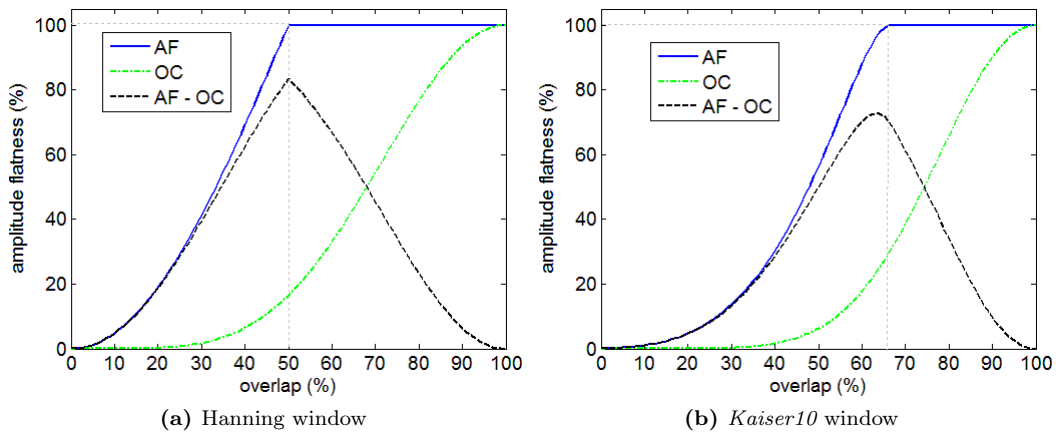


Figure 6.7: Comparative variation of the amplitude flatness (AF) and the overlap correlation (OC) for the Hanning and the Hamming windows.

6.5.3 Computation of Spectral Parameters

The next step after the windowing and overlapping of data segments is the computation of the FFT. In Matlab, the function is based on the Cooley and Tuckey algorithm [122] and is compiled in a computational library dubbed the *Fastest Fourier Transform in the West* (FFTW) [132]. The transform in (6.19) is applied on each windowed data segment of length N . The resultant DFT output $\hat{Y}(k)$ can be written,

$$\hat{Y}(k) = \frac{1}{N} \sum_{n=0}^{N-1} y(n) w(n) \exp(-j2\pi kn/N) \quad k = 0, 1, \dots, N-1, \quad (6.47)$$

where $n = 0, \dots, N-1$ is the time-domain increment and $y(n)$, $w(n)$ are time-dependent discrete signal and the window functions.

The Power Spectrum is obtained using the Parseval theorem. It is the expression of the power contained in the segment (6.27) divided by the power content of the window function (6.30).

$$\text{PS} = 2 \frac{|\hat{Y}(k)|^2}{S_1^2}, \quad k = 0, 1, \dots, N/2 \quad (6.48)$$

The power spectrum is a real number estimate of the power over the positive part of the spectrum. For a geomagnetic signal in time domain in nanotesla (nT), the power is expressed in nT^2 .

The Power Spectrum Density (PSD) is the estimate of power spectrum in the window bandwidth. Hence, the expression of the PSD can be derived from (6.41), (6.31) and (6.18) as follows

$$\text{PSD} = \frac{\text{PS}}{N \text{ENBW}} = 2 \frac{|\hat{Y}(k)|^2}{f_s S_2}, \quad k = 0, 1, \dots, N/2 \quad (6.49)$$

where f_s is the sampling frequency. The units are in $\frac{nT^2}{\text{Hz}}$.

The Amplitude spectrum density is the linear spectrum density, expressed as the square root of the power spectrum density. Its units are in $nT/\sqrt{\text{Hz}}$.

$$\text{ASD} = \sqrt{\text{PSD}} = \sqrt{2} \frac{|\hat{Y}(k)|}{\sqrt{f_s S_2}}. \quad k = 0, 1, \dots, N/2 \quad (6.50)$$

6.5.4 Averaging of segment spectra

After windowing, overlapping and computing the FFT of each segment, stability of the spectra is achieved with the averaging of the segments. As shown in Section 6.4.3, averaging reduces the standard deviation of the data by $1/\sqrt{M}$ where M is the number of segments [130]. Hence, the variance in the data reduces continuously as the number of segments increases leading to more

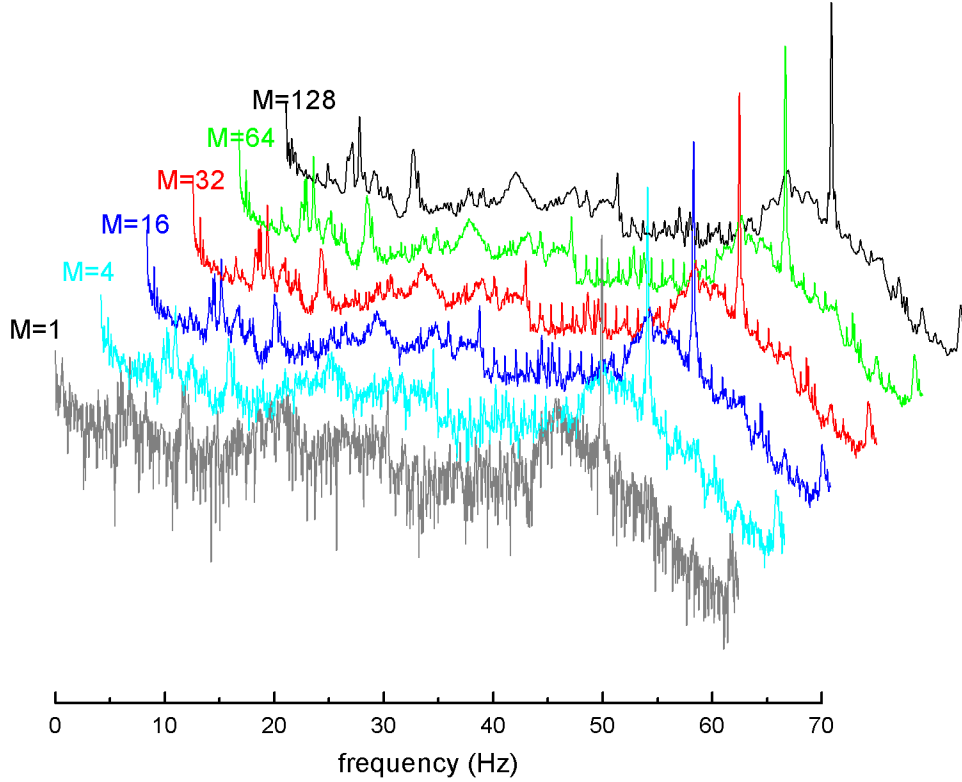


Figure 6.8: Perspective representation of geomagnetic \mathcal{H} spectra PSD on 2007 – 11 – 07 at 1324 UT (the daily maximum power). The total length of the dataset is $N = 4096$ and $M = 1, 4, 16, 32, 64, 128$ represents the number of segments averaged. Notice the powerful peak at 50-Hz corresponding to the power-grid induced magnetic component. The graphs are offset to create an effect of 3D depth for clarity.

stable spectra. Fig. 6.8 shows such a gradual stabilization of the magnetic spectra, with a clear resonance structure appearing with increasing number of averaged segments M . This is true because the magnetic signal in the Earth-ionosphere cavity is a response to a random thunderstorm activity and nonlinear effects in the cavity. On the other hand, the 50 Hz power grid signature is sharp and clear throughout the stabilization process because it is a deterministic sinusoidal signal. The number of segments depends on the window function recommended overlap rate r_{ov} and the total length N and segment length N_S , as follows

$$M = \text{mod} \left\{ \frac{1}{1 - r_{ov}} \left(\frac{N}{N_S} - 1 \right) \right\}. \quad (6.51)$$

In the case of a Hanning and Hamming windows ($r_{ov} = 0.5$), $M \approx 2 \left(\frac{N}{N_S} - 1 \right)$ and for the *Kaiser10* ($r_{ov} = 0.66$), $M \approx 3 \left(\frac{N}{N_S} - 1 \right)$.

6.5.5 Spectra Representation

Daily geomagnetic datasets sampled at 125 Hz of measurements are available at the LSBB server (<ftp://193.52.13.2/pub/data/>). They are sampled for 3 directional axes; North-South (NS),

East-West (EW) horizontal axes and the vertical (VZ) axis. Their spectral parameters can therefore be computed, most particularly the PSD is of interest. To represent the spectra at a chosen instant of the day, the PSD can be computed over a relatively short time scale (hours) and plotted in a two-dimensional power-versus-frequency plot. However, on a longer timescale (day or more), it is necessary to represent the spectra in such a way to visualise the variation of the spectral properties (power and peak frequency) in function of time. The latter representation is called a spectrogram.

Short-term Representation

The input time signal is 24 minutes in length ($N = 18.75 \times 10^4$), subdivided into 128 *Kaiser10* windowed and overlapped segments (45) of length $N_S = 4096$ each. This is to ensure the spectra are stable and to provide 2 orders of magnitude of spectral resolution . From (6.21), $\Delta f = 3 \times 10^{-2}$ Hz and from Table 6.2 the *Kaiser10* resolution is $\sim 2\Delta f$. Fig. 6.8 shows such a two dimensional representation of the PSD as a function of the frequency. Clear resonance patterns are observed in the spectra at $M = 128$ in the vicinity of 8, 12 and 21 Hz along with the power-grid magnetic signature at 50 Hz.

Spectrogram

The spectrogram is a 3D representation of the PSD of the signal in function of frequency and time. It is usually used for long-term measurements of the horizontal geomagnetic field spanning for several days. Time is represented on the horizontal axis, frequency on the vertical axis and the power is represented as a colour projection in the Red-Green-Blue (RGB) format, where the highest magnitude is red and the lowest is blue. The time signal is subdivided into frames 4.3 minute-long ($N = 2^{15}$) which in turn are subdivided into 45 segments of $N_S = 2048$. Each segment is *Kaiser10* windowed and overlapped. The resolution $\Delta f = 6 \times 10^{-2}$ Hz and peak resolution of the window is $\sim 1.2 \times 10^{-1}$ s. Fig. 6.9 represents a daily power spectrum density spectrogram of the ground magnetic field components in logarithmic scale. Stable resonances patterns can be clearly observed in the spectrograms, especially in the NS magnetic component depicted in Fig. 6.9a, where strong peak frequencies at 8, 12 and 21 Hz are observed. A further analysis of polarisation properties in the horizontal magnetic components will provide further resonance properties of EM propagation in the E-I cavity.

6.6 Conclusion

The Fourier transform allows us to detect the periodicities expressed in the magnetic signal. However, the random prevalent component of the geomagnetic signal is not straightforward. The variance in the raw spectra would render the study obsolete without a technique to reduce the variance and stabilise the spectra. This is achieved by a method based on the Welch algorithm [125] which consists of fragmenting the input signal into segments, windowing each segment, and overlapping the segments to reconstruct the information lost in the windowing process. The output segments are Fourier transformed and averaged to obtain an output that is less random and displays clearly the

periodicities of the input signal. In this chapter, an overview of the basics of the Fourier transform of discrete signals was conducted, but more attention was focused on a correct practical treatment of the random stochastic signal. The central tool for processing this type of signal is a window function, which cancels the noise at the lowest level in the stopband and is narrow enough to allow a clear resolution of resonances in the spectra. The Kaiser window has been selected and used to that effect.

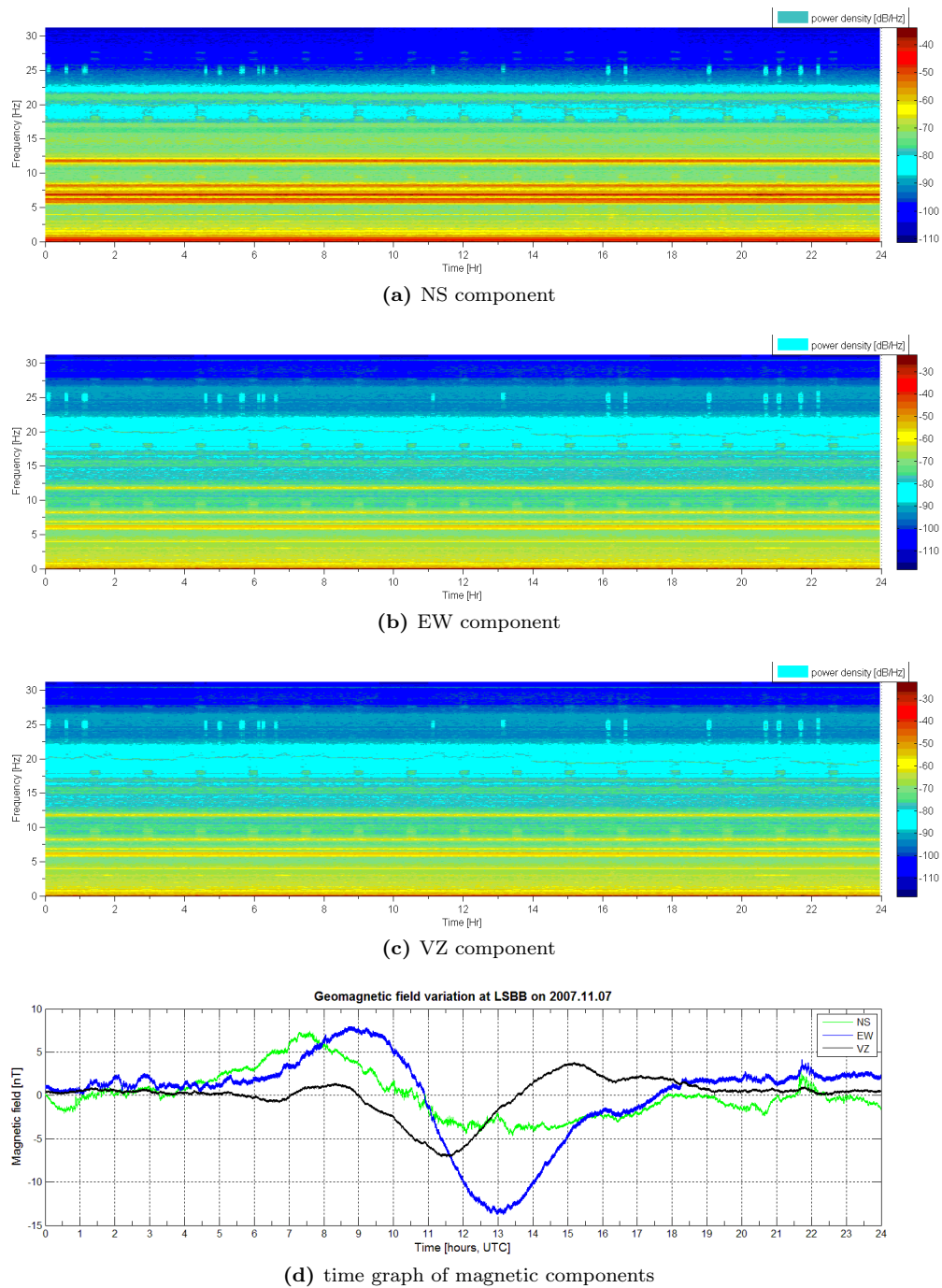


Figure 6.9: Daily **H** spectra represented in the 3 directional components; North-South, East-West and Vertical Z axes. In (a),(b) and (c), the power is represented in dB scale .Datasets are taken on 2007-11-07 and represented in function of Universal Time (UT).

Chapter 7

Polarisation Properties of SQUID Geomagnetic Horizontal Components

7.1 Introduction

The polarisation study of geomagnetic components is an important tool to assess whether the EM resonances measured at an observatory are of a global nature. This is achieved by measuring the coherence of the signal in the frequency range considered. Coherence has two aspects; spatial and temporal coherence. Let us consider a ray of light travelling in empty space; Spatial coherence determines the correlation between waves at different points in space and temporal coherence defines their correlation at different instants in time. For a monochromatic wave, the amplitude $A(t)$ at every point in space is constant and the phase $\phi(t)$ varies linearly with time. The wave is coherent in time-space domain. On the other hand, in case of an incoherent signal (white noise for instance), $A(t)$ and $\phi(t)$ vary irregularly and so rapidly that no correlation can be drawn. In general, natural EM signals behave as a mix of polarised and non-polarised wave components. The polarised spectrum is generally estimated in a tiny bandwidth $\Delta\nu$, so that $\phi(t)$ approximates a linear curve. For a wave of velocity c and wavelength λ , areas of coherence in the signal are determined by $c/\Delta\nu = \lambda^2/\Delta\lambda$ which is called time-space coherence criterion [133].

In ELF propagation, the coherence criterion is relatively large because at the lower part of the ELF range (the SR range [1 – 100 Hz]), frequencies are low enough that the variations of $\phi(t)$ are approximately linear in a considerably large window of time [133]. Theoretical basics of the polarisation of EM waves in continuous media were developed by Landau and Lifshitz [134] and were elegantly used to determine polarisation properties of quasi-monochromatic waves in physical optics by Born and Wolf [133], who developed mathematical tools based on power and cross-correlation of orthogonal components of the EM field. Fowler *et al* [135] applied the technique to natural ULF propagation and obtained satisfactory results for the mitigation of natural and man-made incoherent noise. In the same year, Ogawa *et al* [87] demonstrated that powerful ELF pulses could be detected from different and very distant observatories, the **E** waveforms observed around the globe were highly correlated and showed they originated from a single pulse. The cross-correlation

of horizontal \mathbf{H} components at distant observatories were also measured by [136]. The signals detected were coherent at a level of 90% at the first SR for two stations separated by more than 1100 km. Long-term experimental studies of polarisation properties of SRs were first conducted by Sentman [86, 104] and since then polarisation properties of the SRs have been extensively covered by many other authors especially Nickolaenko and Hayakawa [13, 19].

The term *polarisation* might seem ambiguous in the sense that it is already known that the SRs are by definition TM radial modes; with a non-zero radial \mathbf{E} component and non-zero horizontal \mathbf{H} component. Ideally, the ground is assumed as a perfect conductor at lower ELF range [19]. However, because the TM polarisation is due to the Earth-Ionosphere boundary conditions and the vertical nature of the excitation, it should only be associated with the behaviour in time and space of the radial \mathbf{E} . Nonetheless, the polarisation concerns the horizontal \mathbf{H} components because in reality, the finite conductivity of the earth-ionosphere cavity induces, at the observation site, a vertical (radial) field and a phase delay in the horizontal \mathbf{H} [19]. polarisation properties have been investigated both in the horizontal plane and in the vertical plane: In the horizontal plane, it has been associated mainly to propagation anisotropies in the ionosphere and in the vertical plane to local conductivity anomalies of the lithosphere [137].

Sentman [104] investigated polarisation properties of the SRs for horizontal magnetic components at a ground station located in California. He found the polarisation at the SR to be elliptically polarised in the horizontal plane at the first SR frequency. The values of ellipticity were larger than 0.5 during the day at first resonance peak frequency. The direction of polarisation was clockwise during the day and counter-clockwise at night. However, Rusakov *et al* [138] found that for observatories in the northern hemisphere, the rotation of the horizontal \mathbf{H} was mostly counter-clockwise at resonance frequencies, with an ellipticity value of 0.25 for the first SR. Nickolaenko *et al* [139] noticed that the ellipticity and degree of polarisation remained constant in the vicinity of the first SR. The rotation of the wave was found to be always counter-clockwise both in the simulated model and the experiments.

Due to the anisotropic properties of the medium of propagation of natural EM waves in the ELF range, which is the case for the E-I cavity, polarisation properties of the EM field resonances can be fully determined from the \mathcal{H} components. [13, 104]. Ideally, the study of polarisation properties in the SR range should allow one to separate a worldwide coherent signal from local incoherent noise. The main reason of incoherence may arise from the nature of the source of excitation itself; random in time and location [28]. Powerful tropical thunderstorm centres occurring simultaneously in localised small areas produce signals that are highly coherent but random pulses that occur outside those areas might be observed as incoherent noise [19]. In this chapter, the analysis of polarisation properties will help to analyse the relationship between coherent signal and the incoherent noise. Ellipticity and magnetic wave arrival angle (axis of rotation orientation) will also be evaluated. In addition to this, an attempt will be made to use these polarisation properties to detect the splitting of the first SR mode in the geomagnetic field.

7.2 Computation of Polarisation Properties

Born and Wolf [133] devised a method for calculating polarisation properties of EM partially polarised waves using quasi-monochromatic wave theory in the frequency domain. The method is based

on the power correlation and cross-correlation of the components of the wavefield called coherence matrix (CM). If the wavefield is completely polarised then the matrix determinant is zero. On the other hand, the matrix is non-zero for partially or non-polarised wavefield. We can hence separate non-polarised from polarised components of the field by resolving eigenvalues and eigenvectors associated with the polarised and depolarised wave. The ellipticity, the axis of rotation orientation and direction of polarisation can be henceforth calculated using auto-correlation and cross-correlation analysis of elements of the CM.

Let us consider a quasi-monochromatic wave packet so that the ratio of the bandwidth to the mean frequency of the signal is negligible [133]. In this case, the coherence time of the signal is greater than the average period of the signal, which means that the packet of waves behaves as a monochromatic wave. The two components of the horizontal \mathbf{H} will be studied. they can be defined as

$$H_X = A_1(t) \exp[i(\bar{\omega}t + \varphi_1(t))] \quad (7.1)$$

$$H_Y = A_2(t) \exp[i(\bar{\omega}t + \varphi_2(t))] \quad (7.2)$$

where $\bar{\omega} = 2\pi\bar{\nu}$ is the average angular frequency of the wave packet, $A_1(t), A_2(t)$ respective time-dependent amplitudes and $\varphi_1(t), \varphi_2(t)$ are time-varying phases.

7.2.1 Coherence

The polarisation of the wavefield can be represented as a matrix of the form

$$J = \begin{bmatrix} J_{XX} & J_{XY} \\ J_{YX} & J_{YY} \end{bmatrix} = \begin{bmatrix} \langle H_X H_X^* \rangle & \langle H_X H_Y^* \rangle \\ \langle H_Y H_X^* \rangle & \langle H_Y H_Y^* \rangle \end{bmatrix} \quad (7.3)$$

where H_X^*, H_Y^* are complex conjugates to the horizontal magnetic fields. In case the signal were fully polarised, determinant of the coherence matrix is zero.

$$\det(J) = 0$$

The intensity I of the total wave packet would be obtained by plugging (7.1) and (7.2) into (7.3)

$$I = J_{XX} + J_{YY} = A_1^2 + A_2^2 \quad (7.4)$$

In case the signal is not fully polarised, the determinant of the CM is non-zero, henceforth we can assume that the CM is a sum of depolarised and polarised components of the wave packet. As by definition, the polarised part determinant is zero, it can be written as

$$J_P = \begin{bmatrix} P_{XX} & P_{XY} \\ P_{XY}^* & P_{YY} \end{bmatrix} = \begin{bmatrix} J_{XX} - D & J_{XY} \\ J_{YX} & J_{YY} - D \end{bmatrix} \quad (7.5)$$

where D represents the elements of the depolarised matrix. Hence, by resolving the eigenvalue type problem in (7.5), one can deduce the eigen-elements of the depolarised matrix

$$D = \frac{1}{2}(J_{XX} + J_{YY}) \pm \frac{1}{2} [(J_{XX} + J_{YY})^2 - 4|J|]^{\frac{1}{2}} \quad (7.6)$$

where J is the polarisation matrix. From equations (7.4) and (7.6) we can deduce the total polarised intensity as

$$I_P = [(J_{XX} + J_{YY})^2 - 4|J|]^{\frac{1}{2}} \quad (7.7)$$

The degree of polarisation or coherence of a wave is the ratio of the polarised to the total wave intensity,

$$P_D = \frac{I_P}{I} \quad (7.8)$$

The coherence of the electromagnetic wave can hence be expressed from (7.8) as

$$P_D = \left[1 - \frac{4|J|}{(J_{XX} + J_{YY})^2} \right]^{\frac{1}{2}} \quad (7.9)$$

P_D is always positive and varies from 0 to 1. $P_D = 0$ represent a completely depolarised signal and $P_D = 1$ a totally polarised signal.

7.2.2 Ellipticity

Ellipticity is a property that determines the type and the direction of rotation (or sign) of the polarised EM wave in time. Ellipticity derives from the phase difference between the projections of the components of the field on X and Y axes. As shown in Fig.7.1, the procession of the field vector tip describes an ellipse in the horizontal plane in a clockwise rotation shown by the direction of arrows along the ellipse perimeter. Here, the Z axis is entering the page, because the unit vectors $\vec{u}_{X,Y,Z}$ form an orthogonal and normalised set. The direction of polarisation is referred to as right-handed polarisation (RHP). On the contrary, the polarisation is called left-handed. (LHP) [13, 139]. The variations of the semi-major and semi-minor axes of length a and b control the shape and size of the ellipse; bearing in mind that $b \leq a$, by keeping a constant and decreasing b , it is clear that $b = a$ describes a perfect circle and $b = 0$ a straight line of length a . The intermediate position will be an ellipse as represented in Fig 7.1.

In order to extract elliptical polarisation properties from the CM, we apply to the coordinate axes the condition of rotation of the polarised CM [135, 140].

$$\begin{bmatrix} Y & X \end{bmatrix} \begin{bmatrix} P_{XX} & P_{XY} \\ P_{XY}^* & P_{YY} \end{bmatrix} \begin{bmatrix} Y \\ X \end{bmatrix} = P_{XX}P_{YY}. \quad (7.10)$$

The development of (7.10) yields

$$\frac{Y^2}{P_{YY}} + \frac{2\text{Re}P_{XY}}{P_{XX}P_{YY}} + \frac{X^2}{P_{XX}} = 1 \quad (7.11)$$

Equation (7.11) is a typical equation of an ellipse. We can henceforth define parameters associated with the ellipse described here, the direction of polarisation β and the angle of inclination of the polarisation ellipse θ . The shape of the ellipse can be defined by the angle of polarisation, it is

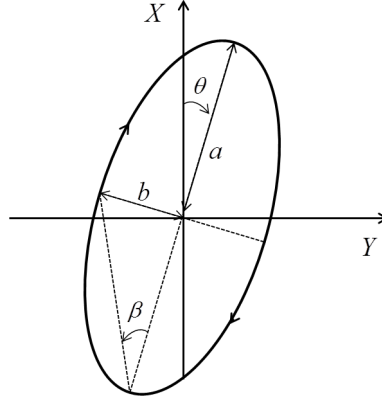


Figure 7.1: Sketch of the elliptical polarisation of the horizontal \mathbf{H} , where a, b represent the semi-major and semi-minor axes of the ellipse. Axes x and y represent the WE and SN directions. θ represents the inclination angle of the major axis of the ellipse to the x axis. The direction of polarisation represented here is right handed in the direction of z .

referred to as the ellipticity ;

$$el = \tan \beta = \frac{b}{a} \quad (7.12)$$

By convention, when the angle $\beta < 0$, the polarisation is clockwise or right-handed (RHP) as shown in Fig.7.1, and $\beta > 0$, the polarisation is counter-clockwise or left-handed (LHP). The value of ellipticity varies as $|el| \leq 1$ with $el = 0$ describing linear polarisation and the case $|el| = 1$, circular polarisation. The sign of el is determined by the sign of the angle β . The variation of the angle β in function of the CM elements can be deduced from the equation (7.11) yielding

$$\sin 2\beta = \frac{i(P_{XY}^* - P_{XY})}{[(P_{XX} - P_{YY})^2 + 4P_{XY}^*P_{XY}]^{\frac{1}{2}}} \quad (7.13)$$

7.2.3 Phase Difference and Ellipticity

The coherence correlation matrix can be applied to the quasi-monochromatic horizontal \mathbf{H} components (7.1) and (7.2) of the CM to establish a relationship between the phase lag between components and the angle of polarisation. The CM becomes;

$$J = \begin{bmatrix} A_1^2 & A_1 A_2 \exp(i(\varphi_1 - \varphi_2)) \\ A_1 A_2 \exp(-i(\varphi_1 - \varphi_2)) & A_2^2 \end{bmatrix} \quad (7.14)$$

The CM shown in (7.14) is equivalent to (7.3). Hence, by using the ellipse equation obtained from the CM, the angle of polarisation β relates to the phase difference between the orthogonal \mathbf{H} as follows

$$\sin(2\beta) = \frac{2A_1 A_2}{A_1^2 + A_2^2} \sin(\varphi_2 - \varphi_1), \quad (7.15)$$

where $(\varphi_2 - \varphi_1)$ or $\Delta\phi$ is the phase difference between the X and Y polarised components. Hence, the ellipticity is related to the phase difference by the relations (7.12) and (7.15) to yield

$$el = \tan \left(\frac{1}{2} \arcsin \left(\frac{2A_1A_2}{A_1^2 + A_2^2} \sin(\Delta\phi) \right) \right) \quad (7.16)$$

7.2.4 Inclination Angle of the polarisation Ellipse

The angle of inclination of the ellipse θ can be deduced from the rotation matrix described in equation (7.10). It is by definition the angle made between the semi-major axis and the x-axis. Hence, if we rotate the polarised CM J_P axes by θ clockwise, we would obtain a diagonal matrix of J_P elements [140]. This expression can be written as

$$J' = CJC^t, \quad (7.17)$$

where C is the clockwise θ -angle rotation matrix, C^t is its transpose matrix and J' is the diagonal matrix,

$$C = \begin{bmatrix} \cos \theta & \sin \theta \\ -\sin \theta & \cos \theta \end{bmatrix}$$

From the combination of (7.5), (7.11) and (7.15), we obtain the relationship between the inclination of the ellipse and the polarisation elements as follows,

$$\tan 2\theta = \frac{2\text{Re}P_{XY}}{P_{XX} - P_{YY}}. \quad (7.18)$$

The angle θ is hence the angle that the major axis of the ellipse makes with the abscissa axis. θ is by convention taken positive in the clockwise direction and is referred to as the arrival angle of the horizontal **H** wave. The extraction of the above-cited parameters of the horizontal **H** polarisation ellipse provides useful information on the propagation properties of the EM wave.

7.3 Application to LSBB Datasets

We use the datasets sampled at 125 Hz of daily geomagnetic measurements available at the LSBB server [113]. The X, Y components in [135] correspond to the NS and EW magnetic components at the LSBB respectively. The time signal is subdivided in 32.8 s ($N = 4096$) segments which are transformed to the Fourier domain using the FFT algorithm to obtain a spectral resolution of 3×10^{-2} Hz. The spectra are accumulated and averaged over a duration of 24 minutes using the Welch's method. A low-pass filter with a cut-off of 30 Hz is applied to limit the spectra to the first three resonances.

7.3.1 Coherence Measure Spectra

The first step will consist in validating the method by testing some datasets. SQUID magnetometers at LSBB are shown to be subject to interference due to nearby magnetic disturbances and also by

the ambient man-made noise [48, 112]. The 50-Hz power grid component is by default eliminated by the low-pass filtering. However, it is possible that other man-made electromagnetic noise could couple to the signal in the considered bandwidth dc -30 Hz. The ideal test day would be with very little seismic and magnetic noise and no man-made noise. Quiet magnetic days are reported by the German Research Centre for Geosciences (GFZ [141]) and the daily seismic data can be found on the US Geological Survey website (USGS, [142]). However, seismic activity is predominant in the ULF range up to few Hz following strong earthquakes [111] and the LSBB is located in one of seismically quietest regions in the world. Seismo-magnetic disturbances will not be considered here. Magnetic disturbances though will be avoided so that all the datasets chosen have a quiet magnetic weather with the geomagnetic index $Kp \leq 2$.

Fig. 7.2 shows a daily spectrogram taken on a quiet day on 2007-09-26 with time (UT) represented as abscissa and frequency represented as ordinates. The power density and wave polarisation properties are represented in colour scale (on an RGB scale, with the red representing the top and blue the bottom of the scale). Fig. 7.2a represents the coherent power density variation of the total horizontal \mathbf{H} . The band at 8 Hz shows a series of maximal plateaux from 0600 – 1000 UT, 1200 – 1400 UT and a series of peaks from 2000 – 2200 UT (also depicted in Fig. 7.4b), corresponding to South-East Asian, African and American thunderstorm centres maximal activity [56, 103]. The coherent power spectrum density is obtained from the modulation of the power density of the horizontal \mathbf{H} and the degree of polarisation of the wave in the frequency domain. From the coherence correlation matrix, polarisation properties are computed in the frequency domain with equations (7.12)-(7.18). Fig. 7.2b is the coherence measure that varies from a minimum of 0.3 to 1. At frequencies around 6.5, 7.6 and 8 Hz, and in the band from 25 to 30 Hz, the spectrum shows a degree of polarisation greater than 0.9. These bands shown here represent a highly correlated signal that might originate from a global source. The minimum of the coherence spectrum is observed in a band centred at 7.8 Hz. The pronounced variation observed in the vicinity of 8 Hz could be a prelude to different resonant modes across the first SR. The ellipticity of the wave is shown in Fig. 7.2c, The red-dish colour represents positive polarisation whereas bluish colour represents the negative direction of polarisation. It is important to mention that the polarisation sign is a matter of a convention; Sentman [86, 104, 143] represents the LHP as negative and RHP as positive ellipticity whereas more recent research on polarisation of SR [13, 19, 139] represent them the other way round. The latter way has been interpreted as a representation in radiophysics perspective where the observer looks the propagating wave along its propagation path, to the contrary of optics, where the observer looks towards the source against the propagation path [13]. The radiophysics' observer perspective has been adopted here; the polarisation is defined in function of the downward axis of rotation Z of \mathcal{H} (pointing towards the centre of the Earth) as shown in Fig. 7.1. However, the angle β described in Fig. 7.1 grows in the anticlockwise direction, implying that the positive direction of polarisation ($el > 0$) is counter-clockwise and the negative direction of rotation ($el < 0$) is clockwise (RHP).

The angle of inclination of the ellipse θ is reported in the Fig. 7.2d, the angle shows great variation around 8 Hz, switching from an angle of -20° at 7.6 Hz to 30° at 8 Hz, which might be associated with different modes propagating around that frequency. It is important to mention that the centres of the bands shown in Fig. 7.2d correspond to the peak of coherence observed in Fig. 7.2b.

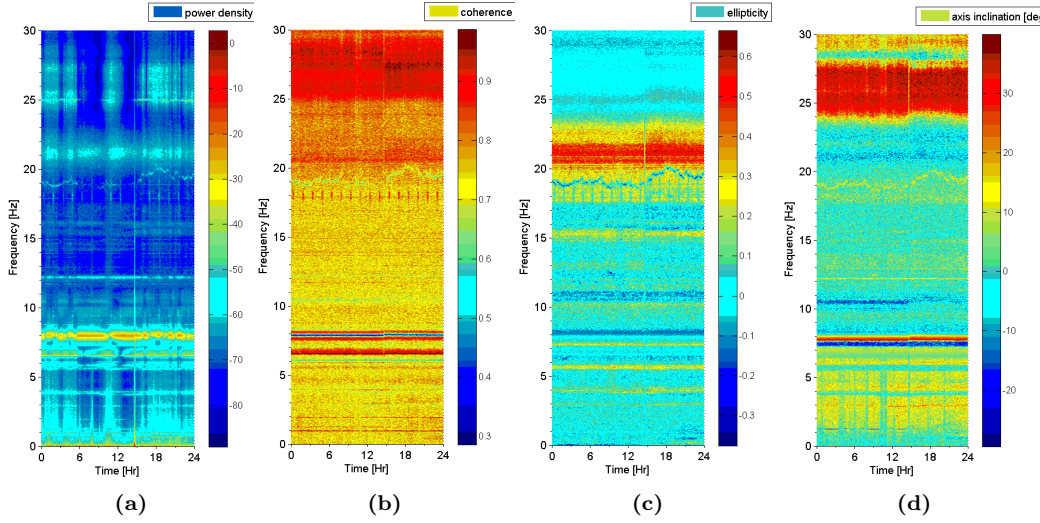


Figure 7.2: Spectrograms showing the variation in frequency and time of the spectra of \mathcal{H} on a quiet day 2007-09-26 (a) the coherent power spectral density (b) coherence (c) the ellipticity of the wave and (d) the polarisation ellipse inclination

7.3.2 Validation of the Coherence Matrix Method

The validation of the CM method will be conducted with magnetic spectra in the vicinity of 8 Hz for two main reasons; firstly because magnetic spectra show great variation both in terms of amplitude and phase around that frequency and secondly, to prospect for the type of modes that propagate in the vicinity of the first SR. The coherence-matrix-eigenvalues observed in the total \mathcal{H} will be compared to the phase difference between the horizontal components of the raw signal filtered across a narrow passband in the vicinity of 8 Hz. The datasets used for the purpose have been selected from days labelled as magnetically quiet by the GFZ. The signal will be sampled during the daily maximum power of the African Thunderstorm activity from 13 : 36 UT.

Digital resonator

A digital resonator is used to filter raw data across a narrow frequency bandwidth around a central resonance. This will help analyse the magnetic signal in a quasi-monochromatic configuration of the coherence matrix components defined in (7.1) and (7.2).

Fig. 7.3 shows the frequency response of the digital resonator used to filter magnetic data H_{EW} and H_{NS} and the resultant spectra of the datasets filtered at the maximum of the daily magnetic activity for each *event*. The filter consists of a two-poles-and-two-zeros bandpass filter with the frequency response characterised by its amplitude and phase. The amplitude is hence defined by

$$|H(e^{j\omega})| = \frac{2 \cdot b_0 \cdot \sin(\omega)}{\sqrt{[1 - 2r \cos(\omega - \omega_0) + r^2][1 - 2r \cos(\omega + \omega_0) + r^2]}} \quad (7.19)$$

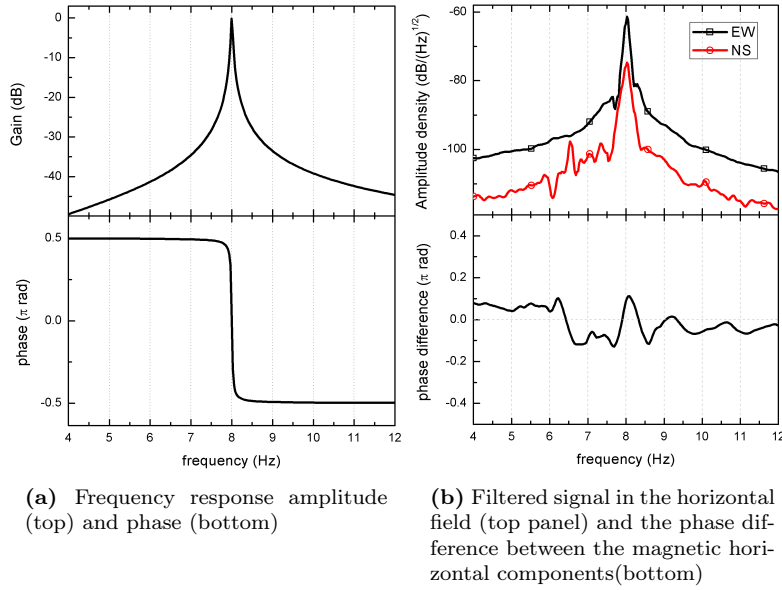


Figure 7.3: Frequency response of the resonator used for polarised event counting. The top graph represents the gain and the bottom the phase variation at the bottom for $f_0 = 8$ Hz, $r = 99.9\%$ and a sample size $N = 4096$. (b) The spectra of the H_{EW} and H_{NS} signal from 2007 – 09 – 26 13 : 36UT at LSBB, filtered through a resonator at 8Hz and (b) phase difference between the components.

and the phase is the angular component of the complex response spectrum given by

$$\phi = \arctan \left(\frac{\Im [H(e^{j\omega})]}{\Re [H(e^{j\omega})]} \right) \quad (7.20)$$

where b_0 is the amplitude, r the pole radius, ω the angular frequency and ω_0 is the resonator frequency in rad/sample. $\Im [H(e^{j\omega})]$ and $\Re [H(e^{j\omega})]$ represents the imaginary and real parts of the resonator frequency response. The central frequency in Hz is the product of the sampling frequency (in samples/second) and the resonator frequency $f_0 = f_s \frac{\omega_0}{2\pi}$. At $f_0 = 8$ Hz, the passband width at -3 dB of the amplitude response is less than 0.1 Hz and the phase shows a linear slow variation in the stopband and a steep π -shift and change of sign in the passband, characteristic of a resonance. The reason for this narrow passband is the need to monitor mode of vibration of the magnetic wave in the close vicinity of a monochromatic frequency component as possible as suggested in Section 7.1.

We focus on the pass-band chosen and ignore the resonances observed in the stopband. The amplitude of the stopband resonances is highly attenuated to -34.7 , -19.7 dB at 6.5, 8.3 Hz respectively. In this case, the major resonant component observed in the filtered signal is the 7.9 Hz attenuated to -9 dB of the peak amplitude. Fig. 7.3 represents the resonator shown in (7.19), (7.20) and the spectrum of the field components filtered at $f_0 = 8$ Hz. From (7.20), the phase difference is calculated, $\Delta\phi|_{f_0=8Hz} = 0.1\pi$ rad. The zeros of phase lag indicate a linearly polarised resonance. Therefore, one may expect linearly polarised resonant components at 6.5, 7.9 and 8.3 Hz. Using (7.16) and the respective amplitudes of the spectra displayed in Fig. 7.3b (top panel), the ellipticity of this event can be deduced; $el|_{f_0=8Hz} = 0.07$, which is relatively a thin ellipse close to the linear polarisation.

In the same way, the magnitude and sign of polarisation of the magnetic wave is computed for each *event* and modes of polarisation are counted and classified into their respective categories.

Coherence Matrix Spectrogram Analysis

The method of the coherence matrix has been efficiently used to extract the polarisation properties from geomagnetic signal [13, 19, 86, 137, 143]. Most of the work has generally concerned the detection of events in short, powerful and localised events such as *ELF transients*. Long-term measurements were also conducted in the study of polarisation properties in \mathcal{H} field in the ELF range [104, 139], but the effect of overlapping and averaging of spectra is not investigated, the aim here is to validate the use of CM method for long-term spectrograms that are stacked and averaged with the Welch process [125] of extracting resonance parameters from the background noise.

The datasets used are sampled on 2007 – 09 – 09 and 2007 – 09 – 26 labelled as *day1* and *day2* respectively. These two dates appear on the GFZ list among the quietest days of the month. Fig. 7.4a shows the spectra sampled and averaged over 24 min. and their polarisation properties. The spectra are chosen at the maximum of the daily activity corresponding to the African Thunderstorm activity for a mid-latitude northern hemisphere observatory [13, 103], shown in Fig. 7.4b. The investigation focuses on the part of the spectra showing a swift variation in polarisation properties as a function of the frequency from 7 – 8 Hz. The first aspect that one may notice is the double peak that is consistently observed in the spectra as shown in Fig. 7.2a, 7.2b, and 7.2c. The maxima at 6.5 and 7.9 Hz are both seen in the averaged power spectra and have been observed in the phase lag sign reversal of the raw bandpass filtered (BPF) signal in the vicinity of 8 Hz in Fig. 7.3b. However, the maximal power of the signal at 8 Hz is at least 20 dB higher than the average power of the first SR as reported in the literature [19, 92].

In Fig. 7.4a, $el(f) = 0$ at 7.63 and 7.78 Hz on *day1* and *day2* respectively. At these values, the CM method predicts a linear polarisation of the horizontal \mathbf{H} component. This linear resonance is located between a peak $+0.23(7.25 \text{ Hz})$ and a bottom at $-0.2(8 \text{ Hz})$ for *day1*. The same at $+0.21(7.16 \text{ Hz})$ and $-0.11(8 \text{ Hz})$ for *day2*. The angle θ of the magnetic wave shows great amplitude variation across the first SR, with minima at $-6, -18.2^\circ$ in the LHP side, $-7.1, -8.1^\circ$ in the RHP side of the resonance and maxima at $+25.1, +31^\circ$ corresponding to the linear resonance, for *day1* and *day2*. This implies that θ rotates clockwise in the LHP region towards the linear resonance and anticlockwise from the linear resonance,

Raw signal Analysis

The two datasets are subdivided into smaller data entities of length $N = 4096$ samples. Because there is no stacking nor averaging of the signal prior to the spectra extraction, the length of the sample must be long enough to allow stable spectra in the SR range. Each spectrum is filtered through the narrow BPF described in Fig. 7.3a at selected frequency values in the vicinity of the first SR (shown in Fig. 7.4a). The ellipticity for each event will be recorded and categorised depending on its magnitude and sign. However, for the sake of mitigating fallacious linear polarisation from incoherent noise that might be embedded in the signal [143], events with linear polarisation are discarded, so that solely events with $|el| > 0.05$ are considered.

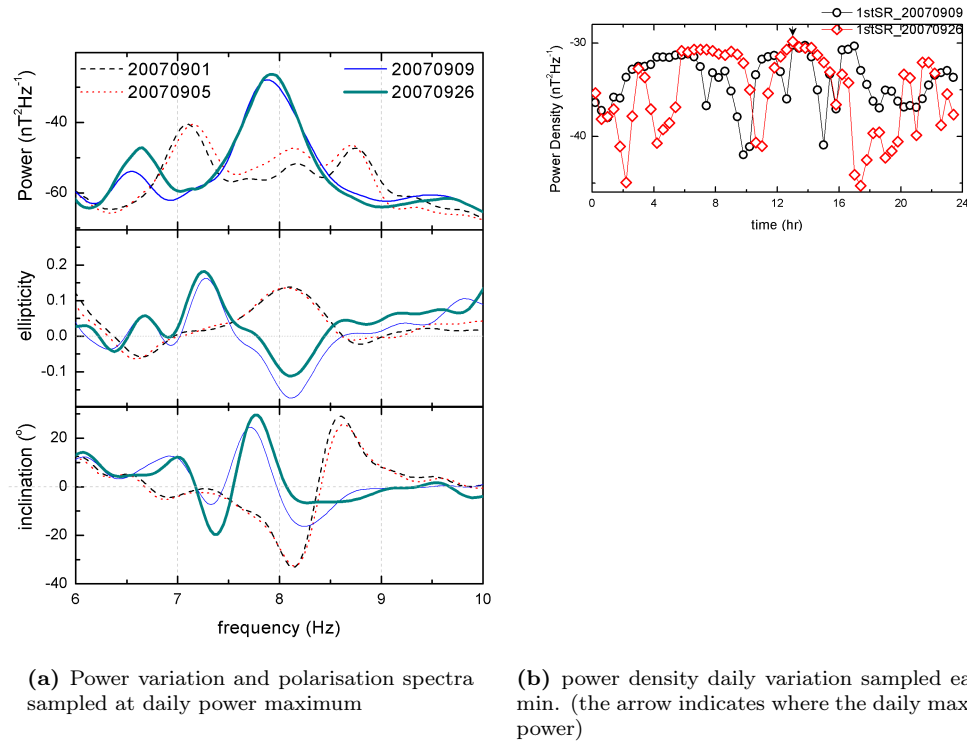


Figure 7.4: The spectra of \mathcal{H} measured on the 2007-09-09 and 2007-09-27 sampled. 13:36 UT along with data sampled on 2007-09-01 and 2007-09-05

Fig. 7.5 shows histograms of event polarisation distribution in their respective ellipticity categories ranging from -1 to 1 with an interval of 0.1 . The line at $el = 0$ marks the separation between LHP and RHP events. The polarisation modes are poorly fitted with a Gaussian distribution, but can be approximated with a Poisson's distribution owed to the stochastic nature of the excitation source and the independent nature of the polarised events both in time and location [13, 19]. The mode populations ratios n_L and n_R for LHP and RHP are counted and their variation is displayed in Fig. 7.7a. A transition from LHP to RHP dominated spectrum is clearly observed for both datasets. In Fig. 7.7b, the ratio n_L/n_R between polarised events is displayed. A ratio of 1 means a fifty-fifty distribution for each polarisation mode, which is a transition between the two modes observed at 7.74 and 7.84 Hz for *day1* and *day2*. In the vicinity of the transition frequency (Fig. 7.5e and h), the mode distribution narrows much closer to the $el = 0$ line, with events with $|el| < 0.1$ gathering a maximum of 66.6% and 68.6% of all the polarised modes for *day1* and *day2* respectively (despite the mitigation of purely linear events described earlier). This implies that the frequency observed at the transition from LHP to RHP in Fig. 7.7b is dominated by linearly polarised events. The tendency to linear polarisation is also observed in Lissajous curves (Fig. 7.6e and 7.6k). Henceforth, the transitional linearly polarised frequency described by the CM method ($el(f) = 0$) is equivalent for the two methods, it is determined with a relative uncertainty of 0.11 and 0.06 Hz respectively.

Fig. 7.6 represents the most frequent polarisation modes observed in every mode category plotted approximately over one period of oscillation, and represented both as time signals and Lissajous curves (see Fig. 7.1 for description). The time graphs Fig. 7.6a and g show the EW lagging the

NS component at 7.4 Hz and the EW leading the NS at 8.1 Hz. Close to 7.8 Hz however, the two polarised waves are in phase due to the fact that close to the linear resonance, the inclination angle reaches a positive maximum in the range shown in Fig. 7.4a(bottom panel). This effect is clearly seen in the narrow ellipses displayed in Fig. 7.6e and k that can be approximately fitted by linear curves. The slope of H_{EW} versus H_{NS} is always positive and the linear polarisation is clearly observed for events in the range close to the linear resonance frequency. Here, the resonance frequency of the linear resonance is the transition between LHP and RHP polarisation modes. In Fig. 7.6d-f and Fig. 7.6j-l, the Lissajous curves are represented. The polarisation is shown as a numerical symbol in increasing order. The clockwise numerical growth represents the RHP and in the other case an LHP mode. Fig. 7.6d and j show a typical LHP polarisation whereas Fig. 7.6f and l are RHP. The transitional polarisation in Fig. 7.6e shows a narrow RHP and an LHP mode in Fig. 7.6k. The narrow ellipses can be explained by the fact that the events with $|el| < 0.05$ have been discarded from the spectra. The difference in sign of polarisation can be shown in Fig. 7.6a,b where the value of 7.8 Hz is slightly beyond the linear resonance for *day1* and below the linear polarisation for *day2*. The sign of the polarisation changes when the frequency of linear polarisation is crossed. Mode population ratios obtained from the narrow bandpass filtering are shown in Fig. 7.7b in the vicinity of 8 Hz. A prevalence of the LHP appear before the linear resonance and a stronger RHP mode dominance is observed afterwards, reaching maximum population of more than 81% and 85% of all the polarisation modes (Fig. 7.7a) for *day1* and *day2* respectively. Henceforth, one would expect that the variation of the ellipticity spectrum to be related with the proportion of polarised mode of the signal.

It is also important to notice that LHP modes show a negative value for θ at 7.3 Hz (IIInd Quadrant), θ rotates clockwise towards frequencies close to the linear resonance (Ist Quadrant) after which it rotates anticlockwise towards the LHP modes after 8 Hz (IIInd Quadrant) (see Fig. 7.1 for clarifications). A gradual and yet similar evolution of $\theta(f)$ pattern is observed in the CM method close to the first SR (in Fig. 7.8), with a positive maximum value of θ reached approximately at the linear polarisation frequency. In the same way as for the ellipticity (Fig. 7.5a), a statistical distribution function θ in the raw signal is done in terms in a set of elements $[-90^\circ, +90^\circ]$ with an interval of 6° . θ is the tangent of the slope of the major diagonal axis of H_{EW} against H_{NS} , provided that the Lissajous curve is centred at the origin (0, 0). Hence, the least square fitting can be used to find the inclination angle;

$$\theta = \arctan \left(\frac{\sum_{i=1}^{N-1} x_i y_i}{\sum_{i=1}^{N-1} x_i^2} \right) \quad (7.21)$$

where x represents H_{NS} elements, y represents H_{EW} and N the length of the datasets. The absolute angle θ can be measured by the BPF method as the sum of an average value and its variation in frequency; $\theta = \theta_{av} + \Delta\theta$. As shown in the bottom panel of Fig. 7.4, the coherence method provides not the absolute angle θ , rather a measure of its variation. In Fig. 7.9a and b, a correlation between the CM and the BPF methods is displayed for $\Delta\theta(f)$. The raw signal BPF method shows an offset average value of $\theta_{av} = -32.5^\circ$ and -30° for *day1* and *day2* respectively. Greater variation is observed in the vicinity of the first SR. Across the same interval, $\Delta\theta$ for both methods (with CM data in parentheses) show peak frequencies of 7.9(-0.27) and 7.8(-0.11) Hz for *day1* and *day2*

respectively.

CM and Bandpass filtering Methods correlation

The daily averaged ellipticity variation in function of the frequency in Fig. 7.3a is compared to the ratio of mode distribution. For the sake of simplicity, we rather proceeded with the comparison of the ellipticity to the mode population ratio, by assuming that a strong mode population in the raw signal should correlate to the predominant mode in the spectral window taken into consideration. The narrow-passband filter in Fig. 7.3 is swept through the frequency spectrum 2 – 30 Hz at a step of 0.1 Hz and polarisation modes with $|el| > 0.05$ are counted at each step for which a ratio between the two observed modes is deduced. We remove the offset and obtain $r_0 = \frac{n_L}{n_R} - 1$ and compare the ratio to the ellipticity in the spectrum 2 – 30 Hz.

In Fig. 7.8a and b, a comparative graph of the ellipticity obtained with the CM method with the narrow-band filtered signal r_0 against the frequency is displayed. $r_0 > 0$ represents a frequency dominated by RHP modes, LHP prevalence is determined by the condition $r_0 < 0$ and $r_0 = 0$ at linear resonance. A good correlation can be observed between r_0 and the ellipticity of the signal computed with the CM. A linear correlation between the ellipticity and the mode ratio can be determined. Hence, the correlation between the ellipticity and the mode ratio is 83% and 60% for *day1* and *day2*.

In Fig. 7.9a and b, $\Delta\theta(f)$ shows a poor correlation in the overall spectrum and but a good correlation in the window from 7 – 9 Hz, for both signals and 24 – 28 Hz for *day2*. The overall correlation coefficient in the window, 0 – 24 Hz is found to be 31% **and** 15% for *day1* and *day2* respectively. In the vicinity of the first SR (from 7 – 9 Hz), better correlation is observed, at 53% and 29% in both cases.

7.4 Signal-to-noise ratio (*snr*)

The CM method becomes very handy because it separates the coherent from the incoherent component of the signal whereas the BPF method does not. Therefore, a comparison between coherent and incoherent signal may explain the discrepancies observed in the spectra, especially in the vicinity of the first SR, by determining bands of strong coherence (or decoherence). The decoherence (depolarisation) coefficient can be defined in function of the polarisation (coherence) coefficient of the wave as [13]

$$D_D = 1 - |P_D|, \quad (7.22)$$

with P_D defined in (7.9). In the same way as P_D , $0 \leq D_D \leq 1$. The decoherence is nil when the signal is completely coherent and maximum for uncorrelated noise. Let us refer to the coherent component as the signal $S(f) = H(f) \cdot P_D$, and the noise $n(f) = H(f) \cdot (1 - |P_D|)$, where $H(f)$ is the spectrum of the magnetic signal. The signal-to-noise ratio can be approximated as

$$snr(f) = \frac{S(f)}{n(f)} = \frac{P_D}{1 - |P_D|} \quad (7.23)$$

Fig 7.10 reveals the variation of $snr(f)$ in the SR band. The peaks observed at (7.1 Hz, 25 dB) in Fig. 7.10a and (6.5 Hz, 20 dB) in Fig. 7.10b clearly indicate a signal that is highly correlated at those values of frequency, with a proportion of the coherent to the incoherent portion of the signal greater than 100 to 1. Due to the poor conductivity properties of the E-I resonator cavity for EM propagation [19], these high values of $snr(f)$ maxima do not most probably originate from the SR background signal. This highly correlated sinusoidal signal might originate from an internal source of SQUID measurement system.

Notice that in the vicinity of the first SR, $snr(f)$ reaches a minimum value in the range 0 – 10 Hz. This might highlight the true nature of the SR. To confirm this behaviour, let us show the nature of the noise spectra $n(f)$ observed. Fig. 7.11 shows the spectra of the incoherent noise signal $n(f)$. Unlike the common notion of electromagnetic noise, these spectra show the same resonance peaks as the coherent signal in Fig. 7.10 centred at 8, 14 and 21 Hz. In particular at 8 Hz, the spectra show roughly $snr(f = 8 \text{ Hz}) \simeq 1$, which means a half-half repartition of coherent and incoherent magnetic component. This observation confirms previous observations made at a mid-latitude station in Lekhta ($64^\circ N, 34^\circ E$) by Nickolaenko *et al* [139] that showed that at the first SR, 50% of the magnetic horizontal component is not polarised. This has been attributed to the wide angle sensitivity of the magnetic antenna (to different thunderstorm areas); the strokes that are out of phase induce a decoherence in time, those randomly scattered all over the world induce space decoherence.

7.5 Conclusion

The coherence matrix is a handy method to analyse polarisation properties in magnetic signals. It provides useful information about the polarisation coefficient of the signal, the phase difference between the components of the horizontal H field and the signal-to-noise ratio. It is based on a matrix of correlation and cross-correlation of components of the field provided that the magnetic signal is made of a linear combination of quasi-monochromatic sinusoidal wave components.

The comparison between spectra obtained with the coherence matrix method and the bandpass filtering of the raw signal generally show a good correlation for events in the vicinity of 8 Hz. Elliptical polarisation is observed in most of the spectra around the first SR, with the resonance of always a change of sign of polarisation at resonance. The most dominant mode slightly below the SR is LHP and RHP modes after resonance. This is followed by a sign reversal of the arrival angle of the EM wave component. This might clearly indicate a resonance in the SR [19, 86, 104].

The shift observed in the resonance patterns might be associated with the change of the SR frequency, the most important aspect of the shift is the frequency change that affects power spectra and all the polarisation parameters in the same way. Nonetheless, the intensity of resonances detected is too high and the peaks seem too narrow for SRs, as previously described in Sections 4.3.3 and 5.4.

2007-09-09

2007-09-26

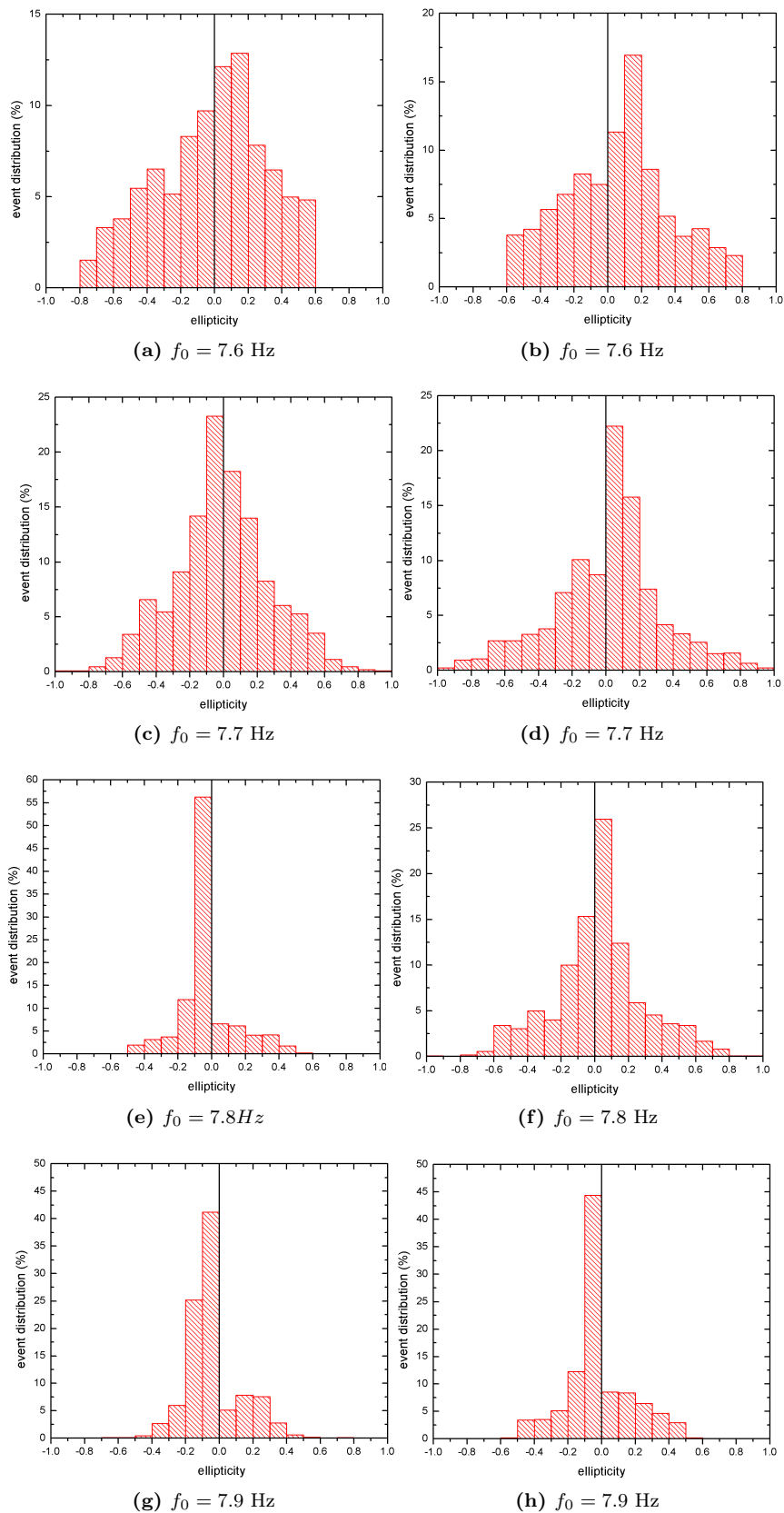
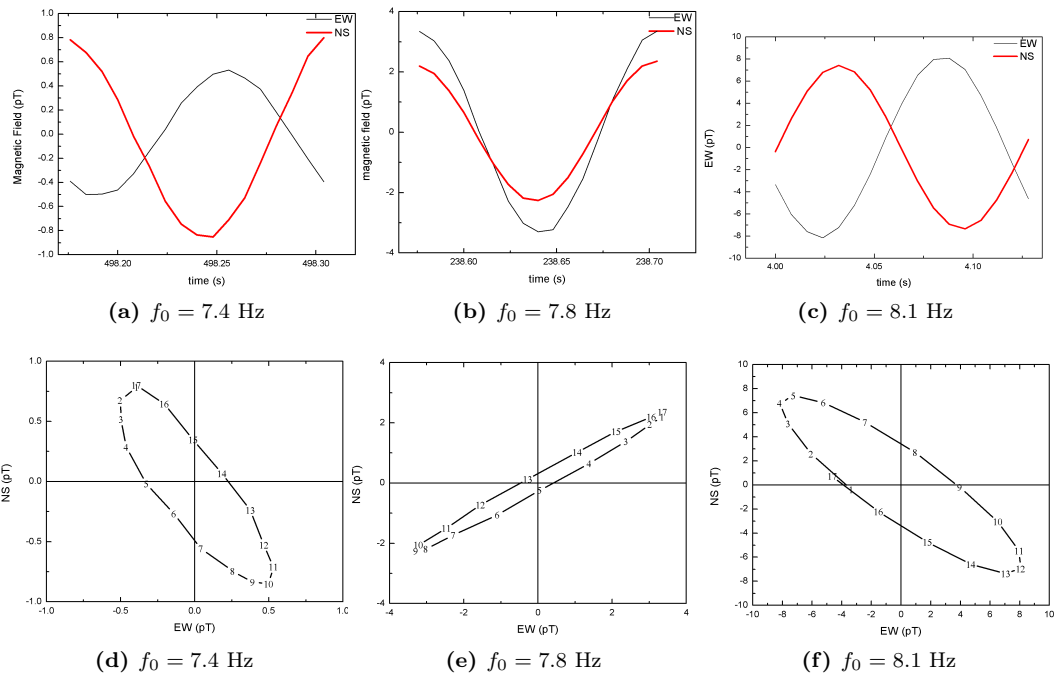


Figure 7.5: Classification of polarised events for the two datasets 2007-09-09 and 2007-09-09-26 in the range 7.6 - 7.9 Hz.

2007-09-09 13:36 UT



2007-09-26 13:36 UT

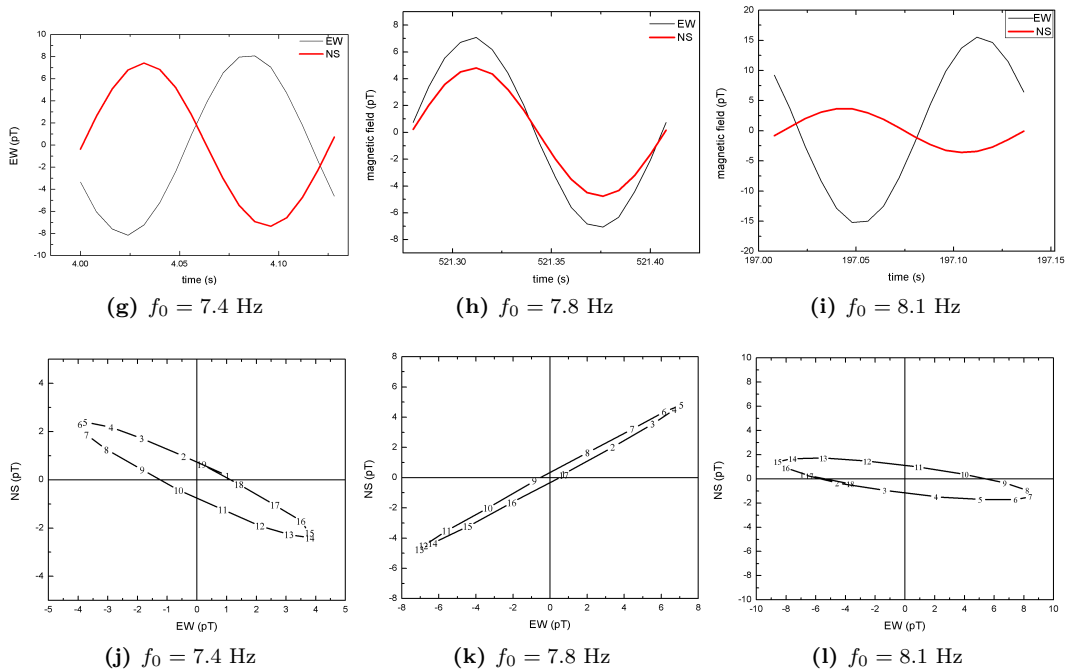


Figure 7.6: Modes of polarisation taken from the maximal amplitude events in the most populous of the ellipticity categories displayed in Fig. 7.5

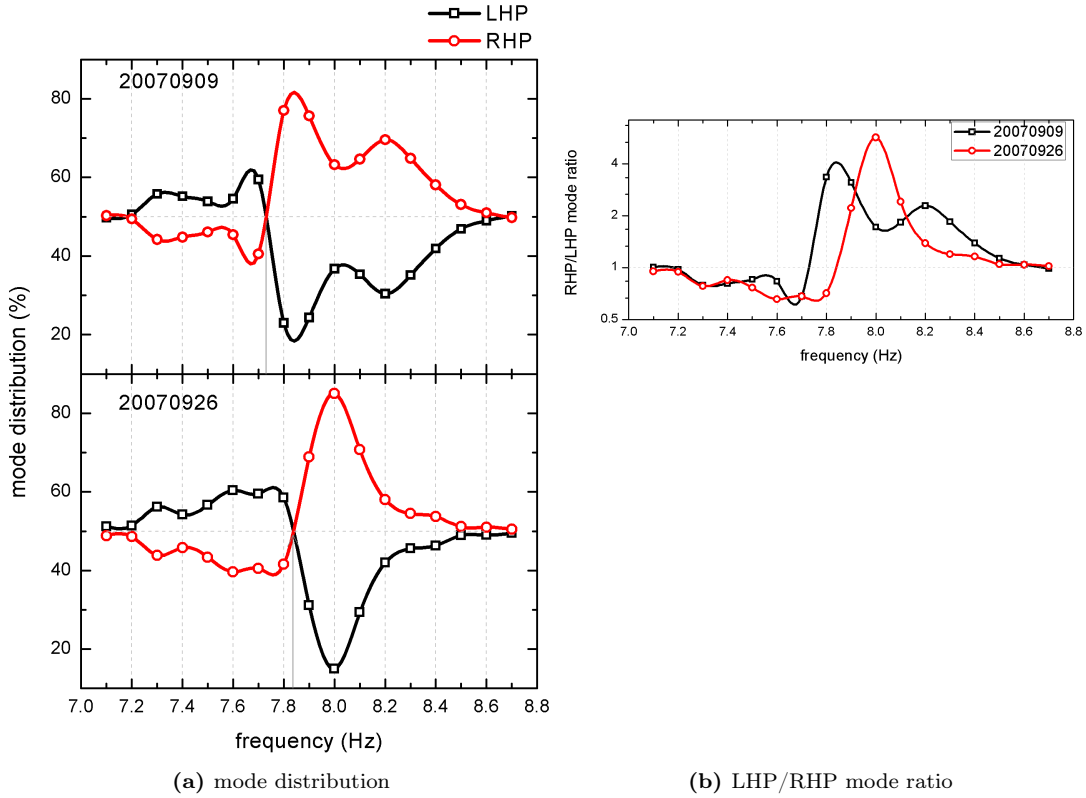


Figure 7.7: The LHP and RHP mode distribution across the first SR on the two datasets on 2007-09-09 and 2007-09-26 described in Fig. 7.5

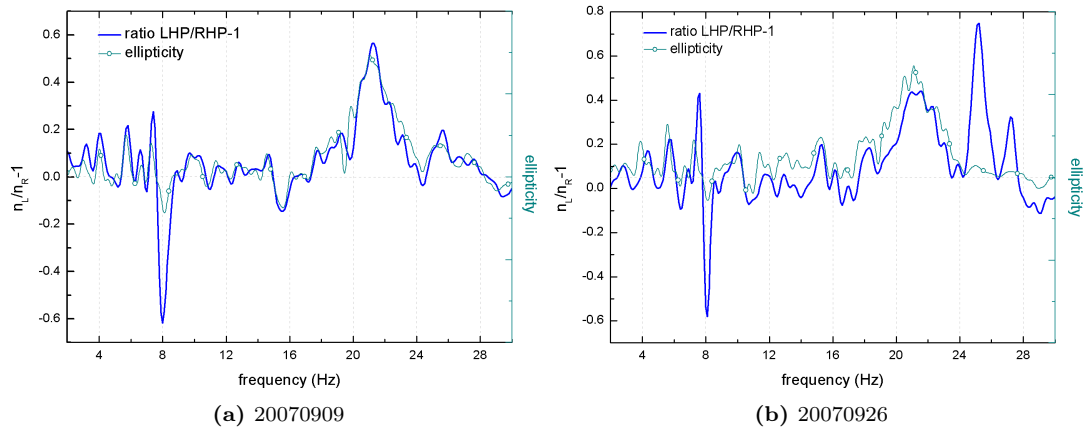


Figure 7.8: Comparative representation of bandpass filtered raw magnetic signal with the averaged ellipticity of the signal on (a) day 1 and (b) day 2

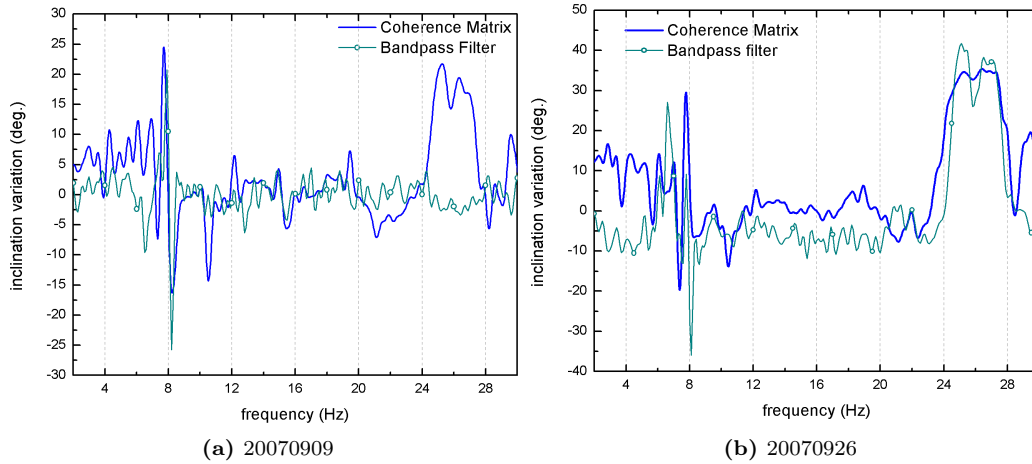
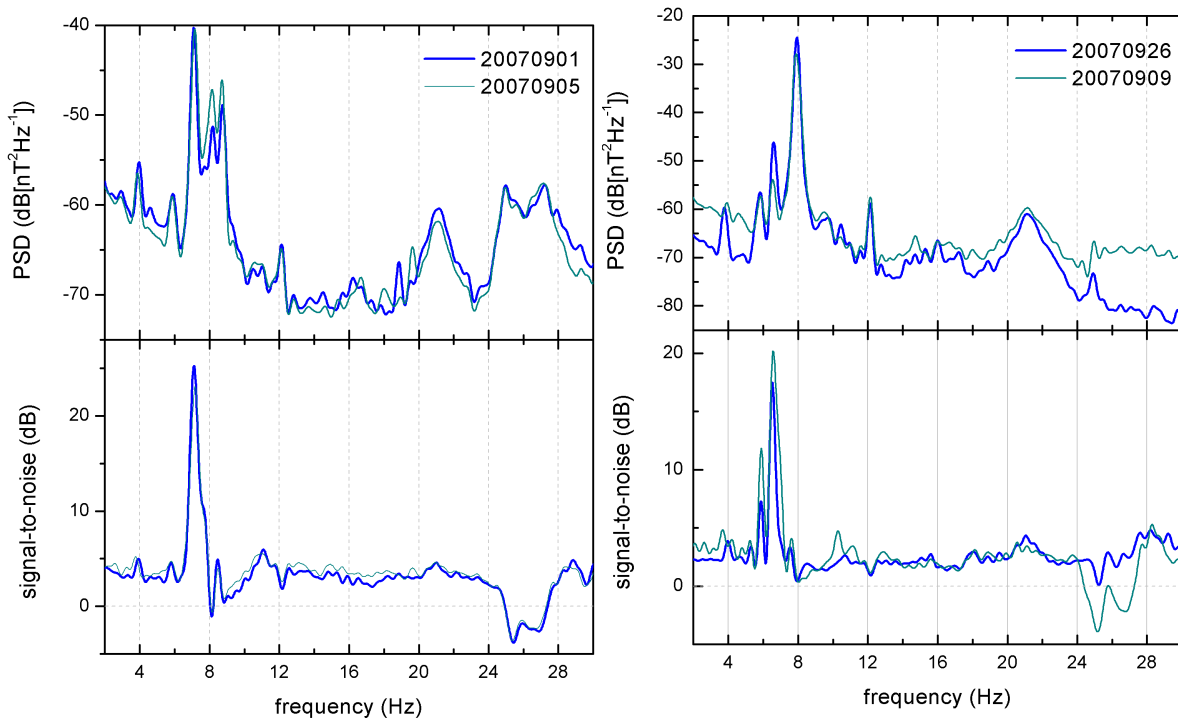


Figure 7.9: Comparative representation of bandpass filtered raw magnetic signal with the of the variation inclination of the signal on (a) day 1 and (b) day 2 sampled at 13:36 UT for 24 min



(a) regime 1, *day1* and *day2* sampled at the daily maximum 1448 UT for 1 hour

(b) regime 2, *day1* and *day2* sampled at the daily maximum 1336 UT for 1 hour

Figure 7.10: Signal-to-noise ratios of geomagnetic signal in two regimes, regime 1 and 2

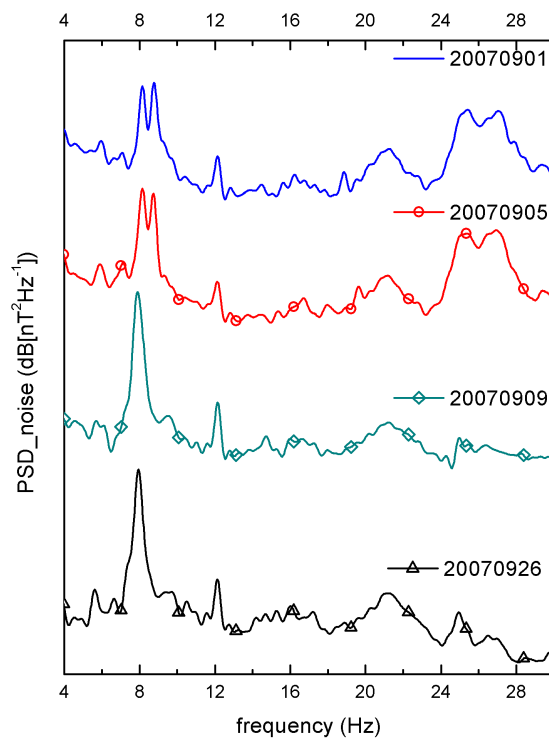


Figure 7.11: Spectra of the incoherent magnetic signals on four quiet days of September 2007

Chapter 8

Correlation of SQUID Datasets in LSBB and HERMANUS with FG and ICM Networks

8.1 Introduction to Dataset Correlation

The MARMOTS network was set to monitor the geomagnetic field at a higher level of sensitivity than the ordinary magnetometers described in Section 5.5. Here, we present an attempt to correlate SQUID with FGM datasets in the time domain, a spectral correlation of SQUID and induction coil magnetometer (ICM) datasets and a correlation between HSQH and [SQUID]². The data are collected from the following networks: MARMOTS for SQUID datasets, *Intermagnet* for fluxgate magnetometers datasets and the CARISMA for ICM data. Finally, a correlation between the two SQUID datasets will be established. A map in Fig. 8.1 shows the distribution of stations around the World.

The [SQUID]² is set in the mid-northern hemisphere in an underground bunker with a very quiet background noise, whereas the HSQH is set in the southern equatorial region, and is installed in an open environment where it detects the full ambient field. The FGMs are located in geographical proximity to the SQUID sites. The 3 European *Intermagnet* sites are less than 500 km radius from the LSBB. In the Southern Hemisphere, Hartebeesthoek station is also in close proximity to Hermanus in comparison to the size of the planet (~ 900 km). The CARISMA stations are high latitude stations in the Arctic region. This is a considerable advantage in monitoring SR because the frequency is not affected by the SOD change from the equatorial thunderstorm hotspots. Moreover, close to polar positions the amplitude of the resonant \mathbf{H} is maximal (antinodal position) as demonstrated in Section 4.3.3. Geomagnetic coordinates for the different stations are gathered in Table 8.1.

As the MARMOTS project is at an early stage, the HSQH system was not fully functional and only two SQUID channels were in use, the \mathcal{H} and the \mathcal{Z} axes. Moreover due to the relatively high

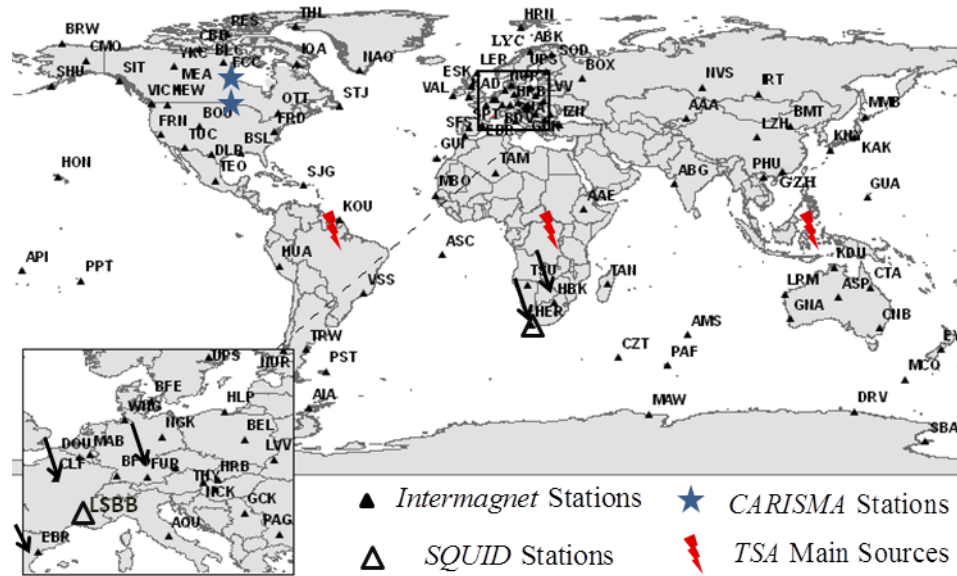


Figure 8.1: Geographical location of the different magnetometer sites that will be used for time correlation. The *Intermagnet* together with SQUID network are represented. The arrows indicate the position of the *Intermagnet* sites considered for the time correlation. The flashes indicate the position of the maximal Thunderstorm activity (TSA). Adapted from [18]

Table 8.1: Names, locations and geodetic coordinates of different magnetic stations in our study.

Magnetometer type	Site	Location, Country	Latitude (°)	Longitude(°)
FGM	CLF	Chambon-la-Forêt, France	48.0	2.3
	EBR	Ebro , Spain	40.82	0.493
	FUR	Furstenfeldenbruck, Germany	48.2	11.3
	HBK	Hartebeetshoek, South Africa	-25.9	27.7
	HER	Hermanus, South Africa	-34.4	19.2
ICM	MSTK	Ministik Lake, Canada	53.3	247
	THRF	Thief River Falls, USA	48.0	263.6
SQUID	HER	Hermanus, South Africa	-34.4	19.2
	LSBB	Rustrel, France	43.92	5.48

noise rejection at Hermanus, the resonance peaks appear in short-lived intense bursts overcoming the noise floor for few minutes. This brings a halt to the possibility of a long-term correlation of the SQUID signals.

8.2 Time Correlation SQUID-FGM Datasets

Time correlation between SQUID and FGM stations is done for datasets of the year 2013 when the HSQH was fully operational. Fig. 8.2 shows a correlation between magnetic datasets obtained on 2013 – 01 – 25 and 2013 – 01 – 26, that we call *day1* and *day2* for convenience. On *day1* a daily decrease in the \mathcal{H} field can be observed in HBK, HER and HSQH component, with a peak around 0800 UT. There is no significant decrease in \mathcal{H} for other stations. A sudden storm commencement at 16 : 30 UT announces the onset of the substorm that lasts few days. It is a minor substorm with $Dst > -50$ nT and $Kp < 4$. On *day2* of the substorm, the Dst decrease in field disappear and all the datasets show a high correlation. These datasets are sampled at 1 minute, hence a maximum frequency content of 8 mHz. This may indicate that frequencies in this range are highly correlated during storm time on a global scale. This aspect has also been demonstrated by Phiri [16] and Matladi [32].

In this regard, some considerations will be taken into account for the geomagnetic weather conditions for our measurements: Disturbance caused by transient ionisation or due to solar X-rays or solar proton emissions absorbed in high latitude ionosphere may modify the conductivity profile of the E-I cavity and consequently cause a slight increase or decrease of the EM resonance properties of the cavity. Solar X-ray bursts cause ionisation at high altitudes between 60 – 70 km without varying the conductivity height profile thus increasing the frequency of the first SR by few fractions of Hz whereas solar proton events generally decrease the lower ionospheric layer to 30 – 40 km, reducing therefore the resonant properties of the cavity [102].

In this chapter, it is therefore preferable to work in quiet magnetic conditions to measure the background SR undisturbed. Moreover, only the coherent component of \mathcal{H} spectra will be represented in this investigation in order to mitigate incoherent local noise. In this way, we make sure that the SR observed are global resonances.

8.3 Schumann Resonances

8.3.1 Quiet Day Spectra at LSBB

As indicated in Section 5.3.1, the Earth’s magnetic field and the magnetospheric dynamics are directly influenced by the Sun’s activity. Quietest magnetic periods are expected at the minimum of the solar activity. As shown in Fig. 5.4, the latest quiet period spans from the year 2007 to 2009. Pozzo di Borgo *et al* [144] identified quiet days in the same period of time that were used to characterise the background magnetic noise in the ULF range. In the year 2007 for instance, the date 2007 – 11 – 07 was selected as the quietest of the month according to the GFZ classification and LSBB seismic dataset investigation. The day shows an overall $Kp = 0$.

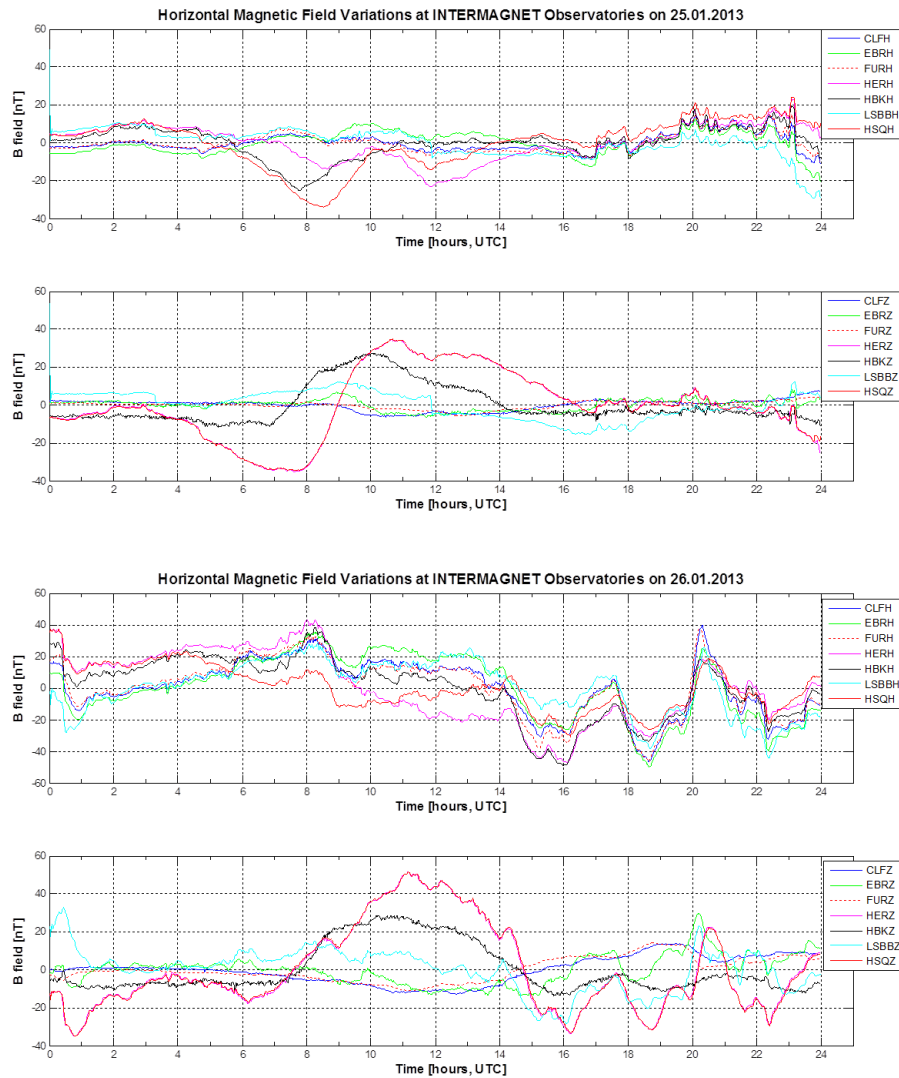


Figure 8.2: Magnetic time variation for H and Z datasets on 2013-01-25 and 2013-01-26 at *Intermagnet* stations CLF, EBR, FUR, HBK, HER and SQUID stations at LSBB and HSQH. At 2013-01-25 16:30 UTC is an onset of a substorm [$Dst < 50$ nT, $Kp < 4$].

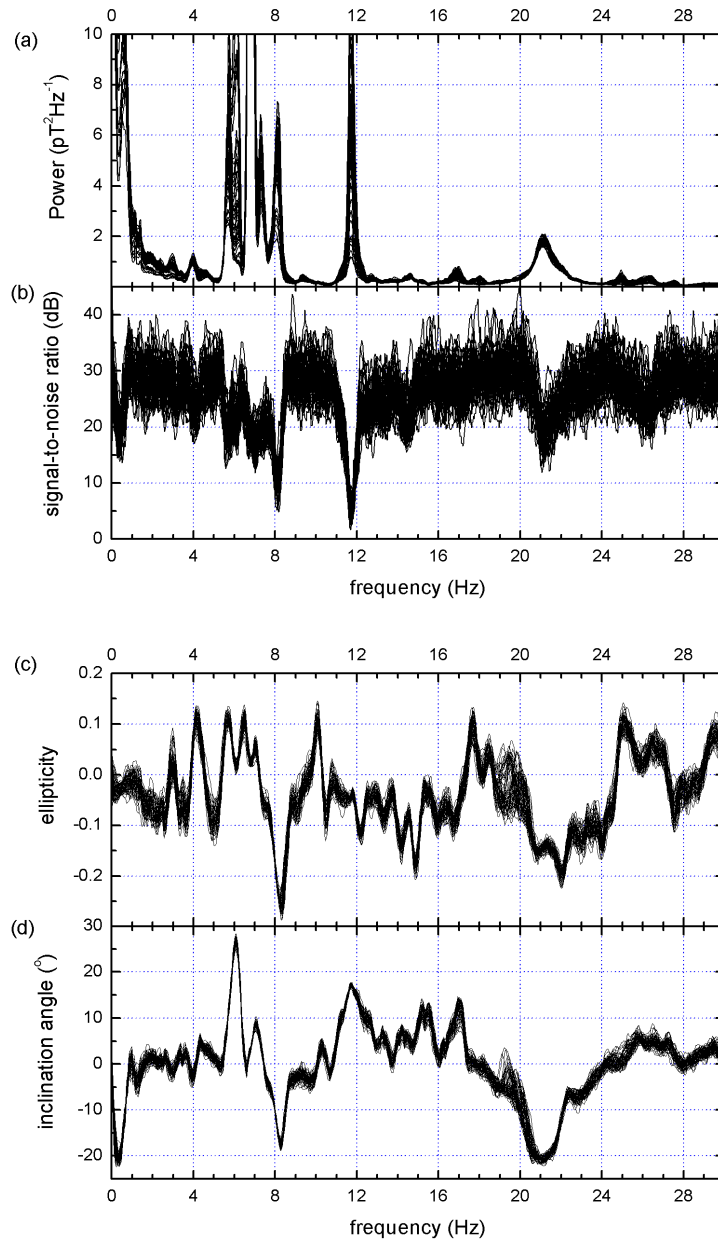


Figure 8.3: Spectral properties of \mathcal{H} obtained from 2007 – 11 – 07 datasets at LSBB. Each graph represents 24 min. of data. (a) polarised PSD (b) signal-to-noise power ratio (c) ellipticity and (d) the inclination of the wave polarisation ellipse. The nuances of black and grey are for visual clarity.

Table 8.2: Average peak characteristics as observed on a quiet day 2007 – 11 – 07 on \mathcal{H} SQUID² datasets.

f (Hz)	PSD($\text{pT}^2\text{Hz}^{-1}$)	Q	snr minimum (dB)	Experimental data in Fig.5.6 [4]		
				f_n	A_n ($\text{pT}^2\text{Hz}^{-1}$)	Q
6	12	5.4	20	7.95	1	3.63
6.8	200	38	16			
8	5.7	18	10			
12	11.7	40	11	14.06	0.36	4.01
14.57	0.3	5.2	5			
21.23	2.20	15.7	14	20.41	0.16	5.38

The same data is used to visualise a quiet ELF spectrum in the Hz range. Fig. 8.3 shows the [SQUID]² \mathcal{H} spectra stacked together. Each graph corresponds to 24 minutes of time data sampled at 8 ms, on which the Welch’s method and Fourier transform are applied as described in Section 6.5.5. The PSD is presented along polarisation properties of the \mathcal{H} wave. In Fig. 8.3a, the average peak power in the vicinity of the first SR is: 6 Hz at $\sim 12 \text{ pT}^2/\text{Hz}$, 7 Hz at $\sim 200 \text{ pT}^2/\text{Hz}$ and 8 Hz at $\sim 6 \text{ pT}^2/\text{Hz}$, which is way above the experimental PSD at the first SR \mathcal{H} component ($\sim 1 \text{ pT}^2/\text{Hz}$ [4, 92]) in quiet magnetospheric conditions. Moreover, the peaks show very high Q-factors for SR which are not consistent with the E-I waveguide low Q properties in Table 8.2.

Fig. 8.3b shows the signal-to-noise ratio spectrum for \mathcal{H} as described in Section 7.4. The parts where the incoherent noise component predominates are indicated by a dip in the snr spectrum. The peak frequencies around 6, 7, 8, 12, 15 and 20 Hz are affected. The decoherence can have two significances: Either the signals are local or the signals originate from an incoherent source and do not form a global resonance [19, 86, 104]. An example of the local decoherence is the 50 – Hz that was previously shown in Fig. 6.8. Its peak power is a few orders of magnitude higher than the background signal. However, because it is a local signal to the LSBB electrical circuitry, in the signal-to-noise spectra it appears as noise component as shown in Fig. 8.4 with a minimal snr amplitude. Another explanation would arise from the thunderstorm random generation process: Out-of-phase lightning strokes occurring within TSA hotspots or strokes randomly scattered all over the world. [13].

In this case, taking into consideration the sharpness of the peaks and the high Q-factor values displayed in Table 8.2, the peaks at 6, 7, 8, 12, 15 and 20 Hz are clearly modulated by local noise. In an internal report to the LSBB in 2010, it was found that while the [SQUID]² was operated in low noise mode (sensitivity = 1.66 nT/V), a ventilation unit in the capsule caused peaks of noise as high as $30 \text{ pT}/\sqrt{\text{Hz}}$ at 10.3 Hz all the 3 [SQUID]² magnetic components [145]. However, the specific data of the experiment could not be retrieved on the LSBB server in order to analyse them using the polarisation matrix method.

In Section 7.3, the polarisation properties indicate a change in the polarity of the \mathcal{H} wave across the first SR. Ellipticity reaches an extremum value ($el = -0.3$) at 8.3 Hz which is typical of the elliptical polarisation of the SR as shown in Fig. 8.3c.

A comparison between the [SQUID]² and experimental data from a polar station are presented in Table 8.2. Considering the power spectral density and Q factor correlation, the two resonances that are experimentally close to SRs are at 14.7 Hz and 21.3 Hz for $n = 2$ and 3 respectively.

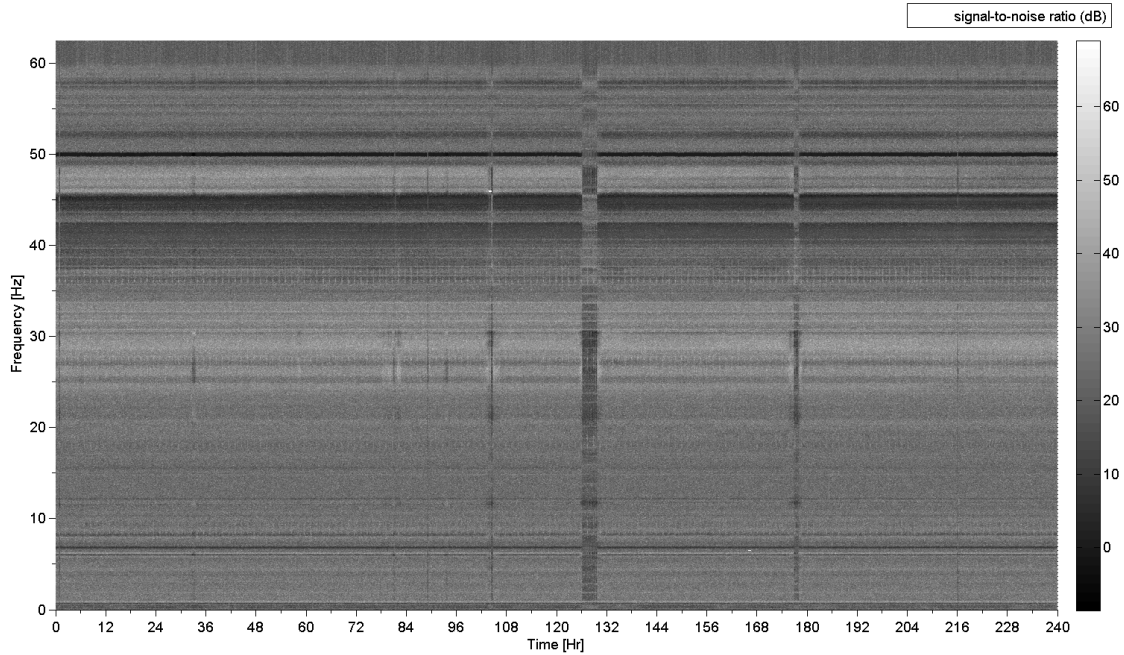


Figure 8.4: Ten day [SQUID]² signal-to-noise power ratio from 2007 – 11 – 01 to 2007 – 11 – 10 encompassing the quietest days of the same month .

Despite the decoherence present in the vicinity of the first resonance frequency, polarisation spectra show ellipticity extrema at 8, 14.5, and 21 Hz. The significance of these extrema is going to be investigated with a study of the correlation between [SQUID]² data and the high latitude ICM.

8.3.2 ELF SQUID-ICM Correlation

In the domain of ELF propagation in the E-I cavity, the measure of the coherence may determine whether a resonant signal in a cavity is global or local. The use of the coherence matrix in Chapter 7 has demonstrated the fact that the signal could be decomposed into its coherent and non-coherent components. The coherent resonant signal measured at a site would hence bear the global resonant signature. To prove the presence of a global signal component in LSBB's [SQUID]² datasets, ICM datasets from the CARISMA network are used and their polarisation properties are compared. The CARISMA datasets are measured by high permeability ICMs located in high latitude region ($\sim 30^\circ$ from the geomagnetic pole). They are sampled on site at 20 Hz thus display only the first SR. Two stations distant of ~ 1200 km in longitude are considered: *Thief River Falls* THRF and *Ministik Lake* MSTK shown in Table 8.1.

ICM Spectral Analysis

A quiet day, 2008 – 08 – 21 is selected for the analysis with overall $Kp < 1$. We start by analysing CARISMA spectral power and polarisation using techniques described in Chapters 6 and 6. Fig. 8.5 shows the spectra of ICM datasets at MSTK and THRF. Except the signals obtained between 12 – 1800 UT, all the plots display low-Q type of resonance peaked in close vicinity of 8 Hz. The

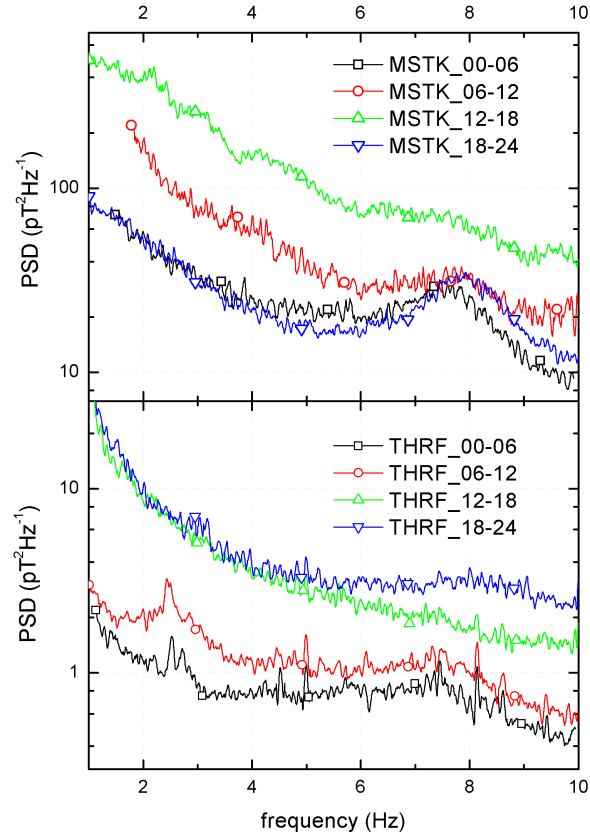


Figure 8.5: Cumulated power densities of \mathcal{H} spectra on 2008 – 08 – 21 obtained at CARISMA stations.

power of the resonances are displayed in Table 8.3. The peak power of resonances in MSTK is considerably larger than that at THRF that might be due to $1/f$ noise in the signal. However, the proximity to the polar antinodal position owed to equatorial predominant TSA excitation may also play a role in the amplification of the SR signal at MSTK.

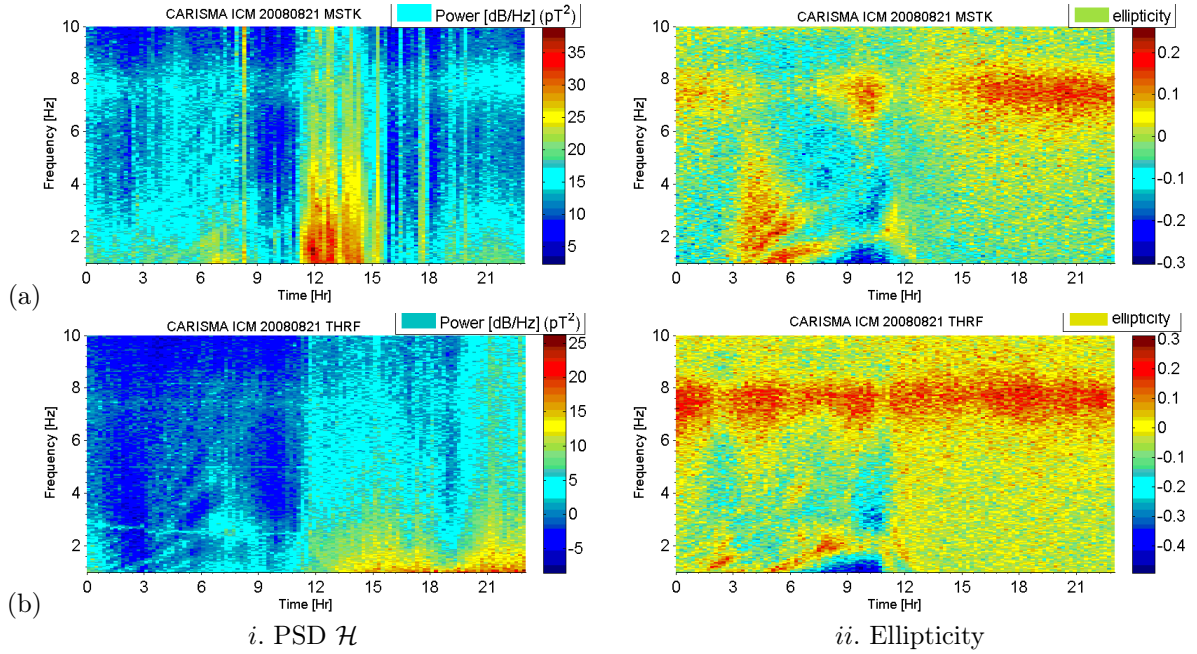
ICM Polarisation Analysis

The study of polarisation of the \mathcal{H} spectra allows us to ascertain the presence of SR in the ICM datasets. As shown in Chapter 7, ground detected SR waves in the Earth-ionosphere cavity are elliptically polarised. The measure of ellipticity is the measure of eccentricity of the horizontal magnetic wave components. Experimentally, it was found that considering that most of the TSA are equatorial excitations [28, 100], northern high latitude detectors will display LHP ($el > 0$) at resonance frequencies. Moreover, previous research confirms a high correlation between the power spectrum and ellipticity resonance patterns observed [19, 86, 104, 143].

Fig. 8.6 shows a comparative set of spectrograms of the horizontal magnetic component power and ellipticity at the two CARISMA stations: The power variation at MSTK (Fig. 8.6a(i)) shows hazy patch of resonance around 8 Hz shown as spectra in the top panel of Fig. 8.5. The presence of the first SR is confirmed in the ellipticity spectrogram in Fig. 8.6a(ii), where it is shown to repeat the

Table 8.3: Resonance parameters of spectra shown in Fig. 8.5. MSTK (top panel) and THRF (bottom).

UT time (hr)	f (Hz)	Q	PSD ($\text{pT}^2\text{Hz}^{-1}$)
00 – 0600	7.45	2.26	37.5
06 – 1200	7.56	2.24	23
12 – 1800	7.69	-	-
18 – 2400	7.37	4.22	28
00 – 0600	7.46	2.2	0.766
06 – 1200	7.55	1.8	1.21
12 – 1800	7.61	-	1.8
18 – 2400	7.59	4.22	8.16


Figure 8.6: Power density and ellipticity daily variation spectrograms of \mathcal{H} at (a) MSTK and (b) THRF, on 2008 – 08 – 21.

pattern of the power of \mathcal{H} . At THRF, Fig. 8.6b(ii) shows a clear ellipticity peak across the first SR, despite the fact that the resonance cannot be clearly seen in the power spectrogram Fig. 8.6b(i).

We notice in the power spectra that the $1/f$ noise is predominant in the second half of the spectrum, say from 1200 UT onwards. Not only global TSA distribution and the distance from the sources influence SR spectra, but also the local time variations. The local time t_L (hr) is related to universal time (UT) as follows [13, 19]:

$$t_L = t_U + 12 \frac{\lambda_i}{\pi} \quad (8.1)$$

where λ_i is the geodetic longitude in radians (positive eastwards). Hence, at CARISMA stations, $t_L = t_U - 7 : 32 : 00$ at MSTK and $t_L = t_U - 6 : 28 : 00$ at THRF. Therefore, the sunrise time 11 : 21 : 00 UT and 11 : 32 : 00 UT for MSTK and THRF respectively [146]¹. Local dawn coincides

¹The sunrise times and dates are calculated with the help of an online software.

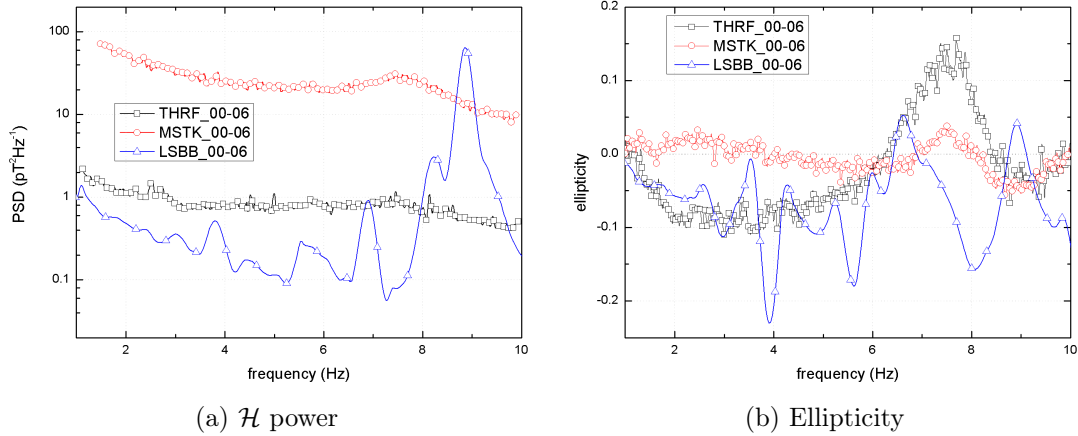


Figure 8.7: Comparative graphs between CARISMA and [SQUID]² \mathcal{H} power and ellipticity spectra on 2008 – 08 – 21.

rather well with the surge of both of the $1/f$ noise observed in both power spectra. Solar radiation ionises and lowers the D-ionospheric boundary on the dayside, and on the nightside, the height is maintained high. The resultant discontinuity is referred to as *terminator*. Model calculations show that the disturbance created by the day-night asymmetry causes $\pm 6\%$ deviation from field amplitude obtained from the uniform cavity model for the first SR [147].

At high latitudes, ellipticity spectra show a local, transversal resonance signals that occur in the nighttime ionosphere in quiet magnetic conditions. The ionospheric Alfvé resonances (IAR) appear as a succession of peaks in \mathcal{H} spectra that are observed at few Hz, below the first SR. The resonance originates from waves trapped in the ionospheric plasma, due to the fact that the lower boundary is sharp at night (small losses occur in time). The magnetospheric boundary is also distinct because of the absence of solar radiation. As dawn approaches, the ion content of the ionosphere increases which in turn modifies the resonance frequency until sunset when suddenly the IAR vanish [13]. At CARISMA stations, the IAR are observed at both stations on 2008 – 08 – 21. The resonances are very clearly observed in the polarisation spectrograms in Fig. 8.6a(i) and 8.6a(ii), as a succession of LHP and RHP chirp signals. MSTK shows more resonances, probably due to the station proximity to the polar regions. Dawn corresponds to the time the IAR signals wane.

Notice that the IAR are characteristic of quiet ionospheric conditions because they appear when the boundaries of the ionospheric layer are not disturbed, mostly at high latitudes. They always appear in polarisation spectra along with SR due to their strong elliptical polarisation. Their peak frequencies range from 0.2 – 8 Hz [13].

[SQUID]²-ICM Correlation

Fig. 8.7 shows the correlation between [SQUID]² spectra and ICM datasets on 2008 – 08 – 21. The data from THRF and MSTK are compared to those from LSBB for early hours of the day when the magnetospheric conditions are the quietest. During these early hours of the day, most of the active thunderstorms are located in South-East Asia [103].

The power graphs of \mathcal{H} show good correlation between MSTK and THRF spectra despite the discrepancy in amplitude in Fig. 8.7a. Around the first SR, CARISMA spectra display a positive LHP resonance (described earlier in Section 8.3.2) as shown in Fig. 8.7a and the LSBB datasets show sharp power peak between 8 – 10 Hz. The correlation between CARISMA and LSBB is poor. In Fig. 8.7b, the LSBB ellipticity spectra show a typical variation described in Section 7.3; between 6 – 9 Hz, the polarity of the wave switches from LHP to RHP at resonance. The extremum of the ellipticity in the RHP range is located in the vicinity of 8 Hz. At this level, we cannot find any correlation between [SQUID]² and ICM spectra in terms of the power spectra, worse is the fact that the peaks of ellipticity are of opposite sign.

Let us attempt to establish a correlation between the two sites by tracking the variation of frequencies of ellipticity extrema as a function of time in the spectra of CARISMA and LSBB, close to the first SR. The diurnal frequency variation can be described as

$$df_1(t_U) = f_1(t_U) - f_{1,\min} \quad (8.2)$$

where f_1 is the first SR peak frequency and $f_{1,\min}$ is its daily minimum. $f_{1,\min} = 7.43$ Hz at MSTK and THRF and 7.85 Hz at LSBB on 2008 – 08 – 21.

Fig. 8.8 shows the diurnal variation of first SR frequency of the horizontal magnetic field in the E-I cavity. A correlation coefficient $r > 30\%$ between CARISMA and LSBB datasets is observed despite ~ 7200 km longitudinal distance between THRF and LSBB. The pattern of the graphs is a double bumped curve with a minimum around 1200 UT. The daily maximum deviation of the peak frequency observed for MSTK and THRF is 0.13 Hz and 0.15 Hz for LSBB dataset.

As demonstrated in Section 4.3.3, the peak frequency of the first SR is strongly dependent upon the Source-Observer distance (f_n increases with SOD in the first quadrant). The daily variation of the first SR peak frequency repeats itself in time and is referred to as *diurnal harmonics* in the literature [103, 148, 149]. Two main types of harmonics may influence the daily variation of SR: 24-hour harmonics originating from the thunderstorm periodic procession around the globe and day-night asymmetry, 12-hour harmonics that might be due to atmospheric tidal waves moving from the sun-heated dayside to the nightside of the ionosphere [149].

8.3.3 SQUID Dataset Correlation in LSBB and Hermanus

We present here data of SQUID spectra obtained simultaneously with [SQUID]² and HSQH systems. The first attempt will correlate the sudden bursts observed in the Hermanus spectra with corresponding spectra in LSBB. Fig. 8.10 shows such signals from February 2013 datasets. The main striking dissimilarity is the difference in the noise floor. HSQH shows noise level of 2 pT²/Hz way above the [SQUID]² at 0.02 pT/Hz at 10 Hz. From these short-lived resonances at Hermanus, properties of the spectra could be derived but not the polarisation properties, due to the fact that at Hermanus only the \mathcal{H} and \mathcal{Z} components are recorded.

On the other hand, a comparison between spectra obtained in Hermanus and LSBB will be done for few hour long datasets. Fig. shows a such spectra taken on 2013 – 04 – 20 from 06 – 0800 UT. The

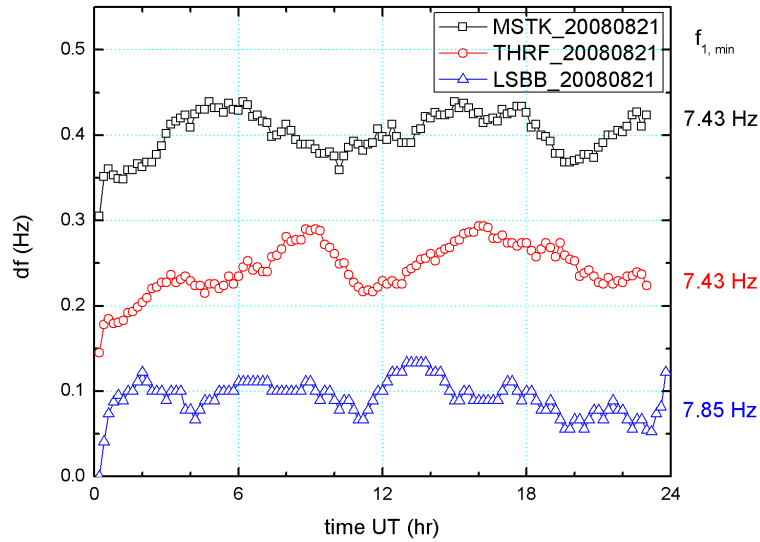


Figure 8.8: Stacked representation of diurnal variation of SR peak frequency of the \mathcal{H} component at MSTK, THRF and LSBB on 2008 – 08 – 21. df represents the difference between the peak frequency at each sampled spectrum and the minimum frequency of the first SR measured in the day

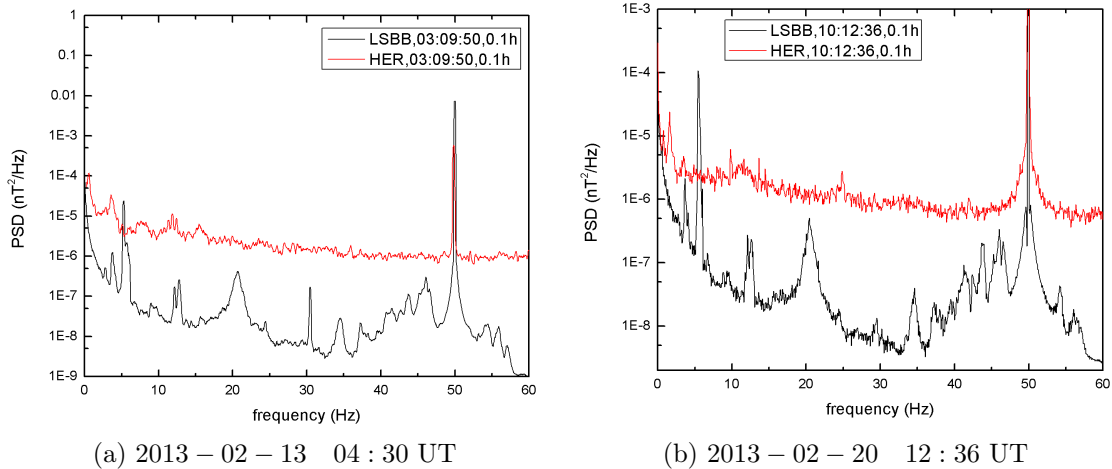


Figure 8.9: \mathcal{H} SQUID data taken at HER and at LSBB taken in the same instant. The durations are indicated in the graph windows in hours.

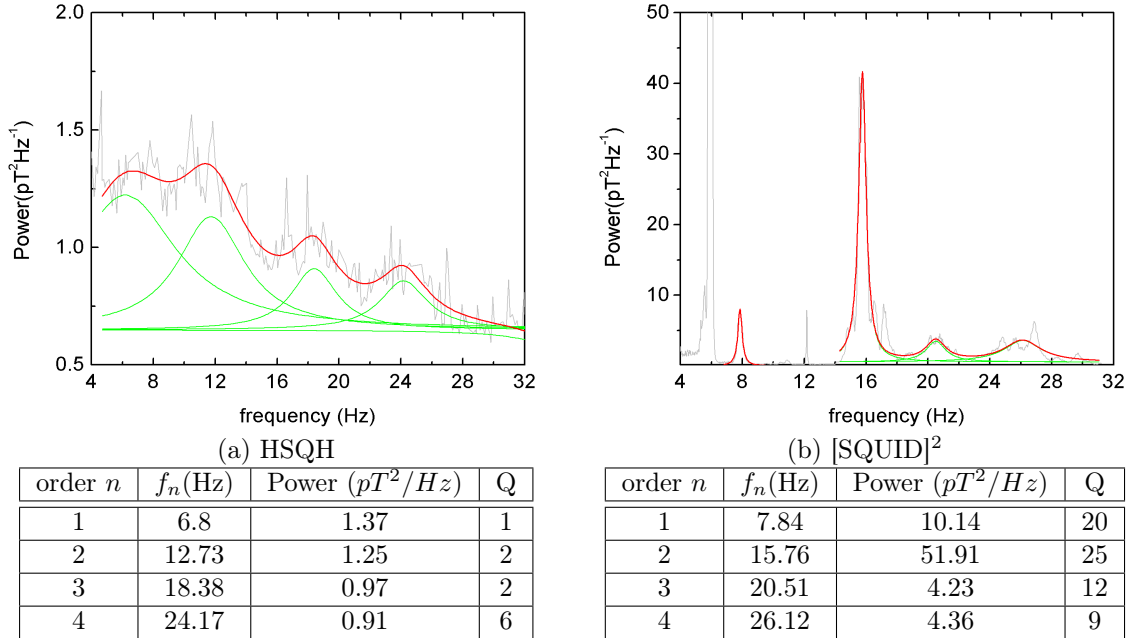


Figure 8.10: \mathcal{H} SQUID data taken simultaneously at Hermanus and LSBB on 2013 – 04 – 20 06 – 0800 UT. The durations are indicated in the labels.

HSQH shows wideband spectra similar to those observed in Section 4.3.3 and the $[\text{SQUID}]^2$ shows sharp spectra with Q factors reaching values of 20 in the first resonance.

So far, SRs Q factors in Hermanus are comparable with the literature despite a very low resonance frequency. The low frequency and the burst-like occurrence of the resonances in the HSQH spectra might be due to the fact that the HSQH is located in a near-field configuration: Hermanus is located in just 4 Mm from the most active thunderstorm centres source in Africa (the Congo basin) and at roughly 1 Mm from the Highveld TSA in South Africa. The Congo basin produces at the least 3 powerful lightning flashes per second all the time [28]².

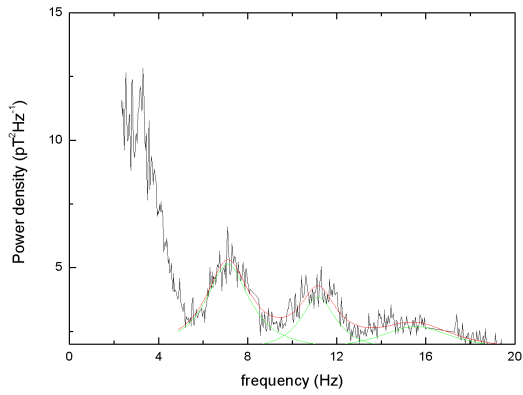
8.3.4 Few Characteristics of HSQH spectra in 2013

Fig. 8.11 shows the different spectra with HSQH \mathcal{H} obtained on some quiet days of the year 2013. The resonances observed are generally lower than the average.

8.4 Conclusion

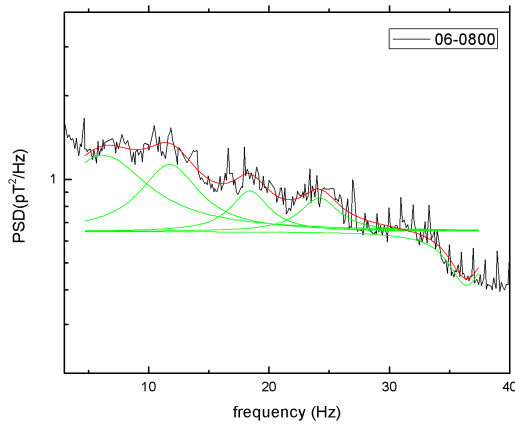
In this chapter, different methods were used to determine SR properties with SQUID and induction coil magnetometers. The polarisation method performs quite well for $[\text{SQUID}]^2$ and ICM data whose peaks are more or less hidden in local noise. The extrema of the ellipticity spectra in the vicinity of the first SR frequency allow us to obtain a curve of the daily frequency variation of the global resonance. Data from the distant magnetic stations in Northern-American Arctic region and

²The Congo basin boasts a minimum of 30 flashes per km² per year over 3 million km².



(a) 2013 – 02 – 27 1700 UT

$f(\text{Hz})$	Q	PSD(pT^2/Hz)
7.10	3	4.29
11.6	5.7	2.66
15.52	3.8	1.22



(b) 2013 – 04 – 20 0400 – 0600 UT

$f(\text{Hz})$	Q	PSD(pT^2/Hz)
6.2	1	0.72
11.7	2.2	0.605
18.4	5.1	0.122
24.2	6.5	0.26

Figure 8.11: Graph showing SRs observed in \mathcal{H}_c component in HSQH

mid-latitudes in Europe provide a considerably correlated frequency variation. From the CARISMA ICM spectra provide the Schumann resonance has a minimum frequency of 7.43 Hz and varies daily by +0.14 Hz. The [SQUID]² resonance varies from a minimum frequency of 7.85 Hz, with a daily variation of +0.15 Hz. A high correlation of the variations confirms that in the vicinity of 8 Hz at LSBB, we observe a global resonance.

The same correlated variation of the first SR frequency has been observed experimentally from widely separated magnetic stations in Europe and Eastern Russia [148] and has been attributed to ionospheric D-layer variations due to the day-night asymmetry. However, more rigorous studies of the SR frequency harmonics showed that the day-night asymmetry expresses itself as a 24-hour harmonic and that the 12-hour period could be attributed to tidal ionospheric phenomena [149].

The comparison between MARMOTS SQUID datasets, however, could not provide any tangible fact proving the correlation between the power spectra, because polarisation parameters could not be used for this effect; only two channels (\mathcal{H} and \mathcal{Z}) were used for this project. We cannot absolutely ascertain that what we saw in HSQH spectra was SR. However the resonances observed displayed the same range of amplitude and the same bandwidth as the background SR signal.

Chapter 9

General Discussion

9.1 Introduction

In this thesis, the analysis of geomagnetic ground signals detected using *dc* SQUID is done. The work is subdivided into three main tasks which consist in; studying the propagation in the Earth-ionosphere cavity using a numerical method, analysing the magnetic field with SQUID magnetometers, and establishing a correlation between SQUID datasets measured at great distances and between SQUID and ICM datasets. In this chapter, we base our discussion on 3 main axes: the originality of our method, the challenges encountered, results and shortcomings.

9.2 The Numerical Model

The FDTD has been extensively used for the Earth-ionosphere modelling. [66] developed a spherical coordinate based system that fits perfectly the E-I cavity. Simpson and Taflove [65] and Yang and Pasko's [72] models are based on spherical coordinates [66]. The method of Taflove [65] adapts the spheroidal shape of the Earth-ionosphere cavity by adopting the Holland design but also by fitting in trapezoidal meshes and pentagonal meshes at the poles. Yang and Pasko [72] use Holland's layout and use three kinds of ionospheric profiles to measure the properties of the resonances in the cavity.

Our model proposes a basic hexahedral Yee's mesh and uses it to measure the propagation in the 3D cavity. The main advantage of the Yee's rectangular mesh is that it minimises numerical dispersion and is quite easy to implement [61]. The use of a stratified medium is also another feature that was used, and the Q-burst type of excitation was chosen because it provides an impulse response for the whole system.

The FDTD model of the entire Earth magnetic field is particularly large, first because of the size of the layout itself and because of hexahedral lattices that have to be small enough to mesh the spherical cavity. The size of the simulation, however, was a challenge for our simulation and the mesh wasn't fine enough because of computational limitations. As a consequence of this, the mesh

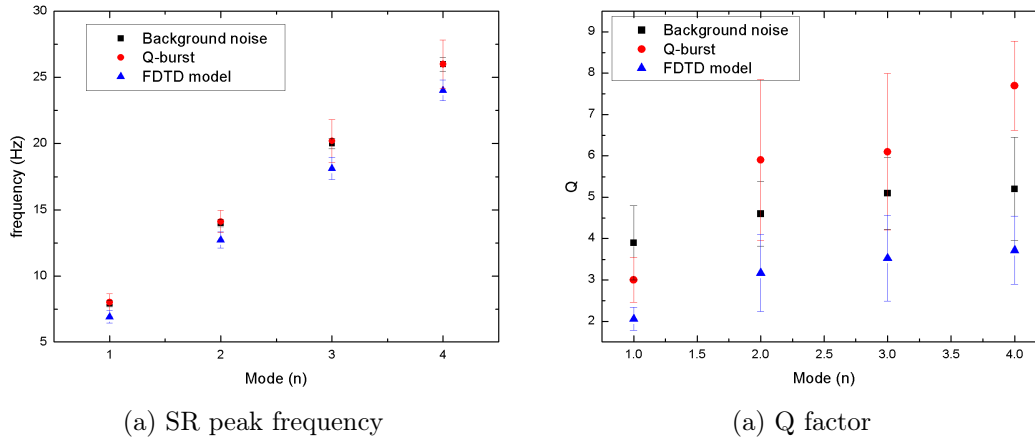


Figure 9.1: Comparison between SR long-term resonance parameters from [19] with FDTD data.

size was not fine enough and the results obtained from the model showed characteristics of a highly-damped cavity. Provided that one had a tight mesh around the spherical surfaces, the hexahedral mesh yields very good results.

A comparative graph of well-established long-term experimental data [19] with our FDTD model data is shown in Fig. 9.1. Note that the resonance parameters obtained with the FDTD are just below all the values obtained with experiments. However, we shouldn't lose focus on the achievement of this part; the initial research objective has been fulfilled because wave attenuation in the cavity is linear and the SR in the cavity has been observed and it has been accounted for.

Nonlinear effects could have been included in the model if we could get computational capabilities that should allow computation of wave propagation in ionospheric magnetised plasma. Magnetised plasma is a system of ionised gas in which the field is frozen-in; in a kind of equilibrium state where ions in the plasma strengthen the magnetic field and the latter, in turn, maintains the ions in rotation around its lines of force. The medium is anisotropic for EM propagation. In the E-I cavity, ionospheric plasma plays a considerable role in the polarisation of ELF detected on the ground [19].

9.3 Polarisation Analysis

The method of polarisation analysis is extensively used in astronomy, in radio science and in optics in order to resolve near-field from far-field patterns in a wavefield. In the E-I resonant cavity, the method is of utmost importance in order to distinguish local from global resonance EM signature, especially because the random generation process and mutual interference of the E-I waves in the cavity. Incoherent (out-of-phase) ELF signals have the same spectral signatures as global resonance signals (in-phase amongst them). Therefore, we devised a method to resolve these components of the same magnetic signal by studying the cross-correlation and self-correlation of the intensity of the horizontal magnetic components.

The outputs of the method are quite considerable as they allow us to separate the coherent to the incoherent magnetic signal, to determine the phase difference in the horizontal magnetic wavefront,

and also to determine the polarisation and angle of arrival of the magnetic wave at the measuring site. In this part of the thesis, only one site could provide the 2 horizontal channels and unfortunately there couldn't be sufficient correlation analysis done between the SQUID datasets.

9.4 SQUID signal correlation

The correlation of SQUID magnetometers distant of some 10,000 km was one of the objectives, however, the correlation could not be established. In this part, we rather establish a correlation between [SQUID]² datasets and CARISMA ICM network at the first SR.

The ICM spectra do not display any similarity in term of power density with [SQUID]² datasets but an analysis of the polarisation provides some similarity in the variation of the first SR. The correlation established for quiet datasets diurnal frequency variation leads us to consider that the SR might be not clearly visible in the LSBB spectra but the polarisation properties help us to unveil hidden properties not necessarily obviously distinguishable in the spectra. A proof of the prowess of the coherence matrix method is that the Ionospheric Alfvén resonances (IAR) that are clearly distinct in the polarisation spectra are barely visible in power spectra. This leads us to reaffirm once again the significance of polarisation properties study for SR.

The challenge that we faced in this part, the polarisation study put aside, was that the peak frequency tracking that allowed us to connect datasets at LSBB and CARISMA variations cannot be done for LSBB and Hermanus SQUID datasets because HSQH shows a high level of noise and that the only detectable peaks are observed with short-lived bursts that last few minutes. From these bursts, we could extract some spectra. Despite the resonance properties which are close to those observed in the background SR data, we do not have any ultimate proof that the spectra observed at Hermanus are Schumann resonances.

9.5 Conclusion

Polarisation parameters provide an ultimate tool for detecting SR. However, the complexity of the SR polarisation pattern is not yet fully understood. We know that in Northern hemisphere, far from equatorial sources the first SR ellipticity is LHP and is a positive maximum in polarisation spectra [19, 86, 104]. From variations of the positions of this peak as the time of day varies, the resonance frequency can be tracked as a function of time.

Previous research has shown that one of the reasons that low-latitude stations in the E-I cavity display a phase shift across its first resonance particularly is the magnetised plasma of the ionosphere, which acts as an anisotropic medium. One of the consequences of this phenomenon is the deflection of the electric field over distance. This has a tremendous consequence on the propagation in the E-I cavity as the electromagnetic wave, even from a single powerful source, is forced to rotate in time. Unfortunately, we could not make a full FDTD model to examine this aspect.

Chapter 10

General Conclusion and Recommendations

The Schumann resonances in the Earth-ionospheric cavity have been investigated using modelling and experimental methods. The SQUID offers many advantages regarding the sensitivity and the dynamic range, but the ultrasensitivity feature comes with issues of a high level of unwanted noise that couples into the detector instead of the wanted signal. A method based on the coherence of the magnetic wave is developed for the horizontal magnetic field and allows one to separate the noisy part from the useful signal. On the other hand, the method allows one to evaluate the polarisation properties induced to an ELF electromagnetic wave by the dispersive medium in which it propagates. The coherence method, when applied to inductance coil magnetometers and SQUIDs, yield a better resolution of the signal from surrounding noise. [SQUID]² elliptical properties are relatively well correlated with CARISMA datasets, and it allows resolving the global signal from the local noise. A globally correlated variation can be observed in ICM and SQUID datasets at the first Schumann resonance.

The simulation of the uniform Earth-Ionosphere cavity with 3D FDTD provides a good approximation of the propagation of the EM wave in a lossy homogeneous cavity. The latter shows a slightly higher attenuation rate of the electromagnetic waves which might be attributed to numerical dispersion in the simulated cavity. The resonant response of the E-I cavity to an EM impulse is observed and the Schumann resonance properties in the cavity are studied. The variations of peak amplitude, SR frequency and Q - factor variation are found to be in agreement with the literature [4,19,92,100]. The advantage of this FDTD model is the fact that despite its simplicity, it provides fairly accurate SR prediction (90% accuracy in the first SR) and allows one to obtain a clear picture of the propagation of EM waves triggered by a discrete pulse and the resonance characteristics of the Earth-ionosphere cavity.

A way forward to complete this study would be to acquire more powerful computational capabilities and incorporate the entire ionospheric magnetised plasma model with fine meshing, so as to obtain the behaviour of the field in real-time and in a medium that is highly dynamic. In terms of measurements, more standard magnetometers (such as the ICM) should be installed at the same

site with the SQUID system in order to establish a day-to-day correlation on site, in order to be able to differentiate the signal from noise locally. Long distance correlations between datasets should be done over a longer period of time so as to establish a pattern of correlation between SQUIDS.

Bibliography

- [1] W. Schumann, "Über die dämpfung der elektromagnetischen eigenschwingungen des systems erde-luft-ionosphäre," *Zeitschrift für Naturforschung A*, vol. 7, no. 3-4, pp. 250–252, 1952.
- [2] J. R. Wait, *Electromagnetic Waves in Stratified Media*. Pergamon Press, Headington, Oxford, 1962.
- [3] J. Clarke and A. I. Braginski, *The SQUID handbook*. Wiley Online Library, 2004.
- [4] S. Toledo-Redondo, A. Salinas, J. Portí, J. Morente, J. Fornieles, A. Méndez, J. Galindo-Zaldívar, A. Pedrera, A. Ruiz-Constán, and F. Anahnah, "Study of schumann resonances based on magnetotelluric records from the western mediterranean and antarctica," *Journal of Geophysical Research: Atmospheres (1984–2012)*, vol. 115, no. D22, 2010.
- [5] C. Greifinger and P. Greifinger, "Approximate method for determining elf eigenvalues in the earth-ionosphere waveguide," *Radio Science*, vol. 13, no. 5, pp. 831–837, 1978.
- [6] V. C. Mushtak and E. R. Williams, "Elf propagation parameters for uniform models of the earth–ionosphere waveguide," *Journal of atmospheric and solar-terrestrial physics*, vol. 64, no. 18, pp. 1989–2001, 2002.
- [7] C. Bruce and R. Golde, "The lightning discharge," *Electrical Engineers-Part II: Power Engineering, Journal of the Institution of*, vol. 88, no. 6, pp. 487–505, 1941.
- [8] M. Ishaq and D. L. Jones, "Method of obtaining radiowave propagation parameters for the earth–ionosphere duct at elf," *Electronics Letters*, vol. 13, no. 9, pp. 254–255, 1977.
- [9] D. R. Barraclough, "International geomagnetic reference field: the fourth generation," *Physics of the Earth and Planetary Interiors*, vol. 48, no. 3, pp. 279–292, 1987.
- [10] C. G. Constable and S. C. Constable, "Satellite magnetic field measurements: applications in studying the deep earth," *The State of the Planet: Frontiers and Challenges in Geophysics*, pp. 147–159, 2004.
- [11] S. W. D. Center, "The international sunspot number," *International Sunspot Number Monthly Bulletin and online catalogue*, 1991-2015. [Online]. Available: <http://www.sidc.be/silso/>
- [12] C. Russell, "The solar wind interaction with the earth's magnetosphere: a tutorial," *Plasma Science, IEEE Transactions on*, vol. 28, no. 6, pp. 1818–1830, 2000.

- [13] A. Nickolaenko and M. Hayakawa, *Schumann Resonance for Tyros*. Springer, 2014.
- [14] S. Tumanski, "Modern magnetic field sensors—a review," *Organ*, vol. 10, p. 13, 2013.
- [15] I. Mann, D. Milling, I. Rae, L. Ozeke, A. Kale, Z. Kale, K. Murphy, A. Parent, M. Usanova, D. Pahud *et al.*, "The upgraded carisma magnetometer array in the themis era," *Space Science Reviews*, vol. 141, no. 1-4, pp. 413–451, 2008.
- [16] T.-J. Phiri, "Correlation between squid and fluxgate magnetometer data for geomagnetic storms," Master's thesis, Stellenbosch: Stellenbosch University, 2013.
- [17] L. J. J. van Vuuren, "Design and test implementation of a global interconnected squid geomagnetometer network," Master's thesis, University of Stellenbosch, 2015.
- [18] Intermagnet. International real-time magnetometry. [Online]. Available: <http://intermagnet.org/index-eng.php>
- [19] A. P. Nickolaenko and M. Hayakawa, *Resonances in the Earth-ionosphere cavity*. Springer Science & Business Media, 2002, vol. 19.
- [20] W. Gilbert, *De magnete*. Courier Corporation, 1958.
- [21] J. J. Love, "Magnetic monitoring of earth and space," *Physics Today*, vol. 61, no. 2, p. 31, 2008.
- [22] J. K. Hargreaves, *The solar-terrestrial environment*. Cambridge Press, 1992.
- [23] M. Balsler and C. Wagner, "Observations of earth-ionosphere cavity resonances," *Nature*, vol. 188, no. 4751, pp. 638–641, 1960.
- [24] M. Balsler and C. A. Wagner, "Diurnal power variations of the earth-ionosphere cavity modes and their relationship to worldwide thunderstorm activity," *Journal of Geophysical Research*, vol. 67, no. 2, pp. 619–625, 1962.
- [25] P. H. Nelson, "Ionospheric perturbations and schumann resonance data." DTIC Document, Tech. Rep., 1967.
- [26] T. Madden and W. Thompson, "Low-frequency electromagnetic oscillations of the earth-ionosphere cavity," *Reviews of Geophysics*, vol. 3, no. 2, pp. 211–254, 1965.
- [27] E. R. Williams, "The schumann resonance: A global tropical thermometer," *Science*, vol. 256, no. 5060, p. 1184, 1992.
- [28] H. J. Christian, R. J. Blakeslee, D. J. Boccippio, W. L. Boeck, D. E. Buechler, K. T. Driscoll, S. J. Goodman, J. M. Hall, W. J. Koshak, D. M. Mach *et al.*, "Global frequency and distribution of lightning as observed from space by the optical transient detector," *Journal of Geophysical Research: Atmospheres (1984–2012)*, vol. 108, no. D1, pp. ACL–4, 2003.
- [29] V. A. Rakov and M. A. Uman, *Lightning: physics and effects*. Cambridge University Press, 2003.

- [30] C. Beggan. (2015) High-frequency magnetometers. British Geological Survey. [Online]. Available: www.geomag.bgs.ac.uk/research/inductioncoils.html
- [31] G. Waysand, P. Barroy, R. Blancon, S. Gaffet, C. Guilpin, J. Marfaing, E. Pozzo di Borgo, M. Pyée, M. Auguste, D. Boyer *et al.*, “Seismo-ionosphere detection by underground squid in low-noise environment in lsbb-rustrel, france,” *The European Physical Journal Applied Physics*, vol. 47, no. 01, p. 12705, 2009.
- [32] T.-K. Matladi, “Correlation between squid and fluxgate magnetometer data-sets for geomagnetic storms: Hermanus,” Master’s thesis, Stellenbosch: Stellenbosch University, 2014.
- [33] C. Kittel, *Introduction to solid state physics*, 8th ed. Wiley, 2005.
- [34] T. P. Orlando and K. A. Delin, *Foundations of applied superconductivity*. Addison-Wesley Reading, MA, 1991, vol. 224.
- [35] F. London, *Superfluids*. Wiley, New York, 1950, vol. 2.
- [36] B. S. Deaver Jr and W. M. Fairbank, “Experimental evidence for quantized flux in superconducting cylinders,” *Physical Review Letters*, vol. 7, no. 2, p. 43, 1961.
- [37] R. Doll and M. Näbauer, “Experimental proof of magnetic flux quantization in a superconducting ring,” *Physical Review Letters*, vol. 7, no. 2, p. 51, 1961.
- [38] J. Bardeen, “Theory of the meissner effect in superconductors,” *Physical Review*, vol. 97, no. 6, p. 1724, 1955.
- [39] L. N. Cooper, “Bound electron pairs in a degenerate fermi gas,” *Physical Review*, vol. 104, no. 4, p. 1189, 1956.
- [40] J. Bardeen, L. N. Cooper, and J. R. Schrieffer, “Microscopic theory of superconductivity,” *Physical Review*, vol. 106, no. 1, p. 162, 1957.
- [41] P. De Gennes, *Superconductivity of Metals and Alloys (Advanced Book Classics)*. Addison-Wesley Publ. Company Inc, 1999.
- [42] A. A. Abrikosov, “Magnetic properties of superconductors of the second group,” *Sov. Phys.-JETP (Engl. Transl.);(United States)*, vol. 5, no. 6, 1957.
- [43] B. D. Josephson, “Possible new effects in superconductive tunnelling,” *Physics letters*, vol. 1, no. 7, pp. 251–253, 1962.
- [44] O. Mukhanov, V. Semenov, and K. Likharev, “Ultimate performance of the rsfq logic circuits,” *Magnetics, IEEE Transactions on*, vol. 23, no. 2, pp. 759–762, 1987.
- [45] J. Rowell, “Magnetic field dependence of the josephson tunnel current,” *Physical Review Letters*, vol. 11, no. 5, p. 200, 1963.
- [46] C. D. Tesche and J. Clarke, “Dc squid: noise and optimization,” *Journal of Low Temperature Physics*, vol. 29, no. 3-4, pp. 301–331, 1977.

- [47] W. Buckel and R. Kleiner, *Superconductivity: Fundamentals and applications*. Wiley-VCH Verlag GmbH & Co. KGaA, 2004.
- [48] S. Henry, E. P. di Borgo, and A. Cavaillou, "Tracking geomagnetic fluctuations to picotesla accuracy using two superconducting quantum interference device vector magnetometers," *Review of Scientific Instruments*, vol. 84, no. 2, p. 024501, 2013.
- [49] A. Cho, "New u.s. rules on helium sales said to stifle competition," *Science*, July 2015. [Online]. Available: www.news.sciencemag.org/chemistry/2015/07
- [50] R. L. McPherron, "Magnetic pulsations: their sources and relation to solar wind and geomagnetic activity," *Surveys in Geophysics*, vol. 26, no. 5, pp. 545–592, 2005.
- [51] Y. L. Alpert, "Resonance nature of the magnetosphere," *Physics Reports*, vol. 339, no. 5, pp. 323–444, 2001.
- [52] P. V. Bliokh, A. P. Nicholaenko, and I. F. Fillipov, "Schumann resonances in the earth-ionosphere cavity," in *Stevenage, Herts., England, Peter Peregrinus, Ltd., (IEE Electromagnetic Waves Series. Volume 9), 1980. 175 p. Translation*, vol. 9, 1980.
- [53] C. Balanis, *Advanced Engineering Electromagnetics*. John Wiley & Sons, 1989.
- [54] J. Galejs, *Terrestrial Propagation of Long Electromagnetic Waves*. Pergamon, Oxford, U.K., 1972.
- [55] S. Errede, *EM Standing Waves in Resonant Cavities*, University of Illinois, 2015. [Online]. Available: www.hep.uiuc.edu/home/serrede/
- [56] A. Nickolaenko, G. Satori, B. Zieger, L. Rabinowicz, and I. Kudintseva, "Parameters of global thunderstorm activity deduced from the long-term schumann resonance records," *Journal of Atmospheric and Solar-Terrestrial Physics*, vol. 60, no. 3, pp. 387–399, 1998.
- [57] A. P. Nickolaenko, M. Hayakawa, I. G. Kudintseva, S. V. Myand, and L. M. Rabinowicz, "Elf sub-ionospheric pulse in time domain," *Geophysical research letters*, vol. 26, no. 7, pp. 999–1002, 1999.
- [58] D. D. Sentman, "Approximate schumann resonance parameters for a two-scale-height ionosphere," *Journal of Atmospheric and Terrestrial Physics*, vol. 52, no. 1, pp. 35–46, 1990.
- [59] K. S. Yee, "Numerical solution of initial boundary value problems involving maxwells equations in isotropic media," *IEEE Trans. Antennas Propag*, vol. 14, no. 3, pp. 302–307, 1966.
- [60] A. Taflove, "Application of the finite-difference time-domain method to sinusoidal steady-state electromagnetic-penetration problems," *Electromagnetic Compatibility, IEEE Transactions on*, no. 3, pp. 191–202, 1980.
- [61] A. Taflove and S. C. Hagness, *Computational electrodynamics*. Artech house, 2005.
- [62] A. Taflove, "A perspective on the 40-year history of fdtd computational electrodynamics," *Applied Computational Electromagnetics Society Journal*, vol. 22, no. 1, p. 1, 2007.

- [63] M. Thèvenot, J.-P. Bérenger, T. MonediÈre, and F. Jecko, "A fdtd scheme for the computation of vlf-lf propagation in the anisotropic earth-ionosphere waveguide," in *Annales des télécommunications*, vol. 54, no. 5-6. Springer, 1999, pp. 297–310.
- [64] S. Cummer, "Modeling electromagnetic propagation in the earth-ionosphere waveguide," *Antennas and Propagation, IEEE Transactions on*, vol. 48, no. 9, pp. 1420–1429, 2000.
- [65] J. J. Simpson and A. Taflove, "Three-dimensional fdtd modeling of impulsive elf propagation about the earth-sphere," *Antennas and Propagation, IEEE Transactions on*, vol. 52, no. 2, pp. 443–451, 2004.
- [66] R. Holland, "Threds: A finite-difference time-domain emp code in 3d spherical coordinates," *Nuclear Science, IEEE Transactions on*, vol. 30, no. 6, pp. 4592–4595, 1983.
- [67] J. J. Simpson and A. Taflove, "Electrokinetic effect of the loma prieta earthquake calculated by an entire-earth fdtd solution of maxwell's equations," *Geophysical research letters*, vol. 32, no. 9, 2005.
- [68] J. J. Simpson, R. P. Heikes, and A. Taflove, "Fdtd modeling of a novel elf radar for major oil deposits using a three-dimensional geodesic grid of the earth-ionosphere waveguide," *Antennas and Propagation, IEEE Transactions on*, vol. 54, no. 6, pp. 1734–1741, 2006.
- [69] J. J. Simpson and A. Taflove, "A novel elf radar for major oil deposits," *Geoscience and Remote Sensing Letters, IEEE*, vol. 3, no. 1, pp. 36–39, 2006.
- [70] —, "Elf radar system proposed for localized d-region ionospheric anomalies," *Geoscience and Remote Sensing Letters, IEEE*, vol. 3, no. 4, pp. 500–503, 2006.
- [71] T. Otsuyama, D. Sakuma, and M. Hayakawa, "Fdtd analysis of elf wave propagation and schumann resonances for a subionospheric waveguide model," *Radio Science*, vol. 38, no. 6, 2003.
- [72] H. Yang and V. P. Pasko, "Three-dimensional finite difference time domain modeling of the earth-ionosphere cavity resonances," *Geophysical research letters*, vol. 32, no. 3, 2005.
- [73] B. Engquist and A. Majda, "Absorbing boundary conditions for numerical simulation of waves," *Proceedings of the National Academy of Sciences*, vol. 74, no. 5, pp. 1765–1766, 1977.
- [74] G. Mur, "Absorbing boundary conditions for the finite-difference approximation of the time-domain electromagnetic-field equations," *Electromagnetic Compatibility, IEEE Transactions on*, no. 4, pp. 377–382, 1981.
- [75] J.-P. Bérenger, "A perfectly matched layer for the absorption of electromagnetic waves," *Journal of computational physics*, vol. 114, no. 2, pp. 185–200, 1994.
- [76] D. B. Davidson, *Computational electromagnetics for RF and microwave engineering*. Cambridge University Press, 2010.
- [77] S. Gedney and A. Taflove, "Perfectly matched layer absorbing boundary conditions," *Computational Electrodynamics: The Finite-Difference Time-Domain Method*, pp. 273–328, 2005.

- [78] D. S. Katz, E. T. Thiele, and A. Taflove, "Validation and extension to three dimensions of the berenger pml absorbing boundary condition for fd-td meshes," *Microwave and Guided Wave Letters, IEEE*, vol. 4, no. 8, pp. 268–270, 1994.
- [79] Z. S. Sacks, D. M. Kingsland, R. Lee, and J.-F. Lee, "A perfectly matched anisotropic absorber for use as an absorbing boundary condition," *Antennas and Propagation, IEEE Transactions on*, vol. 43, no. 12, pp. 1460–1463, 1995.
- [80] W. C. Chew and W. H. Weedon, "A 3d perfectly matched medium from modified maxwell's equations with stretched coordinates," *Microwave and optical technology letters*, vol. 7, no. 13, pp. 599–604, 1994.
- [81] T. Weiland, "Time domain electromagnetic field computation with finite difference methods," *International Journal of Numerical Modelling: Electronic Networks, Devices and Fields*, vol. 9, no. 4, pp. 295–319, 1996.
- [82] B. Krietenstein, R. Schuhmann, P. Thoma, and T. Weiland, "The perfect boundary approximation technique facing the big challenge of high precision field computation," in *Proceedings of the XIX International Linear Accelerator Conference (LINAC 98), Chicago, USA*, 1998, pp. 860–862.
- [83] J. A. Roden and S. D. Gedney, "Convolutional pml (cpml): An efficient fdtd implementation of the cfs-pml for arbitrary media," *Microwave and optical technology letters*, vol. 27, no. 5, pp. 334–338, 2000.
- [84] A. Dennis and E. Pierce, "The return stroke of the lightning flash to earth as a source of vlf atmospherics," *Radio Sci. D*, vol. 68, pp. 777–794, 1964.
- [85] D. L. Jones, "Electromagnetic radiation from multiple return strokes of lightning," *Journal of Atmospheric and Terrestrial Physics*, vol. 32, no. 6, pp. 1077–1093, 1970.
- [86] D. Sentman, "Detection of elliptical polarization and mode splitting in discrete schumann resonance excitations," *Journal of atmospheric and terrestrial physics*, vol. 51, no. 6, pp. 507–519, 1989.
- [87] T. Ogawa, Y. Tanaka, M. Yasuhara, A. Fraser-Smith, and R. Gendrin, "Worldwide simultaneity of occurrence of a q-type elf burst in the schumann resonance frequency range," *Journal of geomagnetism and geoelectricity*, vol. 19, no. 4, pp. 377–384, 1967.
- [88] T. Ogawa and M. Komatsu, "Analysis of q burst waveforms," *Radio Science*, vol. 42, no. 2, 2007.
- [89] —, "Q-bursts from various distances on the earth," *Atmospheric Research*, vol. 91, no. 2, pp. 538–545, 2009.
- [90] A. Nickolaenko, M. Hayakawa, and Y. Hobara, "Q-bursts: Natural elf radio transients," *Surveys in Geophysics*, vol. 31, no. 4, pp. 409–425, 2010.
- [91] P. R. Bannister, "Elf propagation update," *Oceanic Engineering, IEEE Journal of*, vol. 9, no. 3, pp. 179–188, 1984.

- [92] D. D. Sentman, "Schumann resonances," *Handbook of atmospheric electrodynamics*, vol. 1, p. 267, 1995.
- [93] A. C. Cangellaris and D. B. Wright, "Analysis of the numerical error caused by the stair-stepped approximation of a conducting boundary in fdtd simulations of electromagnetic phenomena," *Antennas and Propagation, IEEE Transactions on*, vol. 39, no. 10, pp. 1518–1525, 1991.
- [94] J. B. Lee, D. L. Dart, R. J. Turner, M. A. Downey, A. Maddever, G. Panjkovic, C. P. Foley, K. E. Leslie, R. Binks, C. Lewis *et al.*, "Airborne tem surveying with a squid magnetometer sensor," *Geophysics*, vol. 67, no. 2, pp. 468–477, 2002.
- [95] R. W. Simon, M. J. Burns, M. S. Colclough, G. Zaharchuk, and R. Cantor, "Mr. squid user's guide," Star Cryoelectronics, Tech. Rep., 2010.
- [96] P. Febvre, "Digital squid magnetometer development for geophysics applications validated in low-noise environment," in *IEEE/CSC & EUROPEAN SUPERCOND. NEWS FORUM*, no. 5, 2008, pp. 1–6.
- [97] C. M. R. Fowler, *The solid earth: an introduction to global geophysics*. Cambridge University Press, 1990.
- [98] T. P. O'Brien and R. L. McPherron, "Forecasting the ring current index dst in real time," *Journal of Atmospheric and Solar-Terrestrial Physics*, vol. 62, no. 14, pp. 1295–1299, 2000.
- [99] T. J. Ahrens, *Global earth physics: a handbook of physical constants*. American Geophysical Union, 1995, vol. 1.
- [100] C. Price, O. Pechony, and E. Greenberg, "Schumann resonances in lightning research," *J. of Lightning Res*, vol. 1, pp. 1–15, 2007.
- [101] A. Nickolaenko, "Modern aspects of schumann resonance studies," *Journal of Atmospheric and Solar-Terrestrial Physics*, vol. 59, no. 7, pp. 805–816, 1997.
- [102] S. De, B. De, B. Bandyopadhyay, S. Paul, D. Haldar, and S. Barui, "Studies on the shift in the frequency of the first schumann resonance mode during a solar proton event," *Journal of Atmospheric and Solar-Terrestrial Physics*, vol. 72, no. 11, pp. 829–836, 2010.
- [103] C. Price and A. Melnikov, "Diurnal, seasonal and inter-annual variations in the schumann resonance parameters," *Journal of atmospheric and solar-terrestrial physics*, vol. 66, no. 13, pp. 1179–1185, 2004.
- [104] D. Sentman, "Magnetic elliptical polarization of schumann resonances," *Radio Science*, vol. 22, no. 4, pp. 595–606, 1987.
- [105] M. J. Caruso, T. Bratland, C. H. Smith, and R. Schneider, "A new perspective on magnetic field sensing," *Sensors-Peterborough*, vol. 15, pp. 34–47, 1998.
- [106] M. L. Burrows, *ELF communications antennas*. P. Peregrinus, 1978, vol. 5.

- [107] G. Belyaev, A. Y. Schekotov, A. Shvets, and A. Nickolaenko, "Schumann resonances observed using poynting vector spectra," *Journal of atmospheric and solar-terrestrial physics*, vol. 61, no. 10, pp. 751–763, 1999.
- [108] T. Saito, T. Sakurai, K. Yumoto, T. Tamura, M. Seto, and T. Hayasaka, "Magnetometers for geophysical use part 1. fluxgate magnetometer with a 0.5-m length two-core sensor," *Journal of Geomagnetic Geoelectricity*, 1980.
- [109] T. Saito, T. Sakurai, K. Yumoto, T. Tamura, M. Seto, T. Hayasaka, and I. Aoyama, "Magnetometer for geophysical use part 2. test of twelve kinds of ring core," *Journal of Geomagnetic Geoelectricity*, 1980.
- [110] G. Waysand, D. Bloyet, J. Bongiraud, J. Collar, C. Dolabdjian, and P. Le Thiec, "First characterization of the ultra-shielded chamber in the low-noise underground laboratory (lsbb) of rustrel-pays d'apt," *Nuclear Instruments and Methods in Physics Research Section A: Accelerators, Spectrometers, Detectors and Associated Equipment*, vol. 444, no. 1, pp. 336–339, 2000.
- [111] S. Gaffet, Y. Guglielmi, J. Virieux, G. Waysand, A. Chwala, R. Stolz, C. Emblanch, M. Auguste, D. Boyer, and A. Cavaillou, "Simultaneous seismic and magnetic measurements in the low-noise underground laboratory (lsbb) of rustrel, france, during the 2001 january 26 indian earthquake," *Geophysical Journal International*, vol. 155, no. 3, pp. 981–990, 2003.
- [112] G. Waysand, J. Marfaing, E. P. di Borgo, R. Blancon, M. Pyée, M. Yedlin, P. Barroy, M. Auguste, D. Boyer, A. Cavaillou *et al.*, "Earth-ionosphere couplings, magnetic storms, seismic precursors and tles: Results and prospects of the [squid] 2 system in the low-noise underground laboratory of rustrel-pays d apt," *Comptes Rendus Physique*, vol. 12, no. 2, pp. 192–202, 2011.
- [113] Lsbb. (2013) Laboratoire souterrain à bas bruit. [Online]. Available: <http://www.lsbb.eu/index.php/en/>
- [114] J. Marfaing, J.-J. Bois, R. Blancon, E. P. Di Borgo, G. Waysand, S. Gaffet, M. Yedlin, P. Barroy, M. Auguste, D. Boyer *et al.*, "About the world-wide magnetic-background noise in the millihertz frequency range," *EPL (Europhysics Letters)*, vol. 88, no. 1, p. 19002, 2009.
- [115] J. Marfaing, E. Pozzo di Borgo, G. Waysand, A. Cavaillou, and M. Parrot, "Global observation of 24 november 2006 pc5 pulsations by single mid-latitude underground [squid] 2 system," in *Annales Geophysicae*, vol. 29, no. 11. Copernicus GmbH, 2011, pp. 1977–1984.
- [116] C. Bianchi and A. Meloni, "Terrestrial natural and man-made electromagnetic noise," *Istituto Nazionale di Geofisica e Vulcanologia-Roma*, pp. 1–18.
- [117] S. V. Vaseghi, *Advanced digital signal processing and noise reduction*. John Wiley & Sons, 2008.
- [118] A. V. Oppenheim, R. W. Schaffer, J. R. Buck *et al.*, *Discrete-time signal processing*. Prentice-hall Englewood Cliffs, 1989, vol. 2.
- [119] K. Riley, M. Hobson, and S. Bence, "Mathematical methods for physics and engineering," *American Journal of Physics*, vol. 67, no. 2, pp. 165–169, 1999.

- [120] J. G. Proakis and D. G. Manolakis, *Introduction to digital signal processing*. Prentice Hall Professional Technical Reference, 1988.
- [121] S. J. Orfanidis, *Introduction to signal processing*. Prentice-Hall, Inc., 1995.
- [122] J. Cooley and J. Tukey, "An algorithm for the machine computation of complex fourier series, vol. 19," *Mathematics of Computation*, 1965.
- [123] M. H. Hayes, *Schaum's Outline of Theory and Problems of Digital Signal Processing*. McGraw Hill, 1999.
- [124] H. Schumann, WO König, "Über die beobachtung von atmospherics bei geringsten frequenzen," *Naturwissenschaften*, vol. 41, no. 8, pp. 183–184, 1954.
- [125] P. D. Welch, "The use of fast fourier transform for the estimation of power spectra: A method based on time averaging over short, modified periodograms," *IEEE Transactions on audio and electroacoustics*, vol. 15, no. 2, pp. 70–73, 1967.
- [126] P. M. Broersen, *Automatic autocorrelation and spectral analysis*. Springer Science & Business Media, 2006.
- [127] A. V. Oppenheim and G. C. Verghese, "Signals, systems, and inference," *Class notes for*, vol. 6, 2010.
- [128] M. Cerna and A. F. Harvey, "The fundamentals of fft-based signal analysis and measurement," *National Instruments, Junho*, 2000.
- [129] G. Heinzl, A. Rüdiger, and R. Schilling, "Spectrum and spectral density estimation by the discrete fourier transform (dft), including a comprehensive list of window functions and some new at-top windows," *Internal Report, Max-Planck-Institut für Gravitationsphysik, Hannover, 2002*, 2002.
- [130] F. J. Harris, "On the use of windows for harmonic analysis with the discrete fourier transform," *Proceedings of the IEEE*, vol. 66, no. 1, pp. 51–83, 1978.
- [131] L. Dactron, "Understanding fft windows," *Application Note. lds group*, 2003.
- [132] M. Frigo and S. G. Johnson, "Fftw: An adaptive software architecture for the fft," in *Acoustics, Speech and Signal Processing, 1998. Proceedings of the 1998 IEEE International Conference on*, vol. 3. IEEE, 1998, pp. 1381–1384.
- [133] M. Born and E. Wolf, "Principles of optics, 1964," *New York: Mac-Millan*, 1959.
- [134] L. D. Landau and E. Lifshitz, *Course of Theoretical Physics: Vol.: 8: Electrodynamics of Continuous Media*. Pergamon Press, 1960.
- [135] R. Fowler, B. Kotick, and R. Elliott, "Polarization analysis of natural and artificially induced geomagnetic micropulsations," *Journal of Geophysical Research*, vol. 72, no. 11, pp. 2871–2883, 1967.
- [136] P. Holtham and B. McAskill, "The spatial coherence of schumann activity in the polar cap," *Journal of atmospheric and terrestrial physics*, vol. 50, no. 2, pp. 83–92, 1988.

- [137] V. Roldugin and A. Vasilev, "Variations in the schumann resonance polarization ellipse in the horizontal and vertical planes according to observations at the barentsburg and lozero observatories," *Geomagnetism and Aeronomy*, vol. 52, no. 1, pp. 68–76, 2012.
- [138] N. Rusakov and S. Bakastov, "Rotation of the horizontal projection of a magnetic-field disturbance vector at schumann-resonance frequencies," *Geomagnetism and Aeronomy*, vol. 28, pp. 919–922, 1988.
- [139] A. Nickolaenko, L. Rabinovich, A. Shvets, and A. Y. Shchekotov, "Polarization characteristics of low-frequency resonances in the earth-ionosphere cavity," *Radiophysics and quantum electronics*, vol. 47, no. 4, pp. 238–259, 2004.
- [140] A. Jones, "Difference between polarization and coherence," pp. 223–229, 1979.
- [141] G. R. C. for Geosciences. Quietest and most disturbed day of 2007. [Online]. Available: <http://www.gfz-potsdam.de/en/centre/about-us/>
- [142] U. G. Survey. Worldwide seismic activity. [Online]. Available: <http://earthquake.usgs.gov/earthquakes/>
- [143] D. Labendz, "Investigation of schumann resonance polarization parameters," *Journal of atmospheric and solar-terrestrial physics*, vol. 60, no. 18, pp. 1779–1789, 1998.
- [144] E. P. Pozzo di Borgo, J. Marfaing, and G. Waysand, "Minimal global magnetic millihertz fluctuation level determined from mid-latitude underground observations," *EPL (Europhysics Letters)*, vol. 97, no. 4, p. 49001, 2012.
- [145] E. P. d. B. Shneha Bernard, Pascal Febvre, "Lsbb 3-axis [squid]² magnetometer: Report on measurements of july 27th and july 28th 2010," Laboratoire Souterrain à Bas Bruit, University of Savoie, University of Avignon, Tech. Rep., 2010.
- [146] [Online]. Available: [<http://www.timeanddate.com/>]
- [147] O. Pechony, C. Price, and A. Nickolaenko, "Relative importance of the day-night asymmetry in schumann resonance amplitude records," *Radio Science*, vol. 42, no. 2, 2007.
- [148] V. Roldugin, Y. Maltsev, A. Vasiljev, A. Y. Schokotov, and G. Belyajev, "Diurnal variations of schumann resonance frequency in ns and ew magnetic components," *Journal of Geophysical Research: Space Physics*, vol. 109, no. A8, 2004.
- [149] K. Schlegel and M. Füllekrug, "Diurnal harmonics in schumann resonance parameters observed on both hemispheres," *Geophysical research letters*, vol. 27, no. 17, pp. 2805–2808, 2000.